Synthesis and Electronic Structure Investigation of Ruthenium Complexes Containing Novel Redox-Active Ligands

Von der Fakultät Chemie der Universität Stuttgart
zur Erlangung der Würde eines
Doktors der Naturwissenschaften
(Dr. rer. nat.)
genehmigte Abhandlung

Vorgelegt von

Fabian Ehret

aus Freiburg

Hauptberichter:	Prof. Dr. Wolfgang Kaim
Mitberichter:	Prof. Dr. Dietrich Gudat
Prüfungsvorsitzender:	Prof. Dr. Bernd Plietker
Tag der mündlichen Prüfung:	28.05.2014

INSTITUT FÜR ANORGANISCHE CHEMIE DER UNIVERSITÄT STUTTGART

2014

Acknowledgements

This work was completed from November 2010 to April 2014 at the Institute of Inorganic Chemistry, University of Stuttgart.

First I would like to express my gratitude to my supervisor Prof. Dr. Wolfgang Kaim for giving me the opportunity and the facilities to carry out this thesis work in his group, for all his ideas, discussions, his patience and guidance throughout my research work.

I would also like to thank:

- Dipl. Chem. Martina Bubrin for solving the crystal structures and Dr. Wolfgang Frey performing the X-ray measurements
- Dr. Stanislav Záliš (J. Heyrovský Institute of Physical Chemistry, Department of Electrocatalysis, Prague) for performing the DFT calculations
- Dipl. Chem. Vasileios Filippou for helping out with the spectroelectrochemical measurements
- Dr. José Luis Priego and Prof. Jiménez-Aparicio for SQUID measurements
- Mrs. Barbara Förtsch for elemental analysis and Mrs. Katharina Török and Mrs. Michaela Benzinger for NMR measurements
- Dr. Brigitte Schwederski for proofreading the manuscript

Finally I would like to thank all the members of Institut für Anorganische Chemie, Universität Stuttgart, especially, the group members of Prof. Kaim's and Prof. Sarkar's research group.

Contents

1 Introduction

Interest in complexes of "non-innocent" ligands (NILs) has tremendously increased during the last decades due to their appearance in biological systems[1] and their possible application in molecular electronics,[2] molecular magnetism,[3] light harvesting devices,[4] homogeneous catalysis ,[5] and group transfer reactions.[6]

Originally, the concept of ligand "non-innocence" was developed by Jørgensen in 1966 when he pointed out that "ligands are innocent when they allow oxidation states of the central atoms to be defined"[7] and therefore denoted all other ligands as "suspect" or "non-innocent". By means of this definition Jørgenson intended to highlight the oxidation-state ambiguity of complexes containing redox-active transition metals as well as redox-active ligands, which can give rise to "wrong" oxidation-state assignments.[8] The assignment of "correct" oxidation states does not only serve the simple role of electron bookkeeping, it also provides information about the physical properties and chemical reactivity related therewith.[9] For some ligands the electronic structure of their transition metal complexes in their isolated form ("native state") is unambiguous, whereas ambiguity arises for other oxidation states.[10] Such types of ligands can be labeled as "redox non-innocent". For a more precise description of redox processes and for highlighting their ambiguity, the expressions ligand/metal centered oxidation/reduction are frequently used. The valence situation in different oxidation states of a complex containing an exemplary enediolate/catecholate non-innocent ligand is illustrated in Figure 1.1.

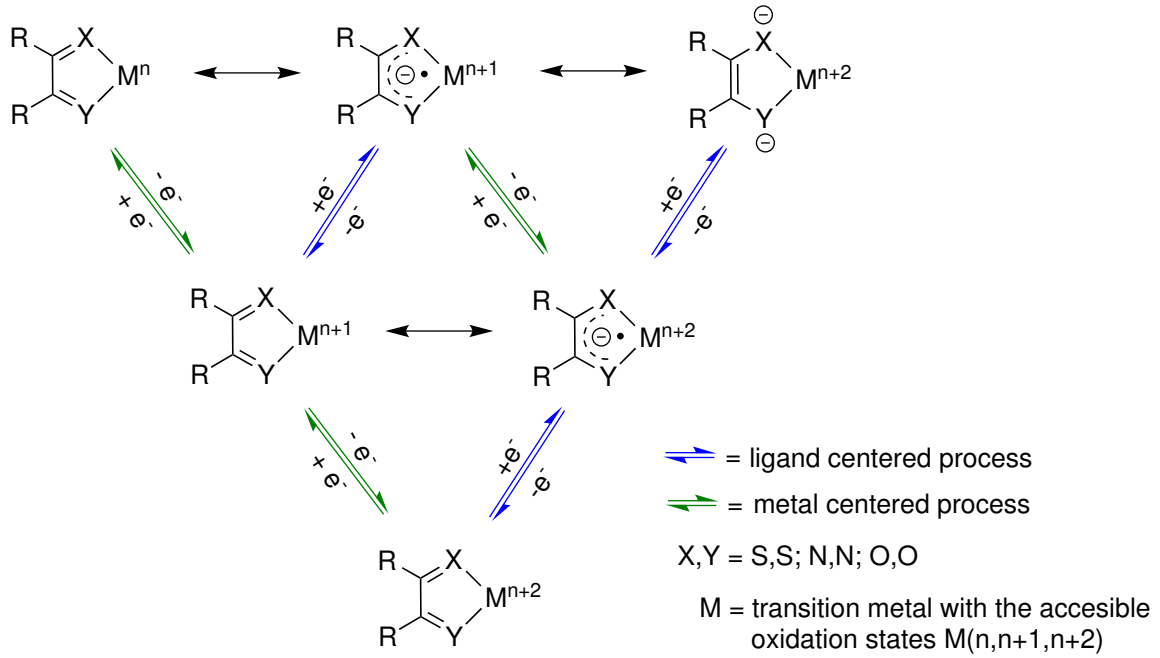

Figure 1.1: *Illustration of non-innocent ligand behavior in various oxidation states.*

Although the expression "non-innocent ligand" is widespread, it is important to mention that non-innocence emerges from particular combinations of metal and ligand rather than being an intrinsic property of a ligand. Therefore Ward and McCleverty declared the more appropriate term "non-innocent behavior" for particular coordination situations in preference to "non-innocent ligand".[11]

There are many different manifestations[12] of non-innocent ligand behavior after electron transfer to or from the NIL, such as structural variations,[13] alternations in the acid/base properties, occasionally accompanied by changes of the coordination mode,[14] and changes in the reactivity of the complex.[15] Such indications can serve either as probe for NIL behavior of already established ligands[16] or as basis for the design and development of new NILs.

For electronic structure determination of transition-metal coordination compounds an extensive toolbox of physical methods is available.[9] As part of this thesis, X-ray crystallography, EPR, NMR, UV-vis-NIR spectroscopy, and SQUID susceptometry are utilized in this regard. To obtain more detailed electrochemical information on the electronic structure of different oxidation states of the compounds, varied experimental setups, combining the spectroscopic methods (EPR/ UV-vis-NIR) with electrochemical methods (=spectroelectrochemistry[17]) are implemented.

Since electron transfer to or from redox-active ligands proceeds through single-electron steps, applying a potential to diamagnetic complexes containing this type of ligands necessarily leads to the formation of paramagnetic species. For reasons of predicting physical and chemical properties, e.g. magnetism or reactivity, it is generally of fundamental importance to obtain a deeper insight into the spin density distribution of paramagnetic coordination compounds. In contrast to the mixed situations,[18] two borderline classes can be defined: a) the ligand centered radical with mainly ligand contribution to the singly occupied molecular orbital (SOMO) and b) the metal centered paramagnetic complexes with mostly metal contribution to the SOMO. Besides various theoretical methods,[19] EPR spectroscopy/spectroelectrochemistry is the most powerful experimental tool for scrutinizing paramagnetic complexes for their spin density distribution.[20]

EPR spectroscopy provides three sources of information:

(1) The isotropic g value: The electron g value has its origin in quantum electrodynamics and is roughly equivalent in utility as the chemical shift is in NMR. Basically the g value is consistent of a second order tensor (matrix), describing a surface in three spatial dimensions. The value of g is therefore anisotropic, i. e. it depends on the relative orientation of the molecule as compared to the magnetic field direction. In solution at room temperature, however, the rotation of small and medium sized molecules is too fast to resolve the different spatial direction on the conventional EPR time scale. Therefore, only the average isotropic g value is

observed in solution. The experimental g value is given through the resonance condition in Equation 1.1.

$$g = \frac{h\nu}{\mu_B H} \tag{1.1}$$

h = Planck constant, ν = frequency, μ_B = Bohr magneton, H = magnetic field

The deviation of the isotropic g value from the free electron value $g_e = 2.0023$ is attributed to the admixture of higher excited states to the radical ground state, resulting from spin-orbit coupling. The spin-orbit coupling constant increases with the atomic number Z and is hence much larger for heavy transition metal atoms than for the lighter second and third row main group atoms, of which most ligands consist. This behavior results from the relativistic origin of spin-orbit interactions.[21] Thus the deviation of the isotropic g value from g_e indicates the participation of the transition metal atom/ion at the SOMO. For heavy transition metal centered spins the isotropic g value is frequently unobservable at room temperature due to line broadening based on fast spin relaxation.

$$g = g_e - \frac{2}{3}\sum_i \sum_n \sum_{kj} \frac{<\Psi_0|\xi_k L_{ik}\delta_k|\Psi_n><\Psi_n|L_{ij}\delta_j|\Psi_0>}{E_n - E_0} = g_e + \Delta g_s \tag{1.2}$$

$g_e = 2.0023$

Ψ_0 : MO of the unpaired electron in the ground state

Ψ_n : all other MOs

ξ_k : spin orbit coupling constant

$L_{ik/ij}$: angular momentum operator for AO at nucleuskj

$L_{ik}\delta_k = 0$except at atom$k$

E_0 : energy of a singly occupied molecular orbital (SOMO)

E_n : energies of empty or doubly occupied molecular orbitals (LUMO or HOMO)

Equation 1.2 illustrates Stone's approximation[22] for the deviation of the g value as function of the spin orbit coupling constant and the energy difference between the SOMO and all other orbitals. Because the energy differences are in the denominator of Equation 1.2, only the neighbouring energy levels (HOMO and LUMO) need to be considered for significant contributions to Δg. With respect to the relative energetic position of the three orbitals, however, two different cases, depicted in Figure 1.2, are possible. If the SOMO is closer in energy to the HOMO than to the LUMO ($E_0 > E_n$), the g value is greater than g_e and vice

versa. Consequently, the relative energy difference of the three frontier orbitals of radical species can be concluded from the deviation from g_e of the isotropic g value.

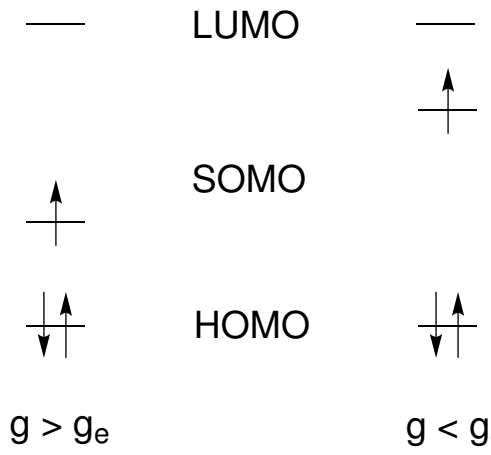

Figure 1.2: *Correlation between the relative energy of the frontier orbitals and the deviation of the g value from g_e*

(2) The g anisotropy: In samples consisting of powders or glassy frozen solutions, the rotation of the molecules is hindered and thus the resonance lines of all three independent spatial directions of the g value appear in the EPR spectrum, conventionally labeled as g_x, g_y and g_z or g_1, g_2 and g_3 respectively. Out of the three principal g values the g anisotropy $\Delta g = g_1\text{-}g_3$ and the average g value $<g>$ (Equation 1.3) can be defined. Since the g anisotropy is related to the spin-orbit coupling constant in similar fashion as in (1), it can also be utilized as a probe for the heavy transition metal participation at the SOMO.

$$<g> = \sqrt{\frac{{g_1}^2 + {g_2}^2 + {g_3}^2}{3}} \tag{1.3}$$

(3) The hyperfine coupling: The coupling of the unpaired electrons in the complex to nuclei with a non-zero spin $I \neq 0$ results in a hyperfine structure of the EPR spectrum. The strength of the coupling is reflected by the hyperfine coupling constant, which is related to the spin density at the coupling nucleus. Hence, the hyperfine coupling constant provides information about the spin density distribution and the coordination environment of a paramagnetic transition metal complex. Unfortunately, the hyperfine structure of transition metal complexes is often insufficiently resolved due to a large number of overlapping lines. A substantial amount of spin density on the metal induces line broadening and may therefore quench the hyperfine structure.

To analyze the electronic structure of diamagnetic coordination compounds with NILs, X-ray crystallography is one of the most compelling methods. This approach utilizes the fact that redox-active ligands undergo structural changes by adopting different oxidation states. These variations can be changes of bond length, bond angles, or torsional angles of the NILs. In

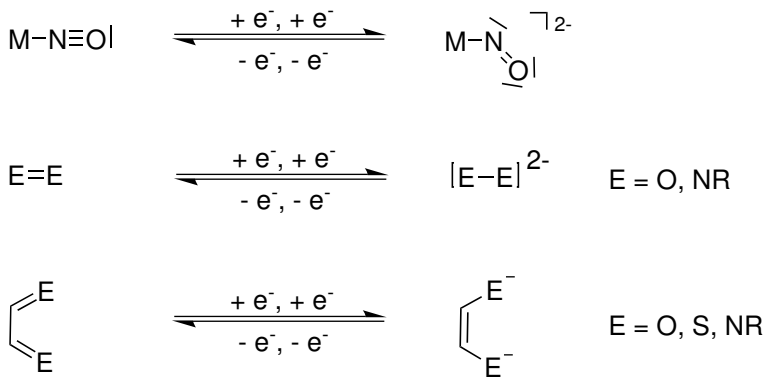

Figure 1.3: *Correlation between the redox state and the structure of some prominent NILs.*

this way the structural manifestations of a ligand can be attributed to a specific oxidation state. In Figure 1.3 the structural variations of some prominent NILs are depicted. Besides diamagnetic systems radical ligands can also be identified by their structural properties. This method of identification especially succeeds, when the unpaired electron at the NIL couples antiferromagnetically to a paramagnetic transition metal center or to another radical ligand, and can therefore not be detected by EPR.

Since Jørgenson introduced the terms "suspect" or "non-innocent" ligand in 1966, a growing number of well established ligand systems has been attributed this character.[23] Moreover, new types of ligands have been designed for the purpose of harnessing their NIL behavior for various applications.[24]

In this doctoral work, the idea of designing new types of NILs as well as revealing the NIL character of well established ligand systems is pursued. For complexation of NILs, ruthenium(II) precursors including a diverse platform of ancillary ligands have been used. Ruthenium(II) with its d^6 electron configuration comprises the advantage of adopting a stable low spin $S = 0$ ground state in octahedral ligand field. Therefore, ligand centered redox processes will result in an organic radical with $S = 1/2$ ground state, which can be investigated by EPR without difficulties. Due to the high spin-orbit coupling constant of ruthenium and the corresponding large g anisotropy, metal centered oxidations resulting in ruthenium(III) are easy to distinguish from ligand centered oxidations by EPR.[25] A reduction of ruthenium(II) to ruthenium(I) is highly improbable, regarding the used set of ancillary ligands.

Chapter 2 describes the synthesis and characterization of the mononuclear ruthenium α-azocarbonyl and α-azothiocarbonyl complexes $Ru(acac)_2(L_O)$, $Ru(acac)_2(L_S)$, $[Ru(bpy)_2(L_O)]PF_6$, and $[Ru(bpy)_2(L_S)]PF_6$ The complexes were experimentally characterized in various oxidation states by X-ray crystallography, NMR, CV, and EPR/UV-vis-NIR spectroelectrochemistry. Additionally DFT and TD-DFT methods were applied for obtaining an insight into the elec-

tronic structure of the compounds.

In Chapter 3 the synthesis and characterization of the dinuclear ruthenium α-azothiocarbonyl complexes $((acac)_2Ru)_2(\mu$-hte-NNCS-$NO_2)$ and $((acac)_2Ru)_2(\mu$-hte-NNCS-$CO_2Et)$ is described. In addition to the experimental methods utilized in Chapter 2, SQUID suszeptometry will be applied for investigation of the complex spin system of the two coordination compounds.

The research goal of Chapter 4 is to reveal the non-innocent character of the class of heteroallylic ligands. Therefore the synthesis and mainly EPR spectroelectrochemical investigation of a variety of different substituted triazenido ruthenium complexes is reported. The substitution pattern leading to the desired triazenyl radical complex is then adopted for the preparation of similar amidinato and guanidinato ruthenium complexes, which will then also reveal their non-innocent character. To investigate the strong NIR absorption of the radical complexes UV-vis-NIR spectroelectrochemistry will be applied.

In Chapter 5 the idea of utilizing amidinyl radical complexes as chromophores for the near infrared is pursued. For this purpose the synthesis of dimethylaminophenyl substituted amidinato complexes containing different metals as well as coordination modes is described. The influence of the metal and coordination mode on the absorption behavior of the radical ligand will be investigated by using UV–vis–NIR spectroelectrochemistry.

2 Mononuclear complexes with hetero-1,3-diene chelate ligands

2.1 Introduction

The 4-center hetero-1,3-diene chelate systems belong to the most widely used redox-active ligands in coordination chemistry.[1,12,23] For the chelation of metal ions the s-cis conformation of the 1,3-diene structure is required. Represented by the general formulation A=B-C=D, the system can undergo reduction in two single-electron steps to yield $^{-}$A-B=C-D^{-}, involving a radical anion intermediate (Scheme 2.1).

A, D = O, S, NR; B, C = N, CR

Figure 2.1: *Redox behavior of the hetero-1,3-diene ligand system.*

Due to the changes in the bond order, and thus in bond lengths, after electron transfer, the non-innocent behavior of such ligands in complexes with redox-active transition metals can be analyzed via structure analysis. Especially the easily reducible azo bond can serve as precise probe for the oxidation state of the ligand (Figure 2.2). Remarkably, even cases of weak and strong π back-donation can be discriminated in diverse azo ligand containing complexes.[13]

In addition to the prototypical symmetrical examples, the α-diimines[26] (including 2,2' -bipyridine[27] and related polypyridyls:[28] A, D = NR; B, C = CR'), the α-dicarbonyls[29] (including the o-quinone/o-semiquinone/catecholate series:[30] A, D = O; B, C = CR'), the α-dithiolenes (A, D = S; B, C = CR'),[31] and the tetraazadienes (A, D = NR; B, C = N)[32] there are also mixed examples such as the α-iminocarbonyl[33] and α-azoimine systems.[34] Of the remaining members of the general series (Figures 2.1, 2.3), the reduced α-oxothione function,[35] and one α-azocarbonyl example[36] have been reported earlier, the latter during attempts to prepare dinuclear compounds of azodicarbonyl ligands. The α-azothiocarbonyl function, however, has

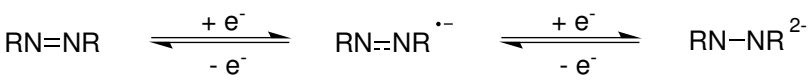

azo (azo)$^{\bullet-}$ dihydrazido

~ 1.25 Å ~ 1.35 Å ~ 1.45 Å

Figure 2.2: *Correlation between the bond length and the redox state of the azo bond.*

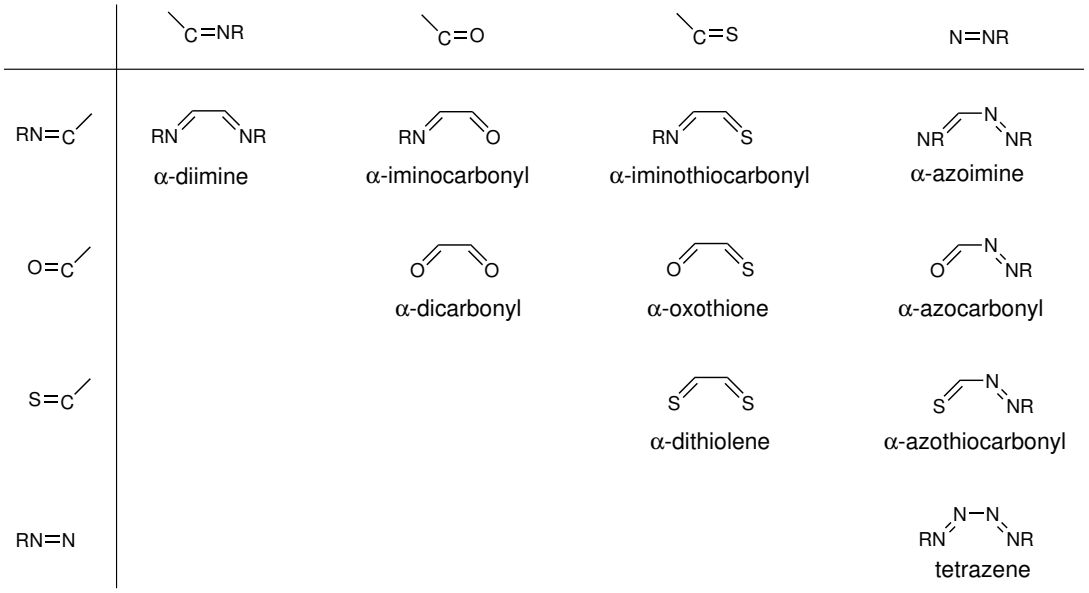

Figure 2.3: *Possible combination of structure elements for a hetero-1,3-diene ligand.*

not been established as bidentate chelate ligand in coordination chemistry to date. This single gap in the series of non-innocent hetero-1,3-diene chelate ligands originates from the difficult accessibility of complexes containing the α-azothiocarbonyl ligand function. While all other ligands in the series can be isolated in free form and can thus react with the appropriate transition metal precursor under straightforward conditions, the α-azothiocarbonyl function is not stable in free form[37] and can therefore not be isolated as pure ligand.

Electron affinity studies have shown the following energy order of the π* MOs of the carbonyl, the thiocarbonyl and the azo group: π*(C=S) $<$ π*(N=N) $<$ π*(C=O) (Figure 2.4).[38] The lowest energy of the π*(C=S) MO can be explained by a stabilization of the orbital resulting from the admixture of a higher lying sulfur 3d orbital. This ranking also indicates the best π-acceptor ability of thiocarbonyl containing hetero-1,3-diene chelate ligands. The ionization energy of the non-bonding orbitals on the heteroatoms follows the same trend as the electron affinity, and therefore reflects the order in electronegativity.

With regard to the unique electron acceptor and donor ability of the thiocarbonyl function, it was highly desirable to establish the α-azothiocarbonyl function as ligand in coordination chemistry, despite the challenges in synthesis. To obtain more detailed information about the different nature of the thiocarbonyl versus the carbonyl group, the synthesis and characterisation of the corresponding complexes containing the α-azocarbonyl function were also required for comparison.

This chapter describes a synthetic approach for the combination of α-azocarbonyl and α-azothiocarbonyl ligands with the electron-rich [Ru(acac)$_2$] and the more electron-deficient [Ru(bpy)$_2$]$^{2+}$ fragments. In the case of the α-azothiocarbonyl complexes, the ligand was

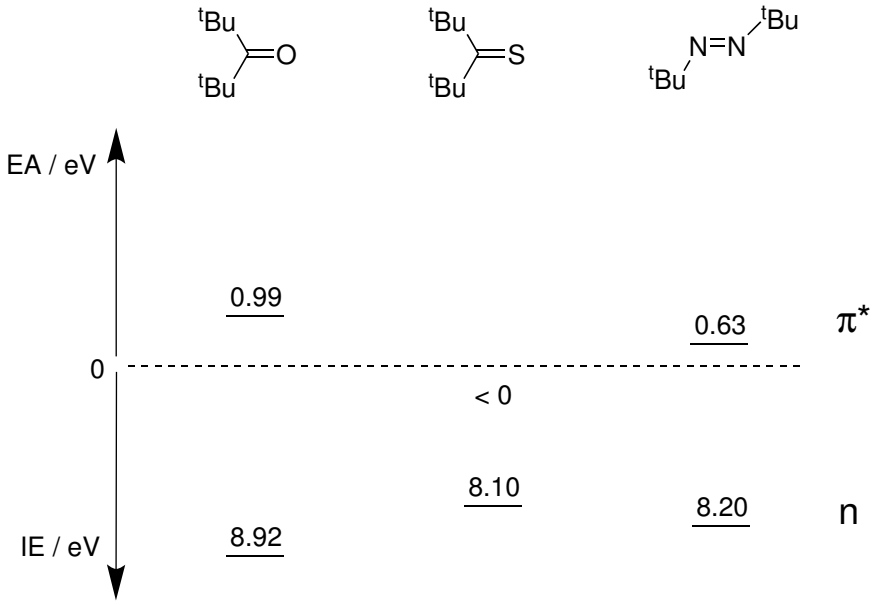

Figure 2.4: *Electron affinity and ionization energy for the azo, carbonyl and thiocarbonyl group in eV.*

generated *in situ* from Bis[α-(phenylhydrazono)phenyl]disulfide. This precursor has now been crystallized and its structure determined. The identities of the isolated ruthenium complexes as well as the non-innocent behavior of the corresponding ligands were revealed by X-ray crystallography. The nature of the other accessible oxidation states was investigated by cyclic voltammetry and spectroelectrochemistry (EPR, UV-vis-NIR). The experimental results were confirmed by DFT calculations.

2.2 Results and Discussion

2.2.1 Synthesis of the α-azocarbonyl complexes

The compounds **2**, **3**, **4**PF_6 have allready been synthesized during the diploma thesis. During the course of this doctoral work, the synthesis for **3**, **4**(PF_6) were optimized as discussed in the following sections and a single crystal of **4**PF_6, suitable for X-ray crystallography, was obtained.

2.2.1.1 Synthesis of the α-azocarbonyl ligand

The α-azocarbonyl ligand N-benzoyl-N'-phenyldiazene (**2/L**$_O$) was synthesized according to a straightforward two step literature procedure.[39] After an additional purification step using column chromatography (silica, CH_2Cl_2/n-hexan), the ligand was isolated in pure form as a deep red oily compound.

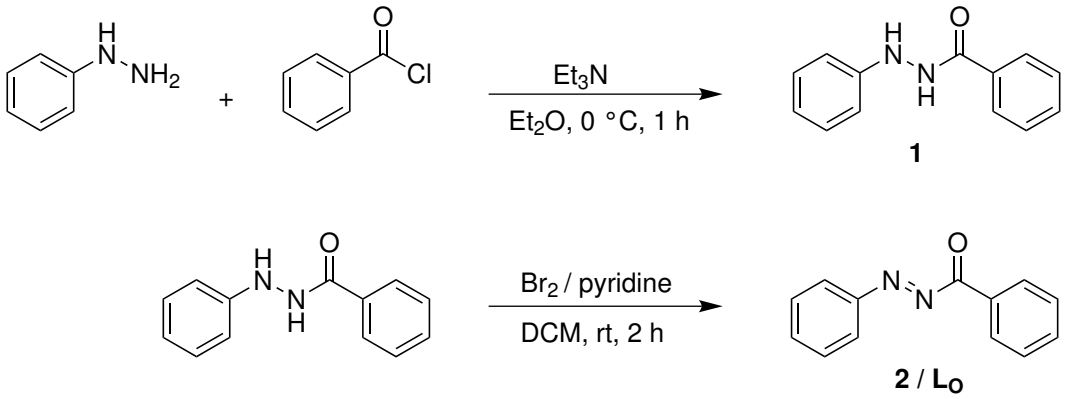

Figure 2.5: *Synthesis of the α-azocarbonyl ligand N-benzoyl-N'-phenyldiazene (**2/L**$_O$)*

2.2.1.2 Synthesis of the donor substituted α-azocarbonyl complex

For the synthesis of the donor substituted ruthenium α-azocarbonyl complex $Ru(acac)_2(L_O)$ (**3**), the general procedure, where a mixture of the complex fragment $Ru(acac)_2(MeCN)_2$[40] and a π-acceptor ligand (here **2**) are refluxed in ethanol under inert atmosphere, did not lead to the formation of the desired product. The failure of this method may be explained by the activation of the already strongly electrophilic α-azocarbonyl function towards the reaction of nucleophiles (e.g. ethanol), due to the coordination to a Lewis acidic metal ion. By changing the reaction conditions to non nucleophilic solvents such as dichloromethane and toluene and to a decreased temperature, the product was isolated in good yield (63 %). After purification with column chromatography (silica, CH_2Cl_2/acetonitrile) a pure red solid was obtained. The diamagnetic compound was characterized by NMR and X-ray crystallography.

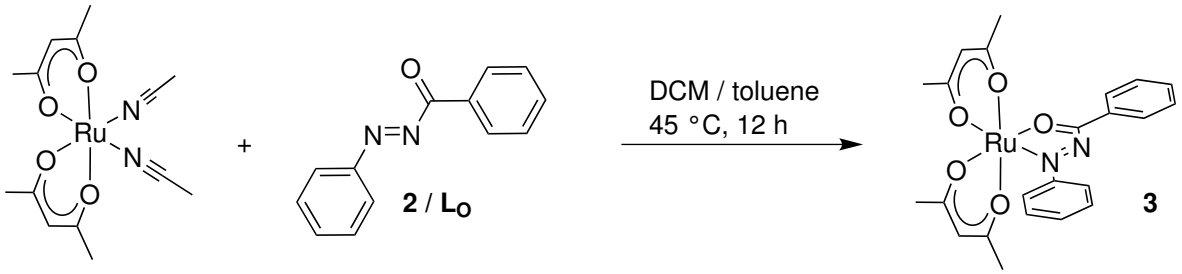

Figure 2.6: *Synthesis of Ru(acac)$_2$(L$_O$)*

2.2.1.3 Synthesis of the acceptor substituted α-azocarbonyl complex

For the synthesis of the acceptor substituted α-azocarbonyl complex [Ru(bpy)$_2$(L$_O$)]PF$_6$[41] (**4**PF$_6$) the reaction conditions also had to be varied, in comparison to the standard conditions. Therefore, the nucleophilic and weakly coordinating ethanol was substituted by the less nucleophilic and also weakly coordinating acetone. After abstraction of the chloride ions in acetone, the activated ruthenium bis(bipyridine) precursor $[Ru(bpy)_2(acetone)_2]^{2+}$ was reacted with **2** under inert atmosphere in acetone. After purification using column chromatography (silica, CH_2Cl_2/acetonitrile), a pure green solid was obtained. Surprisingly, elemental analysis revealed a molecular formula of $C_{33}H_{26}N_6ORuPF_6$ in stead of the expected formula of $C_{33}H_{26}N_6ORuP_2F_{12}$, indicating that the doubly positively charged complex, obtained through the reaction of the metal precursor $[Ru(bpy_2)(acetone)_2]^{2+}$ and the neutral ligand **2**, had to be reduced by one electron during the course of the reaction. The reducing agent could not be identified. Due to the *in situ* reduction, a paramagnetic complex was obtained, which could not be analyzed by NMR. Therefore, EPR and X-ray crystallography were used for the identification of the complex.

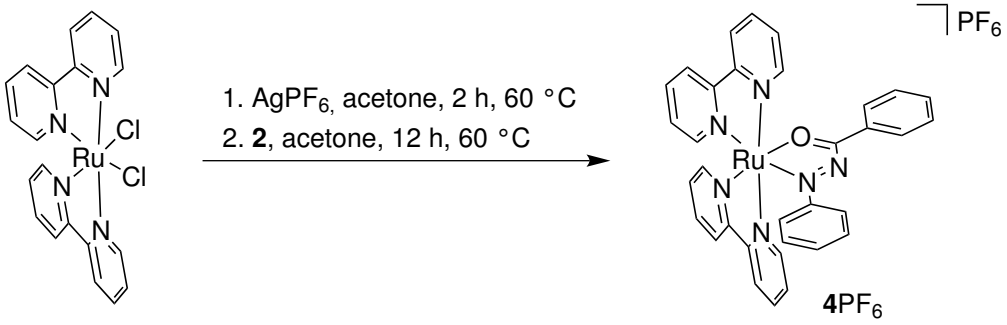

Figure 2.7: *Synthesis of [Ru(bpy)$_2$(L$_0$)]PF$_6$*

2.2.2 Synthesis of the α-azothiocarbonyl complexes

2.2.2.1 Synthetic view on the elusive α-azothiocarbonyl ligand

In contrast to the α-azocarbonyl ligand the corresponding α-azothiocarbonyl ligand is not stable in free from and can therefore not be isolated as a pure ligand. While the the α-azocarbonyl

ligand can be obtained through a two electron oxidation of the 1-acetyl-2-phenylhydrazine with bromine, the treatment of 1-thioacetyl-2-phenylhydrazine[42] with bromine or hydrogen peroxide respectively, results in the formation of the stable bis[α-(phenylhydrazono)phenyl]disulfide[43] (**6**) via one electron oxidation. This behavior can be explained by a thionamide-thiolimide tautomerism. Even though the thionamide **5a** is the thermodynamically favoured tautomeric form, the equilibrium constant in the direction of the thiolimide **5b** seems to be sufficiently high to allow its oxidation with a fast reaction rate. The preferred oxidation of the thiolimine compared to the thionamide results from the low redox potential of thioles.[44] An additional one electron oxidation of **6** with 2,3-dichloro-5,6-dicyano-p-benzoquinone (DDQ) leads to the formation of the actually desired α-azothiocarbonyl **7** which, however, undergoes fast intermolecular cycloaddition to yield **8** (Scheme 2.8).[37]

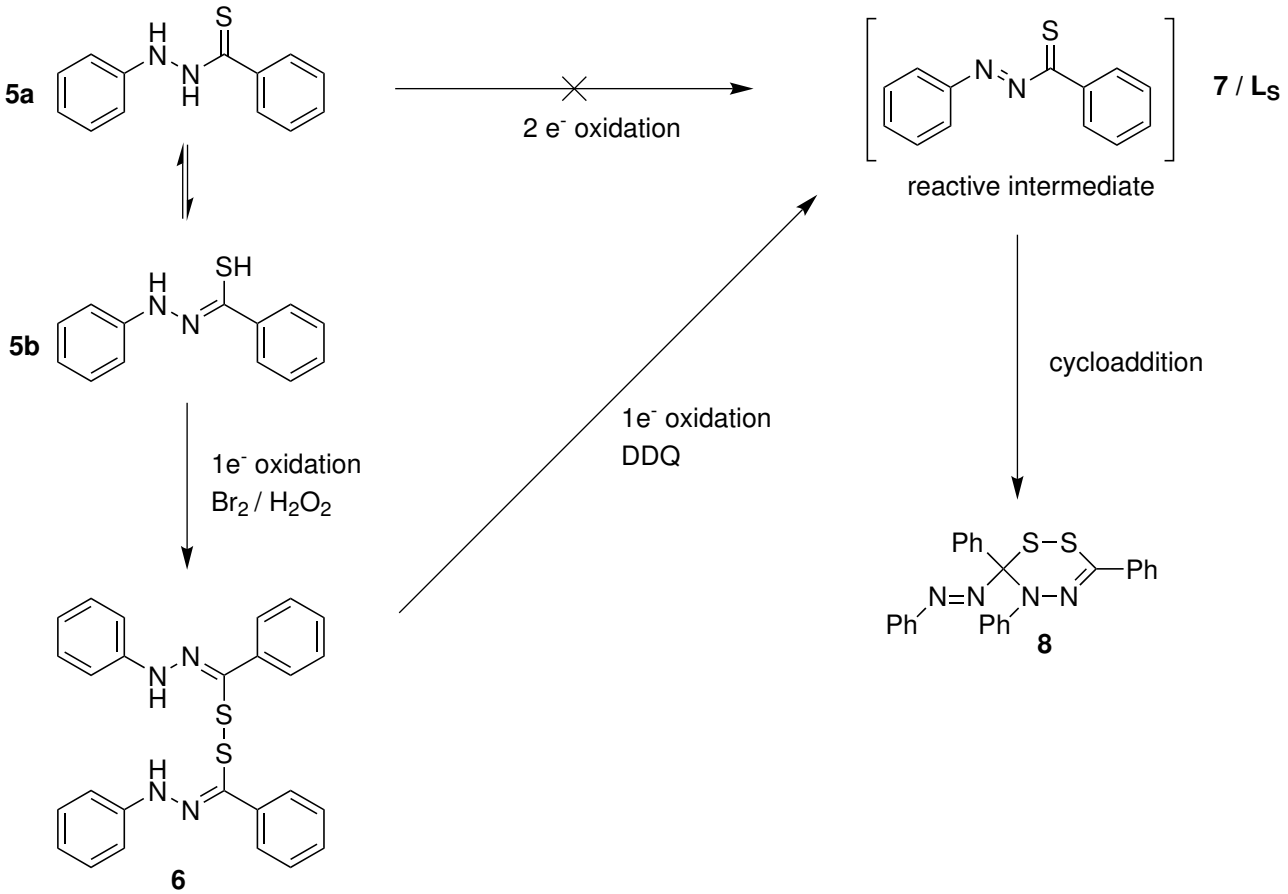

Figure 2.8: *Scheme illustrating the synthetic difficulties regarding the α-azothiocarbonyl ligand.*

2.2.2.2 Synthesis of the donor and acceptor substituted α-azothiocarbonyl complexes

Since the α-azothiocarbonyl ligand can not be isolated in free from, a novel approach for the synthesis of α-azothiocarbonyl containing complexes had to be developed. The fact that compound **6** is, except for an additional hydrogen atom, the dimer of the desired ligand **7**, and

that the disulfide bond is prone to be cleaved under reductive conditions, made compound **6** attractive to be used as precursor for **7**.

For the synthesis of the complex $Ru(acac)_2(L_S)$ (**9**) the metal precursor $Ru(acac)_2(MeCN)_2$ was reacted with the disulfide **6** under the same conditions as for the synthesis of **3**. During the reaction the disulfide bond of **6** was cleaved, most likely by reduction with the electron donating $Ru(acac)_2$ fragment, and a formal hydrogen atom was abstracted, resulting in the formation of **9** in a similarly good yield (61 %) than **3**. After purification with column chromatography (silica, CH_2Cl_2/acetonitrile), a pure red-violet solid was obtained. The diamagnetic compound was characterized by NMR and X-ray crystallography.

The synthesis of $[Ru(bpy)_2(L_S)]BF_4$ **10**BF_4 was conducted under the same conditions as for the synthesis of **4**PF_6, except that disulfide **5** and $AgBF_4$ was used instead of **2** and $AgPF_6$. Again, a cleavage of the disulfide bond and a formal hydrogen abstraction occurred, leading to the monoanionic and paramagnetic complex **10**PF_6, which was characterized by EPR and X-ray crystallography.

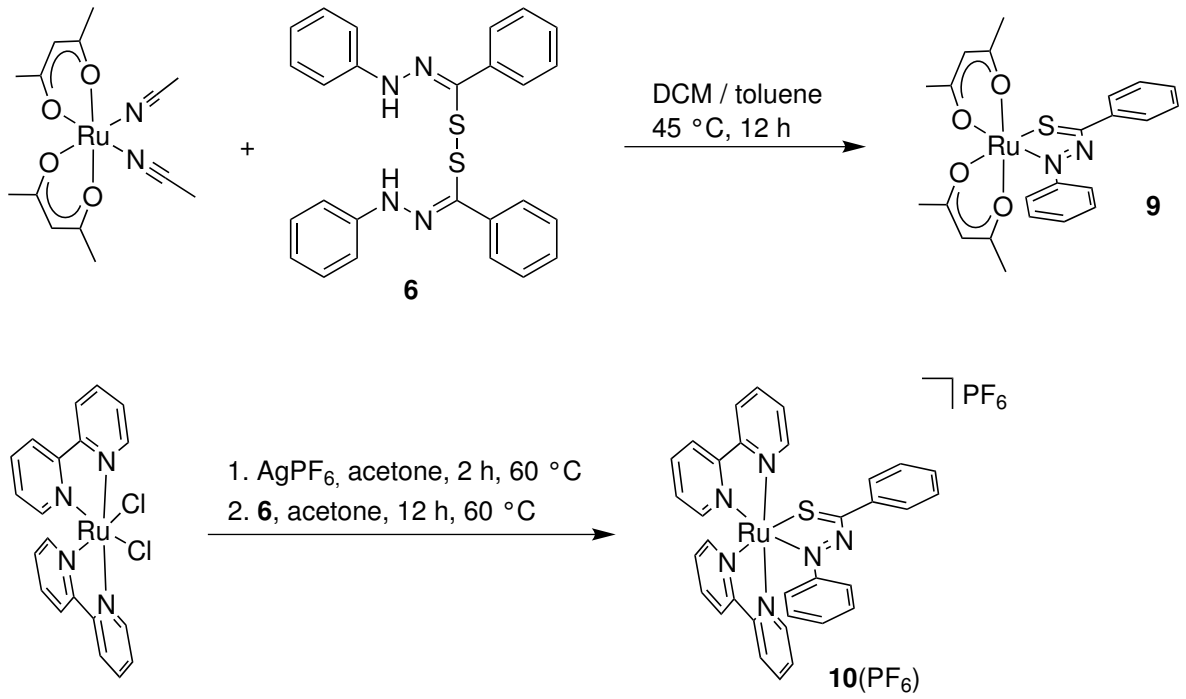

Figure 2.9: *Synthesis of $Ru(acac)_2(L_S)$ and $[Ru(bpy)_2(L_S)]PF_6$*

2.2.3 Molecular structures

Complexes **3**, **4**PF_6, **9** and **10**PF_6, as well as the precursor of the α-azothiocarbonyl ligand **6** could be crystallized for X-ray structure analysis (Figure 2.10–2.14). Crystallization procedures were as follows. Complex **3**: slow evaporation of a solution of **3** in methanol/toluene at 4 °C; **4**PF_6: slow diffusion of Et_2O into a solution of **4**PF_6 in MeCN at 4 °C; **9**: slow evaporation

of a solution of **9** in n-pentane at −20 °C; **10**PF_6: slow diffusion of Et_2O into a solution of **10**PF_6 in MeCN at 4 °C; **6**: slow evaporation of a solution of **6** in n-pentane at −20 °C.

The data reveal rather invariant N-N and N-C distances of between 1.333(1) Å – 1.367(2) Å and 1.322(2) Å – 1.344(1) Å, respectively, indicating bond orders of about 1.5,[45] which can be attributed to a monoanion radical formulation $[RNNC(R')E]^{\bullet-}$ in each case. The C-E (E = O, S) bond lengths also give rise to the fractional bond order between 1 and 2.[46] DFT calculated bond length support the monoanion radical ligand situation for all four complexes. The differences in the N-N bond length also provide information on the spin density of the N-N bond itself, as well as on the spin density on the C-O and C-S bonds, respectively. The longer the N-N distance, the more spin density is localized on the azo bond and the less remains on the C-E bond and vice versa. Hence, a comparison of the N-N and C-E distances in all four complexes indicates a higher spin density on the C-S bond than on the C-O bond, as expected and confirmed by DFT. This observation is also in accordance with the aforementioned (Chapter 2.1) higher electron acceptor ability of the C=S bond as compared to the C=O bond. The slightly longer N-N and shorter N-C distances of $\mathbf{4}^+$ and $\mathbf{10}^+$ in comparison to the corresponding neutral $acac^-$ complexes can be interpreted in terms of more pronounced reduction to the monoanion radical ligands than in the neutral compounds. The Ru-N bond values illustrate the stronger bonds in the antiferromagnetically coupled cases (cf. section 2.5) **3** and **9** (Ru^{III} and $L^{\bullet-}$) with about 0.1 Å shorter Ru-N distances relative to $\mathbf{4}^+$ and $\mathbf{10}^+$.

In summary, the structural data of **3** and **9** give rise to the oxidation state formulation $Ru^{III}(acac)_2(L_O^{\bullet-})$ and $Ru^{III}(acac)_2(L_S^{\bullet-})$, respectively. Complexes $\mathbf{4}^+$ and $\mathbf{10}^+$ can be formulated in means of oxidation states as $[Ru^{II}(bpy)_2(L_O^{\bullet-})]^+$ and $[Ru^{II}(bpy)_2(L_S^{\bullet-})]^+$, respectively.

The structural characterization of the α-azothiocarbonyl ligand precursor **6** with the S-S bond at 2.068(1) Å and the N-N bonds at 1.329(2) Å and 1.331(3) Å support the formulation depicted in Figure 2.22.

Table 2.1: *Representative experimental and DFT calculated bond lengths (Å) the Ru-N-N-C-E chelate rings of* ***3***, ***4***PF_6, ***9***, *and* ***10***PF_6

.

	3		**4**PF_6		**9**		**10**PF_6	
bond	exp.	calc.	exp.	calc.	exp.	calc.	exp.	calc.
Ru-N2	1.902(5)	1.882	2.018(1)	2.055	1.931(1)	1.906	2.010(6)	2.044
Ru-O1	2.029(4)	2.020	2.051(2)	2.030				
Ru-S					2.255(1)	2.274	2.318(2)	2.328
N1-N2	1.355(7)	1.325	1.367(2)	1.336	1.333(1)	1.318	1.355(7)	1.321
N1-C1	1.338(8)	1.344	1.322(2)	1.325	1.344(1)	1.331	1.318(9)	1.320
C1-O1	1.287(7)	1.268	1.297(2)	1.286				
C1-S1					1.696(1)	1.699	1.727(8)	1.726

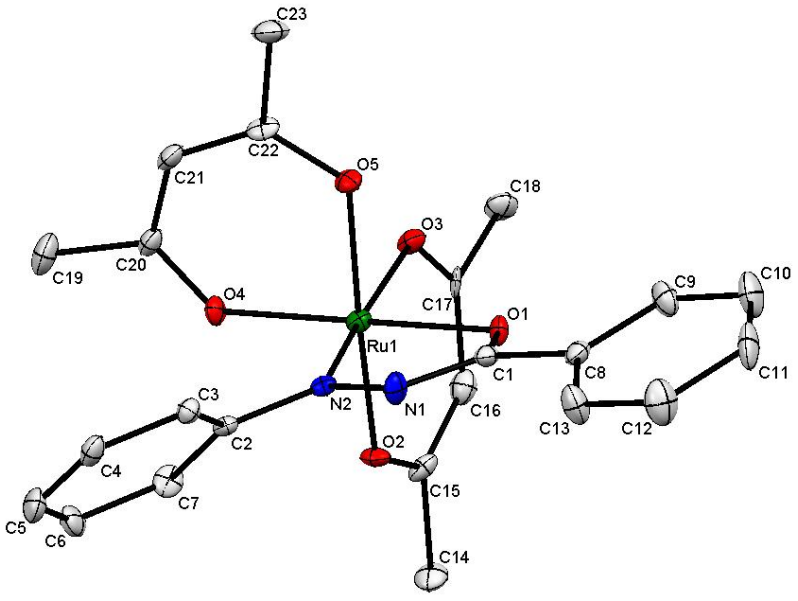

Figure 2.10: *Molecular structure of* ***3*** *in the crystal of* ***3***·*MeOH.*

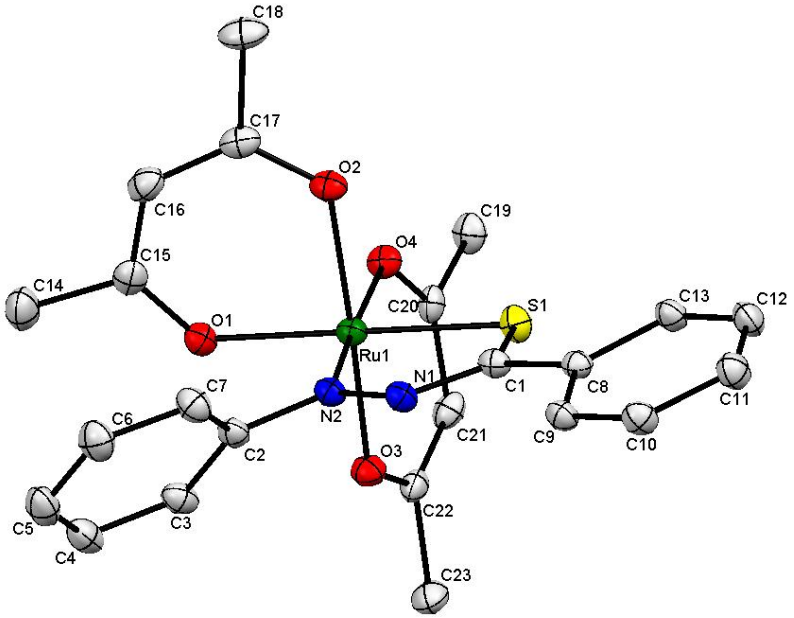

Figure 2.11: *Molecular structure of* ***9*** *in the crystal.*

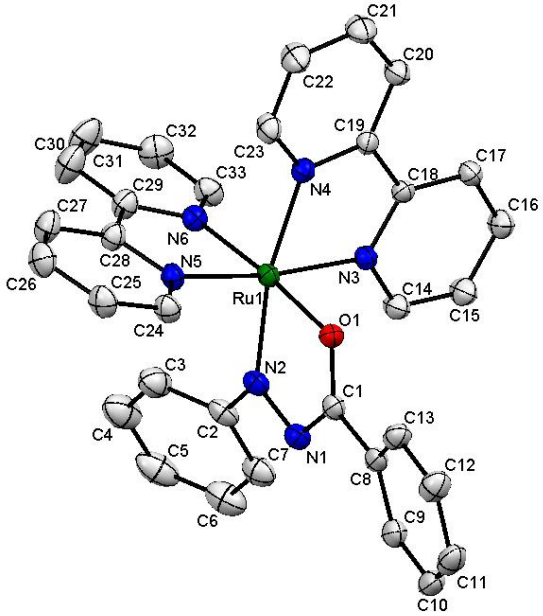

Figure 2.12: *Molecular structure of the cation in the crystal of* ***4***PF_6.

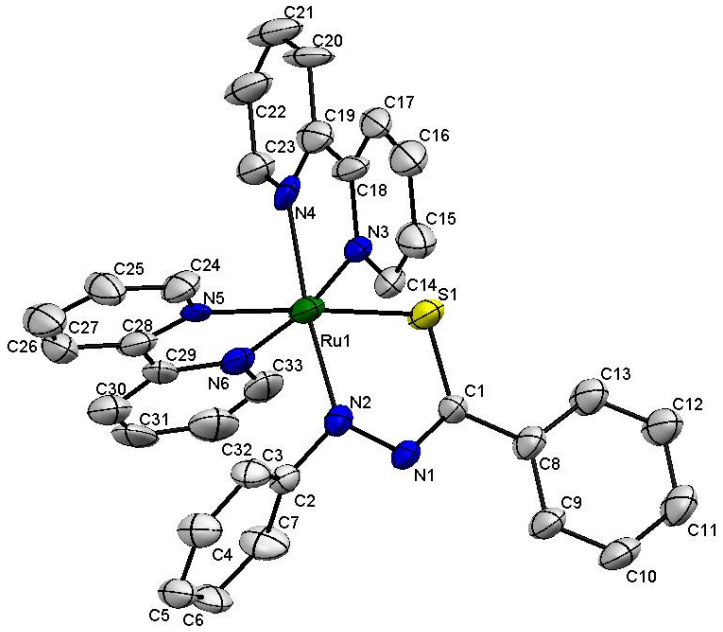

Figure 2.13: *Molecular structure of the cation in the crystal of* ***10***PF_6.

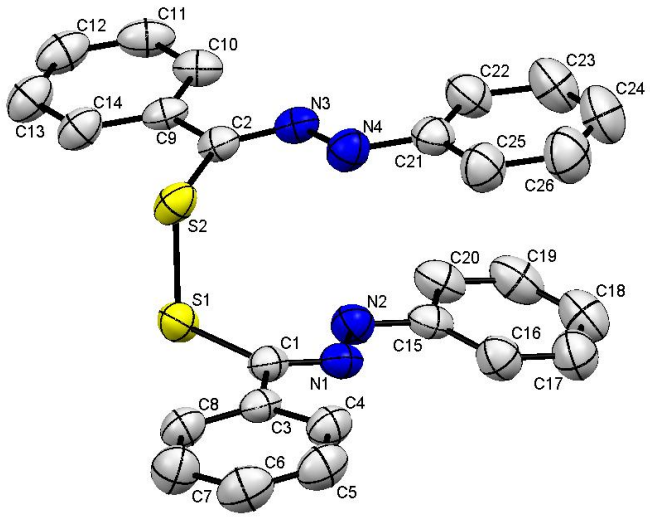

Figure 2.14: *Molecular structure of* ***6*** *in the crystal. Large size of thermal ellipsoids due to measurement at 298 K.*

2.3 ^{1}H-NMR and EPR spectroscopy of the isolated products

The formulation of $Ru^{III}(acac)_2(L_O^{\bullet -})$ and $Ru^{III}(acac)_2(L_S^{\bullet -})$ still raise the question of the relative spin orientation of the ruthenium centered spin at the one electron oxidized metal, Ru^{III}, and the ligand centered spin at the one electron reduced ligand, $L^{\bullet -}$. The two spins could either be oriented parallel (ferromagnetic coupling) involving a paramagnetic $S = 1$ spin system or antiparallel (antiferromagnetic coupling) involving a diamagnetic $S = 0$ spin system. Due to drastic effects of line broadening and chemical shifts of paramagnetic compounds in NMR, the two cases can be discriminated by applying this method.

The complexes **3** and **9** exhibit sharp and unshifted NMR signals within the range of 1–9 ppm, indicating the presence of a strong antiferromagnetic coupling of ligand and metal centered spins in both complexes. An additional evidence for the antiferromagnetic coupling situation is that both complexes are EPR silent. The four singuletts in the aliphatic region are assigned to the CH_3 protons and the two singuletts in the olefinic region to the CH protons of the $acac^-$ ligand. The ten protons in the aromatic region are associated to the phenyl protons of the L_O or L_S ligand, respectively. An exemplary ^{1}H-NMR spectrum of **3** is illustrated in Figure 2.15.

The EPR analysis of $\mathbf{4}^+$ and $\mathbf{10}^+$ in CH_2Cl_2 solution at room temperature gives well resolved spectra with g values of $g = 2.007$ and $g = 2.011$, respectively and hyperfine couplings of ^{14}N ($I = 1$, 99.6 % nat. abundance) and ^{99,101}Ru isotopes (^{99}Ru, $I = 5/2$, 12.7 % nat. abundance; ^{101}Ru, $I = 5/2$, 17.0 % nat. abundance) (Figure 2.16a, and Table 2.3). The calculated values are listed in Table 2.4. The g values are close to the value of the free electron $g_e = 2.0023$ and support the radical ligand formulation with the spin centered predominantly on the ligand. The magnitude of the ^{14}N and ^{99,101}Ru coupling constants (Table 2.3) suggest a ruthenium(II) complex of a semiquinone type radical ligand,[47] whereas the the higher g value for $\mathbf{10}^+$ vs $\mathbf{4}^+$ reflects the spin-orbit coupling contributions from the sulfur atom. A higher metal vs ligand contribution to the SOMO in $\mathbf{10}^+$ results in smaller ^{14}N but higher ^{99,101}Ru coupling constant of $\mathbf{10}^+$ compared to $\mathbf{4}^+$. Calculated spin densities on ruthenium of 0.088 and 0.141 for $\mathbf{4}^+$ and $\mathbf{10}^+$, respectively confirm the ligand radical situation for both complexes as well as the slight differences in the metal vs ligand character of the SOMOs. An exemplary plot of the spin density of $\mathbf{4}^+$ is depicted in Figure 2.16b.

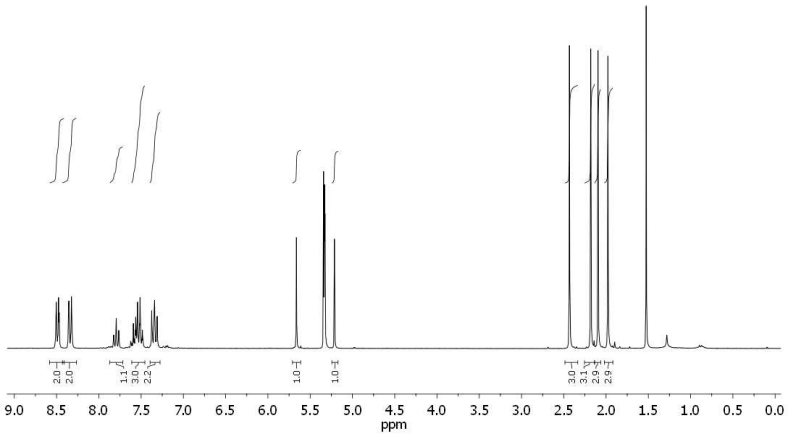

Figure 2.15: *^{1}H-NMR spectrum of **3** in CD_2Cl_2.*

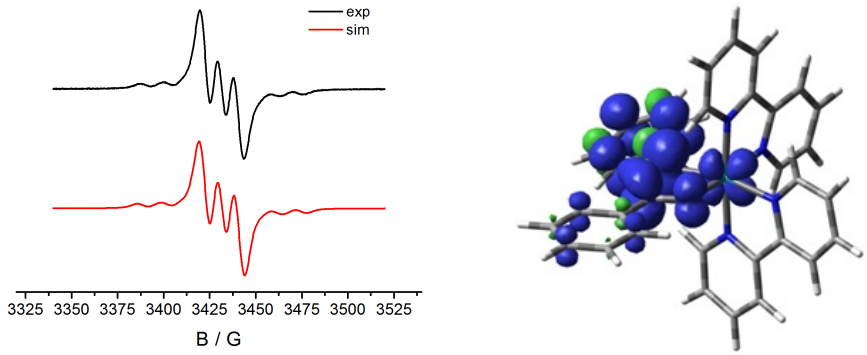

(a) (b)

Figure 2.16: *a) EPR spectrum of **4**$^+$ in CH_2Cl_2 at 298 K; b) DFT calculated (G09/PBE0/6-31G*) spin density of **4**$^+$ (calculated by Dr. Stanislav Záliš).*

2.3.1 Cyclic Voltammetrie

All four isolated complexes undergo one reversible oxidation and one reversible reduction (Figure 2.17 and Table 2.2). The difference in redox potential between the oxidation and reduction processes comprises the stability of the isolated complex towards disproportionation, mathematically described by the comproportionation constant K_c, as function of the potential difference ΔE(Equation 3.2b). Information about the K_c value can be of crucial value for further spectroscopic analysis of complexes, due to the possible contribution of various redox forms to the spectra of an isolated complex. The separation between the reduction and oxidation potentials is much larger for the neutral species **3** and **9** at $\Delta E \sim 1.6$ V vs only $\Delta E \sim 1.0$ V for **4**PF_6 and **10**BF_4. The resulting higher stability of **3** and **9** may result from the

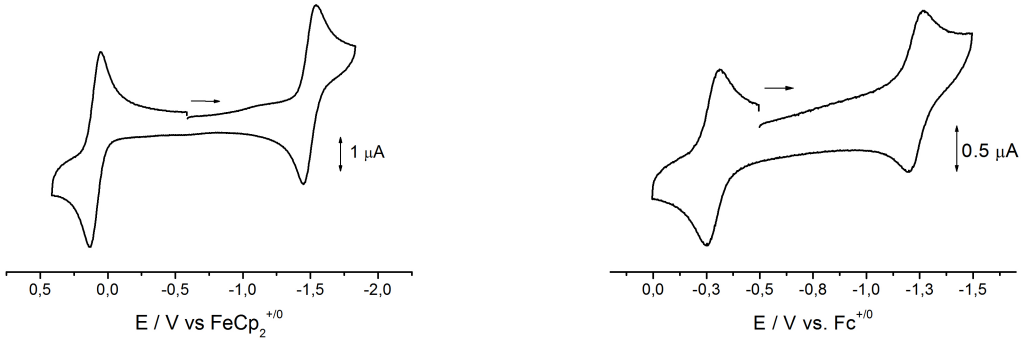

(a) **3** (b) **10**BF_4

Figure 2.17: *Cyclic voltammetry in CH_2Cl_2/0.1 M Bu_4NPF_6 (scan rate 100 mV s).*

Table 2.2: *Redox potentials[a,b] and comproportionation constants (K_c)[c] for **3**, **4**PF_6, **9**, and **10**BF_4.*

compound	$E^0_{298}/V(\Delta E/V)$			K_c
3	0.12	-1.48	(1.60)	1.3 x 10^{27}
4PF_6	-0.21	-1.23	(1.02)	3.0 x 10^{17}
9	0.48	-1.07	(1.55)	1.55 x 10^{26}
10PF_6	-0.14	-0.87	(0.73)	0.73 x 10^{12}

[a] *Potentials E^0_{298}/V vs $Fc^{0/+}$.* [b] *In CH_2Cl_2/0.1 M Bu_4NPF_6/scan rate 100 mV $s^{-}1$.* [c] $RTlnK_c = nF(\Delta E)$.

antiferromagnetic interaction between the ruthenium(III) center and the radical anion ligand. Between corresponding complexes containing L_O and L_S ligands there is a distinct shift of about 0.3–0.4 V to more positive potentials for the sulfur system, reflecting the more facile reduction of the thiocarbonyl vs carbonyl function.[48]

This correlation also suggests a mostly ligand centered electron transfer behavior in the redox series of both, the acceptor and the donor substituted systems (Figure 2.22).

2.3.2 EPR spectroelectrochemistry

The EPR silent compounds **3** and **9** can be converted into EPR active species, through electrochemical oxidation and reduction, with exception of the oxidation of **9**, which is irreversible under the experimental conditions. In EPR spectroelectrochemistry, the procedure of electrolysis is on the time scale of minutes and takes much longer than in UV-vis-NIR spectroelectrochemistry for instance. This can lead to different behavior of a single compound regarding reversibility. The irreversibility of the oxidation of **9** is manifested in the obtained spectrum, which showes a mixture of species and can therefore not be interpreted. In addition, this observation reflects the nature of the thiocarbonyl group, being more difficult to oxidize as

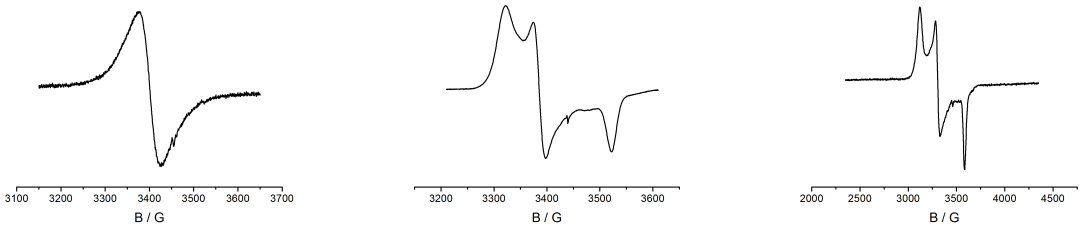

(a) $\mathbf{3}^-$ 298 K (b) $\mathbf{3}^-$ 110 K (c) $\mathbf{3}^+$ 110 K

Figure 2.18: *EPR spectrum of the EPR active species of* ***3*** *electrochemically generated in* CH_2Cl_2*/0.1 M* Bu_4NPF_6*.*

the carbonyl group. The observed spectra of $\mathbf{3}^+$ and $\mathbf{3}^-$ in solution of CH_2Cl_2/0.1 M Bu_4NPF_6 at 110 K and at room temperature (only $\mathbf{3}^-$) are illustrated in Figure 2.18 exemplary for both compounds **3** and **9**. The experimental and DFT calculated data are listed in Table 2.3 and 2.4.

The anions exhibit just one unresolved line with g values in the range of approximately 2.030. This behavior is typical for reduced complexes containing the $Ru(acac)_2$ fragment.[25] The strong π-donating $acac^-$ ligands increase the energy of the metal 4d orbitals, which therefore contribute to the, per se, ligand based SOMO. Thus, the contribution of the heavy transition metal leads to line broadening, quenching the hyperfine structure, and to a rather large deviation of the g value vs g_e. In the low temperature spectra of the anions the three principal g values are well resolved and show g anisotropies of $\Delta g = 0.119$ ($\mathbf{3}^-$) and $\Delta = 0.162$ ($\mathbf{9}^-$). After comparing the values to a list of paramagnetic ruthenium complexes which range from almost pure Ru^{III} species (with large g anisotropy, $\Delta g > 0.5$) to radical complexes of diamagnetic Ru^{II} (with very small g anisotropy), the radical anions can be described as a mixed radical situation $[Ru^{III}(acac)_2(L^{2-})]^- \leftrightarrow [Ru^{II}(acac)_2(L^{\bullet -})]^-$ with a considerable metal contribution to the SOMO, confirming the interpretation of the room temperature spectra. The weak resonance line around $g = 2.0$ in the spectra are assigned to an organic radical impurity, formed during the reduction process.

The g anisotropy of $\Delta g = 0.286$ for the cation $\mathbf{3}^+$ and of $\Delta g = 0.169$ (calc.) for the cation $\mathbf{9}^+$ suggests a predominantly ruthenium(III) situation, according to the formulation $Ru^{III}(acac)_2(L^0)$.

Calculated spin densities on ruthenium of 0.476, 0.742 and 0.49 for $\mathbf{3}^-$, $\mathbf{3}^+$ and $\mathbf{9}^-$ confirm the mixed situation for the anions and the more ruthenium(III) based formulations for the cations. Exemplary plots of the spin density of $\mathbf{3}^+$ and $\mathbf{3}^-$ are depicted in Figure 2.19.

Table 2.3: *EPR data for **3**, **4**, **9**, and **10** in various oxidation states from electrochemical generation in CH_2Cl_2/0.1 M Bu_4NPF_6.*

	$\mathbf{3}^-$	$\mathbf{3}^+$	$\mathbf{4}^+$	$\mathbf{9}^-$	$\mathbf{10}^+$
g^a	2.035	n.o.	2.007	2.025	2.011
g_1^b	2.085	2.220	c	2.092	c
g_2^b	2.045	2.097	c	2.034	c
g_3^b	1.966	1.934	c	1.930	c
g_1–g_3	0.119	0.286	<0.05	0.162	<0.05
$<g>^d$	2.032	2.087		2.020	
$A(^{14}N)^e$	n.o.	n.o.	1.00	n.o.	0.85
$A(^{99,101}Ru)^e$	n.o.	n.o.	1.00	n.o.	1.38

[a] 298 K. [b] 110 K. [c] Unresolved g anisotropy. [d] Calculated from $<g> = ((g_1^2 + g_2^2 + g_3^2)/3)^{1/2}$ *. [e] Coupling constants A in mT from 298 K spectra. The spectrum of **9**$^+$ could not be analyzed.*

Table 2.4: *DFT calculated EPR data for **3**, **4**, **9**, and **10** in various oxidation states.*

	$\mathbf{3}^-$	$\mathbf{3}^+$	$\mathbf{4}^+$	$\mathbf{9}^-$	$\mathbf{9}^+$	$\mathbf{10}^+$
g_1^b	2.073	2.164	2.028	2.050	2.138	2.038
g_2^b	1.993	2.065	2.006	1.996	2.077	2.002
g_3^b	1.952	1.938	1.996	1.952	1.969	1.985
g_1–g_3	0.121	0.226	0.032	0.098	0.169	0.053
$<g>^a$	2.007	2.056	2.010	1.999	2.061	2.009
$A(^{14}N)^b$			0.94			0.85
$A(^{99,101}Ru)^b$			0.09			1.38
Ru spin density	0.476	0.742	0.088	0.498		0.141

[a] Calculated from $<g> = ((g_1^2 + g_2^2 + g_3^2)/3)^{1/2}$*. [b] Coupling constants A in mT.*

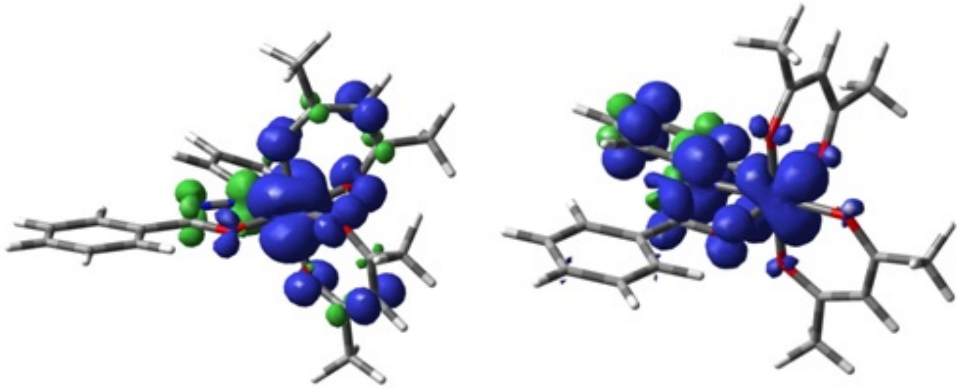

(a) $\mathbf{3}^+$ (b) $\mathbf{3}^-$

Figure 2.19: *DFT calculated spin density of the EPR active species of* ***3*** *(calculated by Dr. Stanislav Záliš).*

2.3.3 UV-vis-NIR spectroelectrochemistry

UV–vis–NIR spectroelectrochemical measurements using an OTTLE cell[49] are illustrated in the Figures 2.20–2.21 and the data are summarized in Table 2.5. The data are being discussed in the following, based on structural and EPR results and on TD-DFT calculations.

The lowest energy intense band for the neutral complexes **3** and **9** appears in the visible region (502 and 545 nm, respectively) and can be attributed to allowed HOMO-2—LUMO MLCT/IL transitions. The oxidation of both complexes results in a bathochromic shift leading to absorption bands, assigned to MLCT transitions, with maxima at 625 nm each. The weak transition for $\mathbf{3}^+$ at 1100 nm (1008 nm calc.) is attributed to a βHOMO $\rightarrow$ βLUMO d-d excitation. On reduction to a mixed $[Ru^{III}(acac)_2(L^{2-})]^- \leftrightarrow [Ru^{II}(acac)_2(L^{\bullet-})]^-$, an even stronger bathochromic shift, assigned to a MLCT transition, is observed. The radical anion complexes $\mathbf{4}^+$ and $\mathbf{10}^+$ show long-wavelength absorption maxima around 650 and 450 nm, respectively. TD-DFT analysis assigns those bands to MLCT transitions involving the L_O or L_S ligand, respectively (MLCT($L^{\bullet-}$)), and to MLCT transitions involving the bpy ligand (MLCT(bpy)). The transitions result from excitations from metal based βHOMO-1 and βHOMO-2 into ligand based βLUMO and βLUMO+1. On reduction to the neutral $Ru^{II}(L^{2-})$ configuration a broad band in the NIR region around 1000 nm appears, which can be assigned to a ligand-to-ligand charge transfer (LLCT) with L^{2-} as donor and bpy as acceptor. Such LLCT bands are characteristic for complexes of the $Ru(bpy)_2$ fragment in their reduced form.[50] Additional MLCT bands can be observed at about 470 nm and below. The oxidation is accompanied by bands around 530 nm (489 nm calc.), which are attributed to HOMO-2–LUMO MLCT/IL transitions. Remarkably, these values coincide with those of **3** and **9** which were structurally established as $Ru^{III}(L^{\bullet-})$ species. Due to the high ligand participation in the SOMO, however,

it seems to be more adequate to describe the system as a mixed situation $[Ru^{III}(bpy)_2(L^{\bullet -})]^{2+}$ $\leftrightarrow$ $[Ru^{II}(bpy)_2(L^0)]^{2+}$.

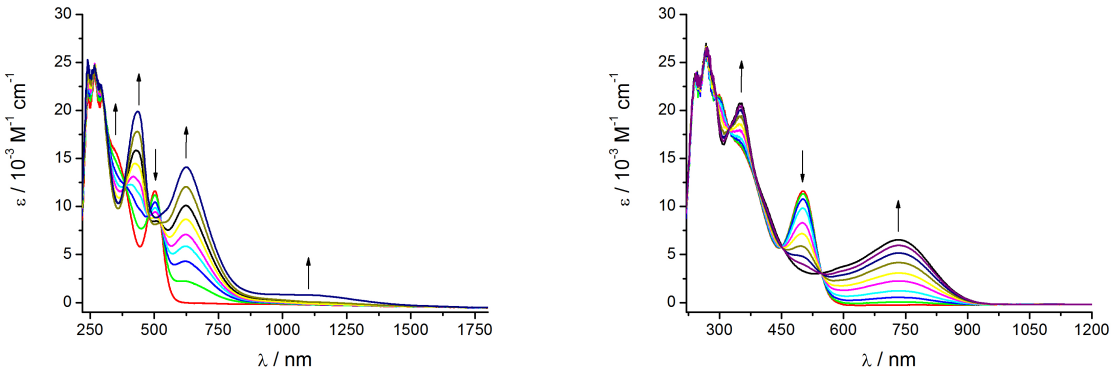

(a) **3** → **3**$^+$ (b) **3** → **3**$^-$

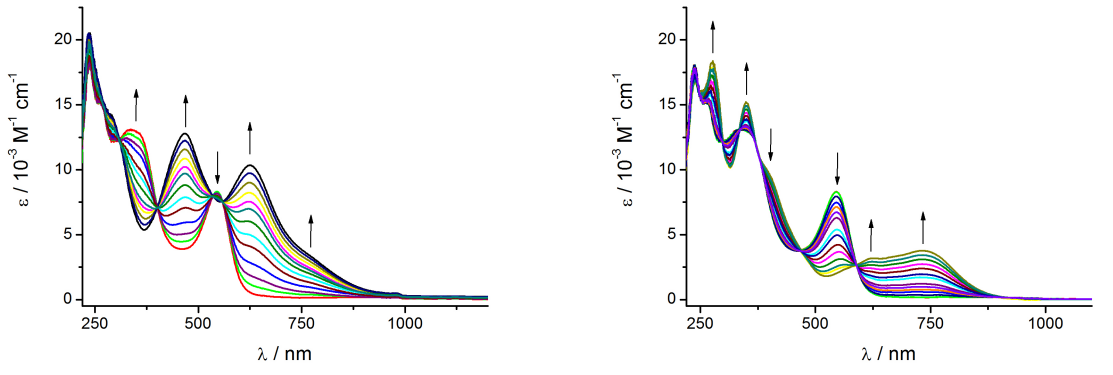

(c) **9** → **9**$^+$ (d) **9** → **9**$^-$

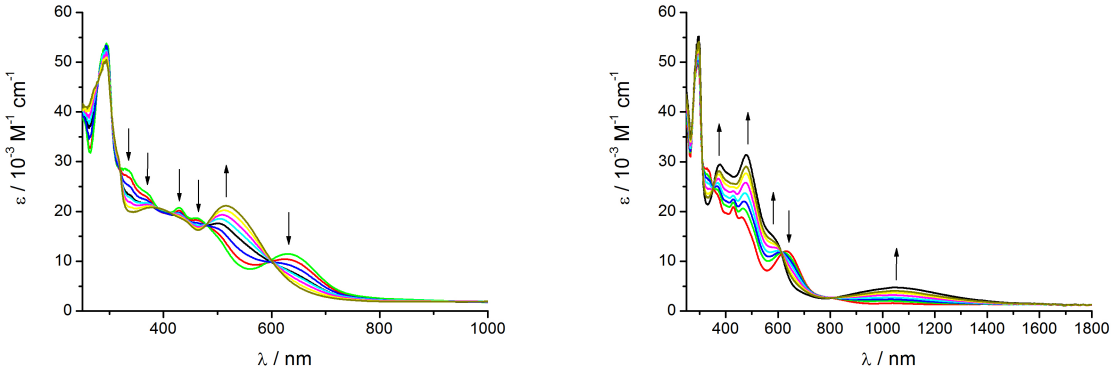

(e) **4**$^+$ → **4**$^{2+}$ (f) **4**$^+$ → **4**

Figure 2.20: *UV–vis–NIR spectroelectrochemical response of **3**, **4**$^+$ and **9** in CH_2Cl_2/0.1 M Bu_4NPF_6 (**3** and **4**$^+$ were measured by Ralph Hübner).*

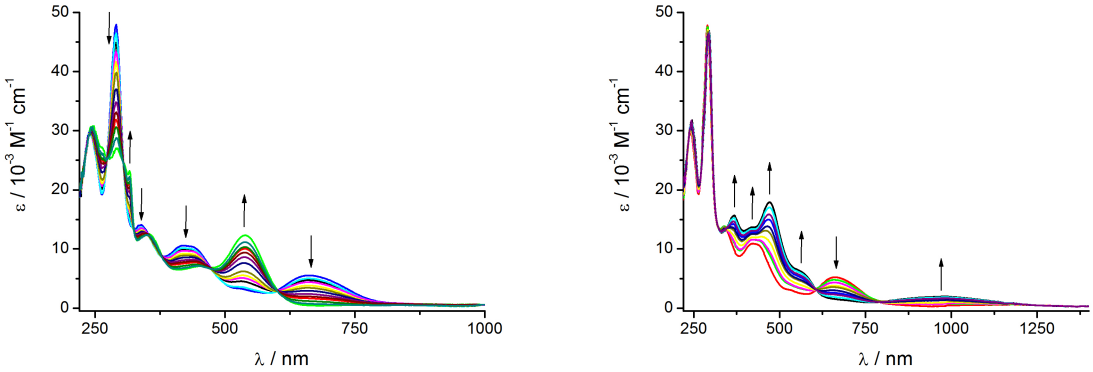

(a) $\mathbf{10}^{+} \rightarrow \mathbf{10}^{2+}$ (b) $\mathbf{10}^{+} \rightarrow \mathbf{10}$

Figure 2.21: *UV–vis–NIR spectroelectrochemical response of* $\mathbf{10}^{+}$ *in* CH_2Cl_2*/0.1 M* Bu_4NPF_6*.*

Table 2.5: *UV–vis–NIR data for* ***3***, ***4***, ***9***, *and* ***10*** *in various oxidation states from OTTLE spectroelectrochemistry in* CH_2Cl_2*/0.1 M* Bu_4NPF_6*.*

complex	λ_{max} [nm] ($\epsilon[M^{-1}cm^{-1}]$)
3	349(16 000), 502(11 700)
$\mathbf{3}^{+}$	436(19 900), 625(14 100), 1100sh
$\mathbf{3}^{-}$	353(20 800), 733(6 500)
4	295(54 900), 378(29 500), 478(31 400), 577(15 500), 1039(4 800)
$\mathbf{4}^{+}$	295(53 500), 334(28 400), 369(23 800), 429(20 800), 461(18 500), 630(11 500)
$\mathbf{4}^{2+}$	295(50 100), 381(21 000), 517(21 300)
9	335(13 100), 358(12 800), 545(8 300)
$\mathbf{9}^{+}$	285(14 400), 464(12 800), 625(10 400), 760sh
$\mathbf{9}^{-}$	276(18 400), 350(15 200), 400(9 700), 624(3 200), 735(3 800)
10	291(48 100), 366(15 900), 420(13 800), 472(18 200), 560(6 600), 977(2 200)
$\mathbf{10}^{+}$	291(48 100), 339(14 200), 413(10 600), 438(10 500), 660(5 700)
$\mathbf{10}^{2+}$	262(427 500), 291(27 000), 316(23 300), 350(12 700), 539(12 500)

2.4 Conclusion

This chapter presents the synthesis of ruthenium complexes with two novel redox-active hetero-1,3-diene ligands, including a new strategy for *in situ* generation of the elusive α-azothiocarbonyl ligand.[51] The two ligands L_O and L_S can behave as non-innocent towards the donor and acceptor substituted ruthenium fragments. Crystal structure analysis reveals that all four isolated forms contain the anion radical ligands, $L_O^{\bullet-}$ and $L_S^{\bullet-}$. The $acac^-$ containing complexes can be described as antiferromagnetically coupled biradicals $Ru^{III}L^{\bullet-}$ ($S = 0$), whereas the bpy substituted complexes are characterized as radical species $Ru^{II}L^{\bullet-}$ ($S = ½$) with only little metal contribution to the SOMO. EPR spectroscopic interpretation of the electrochemically generated radical forms of the $acac^-$ substituted complexes results in the formulation of $Ru^{III}(L_0)$ for the cation and $Ru^{III}(L^{2-}) \leftrightarrow Ru^{II}(L^{\bullet-})$ for the anion. Changes in the redox behavior of the four complexes are determined rather by the variation the ancillary ligands $acac^-$ vs bpy than by the exchange of the hetero-1,3-diene ligand L_O vs L_S. Whereas the ancillary ligands define the nature of the electronic structure of the complexes, L_O and L_S reflect the better π-acceptor behavior of C=S vs C=O by the means of slight shifts in the electrochemical potentials. The resulting related redox series are illustrated Figure in 2.22.

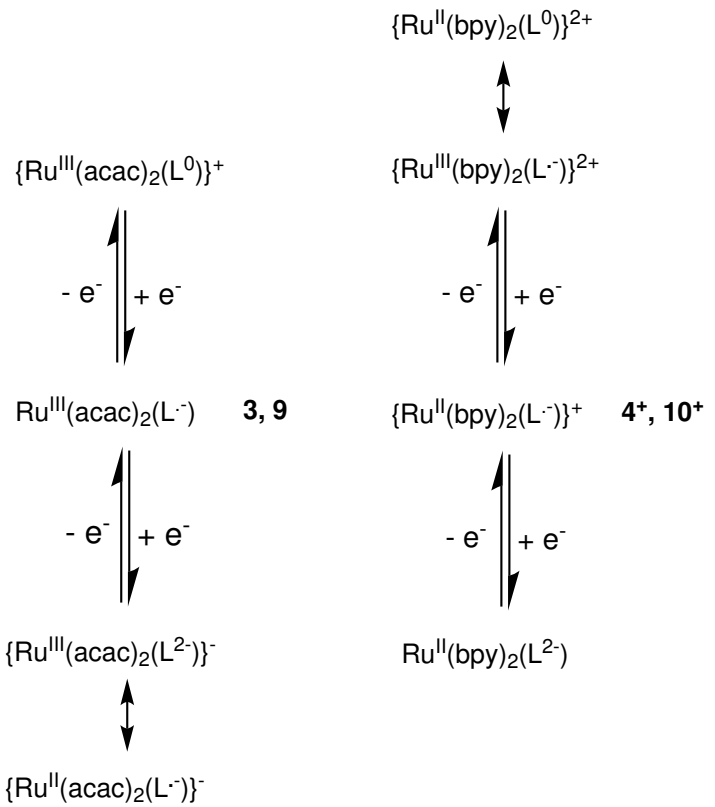

Figure 2.22: *Redox series of donor and acceptor substituted ruthenium α-azocarbonyl and α-azothiocarbonyl complexes.*

3 Dinuclear bis(α-azothiocarbonyl) complexes

3.1 Introduction

After the new α-azothiocarbonyl chelate ligand function was introduced to coordination chemistry (Chapter 1) in the form of mononuclear ruthenium complexes, an expansion of the amount of examples of coordination compounds containing this elusive ligand system was highly desired. This chapter describes an alternative route for the *in situ* generation of the α-azothiocarbonyl ligand function to yield dinuclear 1,3,5-trienediyl-bridged ruthenium complexes. The synthesis includes a new type of ring opening of thiophenes[52] and a C-C coupling reaction.

As the key step in the heterogeneous hydrodesulfurization (HDS)[53] process, transition metal mediated ring opening reactions of thiophenes are of great industrial importance and a variety of homogeneous model systems[54] have been developed under this aspect. In all of those examples an oxidative insertion into the C-S bond of the thiophene is involved, whereas in the reaction described in this chapter, a five membered Ru-N-N-C-S chelate ring is formed after the cleavage of the C-S bond.

A further remarkable feature of the system described here is the coupling of the non-innocent α-azothiocarbonyl ligand configuration to a 1,3,5-hexatrienediyl (hte) unit. As a small prototypical oligoolefin, the 1,3,5-hexatrienediyl entity has been investigated theoretically and experimentally,[55] regarding its function as intermediate in the cyclotrimerization of acetylene[56] to produce benzene according to W. Reppe[57] and its bridging function in electron transfer situations.[58] These resulting complexes can be described as conventional organometallic species in which the metals are directly connected to the 1,3,5-hexatrienediyl-bridge via a C-M bond. In

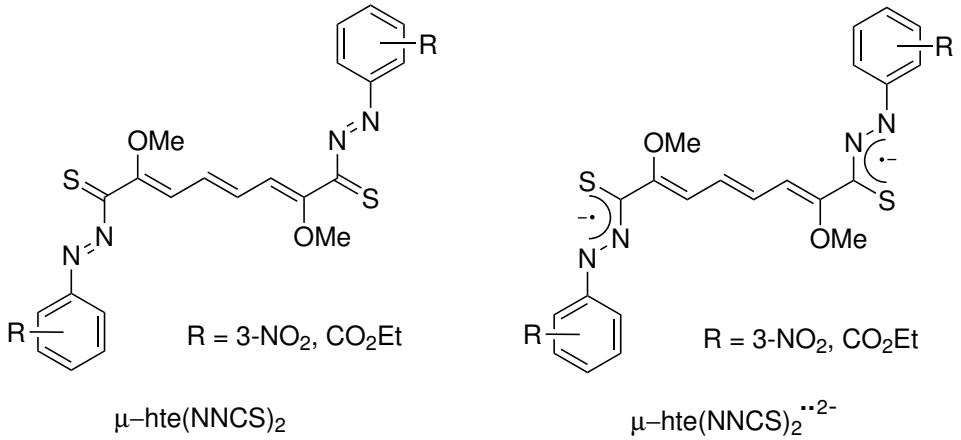

Figure 3.1: *The new 1,3,5-hexatriene bridged bis(α-azothiocarbonyl) ligand in its oxidized (left) and its doubly reduced diradical form (right).*

the μ-hte(NNCS) ligand configuration (Figure 3.1), however, the α-azothiocarbonyl function serves as redox-active linker connecting the two metal centers via the 1,3,5-hexatrienediyl-bridge. The ability of the μ-hte$(NNCS)_2$ non-innocent bridging ligand to form diradicals[59] in its doubly reduced form μ-hte$(NNCS)_2^{2-\bullet\bullet}$ makes it attractive for possible applications in magnetic materials and opens alternative pathways for intervalence charge transfer mechanisms in mixed-valence situations (hole versus electron exchange[60]).

The concept of "mixed-valence" is a ubiquitous phenomenon, appearing in biological, organic, organometallic, and inorganic systems.[61] In coordination chemistry, mixed valence is defined through the occurrence of different metal oxidation states in dinuclear or polynuclear metal complexes of homo- or hetero-metallic nature. Such frameworks have received a lot of attention due to their role as model compounds for biological systems and their application potential in molecular electronics. Especially mixed-valence complexes of ruthenium,[60] originating from the archetypal Creutz-Taube ion[62] (Figure 3.2), are under permanent investigation, in order to modify and study the thermodynamic and kinetic stability of the neighboring oxidation states Ru^{III} and Ru^{II}.[63]

The main feature of mixed-valence transition metal complexes is their capacity for exchanging their valence electrons. The rate constant of this exchange, indicating the degree of electron delocalization between the metal centers, can be of very different magnitude, depending on the thermal activation barrier between the localized valence tautomers.
Based on the extent of electronic delocalization, Robin and Day[64] divided mixed valent complexes into three different classes (I–III), also known as the Robin-Day classification. Class I type complexes (Equation 3.1 **A**) do not exhibit any electronic coupling and thus separate oxidation states can be assigned to the different metal centers. In contrast, the metal centers in Class III type complexes (Equation 3.1 **B**) are electronically equal and adopt the the same, uneven, oxidation state in a fully valence delocalized arrangement. In Class II type complexes the electronic coupling between the metal centers is apparent but weak, because the different states are separated by a thermal activation barrier.[65] In the case of redox-active bridging ligands an additional class of di- or polynuclear complexes, labeled as radical complexes (Equation 3.1 **C**), emerges. This type of complex exhibits a radical bridging ligand rather than metal-centered mixed valence.

The strength of electronic coupling can be influenced by several factors such as symmetry of the complex, electronic properties of the ancillary ligands, distance between the metal centers,

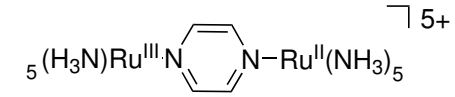

Figure 3.2: *Molecular structure of the Creutz-Taube ion.*

$[L_xM^n(\mu\text{-BL})M^{n+1}L_x]$
A, localized mixed valence

$[L_xM^{n+0.5}(\mu\text{-BL})M^{n+0.5}L_x]$ (3.1)
B, delocalized mixed valence

$[L_xM^{n+1}(\mu\text{-BL}^{\bullet-})M^{n+1}L_x]$
C, radical complex

electronic nature of the bridging ligand, nature of the metal, and orbital overlap between the metal πd orbitals and the π type MOs of the bridging ligand.[66–69]

In complexes of high symmetry all coordination sites accomodate different redox-states of the metals in the same way, and thus foster a electron delocalized situation. Also the choice of the ancillary ligands can have a strong impact on the extent of coupling, since electron rich metals are prone to exhibit a stronger coupling than electron poor metals.[48,70] With respect to the bridging ligand different factors play an important role. As the metal-metal interaction in mixed-valent systems depends on the metal-metal distance, it can be tuned by varying the length of the bridge.[69] Also, the relative energy of the frontier orbitals of the bridge and the dπ orbitals of the metal can lead to different types of electron transfer mechanisms. Whereas for acceptor bridges with low lying LUMOs an electron exchange mechanism is favored, donor bridges with high lying HOMOs promote an electronic coupling via a hole exchange mechanism.[71]

Among various methods for the characterization of mixed-valence coordination compounds cyclic voltammetry and UV-vis-NIR spectroscopy provide the most valuable information. Since a strong electronic coupling stabilizes the mixed-valence species towards disproportionation, the comproportionation constant K_c, obtained from electrochemical potential differences, is one of the most essential parameters. Equation 3.2a represents the equilibria, which are the basis for the calculation of K_c according to Equation 3.2b. The higher the potential difference

$$\underset{\text{Red}}{[L_xM^{n+1}(\mu\text{-BL})M^{n+1}L_x]} \underset{(E_1)}{\overset{+e^-}{\underset{-e^-}{\rightleftharpoons}}} \underset{\text{Int}}{[L_xM^{n}(\mu\text{-BL})M^{n+1}L_x]} \underset{(E_2)}{\overset{+e^-}{\underset{-e^-}{\rightleftharpoons}}} \underset{\text{Red}}{[L_xM^{n}(\mu\text{-BL})M^{n}L_x]} \quad (3.2a)$$

$$K_c = \frac{[Int]^2}{[Red][Ox]} = 10^{\frac{\Delta E}{59mV}} \quad \text{at 298 K} \quad (3.2b)$$

$$\Delta E = E_2 - E_1; RTlnK_c = nF\Delta E$$

$$[L_xM^n(\mu\text{-BL})M^{n+1}L_x] \xrightarrow[IVCT]{h\nu} [L_xM^n(\mu\text{-BL})M^{n+1}L_x]^* \quad (3.3a)$$

$$[L_xM^{n+0.5}(\mu\text{-BL})M^{n+0.5}L_x] \xrightarrow[IVCT]{h\nu} [L_xM^{n+0.5}(\mu\text{-BL})M^{n+0.5}L_x]^* \quad (3.3b)$$

between the two reversible redox processes, the higher the value of K_C and the stronger the electronic coupling.

A second evidence for a mixed-valence situation of Class II–III is the appearance of an intervalence charge-transfer (IVCT) absorption band in the NIR region. This type of absorption originates from an intermolecular electronic transition from the lower-valent to the higher-valent metal center,[72] as illustrated in Equation 3.3a–b. For a discrimination between Class II and Class III systems, different parameters of the IVCT band, such as energy of the transition, intensities, band shapes, and line width, must be considered.[73] The connection between these parameters and the electronic interaction were described by Hush.[74] The interpretation of such correlation data, however, is not always straightforward. Especially in cases where the bridging ligand can behave non-innocently, features of ligand centered radical intermediates can be mistaken for mixed-valence situations.

An additional feature of dinuclear coordination compounds containing two equivalent bidentate ancillary ligands at approximately octahedrally configured metal centers, is their appearance in different isomeric forms. Such complexes can thus exist as *meso* ($\Delta\Lambda$) and *rac* ($\Delta\Delta$ / $\Lambda\Lambda$) stereoisomers (Figure 3.3).[75,76,77] The nature of the corresponding mixed-valence situations, such as electrochemical and spectroscopic behavior is not much affected by the symmetry of the complex.[75] Consequently, this type of isomerism has only little influence on the valence-exchange mechanism. Nevertheless, the two stereoisomers can be discriminated by NMR spectroscopy of their diamagnetic non-mixed-valent forms.[78]

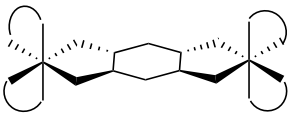

meso

rac

Figure 3.3: *Diastereomers of symetrically substituted dinuclear complexes.*

3.2 Results and Discussion

3.2.1 Synthesis

Since the results from Chapter 2 have illustrated the possibility for the *in situ* generation of the elusive α-azothiocarbonyl ligand from precursor **6**, there was demand for alternative precursor compounds, leading to different α-azothiocarbonyl containing complexes. For this purpose another organic compound including the N-N-C-S fragment and undergoes organic transformation reaction was required. From literature it is known that thiophene substituted tetrazines undergo such transformations in the reaction with $Ru(acac)_2(MeCN)_2$.[79] To ensure the presence of the N-N-C-S fragment, the focus was directed on azo containing thiophenes. For improved crystallization behavior of the resulting complex and simple synthetic accessibility, the acceptor substituted 2-azothiophenes[80] **11** and **12** were tested towards the reaction with $Ru(acac)_2(MeCN)_2$. Additionally, the presence of the strong acceptor groups NO_2 and CO_2Et, was expected to facilitate the reaction with the strongly electron donating $Ru(acac)_2(MeCN)_2$.

The reactions of $Ru(acac)_2(MeCN)_2$ with **11** and **12** were performed under the same reaction conditions as for the synthesis of complexes **3** and **9** (CH_2Cl_2/toluene, 50 °C, 12 h, equimolar reagents). After purification with column chromatography (silica, CH_2Cl_2/MeCN) and recrystallization from n-hexane, a pure green solid was obtained in both cases. After obtaining a single crystal suitable for X-ray crystallography, the structure of **13** could be determined. Surprisingly, the reaction yielded a dimer of the used educts. The molecular structure of the complex can be described as a dinuclear ruthenium bis(acac) complex bridged by a two α-azothiocarbonyl chelate containing functions coupled by a 1,3,5-hexatrienediyl unit. Obviously, the unexpected reaction had to involve a ring opening of the thiophene and subsequent C-C coupling. Unfortunately, the reaction mechanism could not be determined. Attempts to trap possible radical intermediates with the spin trap 2,2,6,6-Tetramethylpiperidine 1-oxyl

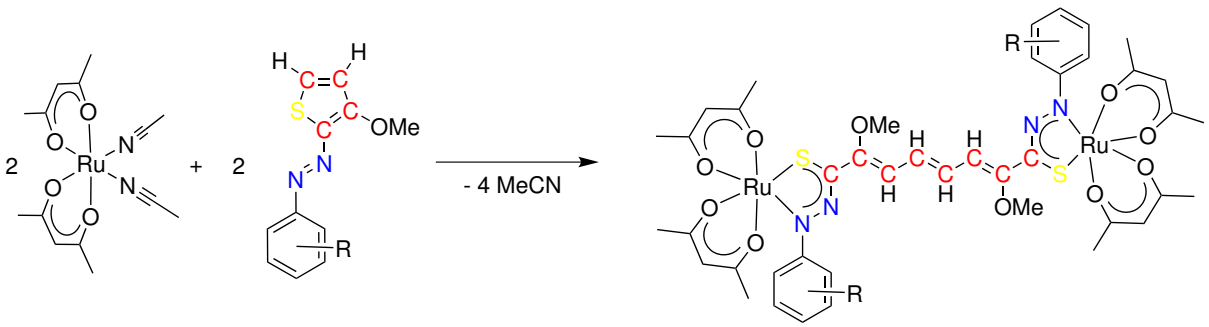

11: R = 3-NO_2
12: R = 4-CO_2Et

13: R = 3-NO_2
14: R = 4-CO_2Et

Figure 3.4: *Synthesis of dinuclear bis(α-azothiocarbonyl) ruthenium complexes.*

(TEMPO) or possible carbene intermediates with alkenes (cyclohexene) or organic sulfides (dibutylsulfide or tetrahydrothiophene) were not successful. Due to the strong donor ability of $Ru(acac)_2(MeCN)_2$ and the strong acceptor ability of the azothiophenes **11** and **12** an electron transfer from the $Ru^{II}(acac)_2$ fragment to the azothiophene, inducing the ring opening and C-C coupling, is proposed.

Reactions of **11** and **12** with the $[Ru(bpy)_2(acetone)_2]^{2+}$ fragment under the same reaction conditions as for $\mathbf{10}(PF)_6$ (acetone, 60 °C, 12h) did not give any product.

3.2.2 Molecular Structure

Complex **13** and its ligand precursor **11** could be crystallized for X-ray structure analysis (Figure 3.5 and 3.6).Crystallization procedures were as follows. **13**: slow diffusion of n-hexane into a solution of **13** in 1,2-dichlorobenzene/CH_2Cl_2. **9**: slow evaporation of a solution of **11** in ethyl acetate.

The comparison of the bond lengths in the Ru-N-N-C-S chelate ring of **13** and **9** (Table 3.7) shows only a marginal variation. According to literature,[45] the bond lengths of **9** were attributed to the presence of a singly reduced α-azothiocarbonyl ligand and a Ru^{III} center. Thus, the μ-hte-$(NNCS\text{-}NO_2)_2$ ligand can be considered as doubly reduced, involving two singly reduced terminal α-azothiocarbonyl functions coupled by a 1,3,5-hexatrienediyl bridge. Consequently, the electrons for the reduction come from the $Ru^{II}(acac)_2$ fragment, which attributes a non-innocent behavior to the system and which is in accordance with the postulated reaction mechanism where the ring opening of the thiophene occurs after a one electron

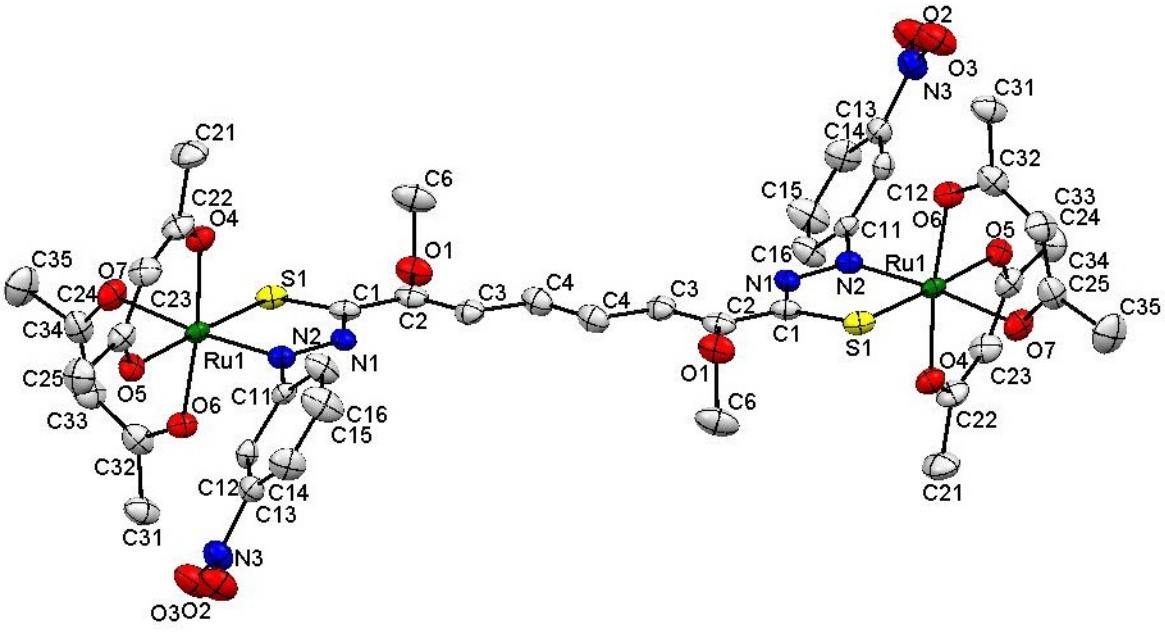

Figure 3.5: *Molecular structure of **13** in the crystal. Solvent molecules are omitted for clarity.*

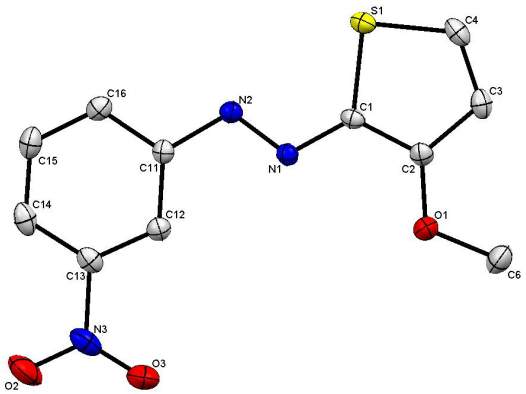

Figure 3.6: *Molecular structure of* ***11*** *in the crystal.*

Table 3.6: *Torsional angle (°) of the 1,3,5-hexatriene bridge in* ***13****.*

bond	torsional angle (°)
N1-C1-C2-C3	0.9(9)
C1-C2-C3-C4	178.4(6)
C2-C3-C4-C4'	180.0(8)
C3-C4-C4'-C3'	180.0(6)

reduction of the ligand precursor. The structural evidence for the bridging 1,3,5-hexatrienediyl entity lies in the variation of the C-C bond lengths of the bridge, alternating between $\sim$ 1.35 Å, indicating a C=C double bond and $\sim$ 1.44 Å, indicating a C-C single bond, respectively. The angle of torsion of the bridge (Table 3.6) of around 180° or 0°, respectively, illustrates the planarity of the bridging element in the hte-NO_2 ligand, resulting in a strong conjugation of the π electrons. A metal-metal distance of 14.5 Å might decrease the strength of electronic coupling in a possible singly reduced Ru^{II}/Ru^{III} mixed-valent species. The presence of an inversion center between the C4 and the C4' atoms in the 1,3,5-hexatriene bridge provides evidence that complex **13** exists as *meso* stereoisomer. The resemblance of the spectra of **13** and **14**, discussed in the following section, give rise to the assumption of a similar structure for **14**, excluding the isomerism. The N1-N2 bond length of 1.274(2) Å of the ligand precursor **11**, clearly indicates a N=N double bond which is polarized due to the different electron donating 3-methoxythiophene and electron accepting 3-nitrophenylsubstituents. The effect of polarization is reflected in the different C-N_{azo} bond lengths of d(C11-N2) = 1.424(2) and d(C11-N2) = 1.359(2).

Table 3.7: *Bond lengths (Å) in the Ru-N-N-C-S chelate ring (**9** and **13**) and the 1,3,5-hexatriene bridge (**13**).*

	bond lenth (Å)		
bond	**13**	**9**	**11**
S1-C1	1.699(7)	1.696(1)	1.743(2)
C1-N1	1.352(8)	1.344(1)	1.359(2)
C11-N2[a]	1.426(8)	1.430(2)	1.424(2)
N1-N2	1.331(7)	1.333(1)	1.274(2)
Ru1-S1	2.263(2)	2.558(4)	
Ru1-N2	1.947(5)	1.931(1)	
C1-C2	1.440(9)		1.397(2)
C2-C3	1.35(1)		1.397(2)
C3-C4	1.421(9)		1.363(2)
C4-C4	1.36(1)		

[a] *Nomenclature: C2-N2 for **9***

3.2.3 ^{1}H-NMR and EPR spectroscopy of the isolated products

As in Chapter 2, the formulation $\{(Ru^{III}(acac))_2(\mu\text{-hte}(NNCS)_2^{\bullet\bullet 2-})$, resulting from crystal structure analysis, raises questions about the relative orientation of the spins of the unpaired electrons at the metal and the ligand. In this case, however, the spin system is much more complicated due to the presence of four unpaired electrons which can undergo mutual coupling. The possible spin orientation in a four-spin system can lead to a singlet (S = 0, ↑↓↑↓), triplet (S = 1, ↑↓↑↑) or quintet (S = 2, ↑↑↑↑) state, which differ in their energies. The energetic order of the three states depends on several factors, such as the coordination environment, temperature, and applied magnetic field. The complexes **13** and **14** exhibit sharp and unshifted NMR (400 MHz) signals within the range of 1–9 ppm, indicating a diamagnetic singlet ground state for both compounds at high magnetic fields ($\sim$ 9.4 T) as applied in a 400 MHz NMR spectrometer at room temperature.

The four singlet signals in the aliphatic region between 1 and 3 ppm are assigned to the CH_3 protons of the $acac^-$ ligand. The six protons at around 4 ppm are attributed to the methoxy group located at the C-2 carbons of the 1,3,5-hetatiene entity. In the olefinic region between 5 and 6 ppm two singlets, assigned to the CH protons of the $acac^-$ ligand, appear. The four doublets in the aromatic region between 7 and 9 ppm are attributed to the four protons of the 1,3,5-hextatriene bridge and the four protons at the two phenyl rings. Additionally, complex **14** exhibits a quartet at 4.37 ppm and a triplet at 0.92 ppm which can be assigned to the ten protons of the ethyl ester groups.

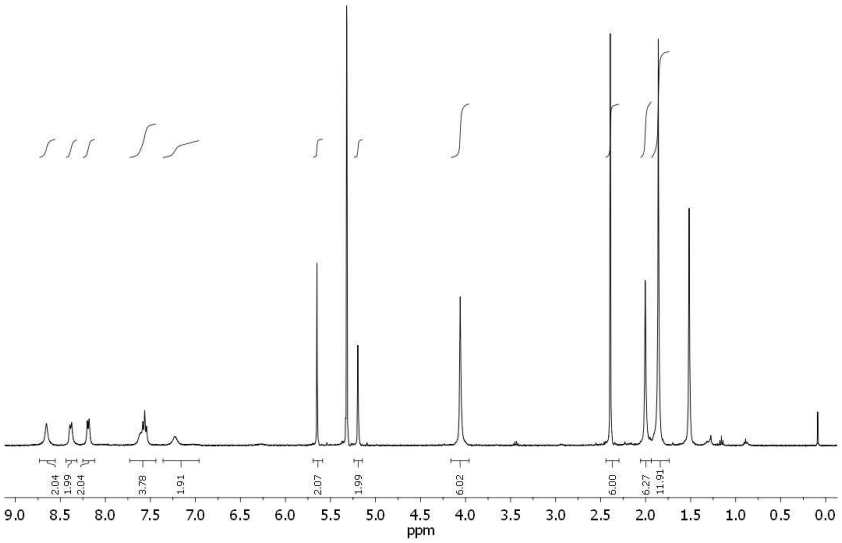

Figure 3.7: *^{1}H NMR spectrum of **13** in CD_2Cl_2 at 298 K.*

The number of lines appearing in the ^{1}H-NMR spectra also provides information about the symmetry of the complexes. As already mentioned in the introduction, the complexes can appear in two different types of stereoisomers, either as *meso* ($\Delta\Lambda$) or as *rac* ($\Delta\Delta$ / $\Lambda\Lambda$) forms, which can be discriminated by NMR spectroscopy. For complexes **13** and **14** the protons of the acac$^-$ ligand serve as precise probe for the "isomeric purity" of the compounds. The presence of four singlets attributed to the CH_3 protons of the acac$^-$ ligand and two singlets attributed to the CH protons of the acac$^-$ ligand, confirms the appearance of only one isomer in the sample. A mixture of two isomers would result in twice the number of lines for the acac$^-$ ligand. Complex **13** has already been characterized by crystallography as the *meso* isomer. The stereoisomeric form of complex **14** is still unclear. Nevertheless, the electrochemical and spectroscopic features of the complex are only little affected by the isomerism. A representative ^{1}H-NMR spectrum of **13** is illustrated in Figure 3.7.

To check for different spin states, solid state and frozen solution EPR spectra of **13** and **14** at various temperatures have been recorded. Both compounds are EPR silent at 298 K and 110 K, whereas at 10 K an intensive resonance line was observed in both solid state and in frozen solution. The EPR spectra of **13** are exemplarily illustrated in Figure 3.8. A g anisotropy g_1-g_3 of around 0.23 (Table 3.11) indicates a high spin density at the ruthenium centers. In the case of a triplet state the latter observation would suggest an antiferromagnetic coupling between the ligand centered spin and a ferromagnetic coupling between the ruthenium centered spins. A half field signal,[81] indicating a triplet state, is not observed in the spectra which, however, does not exclude the presence of a triplet state. The appearance of an EPR signal in frozen solution gives rise to the assumption that the paramagnetism does not originate from intermolecular interactions in the solid state.

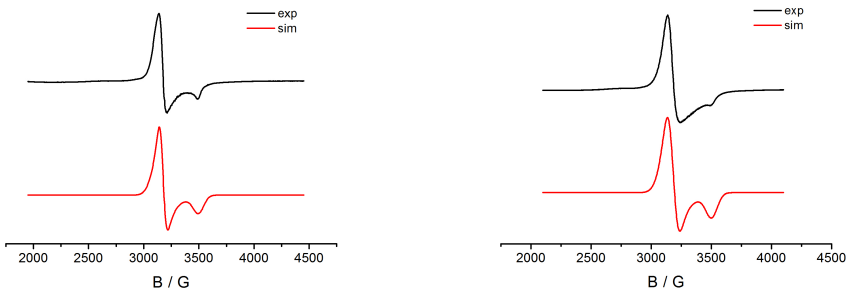

(a) **13** at 10 K; frozen solution (b) **13** at 10 K; solid state

Figure 3.8: *EPR spectrum of **13** in a) frozen solution and b) solid state at 10 K. g values are listed in Table 3.11*

In summary, ^{1}H-NMR and EPR measurements provide first indications about the field and temperature dependency of the spin system. To obtain a deeper insight into the nature of the spin system at various temperatures and magnetic field strength, SQUID suszeptometry measurements were applied to the complexes **13** and **14**. The results are discussed in the following section.

3.2.4 SQUID suszeptometry

To explore the magnetic behavior of **13** and **14**, magnetization measurements were conducted at fields between -5 Tesla and 5 Tesla and temperatures of 2 K and 300 K. Additionally, the susceptibilities were measured over a temperature range of 2 to 300 K at the constant field of 0.05 Tesla, 0.1 Tesla, 1 Tesla and 5 Tesla. The plots of the measurements for **13** and **14** are illustrated in the Figures 3.9–3.12. The measurements as well as the description of the experiments were done by Dr. José Luis Priego and Prof. Jiménez-Aparicio.

The magnetization measurements at 300 K show an essentially diamagnetic response of both compounds before subtracting the diamagnetic background. Thus, the complex **13** displays a decreasing almost linear dependence typical of a diamagnetic substance (Figure 3.9a). Until about 0.02 Tesla the magnetization increases, whereas from 0.02 to 5 Tesla a strong decrease is displayed. When the diamagnetic contribution is subtracted, the shape of the curve remains substantially the same. In the case of compound **14** a similar behavior is observed although the magnetization strongly increases until 0.6 Tesla and from this magnetic field quickly decreases to 5 Tesla (Figure 3.9b). Thus, at 300 K the behavior of both complexes is typical of diamagnetic substances except in a very weak magnetic field. It is noteworthy, however, that complex **14** shows paramagnetism up to 0.6 Tesla whereas complex **13** shows paramagnetic behavior only to 0.02 Tesla. In any case, the rapid increase of the magnetization, especially in complex **14**, suggests the existence of ferromagnetic interactions. In contrast, the magnetization measurements at 2 K for both compounds display a typical S-shaped curve

Table 3.8: *Filed and temperature dependency of the magnetic behavior of **13** and **14**.*

	high fields ($>$ 200 mT)	low fields ($<$ 200 mT)
high temp. (300 K)	diamagnetic	paramagnetic
low temp. (2 K)	paramagnetic	paramagnetic

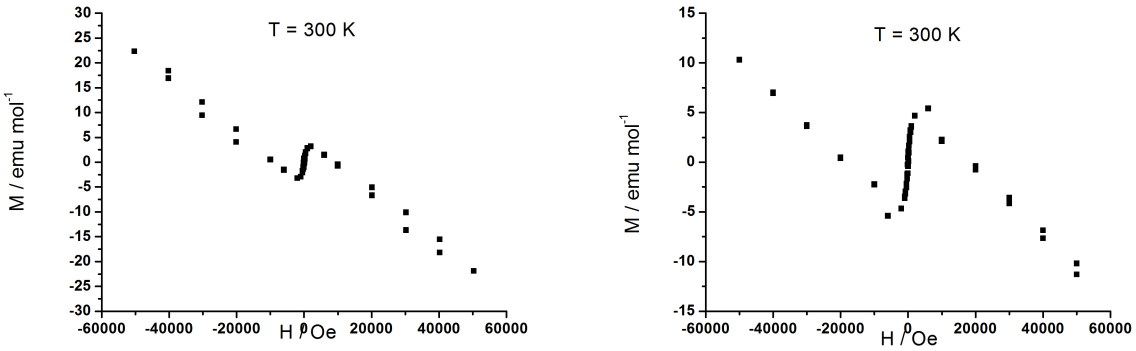

(a) **13** at 300 K (b) **14** at 300 K

Figure 3.9: *Representation of the magnetization versus magnetic field for **13** and **14** at 300 K (measured by L. S. Priego).*

which suggests the existence of paramagnetism/ferromagnetism (Figure 3.10). As a result of the magnetization measurements, for both complexes a paramagnetic character can be found at low temperatures and low or high magnetic fields and at high temperatures in combination with low magnetic fields. A diamagnetic character is only attributed at high temperatures and high magnetic fields. These observations are confirmed by the previously described EPR and NMR data. The field and temperature dependence of the magnetic behavior of **13** and **14** are summarized in Table 3.8.

In order to understand the magnetic behavior of these complexes the variation of the magnetization versus temperature at the constant field of 0.05 Tesla, 0.1 Tesla, 1 Tesla and 5 Tesla was carried out. In both compounds a dependence of the magnetic susceptibility on the strength of the magnetic field has been found (Figure 3.11). For both complexes the magnetic susceptibility at 0.05 Tesla and 0.1 Tesla shows the continuous increase with decreasing temperature typical of paramagnetic samples. At higher magnetic fields, however, the magnetic susceptibility values increase at low temperatures but show zero or negatives values at higher temperatures ($>$50 K for **13** and $>$150 K for **14**). This behavior is well reflected in the representation of the magnetic moment with the temperature (Figure 3.12). Thus, at 0.05 and 0.1 Tesla the variation of the magnetic moment with the temperature basically shows a continuous decrease to reach a μ_{eff} value of 0.5 μ_B for **13** and 0.6 μ_B for **14** which are lower than the expected for one unpaired electron. The magnetic moments at room temperature are

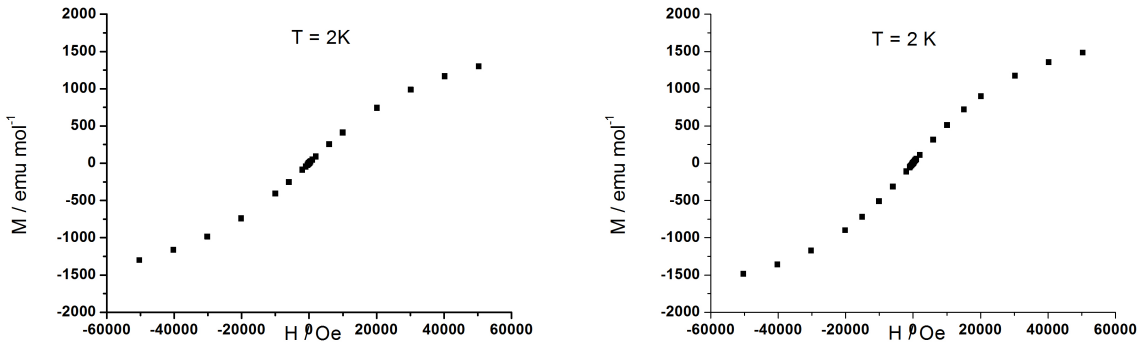

(a) **13** at 2 K (b) **14** at 2 K

Figure 3.10: *Representation of the magnetization versus magnetic field for **13** and **14** at 2 K (measured by L. S. Priego).*

3.2 μ_B (at 0.05 T) and 2.8 μ_B (at 0.1 T) for **13** and 3.4 μ_B (at 0.05 T) and 3.0 μ_B (at 0.1 T) for **14** which are close to the expected values for two unpaired electrons per molecule. In these curves, however, maxima at about 80 K and 70 K for **13** and **14**, respectively, are observed, suggesting the existence of both ferro- and antiferromagnetic interactions. In contrast, at 1 and 5 Tesla a sudden transition from a paramagnetic state to a diamagnetic one occurs at 57 K and 48 K, respectively for **13**. Similar transitions at 144 K and 122 K for **14** are also observed. Thus, at high magnetic field both complexes are diamagnetic at room temperature which is in accordance with the magnetization measurements at 300 K. Moreover, in complex **14** at both magnetic fields the magnetic moment increase from 144 and 122 K to reach a maximum at about 66 K (the exact value of the maximum cannot be established due to the presence of traces of oxygen which are difficult to eliminate due to the weak signal of the compound) and then decreases again until 2 K.

At low magnetic fields the continuous increase of the effective magnetic moment μ_b from 0.5 μ_b at 2 K to around 3.0 μ_b at 300 K suggests the presence of a singlet ground state as well as thermally accessible spin states of higher multiplicity which become populated by an increase of the temperature. The drop of the effective magnetic moment to $\mu_b = 0$ at high magnetic fields and temperatures, however, is still an open question which can not be explained satisfactorily. The idea that the energy gap between the ground and the excited state increases with an increase of the magnetic field does still not explain the inverse temperature dependence of the population of the excited states of higher multiplicity. A further problem is that the experimental magnetic data of **13** and **14** could not be fitted to obtain a value for the exchange coupling constant J, since the the magnetization versus the magnetic field as well as the magnetic susceptibility towards temperature change with the magnetic field is not linear. This results in a different coupling constant at each magnetic field. Magnetic

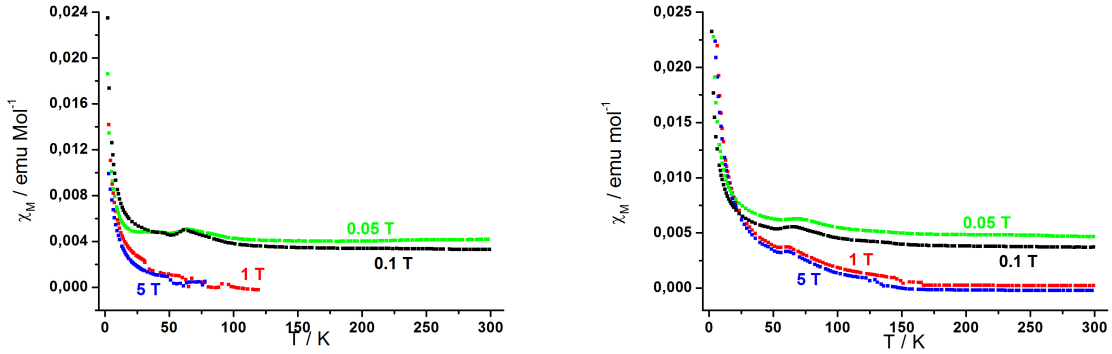

(a) **13** (b) **14**

Figure 3.11: *Temperature dependence of the magnetic susceptibility of **13** and **14** measured under magnetic fields of 0.05 T (green), 0.1 T (black), 1 T (red) and 5 T (blue) (measured by L. S. Priego).*

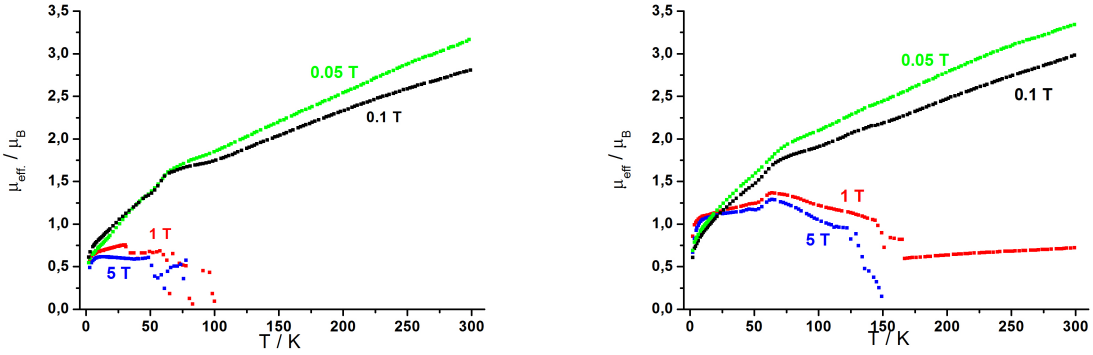

(a) **13** (b) **14**

Figure 3.12: *Temperature dependence of the magnetic moment of **13** and **14** measured under magnetic fields of 0.05 T (green), 0.1 T (black), 1 T (red) and 5 T (blue) (measured by L. S. Priego).*

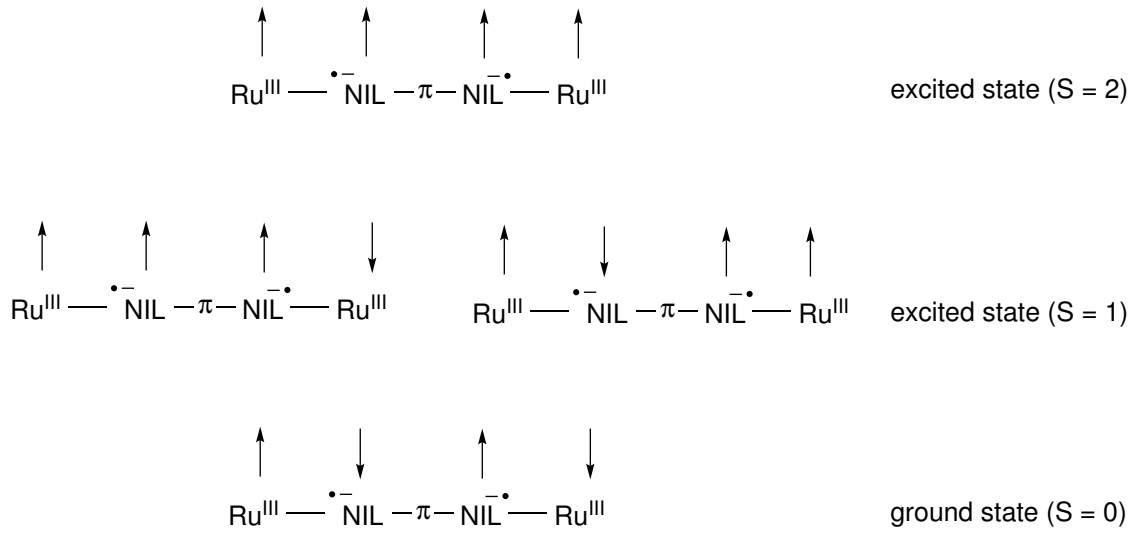

Figure 3.13: *Illustration of the possible spin orientation in the ground and the excited states.*

transitions induced by a change in magnetic field strength are well known in chemistry,[82] but the complicated magnetic behavior of the complexes **13** and **14** is quite unique.

3.2.5 DFT Calculations

Geometry optimizations of the neutral complex **13** were performed for ^{1}A, ^{3}A and ^{5}A electronic states using UKS and RKS approaches. The lowest energy state was obtained for unrestricted singlet state with antiparallel spins on the Ru^{III} centers. The calculated singlet – triplet energy difference is 0.17 eV. Geometrical parameters calculated for UKS ^{1}A state reasonably well describe the experimental structure as indicated in Table 3.9. The DFT calculated spin density in the unrestricted singlet state of **13** is mainly localized on the metal centers and the μ-hte$(NNCS)_2$ bridging ligand (Figure 3.14). The calculations yield absolute values of spin densities of 0.57 and 0.37 for each ruthenium and the μ-hte$(NNCS)_2$ ligand, respectively. All calculations were performed by Dr. Stanislav Záliš.

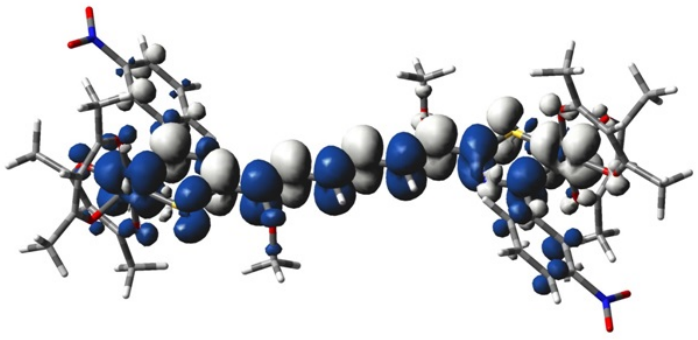

Figure 3.14: *DFT calculated spin densities in the unrestricted singlet state of **13**. Blue areas indicate positive and gray areas negative spin densities.*

Table 3.9: *Comparison of experimental and DFT calculated bond lenths (Å) and angles (°) in the Ru-N-N-C-S chelate ring for* ***13***

		calc.		
bond	exp.	^{1}A (SB-UKS)	^{1}A (RKS)	^{3}A
S1-C1	1.699(7)	1.713	1.689	1.748
C1-N1	1.352(8)	1.348	1.341	1.360
N1-N2	1.331(7)	1.295	1.308	1.286
Ru-S1	2.263(2)	2.242	2.243	2.257
Ru-N1	1.947(5)	1.969	1.920	2.001
angle				
N2-Ru1-S1	82.0(2)	82.6	82.3	83.2
C1-S1-Ru1	97.8(2)	97.3	96.9	96.7
N1-N2-Ru1	124.3(4)	123.5	123.8	123.3
N2-N1-C1	114.0(5)	115.3	114.5	116.0
N1-C1-S1	120.9(5)	120.5	120.3	120.6

3.2.6 Cyclic Voltammetry

The complexes **13** and **14** were investigated by cyclic voltammetry in CH_2Cl_2/0.1 M NBu_4PF_6 at 298 K and 220 K. The experimental data are summarized in Table 3.10 and exemplary plots of the cyclic voltammogram of **13** at 298 K and at 220 K are illustrated in Figure 3.15, respectively. Since the difference of the data for **13** and **14** is negligible, an interpretation based on the influence of nitro versus ethyl ester substitution is not warranted.

At room temperature both complexes undergo two reversible reductions at half-wave potentials of around -0.85 V and -1.02 V, respectively, and one irreversible oxidation at an anodic potential of 0.39 V. The irreversibility of the oxidation process of **13** and **14** in comparison with the reversible process of **9** can be explained by the substitution with the strong π-accepting nitro (**13**) and ethyl ester group (**14**), respectively. At lower temperature (220 K) the irreversible oxidations split up into two reversible oxidations at half-wave potentials at around 0.36 V and 0.50 V, respectively. The shift of the oxidation of **13** and **14** to lower potentials as compared to **9** is not in accordance with the acceptor substitution of the μ-hte$(NNCS)_2$ ligand function. Facilitated oxidation may result from the delocalization of the unpaired electrons at two α-azothiocarbonyl fragments over an expanded 1,3,5-hexatriene π-system, increasing the energy of the HOMO. Additionally, the π-donating methoxy group in 1-position of the 1,3,5-hexatriene bridge may as well contribute to the negative potential shift of the oxidation for **13** and **14** versus **9**. Regarding the positive shift of the reduction potential concerning the dinuclear complexes **13** and **14** versus the mononuclear complex **9**, the data are in ac-

Table 3.10: *Redox potentials[a,b] and comproportionation constants (K_c)[c] for* ***13*** *and* ***14****.*

compound	E^0_{220K}/V		$E^0_{298K}/V(\Delta E/V)$			K_c^{298K}
13	0.48	0.34	-0.85	-1.02	(0.17)	760
14	0.51	0.37	-0.84	-1.02	(0.18)	1120

[a] Potentials E^0/V vs $Fc^{+/0}$. [b] In CH_2Cl_2/0.1 M Bu_4NPF_6/scan rate 100 mV s^{-1}. [c] $RTlnK_c = nF(\Delta E)$.

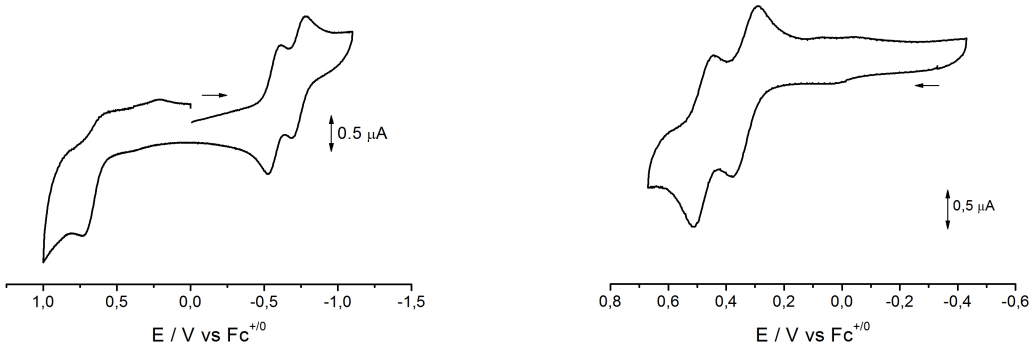

(a) **13** at 298 K (b) **13** at 220 K

Figure 3.15: *Cyclic voltammogram of* ***13*** *in CH_2Cl_2/0.1 M Bu_4NPF_6 at a) 298 K and b) 220 K (scan rate 100 mV s^{-1}).*

cordance with the substitution pattern of the α-azothiocarbonyl ligand function. The low comproportionation constants of K_c = 760 (**13**) and K_c = 1120 (**14**), respectively, suggest a localized (Class II) mixed-valent situation. The low comproportionation constants, caused by weak electronic coupling can be explained through the large metal-metal distance of about 14.5 Å.

3.2.7 EPR spectroelectrochemistry

The complexes **13** and **14**, EPR silent at 110 K, can be converted into EPR active species through electrochemical oxidation and reduction. Since the oxidation processes of both compounds are only reversible at low temperatures, the electrolysis for obtaining the oxidized species was done at 220 K. The experimental data are summarized in Table 3.11 and exemplary plots of the EPR spectra of $\mathbf{13}^+$ and $\mathbf{13}^-$ at 110 K are illustrated in Figure 3.16 and **13** at 10 K in Figure 3.8.

The oxidation of **13** and **14** resulted in rhombic EPR signals with large g anisotropies of Δ g = 0.413 and Δ g = 0.464, respectively, indicating a predominantly metal localized spin distribution and thus a ligand centered oxidation. After reduction two alternative electronic situations are possible. Either the reduction occurs at the metal and thus results in a Ru^{II}/Ru^{III} mixed-valence situation or the reduction occurs at the μ-hte$(NNCS)_2^{\bullet\bullet 2-}$ bridging ligand and

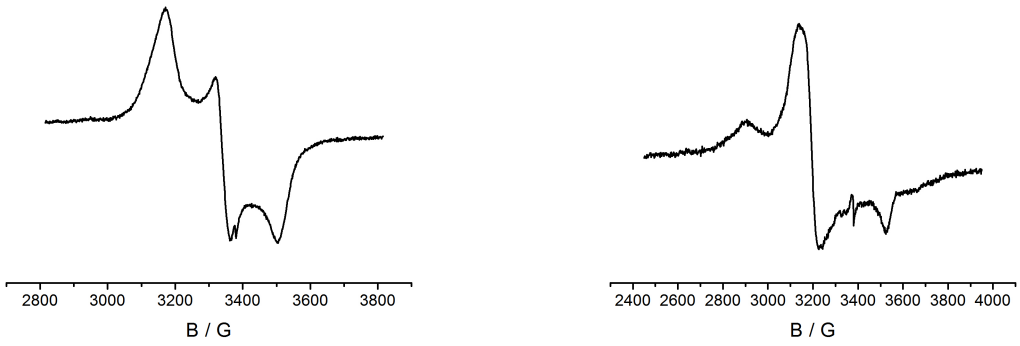

(a) $\mathbf{13}^{-}$ at 110 K (b) $\mathbf{13}^{+}$ at 110 K

Figure 3.16: *EPR spectra of $\mathbf{13}^{-}$ and $\mathbf{13}^{+}$ (electrolysis at 220 K) in CH_2Cl_2/0.1 M Bu_4NPF_6 at 110 K.*

Table 3.11: *EPR data for **13**, and **14** in various oxidation states from electrochemical generation in CH_2Cl_2/0.1 M Bu_4NPF_6.*

g values	$\mathbf{13}^{-,a}$	$\mathbf{13}^{b}$	$\mathbf{13}^{+,c}$	$\mathbf{14}^{-,a}$	$\mathbf{14}^{b}$	$\mathbf{14}^{+,a}$
g_1^b	2.134	2.146	2.332	2.132	2.151	2.334
g_2^b	2.029	2.118	2.117	2.026	2.118	2.123
g_3^b	1.932	1.918	1.919	1.930	1.914	1.870
g_1–g_3	0.202	0.228	0.413	0.202	0.237	0.464
$<g>^d$	2.033	2.063	2.129	2.031	2.064	2.118

[a] 110 K. [b] 10 K. [c] 110K (electrolysis at 220 K). [d] Calculated from $<g> = ((g_1^2 + g_2^2 + g_3^2)/3)^{1/2}$.

results in a radical ligand complex. A rather unlikely situation due to the electronic coupling of the unpaired electrons of the bridging ligand. The reduced species of both complexes are EPR silent at room temperature and show a rhombic signal with a g anisotropy of Δ g = 0.202 at 110 K, which clearly reveals the expected predominantly but not exclusively metal centered spin distribution. Hence, the conjunction of the EPR data with the low comproportionation constants (K_c = 760 (**13**), K_c = 1124 (**14**)) suggest a localized (Class II) mixed-valent situtation.

3.2.8 UV-vis-NIR spectroelectrochemistry

UV−vis−NIR spectroelectrochemical measurements on complexes **13** and **14** using an OTTLE cell[49] are illustrated in Figure 3.17 and the data are summarized in Table 3.12. Since the spectra of **13** and **14** could not yet be satisfactorily reproduced by TD-DFT calulations due to the complicated spin system and the complexity of the variety of electronic transitions related

Table 3.12: *UV–vis–NIR data for **13** and **14** in various oxidation states from OTTLE spectroelectrochemistry in CH_2Cl_2/0.1 M Bu_4NPF_6.*

complex	λ_{max} [nm] ($\epsilon[M^{-1}cm^{-1}]$)
13	218(45 200), 270(43 000), 457(22 000), 598(25 900), 712(21 700)
$\mathbf{13}^-$	218(45 200), 270(44 900), 437(17 900), 588(19 000), 729(19 500), 1090(12 300),
$\mathbf{13}^{2-}$	218(18 700), 274(49 100), 370(30 400), 432(28 300), 553(18 700), 786(10 600)sh, 938(5 900)sh
14	218(45 900), 273(35 600), 458(24 700), 597(27 200), 688(22 400)
$\mathbf{14}^-$	218(45 900), 273(37 400), 337(27 900), 450(22 200), 593(19 900), 732(19 200), 1090(12 700)
$\mathbf{14}^{2-}$	218(42 600), 276(41 000), 420(34 700), 584(21 400), 774(12 500)sh, 938(6 600)sh

therewith, the interpretation of the spectra is based on the calculations of the structurally related complex **9**.

Since the high energy band of complex **9** at 545 nm is attributed to an MLCT/IL transition, so are the most intensive long wavelength absorptions of **13** and **14** at 712 nm and 688 nm, respectively, attributed to this character. The shift to higher wavelengths may result from a lowering of the ligand LUMOs due to the expanded π system and the strong π acceptor substituents of the bridging ligands containing the α-azothiocarbonyl fragment. After reduction of **13** and **14**, in contrast to **9**, a band in the near infrared region around 1700 nm ($\epsilon =$ 4700 M^{-1} cm^{-1}) appears. This band is assigned to an inter valence charge transfer (IVCT) transition of a $Ru^{II}Ru^{III}$ mixed-valent species. The IVCT band intensity and shape of $\epsilon_{max} \leqslant$ 5000 M^{-1} cm^{-1} and $\Delta\nu_{1/2} \geqslant$ 2000 cm^{-1} suggests a weak electronic interaction (Class II) between the two ruthenium centers.[73] After the second reduction a Ru^{II}/Ru^{II} is formed and as a consequence the IVCT band disappears.

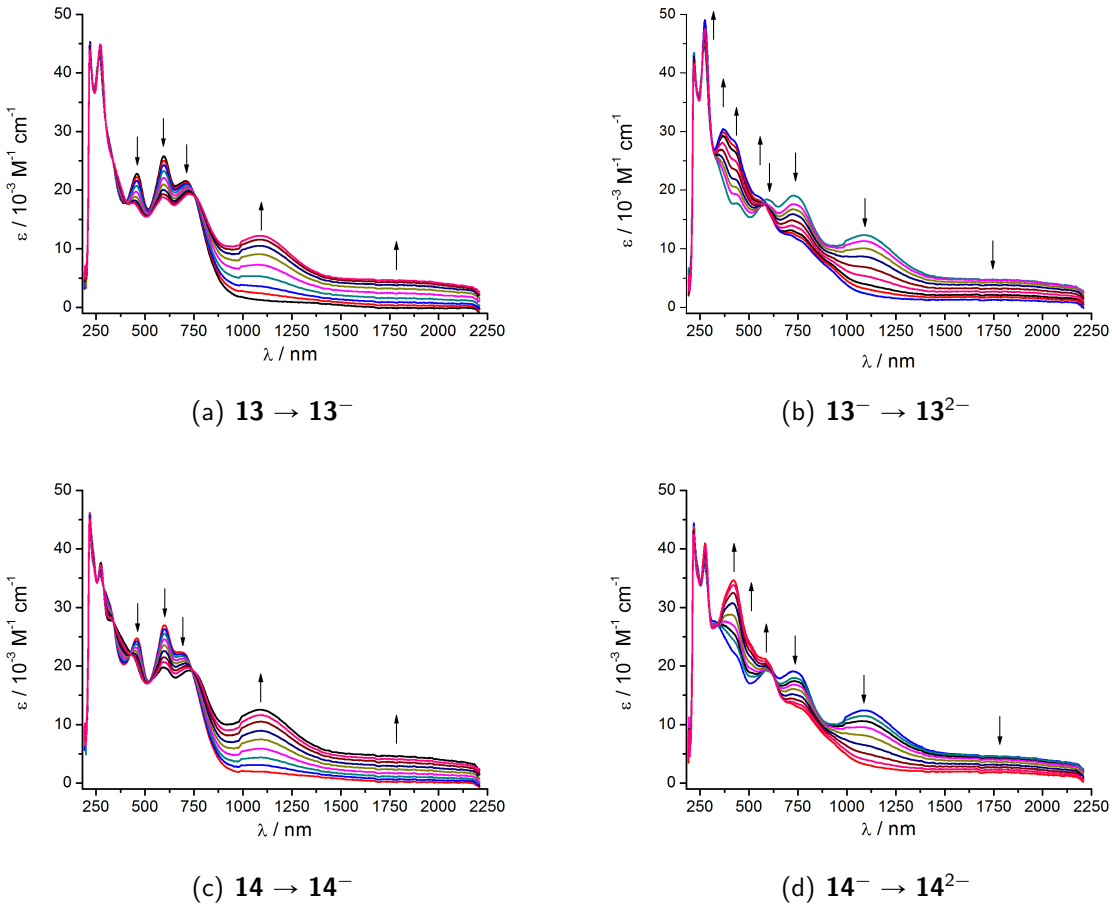

(a) **13** → **13**$^{-}$ (b) **13**$^{-}$ → **13**$^{2-}$

(c) **14** → **14**$^{-}$ (d) **14**$^{-}$ → **14**$^{2-}$

Figure 3.17: *UV–vis–NIR spectroelectrochemical response on stepwise reduction of **13** and **14** in CH_2Cl_2/0.1 M Bu_4NPF_6.*

3.3 Conclusion

This chapter describes the first synthetic pathway to dinuclear ruthenium complexes with non-innocent α-azothiocarbonyl ligands. The *in situ* synthesis of the elusive α-azothiocarbonyl ligand system was achieved through a ring opening reaction of acceptor substituted 2-azothiophenes and subsequent C-C coupling. Remarkably, the new type of reaction cascade lead to the formation of a 1,3,5-hexatrienediyl bridged α-azothiocarbonyl ligand chelate function connecting two $Ru(acac)_2$ metal fragments. In contrast to Chapter 2 where donor $Ru(acac)_2L_S$ and acceptor substituted $[Ru(bpy)_2L_S]^+$ complexes were obtained, with this approach only donor substituted $(acac)_2Ru\mu$-hte$(NNCS)_2Ru(acac)_2$ complexes were accessible. Crystal structure analysis revealed the existence of the bridging ligand in its doubly reduced diradical form μ-hte$(NNCS)_2^{\bullet\bullet 2-}$, supporting the proposed reaction mechanism which includes an electron transfer from the reducing $Ru(acac)_2$ fragment to the 2-azothiophene, inducing the ring opening of the latter. The obtained system M-NIL-$\mu-\pi$-NIL-M represents a unique coordina-

tion arrangement which results in a hitherto unknown type of four-spin system of the type M$^{\bullet}$–$^{\bullet}\mu$-BL$^{\bullet}$–$^{\bullet}$M, which displays a complicated magnetic behavior. Based on SQUID suszeptometry measurements a singlet ground state with thermal accessible excited states of higher multiplicity is suggested. DFT calculations based on geometry optimizations including an unrestricted broken symmetry approach confirm the existence of a singlet ground state and assign a singlet – triplet energy difference of 0.17 eV which is, however, much higher than the thermal energy barrier of 0.025 eV at room temperature, and thus doubts the origin of the paramagnetic magnetic behavior. To resolve this dispute a more detailed analysis of the system will be required.

Both complexes can be reduced in two reversible one-electron steps, forming a mixed-valent intermediate which is identified by IVCT absorption in the near infrared (e.g. $\lambda_{max} = 1700$ nm; $\epsilon = 4700$ M^{-1} cm^{-1})). The low comproportionation constants of $K_c = 760$ and $K_c = 1124$ of these intermediates along with the rhombic EPR signal suggest a localized (Class II) mixed-valent situation, favored by the large metal-metal distance of about 14.5 Å. The oxidized forms of the complexes are only accessible at low temperature and exhibit a g anisotropy of more than double the value of the singly reduced species, indicating an even more Ru^{III} localized spin situation.

The electronic structure of the experimentally accessible oxidation states is illustrated in a simplified scheme in Figure 3.18.

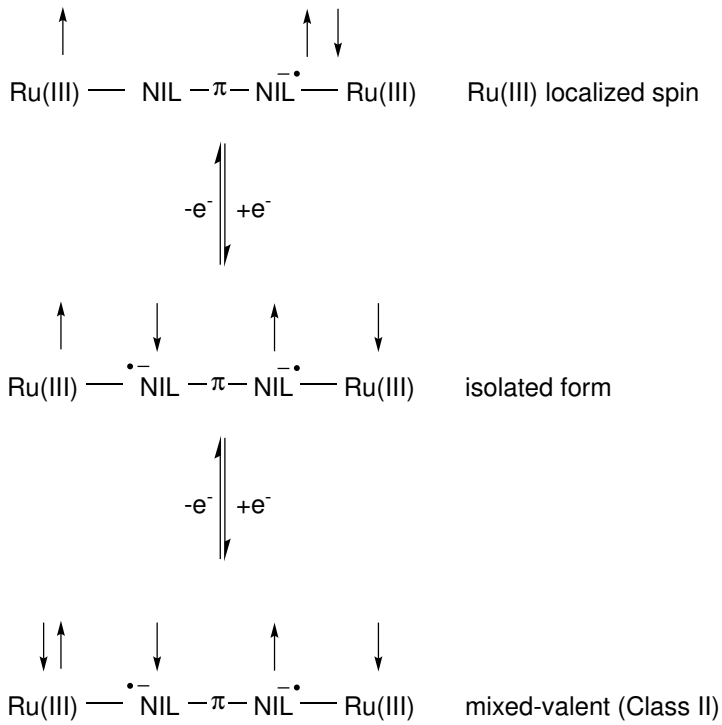

Figure 3.18: *Electronic structure and proposed spin situation of* ***13*** *and* ***14*** *in various oxidation states.*

4 Triazenide, amidinate and guanidinate as new non-innocent ligands

4.1 Introduction

In the previous chapters the α-azothiocarbonyl ligand, forming five-membered chelate rings upon coordination was established as a new member in the series of the redox-active hetero-1,3-diene ligands. An expansion of the ring size to a six-membered chelate coordination type leads to the prominent β-ketaminate and β-diketonate ligands. Their non-innocent character was lately revealed in a more indirect fashion ("hidden non-innocence" or "fractional non-innocence") .[83] A decrease in ring size to a four-membered chelate coordination type results with the well known class of the heteroallylic ligands, which were thought to behave innocently up do date. The bidentate coordination mode and the variation in the chelate ring size by examples of the N-donor ligand types of β-ketaminate, 1,4-diazabutadienes and the amidinates is illustrated in Figure 4.1. Whereas the neutral 1,4-diazabutadienes can undergo two one-electron reductions the anionic β-ketaminate and amidinate ligands can be expected to under go a one electron oxidation to yield neutral radicals. However, none of the heteroallylic ligands could be detected in its neutral radical coordination mode. Free triazenyl radicals have been reported only as transient species derived from organic azides, showing spin density concentrated on the peripheral nitrogen centers.[84]

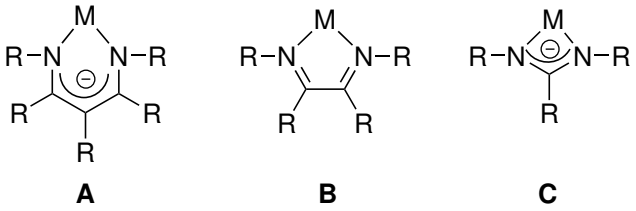

Figure 4.1: *The chelating coordination modes of the β-diketonate (**A**), 1,4-diazabutadiene (**B**) and amidinate (**C**) ligands.*

The goal of this chapter is to reveal the potential for non-innocent character of different kinds of heteroallylic ligands in complexes with ruthenium. It will be shown that oxidation of Ru^{II} complexes with heteroallylic ligands can result either in a $Ru^{III}(L^{-})$ or in a $Ru^{II}(L^{0})$ situation (Figure 4.2). The ambivalent behavior was achieved by the tuning the electronic structure of the complexes, and by variation of the substituents at the heteroallylic as well as ancillary ligands. Therefore, the triazenido, amidinato and guanidinato forms were used, since their substitution pattern can be easily varied. Other potentially non-innocently behaving

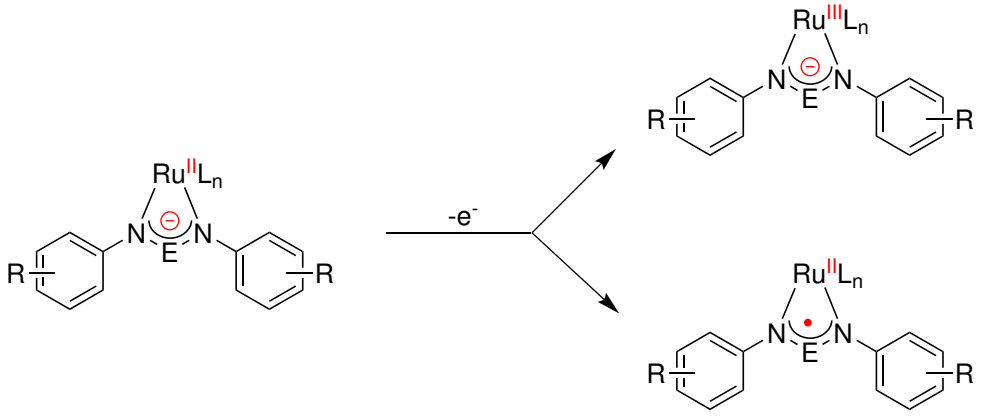

E = N: triazenido; E = CR: amidinato; E = CNR_2: guanidinato

Figure 4.2: *The different pathways for the oxidation of a Ru^{II} complex with triazenido, amidinato or guanidinato ligands.*

ligands containing heteroatoms of the second row are the nitro/nitrito (N or O binding) and the carboxylato ligands.

Besides their potentially redox-active character discussed in this capter, heteroallylic ligands have been investigated intensely regarding various properties. As promising alternatives for cyclopentadienyl-based ligands the N-centered donor ligands have made a comeback in various fields of coordination and organometallic chemistry.[85] Compared to the cyclopentadienyl-based ligands their electronic and steric properties can more easily be tuned by varying the substituents at the N and C atoms, since synthetic routes are much more convenient. In addition to the chelating coordination mode, this type of ligand can also function as bridging ligand for di- or polynuclear metal complexes. The short distance between the coordinating heteroatoms provides an ideal environment for the implementation of short metal-metal distances and thus for the stabilization of metal-metal multiple bonds.[86] The preference for chelating versus bridging coordination mode mainly depends on the size of the substituents on the central carbon atom (for amidinato, guanidinato and carboxylato ligands). Another important feature of the triazenido, amidinato and guanidinato ligands is their high basicity, with pK_a values of the corresponding protonated forms of between pK_a = 5–13,[87] which furnishes a strong donor character to these ligands. Due to the better mesomeric stabilization of the corresponding cationic form, the guanidines are the strongest bases in this series. Compared to the amidinato and the guanidinato ligand the triazenido ligand is less electron donating due to a lower charge density on the coordinating N-atoms,[88] resulting in a more electrophilic character of the coordinated metal.

4.2 Results and discussion

At the beginning of this project the conditions under which a triazenyl, amidinyl or guanidiny radical complex could be stabilized were not known. Therefore, ruthenium complexes containing different ancillary ligands as well as different substituted heteroallylic ligands had to be scrutinized in this regard. Since the synthesis of various substituted triazenes is more convenient than that of the corresponding amidines and guanidines, the initial project focused on the synthesis of different substituted ruthenium triazenido complexes. The aim was to create an adequate substitution pattern for the stabilization of triazenyl radical ligands, which could then be transferred to the synthesis of ruthenium containing amidinato and guanidinato complexes to obtain the corresponding radical complexes after one electron oxidation.

4.2.1 Synthesis of triazenido ruthenium complexes

4.2.1.1 Synthesis of triazene precursors

The triazenes H**15**, H**16** and H**17** were synthesized according to a one step literature procedure[89] starting from the corresponding aniline. The triazene H**18** was synthesized according to a literature procedure[90] starting from *tert*-butylazide and *tert*-butyllithium (Figure 4.3).

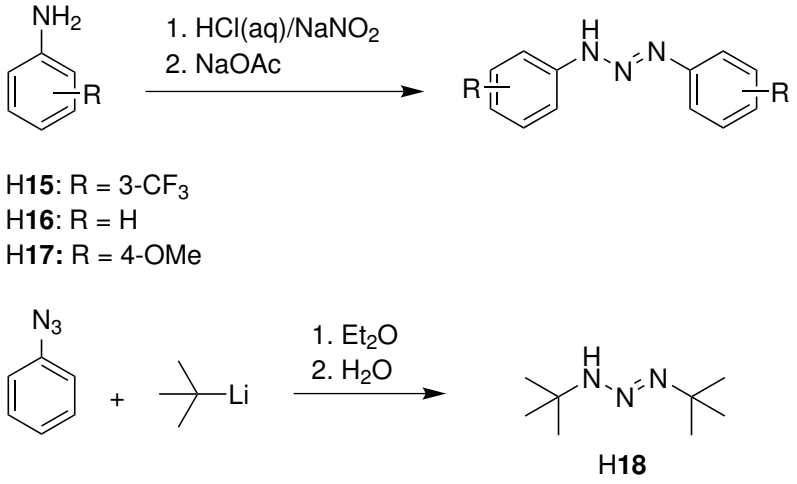

Figure 4.3: *Synthesis of the triazene ligands.*

4.2.1.2 Synthesis of triazenido Ru(bpy)$_2$, Ru(4,4'-EtCO$_2$-bpy)$_2$ and Ru(pap)$_2$ complexes

The metal precursors Ru(bpy)$_2$Cl$_2$[91](bpy = 2,2'-bipyridine), Ru(4,4'-EtCO$_2$-bpy)$_2$Cl$_2$[92] and α-Ru(pap)$_2$Cl$_2$[93] (pap = 2-phenylazopyridine) were synthesized according to literature procedures. AgBF$_4$ was used for activation of the metal precursors by chloride abstraction.

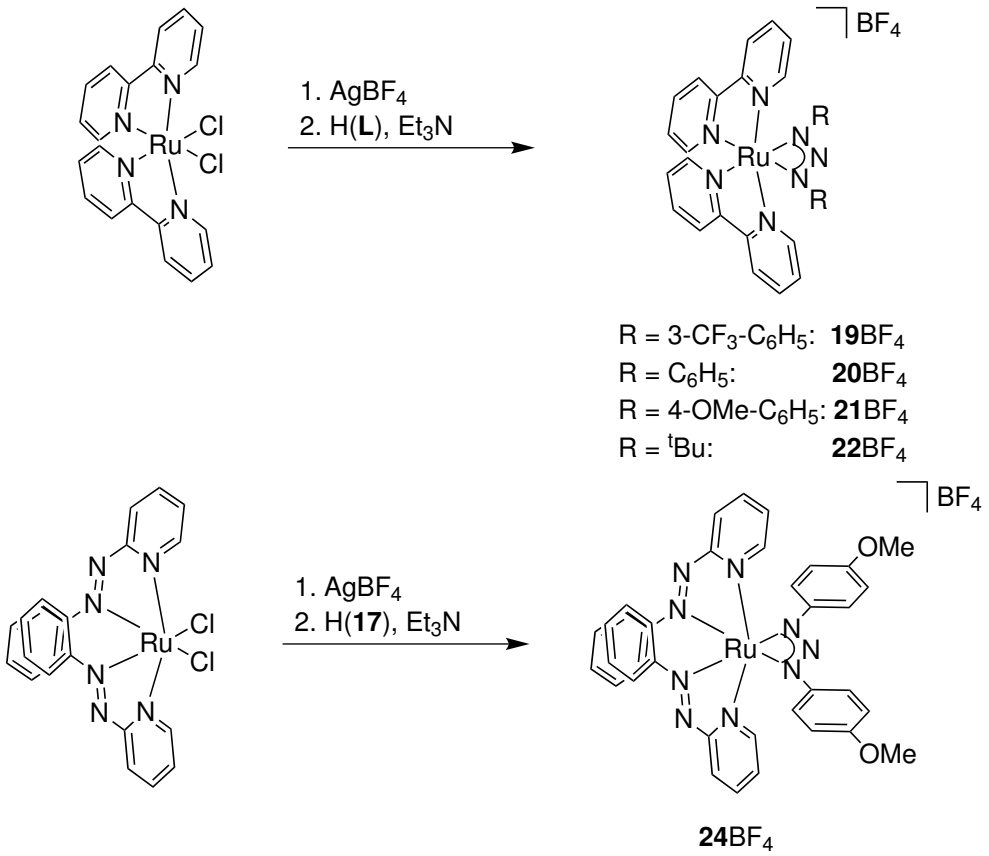

Figure 4.4: *Synthesis of the bis(bpy), bis(4,4'-$EtCO_2$-bpy) and bis(pap) substituted triazenido ruthenium complexes.*

4.2.1.3 Synthesis of the p-cymene substituted triazenido ruthenium complexes

For reasons of favoring a ligand centered oxidation of the complex, p-cymene (p-cym) substituted ruthenium complexes containing the deprotonated 1,3-bis(4-methoxyphenyl)triazene (**17**$^-$) were prepared with various ancillary ligands. The ruthenium precursor $[Ru(p\text{-}cym)Cl_2]_2$ is comercially available.

Ru(p-cym)Cl(**17**) (**25**) was synthesized by reacting the comercially available precursor $[Ru(p\text{-}cym)Cl_2]_2$ under deprotonation with H**17**. $AgBF_4$ was used for activation of the metal precursors by chloride abstraction.

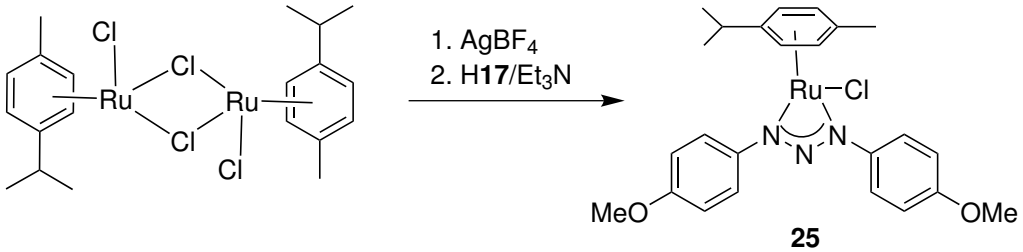

Figure 4.5: *Synthesis of the p-cymene substituted triazenido complexes.*

Ru(p-cym)CN(**17**) (**26**) was synthesized by reacting **25** with an excess of KCN in acetonitrile under reflux. The π-accepting CN^- ligand was introduced to withdraw electron density via backbonding from the Ru^{II} to favor the triazenido oxidation.

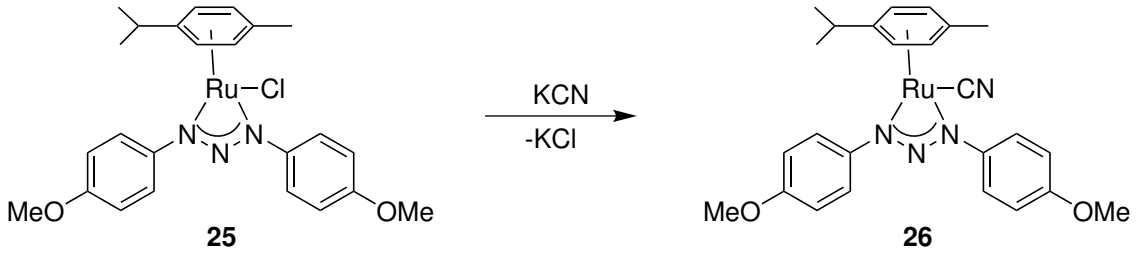

Figure 4.6: *Synthesis of the p-cymene substituted triazenido complexes.*

[Ru(p-cym)MeCN(**17**)]SbF_6 (**27**SbF_6) was synthesized by reacting **25** with one equivalent of $AgSbF_6$ in acetonitrile under reflux. $AgSbF_6$ was used for chlorid abstraction to obtain a better crystalisation behavior of the resulting complex. The neutral acetonitril ligand was introduced to increase the positive charge at Ru^{II} to favor the triazenido oxidation.

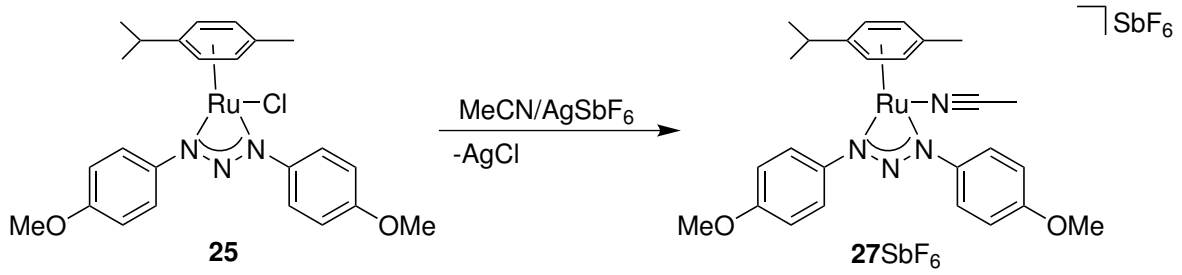

Figure 4.7: *Synthesis of the p-cymene substituted triazenido complexes.*

4.2.2 Molecular structures of the ligand and the triazenido complexes

The ligand precursor H**17** as well as the complexes **21**ClO_4 and **27**SbF_6 could be crystallized for X-ray structure analysis (Figure 4.9–4.10). Crystallization procedures were as follows. H**17**: slow evaporation of a solution of H**17** in CH_2Cl_2/n-hexane; Complex **21**ClO_4: slow diffusion of Et_2O into a solution of **21**PF_6 and NBu_4ClO_4 in MeCN; **27**SbF_6: slow diffusion of Et_2O into a solution of **27**SbF_6 in MeCN. The data of the important bond lengths and angles are summarized and compared with those of the uncoordinated triazene H**17** in Table 4.13.

The N-N bond lengths of the free triazene do not represent the typical even bond order, since the N2-N3(H) bond distance of 1.316(2) Å is too short for an ordinary N-N single bond ($\sim$ 1.35 Å) and the N1-N2 bond of 1.293(2) Å is too long for N=N ($\sim$ 1.25 Å), indicating N-N bond orders of around 1.5 caused by a partial charge delocalization. After deprotonation and coordination the changes in the N-N bond lengths are only marginal. The deviation of

Table 4.13: *Selected bond lengths (Å) and angles (°) in the Ru-N1-N2-N3 chelate ring.*

bond (Å)	**21**ClO_4	**27**SbF_6	H**17**
Ru1-N1	2.072(2)	2.090(3)	
Ru1-N3	2.078(2)	2.058(3)	
N1-N2	1.312(3)	1.314(4)	1.293(2)
N2-N3	1.316(3)	1.313(4)	1.316(2)
angle (°)			
N1-N2-N3	103.9(2)	102.6(3)	112.8(1)

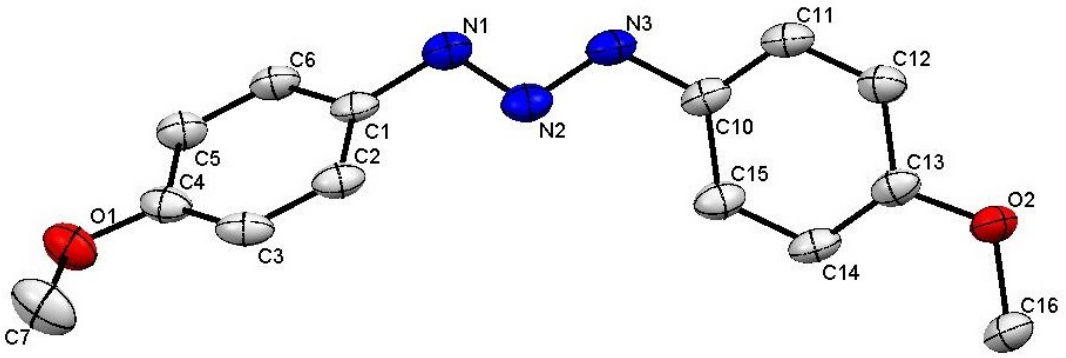

Figure 4.8: *Molecular structure of H**17** in the crystal.*

the N1-N2-N3 angle in the complex (103°) from the angle of the free triazene (113°) can be explained by a distortion due to chelate coordination to the metal center.

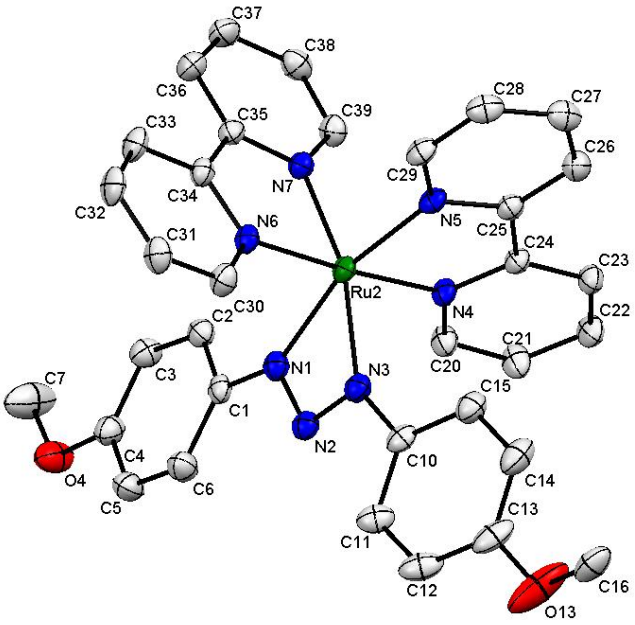

Figure 4.9: *Molecular structure of* ***21***$^+$ *in the crystal of* ***21***ClO_4.

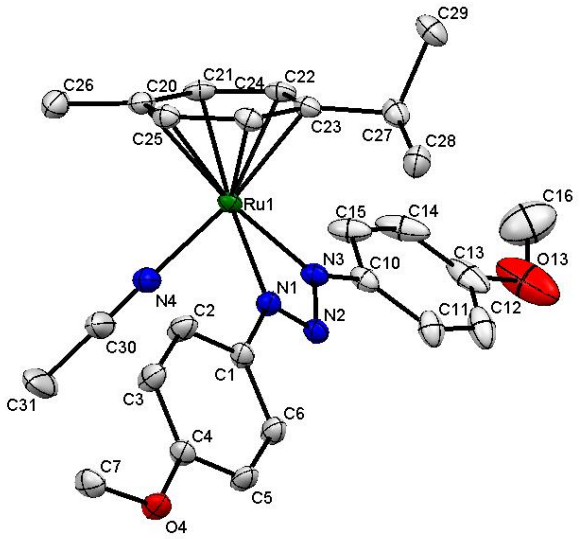

Figure 4.10: *Molecular structure of* ***27***$^+$ *in the crystal of* ***27***SbF_6.

4.2.3 Cyclic voltammetry of the triazenido ruthenium complexes

All ruthenium triazenido complexes (Figures 4.4–4.7) were investigated by cyclic voltammetry in 0.1 M CH_2Cl_2/NBu_4PF_6 at a scan rate of 100 mv/s. Exemplary plots of the cyclovoltammograms are illustrated in Figure 4.11. The redox potentials are summarized in Table 4.14.

The $Ru(bpy)_2$ complexes **19**BF_4–**22**BF_4 exhibit one irreversible reduction which is attributed to a process at the bpy ligand, since the triazenido ligands are not reducible. On substitution of both bpy ligands by the acceptor substituted 4,4'-$EtCO_2$-bpy or the even stronger π-acceptor ligand pap, the resulting complexes **23**BF_4 and **24**BF_4 show two reversible reductions, one at each of the acceptor ligands.[94]

Nevertheless, the aim of generating a stable triazenyl radical complex through a one electron oxidation places a higher importance on the oxidation processes which are discussed in the following. By varying the substituents at the triazenido ligand from electron withdrawing (R = 3-CF_3-C_6H_5, **19**BF_4) to electron donating (R = 4-OMe-C_6H_5, **21**BF_4) the oxidation potentials shift gradually towards lower potentials from $E_{1/2}$ = 0.45 V to $E_{1/2}$ = -0.10 V. After the replacement of the π-donating/σ-accepting 4-methoxyphenyl substituent by a purely σ-donating *tert*-butyl substituent the oxidation potential decreases further to a value of $E_{1/2}$ = -0.12 V for **22**BF_4. The fact that the N,N'-dialkyl complex **22**BF_4 exhibits only one oxidation leads to the conclusion that the triazenido ligand participates in the second oxidation of complexes **20**BF_4 and **21**BF_4. On substitution of the bpy ligands by the stronger π-accepting 4,4'-$EtCO_2$-bpy and pap ligands the oxidation potential increases to the higher values of $E_{1/2}$ = 0.12 V for **23**BF_4 and $E_{1/2}$ = 0.33 V for **24**BF_4, respectively. All p-cymene containing complexes exhibit one reversible and one irreversible oxidation. In Figure 4.11e a cyclovoltammogram of **27**SbF_6 is depicted in which i) only the first and ii) both oxidations are displayed, since

Table 4.14: *Redox potentials[a] of triazenido ruthenium complexes.*

complex	E^0_{298} / V vs $Fc^{+/0}$			
19BF_4		0.45	-1.88[c]	
20BF_4	1.18 [b]	0.22	-1.90[c]	
21BF_4	0.63	-0.10	-2.06[c]	
22BF_4		-0.12		
23BF_4		0.13	-1.43	-1.80
24BF_4		0.33	-0.70	-1.38
25	0.91[b]	0.24		
26	0.95[b]	0.26		
27SbF_6	0.91[b]	0.39		

[a] *In CH_2Cl_2/0.1 M Bu_4NPF_6/scan rate 100 mV s^{-1}.* [b] *Anodic peak potential.* [c] *Cathodic peak potential.*

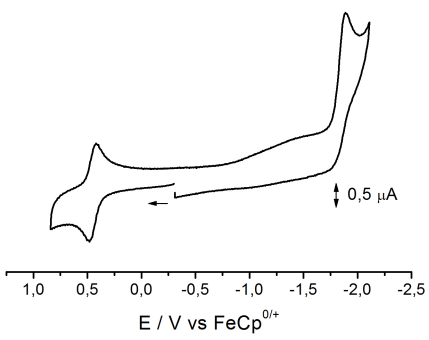

(a) **19**BF_4

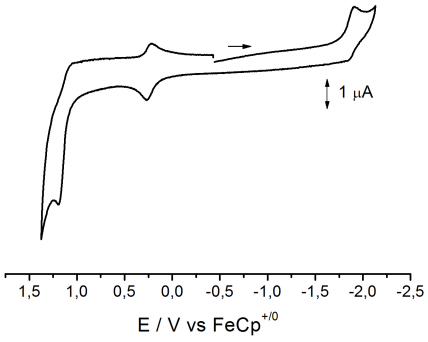

(b) **20**BF_4

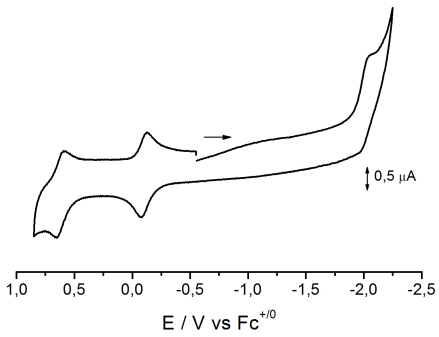

(c) **21**BF_4

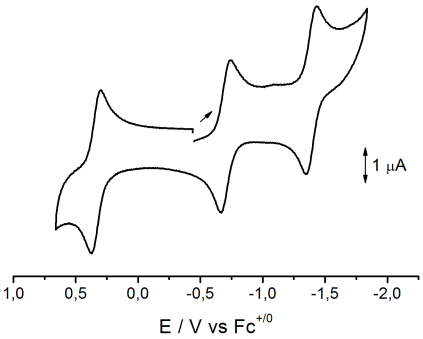

(d) **24**BF_4

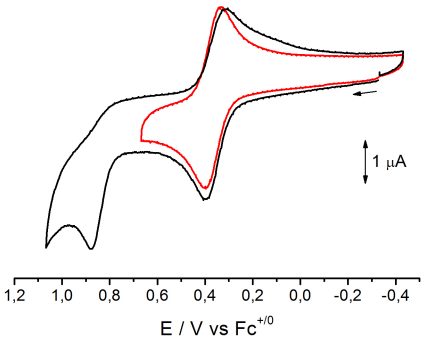

(e) **27**SbF_6 Red: only first oxidation; Black: first and second oxidation.

Figure 4.11: *Cyclic voltammetry of the triazenido ruthenium complexes in CH_2Cl_2/0.1 M Bu_4NPF_6 (scan rate 100 mV s^{-1}).*

the first oxidation is only fully reversible if the second oxidation is not monitored. For the p-cymene containing complexes the effect on the oxidation potential by exchangeing a π-donating chlorido (**25**) with a π-accepting cyano ligand (**26**) is marginal, with a shift of only Δ E = 0.02 V to higher potential. An exchange of the chlorido ligand by the neutral acetonitrile ligand, however, shifts the oxidation potential from $E_{1/2}$ = 0.24 V (**24**) to $E_{1/2}$ = 0.39 V (**27**SbF_6).

This effect can be explained by an increase of the overall charge of the complex from 0 to +1, resulting in a higher oxidation potential.

Because the influence of the substitution pattern of the complexes towards the oxidation potential is not in correlation with the influence towards the nature of the oxidation (ruthenium vs triazenido), EPR spectroelectrochemistry needs to be applied to all complexes. The results are discussed in the following section.

4.2.4 EPR spectroelectrochemistry of the triazenido ruthenium complexes

Cyclic voltammetry experiments revealed at least one reversible oxidation for each of the triazenido complexes. To get an insight into the nature of the oxidation process (ruthenium vs triazenido) the oxidized forms of the triazenido ruthenium complexes were investigated by EPR spectroscopy. Literature data suggest that the reductions of complexes **23**BF_4 and **24**BF_4 occur at the strongly π-accepting ancillary ligands 4,4'-EtCO_2-bpy or pap, respectively.[94] Their reduction processes shall therefore not be discussed in this section. Exemplary plots of the EPR spectra of $\mathbf{19}^{2+}$, $\mathbf{21}^{2+}$, $\mathbf{24}^{2+}$, $\mathbf{25}^{+}$ and $\mathbf{26}^{2+}$ are depicted in Figures 4.12 and 4.13. The EPR data as well as the potentials of the first oxidation of all complexes are summarized in Table 4.15, indicating that the oxidation potentials and the g values are not in correlation.

The rhombic EPR signal of complex $\mathbf{19}^{2+}$ with a g anisotropy of $\Delta g = 0.451$ at 110K indicates a predominantly ruthenium centered spin situation $Ru^{III}(L^{-})$. By exchanging the electron withdrawing 3-CF_3 with an electron donating 4-OMe ($\mathbf{21}^{2+}$) group, the g anisotropy decreases to a value of $\Delta g = 0.100$ at 110 K, suggesting a mixed situation with approximately

Table 4.15: *EPR and electrochemical data of the mono-oxidized triazenido ruthenium complexes.*[a]

complex	$E_{1/2}$	g_{iso} (298 K)	g_1, g_2, g_3 (110 K)	g_1-g_3
$\mathbf{19}^{2+}$	0.45	2.194	2.350, 2.273, 1.899	0.451
$\mathbf{20}^{2+}$	0.22	2.104	2.185, 2.142, 1.954	0.231
$\mathbf{21}^{2+}$	-0.10	2.048	2.087, 2.064, 1.987	0.100
$\mathbf{22}^{2+}$	-0.12	2.154	2.273, 2.243, 1.938	0.047
$\mathbf{23}^{2+}$	0.13	2.032	2.056, 2.039, 1.995	0.061
$\mathbf{24}^{2+}$	0.33	2.011	[e]	< 0.02
$\mathbf{25}^{+}$	0.24	2.011[b]	[e]	< 0.02
$\mathbf{26}^{+}$	0.26	2.011[c]	[e]	< 0.02
$\mathbf{27}^{2+}$	0.39	2.007[d]	[e]	< 0.02

[a] *Potentials $E_{1/2}$ versus $Fc^{+/0}$ from cyclic voltammetry in CH_2Cl_2/0.1 M Bu_4NPF_6; EPR data from electrolysis in CH_2Cl_2/0.1 M Bu_4NPF_6; X band results.* [b] *Hyperfine splitting: 0.66 mT (2 x ^{14}N), 0.55 mT (1 x ^{99,101}Ru).* [c] *Hyperfine splitting: 0.66 mT (2 x ^{14}N), 0.37 mT (1 x ^{99,101}Ru).* [d] *Hyperfine splitting: 0.199 mT (1 x ^{14}N), 0.629 mT (2 x ^{14}N), 0.127 mT (6 x ^{1}H), 0.109 mT (2 x ^{1}H), 0.080 mT (2 x ^{1}H), 0.094 mT (4 x ^{1}H), 0.272 mT (1 x ^{99,101}Ru). Linewidth: $\Delta B_{1/2} = 0.07$ mT.* [e] *g anisotropy not resolved.*

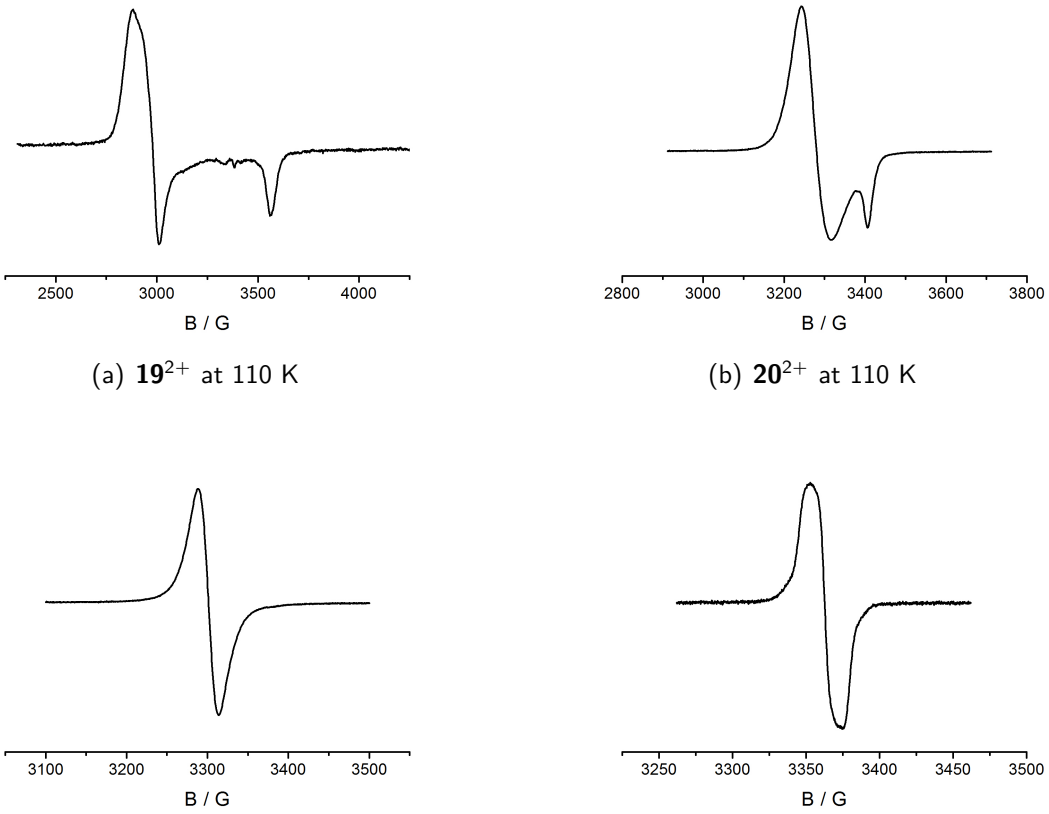

(a) $\mathbf{19}^{2+}$ at 110 K

(b) $\mathbf{20}^{2+}$ at 110 K

(c) $\mathbf{21}^{2+}$ at 298 K

(d) $\mathbf{24}^{2+}$ at 298 K

Figure 4.12: *EPR spectra of the oxidized triazenido complexes in CH_2Cl_2/0.1 M Bu_4NPF_6.*

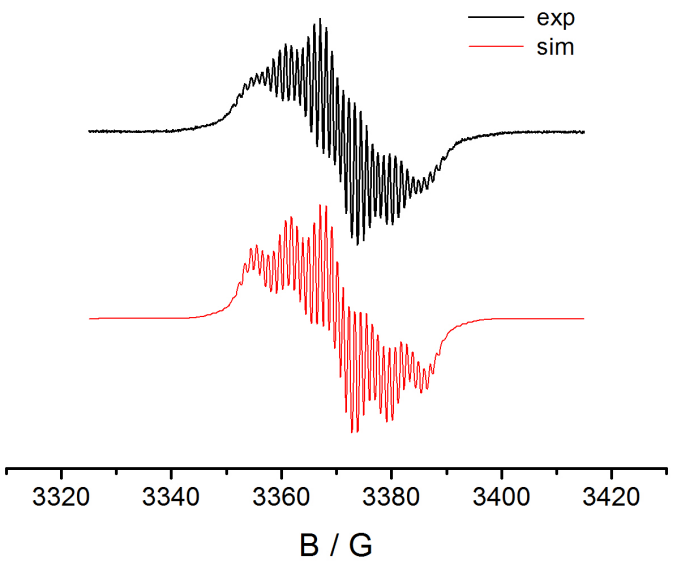

Figure 4.13: *EPR spectrum of $\mathbf{27}^{2+}$ in CH_2Cl_2/0.1 M Bu_4NPF_6 at 298 K.*

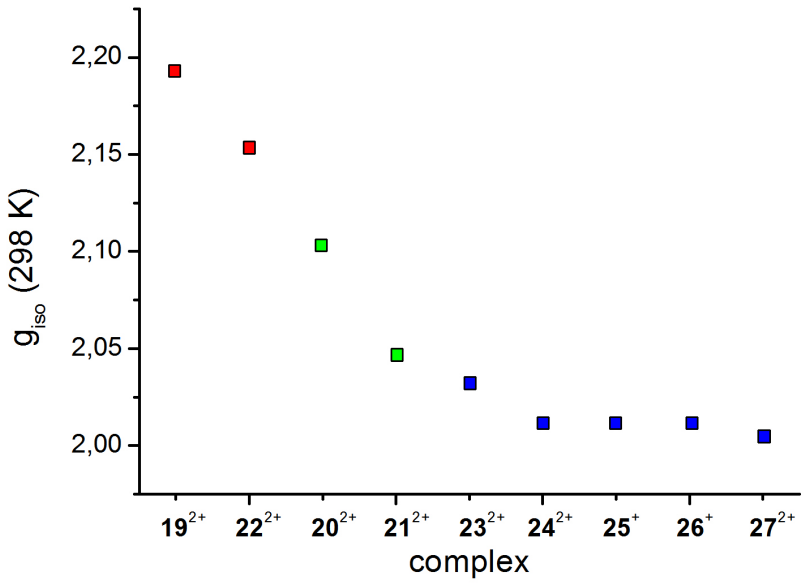

Figure 4.14: *Illustration of the correlation between the substitution pattern of the triazenido complexes and the isotropic g value. Red: $Ru^{III}(L^{-})$ complex; green: mixed radical situation $Ru^{III}(L^{-}) \leftrightarrow Ru^{II}(L^{\bullet})$; blue: triazenyl radical complex $Ru^{II}(L^{\bullet})$.*

equal spin density on ruthenium and the triazenido ligand $Ru^{III}(L^{-}) \leftrightarrow Ru^{II}(L^{\bullet})$. To hamper Ru^{II} oxidation and favor the oxidation of the triazenido ligand, the weakly π-accepting bpy ligands were substituted with the strongly π-accepting 4,4'-$EtCO_2$-bpy or pap ligands, respectively. The influence of replacement is nicely shown in the EPR spectra of complexes $\mathbf{23}^{2+}$ and $\mathbf{24}^{+}$ which exhibit a g anisotropy of $\Delta g < 0.02$ at 110K and isotropic g values of around 2.011 at 298 K. The isotropic g values suggest predominant ligand contributions to the SOMO $Ru^{II}(L^{\bullet})$. The metal contribution, however, is still high enough to cause a line broadening which quenches the hyperfine structure in the spectra. Since a hyperfine structure resulting from the coupling to N and H atoms of the triazenyl radical ligand would be a clear evidence for the desired ligand centered oxidation, a different set of ancillary ligands had to be introduced. The new strategy included the replacement of the π-accepting/σ-donating 4,4'-$EtCO_2$-bpy or pap ligand through the π-accepting but not σ-donating p-cymene ligand. This approach was thought to decrease the electron density at Ru^{II} center and thus inhibit its oxidation. For reasons of synthetic accessibility the first p-cymene substituted complex investigated ($\mathbf{25}^{+}$) included a π-donating chlorido ligand. This substitution had no effect on the isotropic g value of $g = 2.011$ at 298 K, however, a poorly resolved quintet with coupling constants of $A_1 = 0.66$ mT (2 x ^{14}N) and $A_2 = 0.55$ mT (1 x $^{99,101}Ru$) emerged in the spectrum. The quintet structure of triazenyl radicals can be explained by the symmetry of the SOMO which has a node located at the central N atom, diminishing spin density and therefore its coupling constant. An

exchange of the π-donating chlorido ligand with a π-accepting cyano ligand had no influence on neither the g value nor on the hyperfine structure. The replacement of the chlorido ligand with a neutral π-accepting acetonitril ligand ($\mathbf{27}^{2+}$), however, resulted in a decrease of the g value to g = 2.007 and the appearance of a well resolved hyperfine structure. The spectrum could be simulated (Figure 4.13) using the coupling constants displayed in the footnote in Table 4.15. An increase of the overall charge around the ruthenium center facilitates a ligand centered oxidation and explains the ligand substitution effect of cyano versus acetonitrile. The observation of a low g value close to that of the free electron with $g_e = 2.0023$ along with the hyperfine splitting is a clear evidence for an almost purely ligand centered oxidation resulting in a triazenyl radical complex. Complex $\mathbf{27}^{2+}$ is the first example of a metal stabilized triazenyl radical. The remarkable correlation between the structures of the complexes and the isotropic g value is visualized in the diagram of Figure 4.14.

4.2.5 DFT calculations of the triazenido ruthenium complexes

To add theoretical insight into the electronic structures of the triazenido complexes in their singly oxidized forms the spin densities of complexes $\mathbf{19}^{2+}$, $\mathbf{21}^{2+}$ and $\mathbf{27}^{2+}$ were calculated using DFT methods. All calculation were performed by Dr. Stanislav Záliš on a G09/PBE0/6-311G(d)/PCM-CH_2Cl_2 level of theory. Plots of the spin densities are depicted in Figure 4.15 and the data are summarized in Table 4.16

The calculations confirm the experimental results of the EPR spectroelectrochemistry. Whereas a spin density at ruthenium of 72.6 % for $\mathbf{19}^{2+}$ indicates a predominantly ruthenium-centered radical $Ru^{III}(L^-)$, the spin density at ruthenium of only 0.4 % for $\mathbf{27}^{2+}$ clearly confirms the existence of a triazenyl radical complex $Ru^{II}(L^\bullet)$. The ruthenium spin density of 18.5 % for $\mathbf{21}^{2+}$ is interpreted as a mixed orbital situation in which the radical exhibits metal as well as ligand character $Ru^{III}(L^-) \leftrightarrow Ru^{II}(L^\bullet)$.

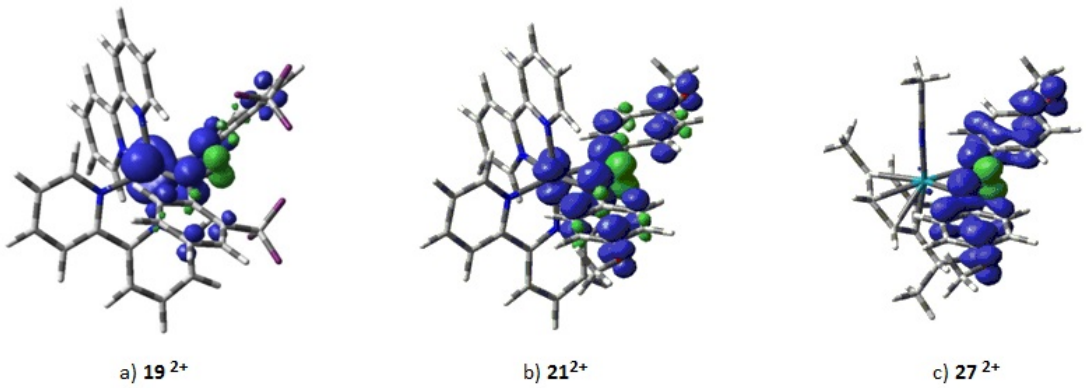

Figure 4.15: *Plots of the DFT calculated (G09/PBE0/6-311G(d)/PCM-CH_2Cl_2) spin densities of representative triazenido ruthenium complexes.*

Table 4.16: *DFT calculated (G09/PBE0/6-311G(d)/PCM-CH_2Cl_2) spin densities of representative triazenido ruthenium complexes.*

	$\mathbf{19}^{2+}$	$\mathbf{21}^{2+}$	$\mathbf{27}^{2+}$
ρ Ru	0.726	0.185	0.004
ρ N1	0.136	0.251	0.243
ρ N2	-0.078	-0.149	-0.157
ρ N3	0.136	0.251	0.243
ρ R1	0.056	0.240	0.336
ρ R2	0.056	0.240	0.336

4.2.6 UV-vis-NIR spectroelectrochemistry of the triazenido ruthenium complexes

UV−vis−NIR spectroelectrochemical measurements of all triazenido ruthenium complexes using an OTTLE cell[49] are illustrated in Figures 4.21–4.17 and summarized in Table 4.21. The spectra are discussed briefly based on EPR results and literature reports, since no TD-DFT calculations for an exact band assignment are available. For the characterization of Ru^{III} or triazenyl radical complexes only the oxidation processes are of interest and are therefore discussed exclusively.

The $Ru(bpy)_2$ complexes $\mathbf{19}^{+}$–$\mathbf{21}^{+}$ exhibit a low energy transition around 465 nm, which are at a similar energy level as the ruthenium-based MLCT transitions in $[Ru(bpy)_3]^{2+}$ (455 nm).[95] Through an exchange of the phenyl groups at the triazene with the stronger electron donating *tert*-butyl group (**22**) the MLCT band shifts to lower energy of 537 nm. Upon ruthenium centered oxidation of $\mathbf{19}^{+}$ and for $\mathbf{21}^{+}$ a hypsochromic shift of the MLCT band is expected, however, a band in the near infrared region at 960 nm for $\mathbf{19}^{2+}$ and 740 nm $\mathbf{21}^{2+}$ emerges. This low energy band may be explained by the allowance of an LMCT transition from the triazenido ligand to the t_{2g} orbitals of ruthenium after oxidation. Complexes $\mathbf{20}^{2+}$ and $\mathbf{21}^{2+}$, with their more ligand-centered spin density exhibit a low energy band at even higher wavelengths of around 1030 nm, which might indicate a predominantly intra ligand charge transfer (ILCT) transition.

In agreement with MLCT transitions around 550 nm for related amidinato complexes containing the $Ru(pap)_2$ fragment,[96] complexes $\mathbf{23}^{+}$ and $\mathbf{24}^{+}$ exhibit a low energy transition at 560 nm and 530 nm, respectively. The predominantly ligand centered oxidation results in a bathochromic shift of these MLCT transitions to 750 nm ($\mathbf{23}^{+}$) and 895 nm ($\mathbf{24}^{+}$), which may also be attributed to a mixed LMCT/ILCT transition.

The MLCT transitions of the Ru(p-cym) triazenido complexes occur around 415 nm and are therefore higher in energy than the MLCT transitions of the complexes containing the stronger π-accepting nitrogen-based heterocyclic ligands. Oxidation of the p-cymene complexes results in the appearance of a near infrared absorption band. Due to the triazenyl radical character

of the singly oxidized complexes, as evidenced by EPR spectroscopy, these low energy bands are attributed mainly to an ILCT. The near infrared ILCT transitions are of remarkably high intensities and narrow line widths: 872 nm (ϵ = 26 700 M^{-1} cm^{-1}; $\Delta_{1/2}$ = 1100 cm^{-1}) for $\mathbf{25}^{+}$, 880 nm (ϵ = 29 800 M^{-1} cm^{-1}; $\Delta_{1/2}$ = 845 cm^{-1}) for $\mathbf{26}^{+}$ and 900 nm (ϵ = 34 000 M^{-1} cm^{-1}; $\Delta_{1/2}$ = 715 cm^{-1}) for $\mathbf{27}^{2+}$, pointing to small geometry differences between ground and excited state.

Table 4.17: *UV–vis–NIR data for **19–27** in various oxidation states from OTTLE spectroelectrochemistry in CH_2Cl_2/0.1 M Bu_4NPF_6.*

complex	λ_{max} [nm] (ϵ (M^{-1} cm^{-1}))
$\mathbf{19}^{+}$	240(29 700), 290(46 200), 330(21 300), 460(14 600), 480(4 700)
$\mathbf{19}^{2+}$	245(36 300), 315(33 000), 340(18 700), 965(3 600)
$\mathbf{20}^{+}$	243(35 700), 287(46 000), 343(23 600), 475(21 800), 630(1 100)
$\mathbf{20}^{2+}$	243(35 700), 271(39 000), 365(24 600), 510(14 100), 626(600), 1055(7 600)
$\mathbf{21}^{+}$	247(34 500), 290(56 900), 336(23 300), 470(21 000), 576(3 900), 660(2 000)
$\mathbf{21}^{2+}$	247(29 200), 285(42 300), 406(21 800), 536(16 900), 573(44 100), 681(5 600), 748(9 000), 1020(5 800)
$\mathbf{21}^{3+}$	247(29 200), 285(42 300), 390(18 900), 504(21 000), 573(20 600), 687(11 100), 751(24 200), 990(4 700), 1370(500)
$\mathbf{22}^{+}$	243(21 900), 294(27 100), 350(11 100), 405(6 300), 473(6 400), 535(7 500), 680(600)
$\mathbf{22}^{2+}$	263(23 800), 303(20 200), 314(19 600), 350(5 500), 384(3 100), 740(2 900)
$\mathbf{23}^{+}$	230(44 700), 310(66 100), 465(30 400), 565(9 300), 756(2 000)
$\mathbf{23}^{2+}$	230(44 700), 305(53 700), 410(26 000), 534(22 900), 573(50 500), 681(4 600), 756(15 500), 970(7 100), 1250(1 900)
$\mathbf{24}^{+}$	243(29 900), 306(28 900), 437(19 700), 533(10 800), 625(2 500)
$\mathbf{24}^{2+}$	229(24 200), 275(21 200), 350(27 800), 379(27 800), 538(28 000), 569(51 000), 730(7 000), 817(8 600), 897(21 300)
25	217(18 500), 252(20 600), 314(14 400), 410(23 300)
$\mathbf{25}^{+}$	217(18 500), 250(13 000), 340(12 200), 560(32 300), 542(55 100), 775(13 200), 872(26 800)
26	248(14 200), 320(9 600), 422(18 400)
$\mathbf{26}^{+}$	245(8 300), 334(10 700), 511(26 700), 541(48 800), 710(5 400), 790(9 600), 880(29 800)
$\mathbf{27}^{+}$	247(21 450), 306(11 300), 410(20 600)
$\mathbf{27}^{2+}$	247(12 400), 324(12 00), 524(27 300), 560(37 600), 718(3 000), 821(6 600), 903(33 900)

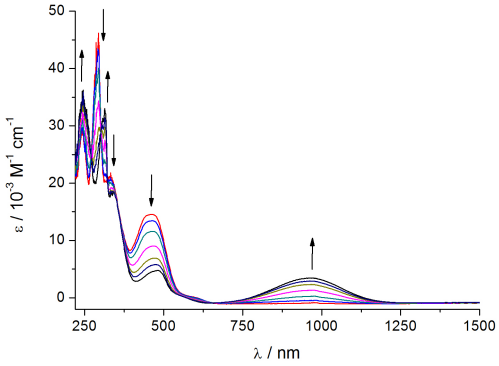

(a) $\mathbf{19}^{+} \rightarrow \mathbf{19}^{2+}$

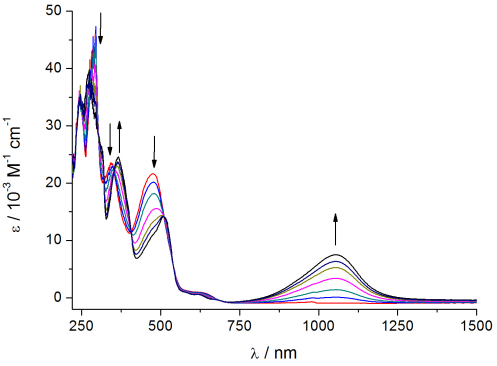

(b) $\mathbf{20}^{+} \rightarrow \mathbf{20}^{2+}$

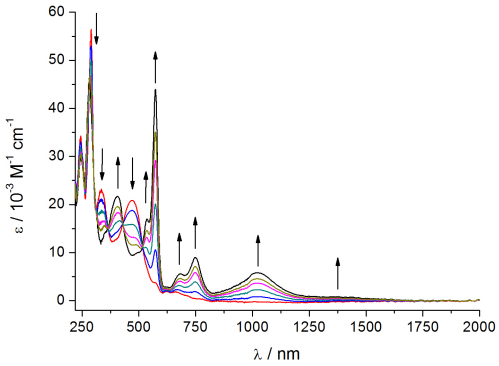

(c) $\mathbf{21}^{+} \rightarrow \mathbf{21}^{2+}$

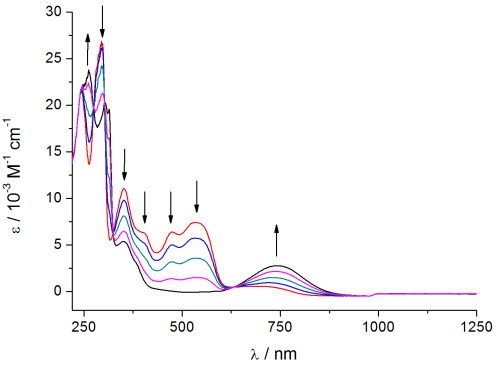

(d) $\mathbf{22}^{+} \rightarrow \mathbf{22}^{2+}$

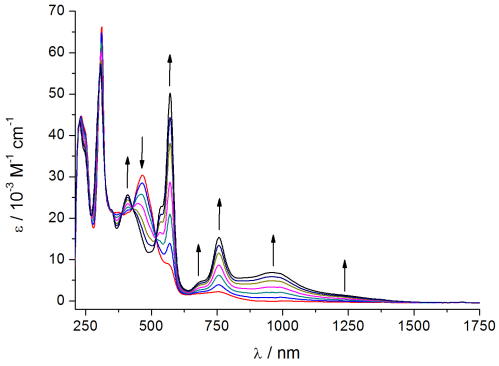

(e) $\mathbf{23}^{+} \rightarrow \mathbf{23}^{2+}$

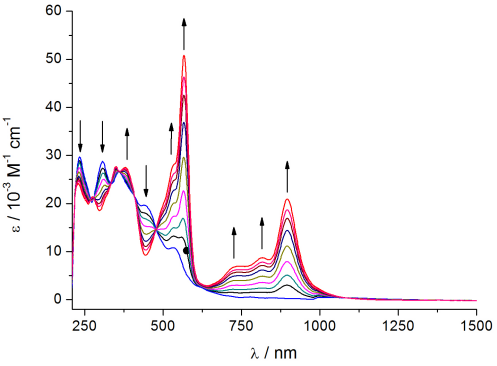

(f) $\mathbf{24}^{+} \rightarrow \mathbf{24}^{2+}$

Figure 4.16: *UV–vis–NIR spectroelectrochemical response on oxidation of triazenido ruthenium complexes in CH_2Cl_2/0.1 M Bu_4NPF_6.*

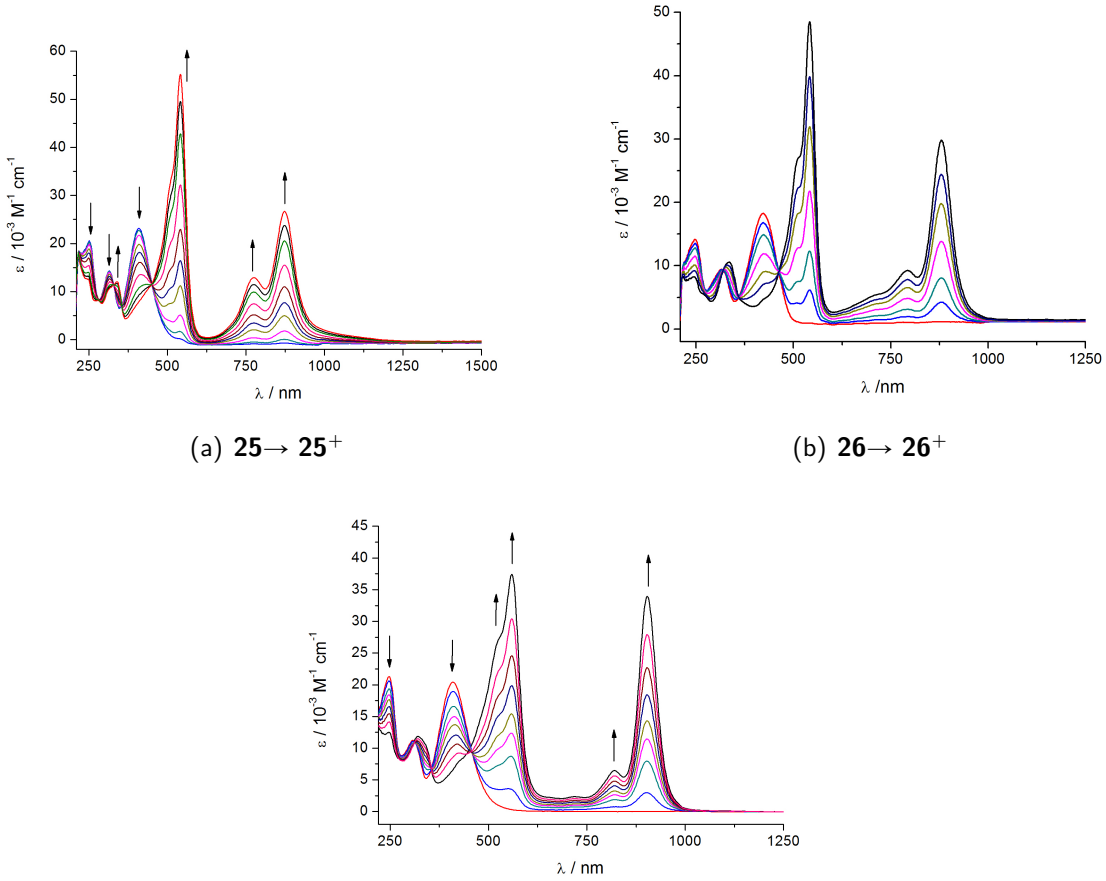

(a) **25**→ **25**$^+$

(b) **26**→ **26**$^+$

(c) **27**$^+$ → **27**$^{2+}$

Figure 4.17: *UV–vis–NIR spectroelectrochemical response of triazenido ruthenium complexes on oxidation in CH_2Cl_2/0.1 M Bu_4NPF_6.*

4.2.7 Synthesis of the amidinato and guanidinato ruthenium complexes

Since the synthetic approach utilized for the triazenido complexes resulted in the observation of Ru^{III} as well as triazenyl radical complexes, this strategy was adopted for the synthesis of amidinato and guanidinato complexes which can exhibit a Ru^{III}, a mixed and a ligand centered radical (amidinyl, guanidinyl) complex after oxidation. H**L** stands for the neutral amidine or guanidine, respectively, as precursor for the deprotonated amidinato or guadinato ligand **L**$^-$ and not for the corresponding amidinium or guanidinium cations.

4.2.7.1 Synthesis of the amidine ligand precursor

The aminidine ligand precursor H**28** was synthesized according to a literature procedure[97] by reacting p-anisidine with ethyl ortho-acetate at 140 °C for 3 h.

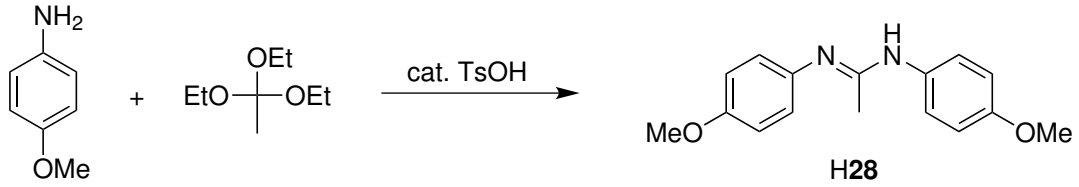

Figure 4.18: *Synthesis of the 4-methoxy substituted amidine ligand **28**.*

4.2.7.2 Synthesis of the guanidine ligand

Due to the methoxy substituents the guanidine ligand precursor H**29** can not be directly obtained from corresponding thiourea in a one step reaction with permanganate. Therefore, a published three step procedure[98] starting from the corresponding thiourea was used for the synthesis of the protonated guanidine ligand.

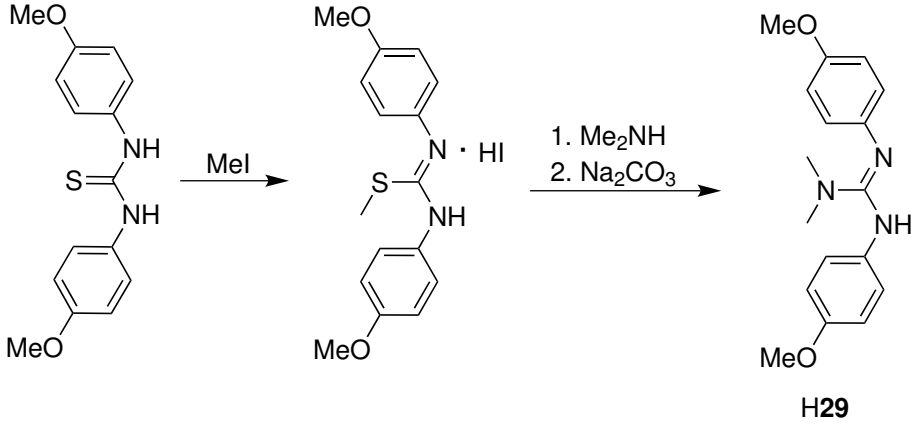

Figure 4.19: *Synthesis of the 4-methoxy substituted guanidine ligand H**29** precursor.*

4.2.7.3 Synthesis of the amidinato and guanidinato complexes with Ru(bpy)$_2$

A strong base for the deprotonation of the aminidine and guanidine ligands had to be used to obtain good yields for the Ru(bpy)$_2$ amidinato and guanidinato complexes. Potassium hydroxide instead of triethylamine was used and the solvent was changed from acetone to ethanol. Otherwise, the reaction procedure was the same as for the Ru(bpy)$_2$ triazenido complexes. After purification using column chromatography the complexes [Ru(bpy)$_2$(**28**)]PF$_6$ ((**30**)PF$_6$) and [Ru(bpy)$_2$(**29**)]PF$_6$ ((**31**)PF$_6$) were obtained as pure reddish brown solids.

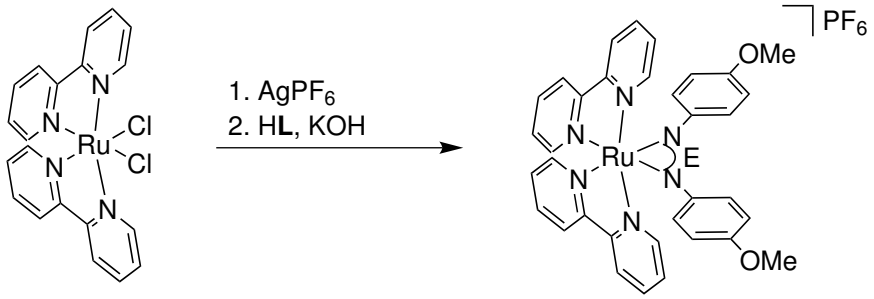

30PF_6: E = C-CH_3
31PF_6: E = C-N$(CH_3)_2$

Figure 4.20: *Synthesis of the complexes (**30**)PF_6 and (**31**)PF_6.*

4.2.7.4 Synthesis of the amidinato and guanidinato complexes with Ru(p-cym)

During the first attempts of synthesis it was observed that the p-cymene containing ruthenium amidinato and guanidinato complexes are not as stable as their triazenido analogs, meaning that the complexes could not be purified with column chromatography. Therefore, different reaction conditions, leading to less side products and to a better purification of the product had to be worked out. For that purpose a mixture of $[Ru(p\text{-}cym)Cl_2]_2$ and the aminidine/guanidine was stirred with an excess of potassium carbonate in acetone at ambient temperature for 3 h. After the precipitate was filtered through celite the solvent of the filtrate was removed and the remaining solid was recrystallized from CH_2Cl_2/n-hexane to obtain the complexes Ru(p-cym)Cl(**28**) **32** and Ru(p-cym)Cl(**29**) **33** as pure orange solids.

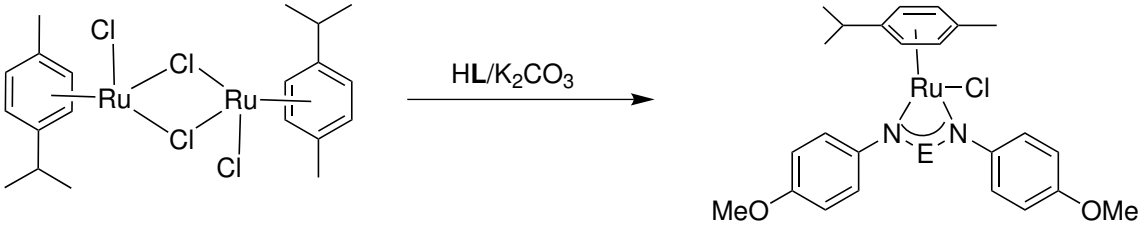

32: E = C-CH_3
33: E = C-N$(CH_3)_2$

Figure 4.21: *Synthesis of the complexes **32** and **33**.*

As described above, in order to obtain a triazenyl radical after oxidation the chlorido ligand of complex **27**SbF_6 had to be substituted with an acetonitrile ligand. Unfortunately, the corresponding complexes [Ru(p-cym)MeCN(**28**)]SbF_6 and [Ru(p-cym)MeCN(**29**)]SbF_6 could not be isolated due to their lack of stability and poor crystallization behavior. Therefore a different monodentate π-acceptor ligand had to be found, to provide a higher stability and a better crystallization behavior. For synthetic reasons the chlorido ligand was substituted with a pyridine (py) ligand, since the chloride anion can easily be abstracted with $TlPF_6$ in a solution

of **32** or **33** in pyridine. $TlPF_6$ was used instead of $AgSbF_6$ because AgCl is highly soluble in pyridine. In contrast to the complexes **32** or **33** the complexes [Ru(p-cym)(py)(**28**)]PF_6 (**34**PF_6) and [Ru(p-cym)(py)(**28**)]PF_6 (**35**PF_6) are stable enough to be purified by column chromatography.

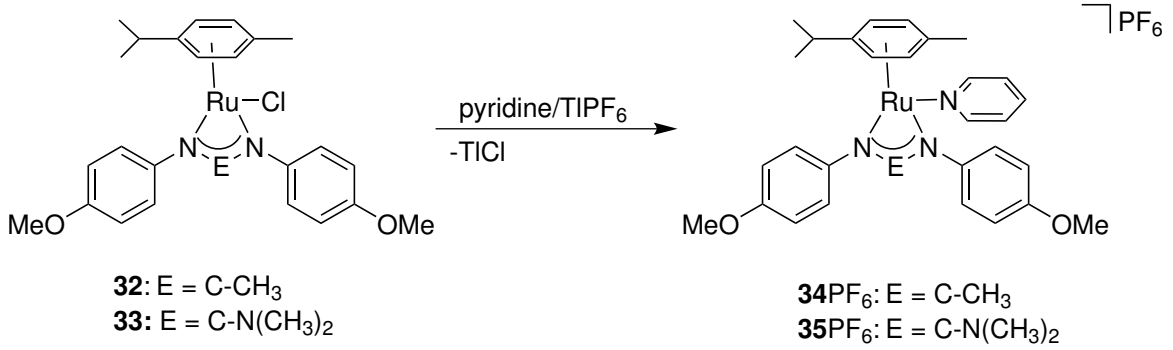

32: E = C-CH_3
33: E = C-$N(CH_3)_2$

34PF_6: E = C-CH_3
35PF_6: E = C-$N(CH_3)_2$

Figure 4.22: *Synthesis of the complexes **34**PF_6 and **35**PF_6.*

4.2.8 Molecular structures of the amidinato- and guanidinato- ruthenium complexes

Complexes **30**OTf, **31**PF_6, 32, 33 and **34**BPh_4 could be crystallized for X-ray structure analysis (Figure 4.23–4.27). Crystallization procedures were as follows. Complex **30**OTf: slow diffusion of Et_2O into a solution of **30**PF_6 and NBu_4OTf in MeCN; **31**PF_6: slow diffusion of Et_2O into a solution of **31**PF_6 in MeCN; **32**: slow evaporation of a solution of **32** in CH_2Cl_2/n-hexane; **33**: slow evaporation of a solution of **33** in CH_2Cl_2/n-hexane; **34**BPh_4: slow diffusion of n-hexane into a solution of **34**PF_6 and NBu_4BPh_4 in CH_2Cl_2. The data of the important bond lengths and angles are summarized and compared with those of the uncoordinated amidine H**37** and guanidine H_5C_6-N1-C1(CR_2)-N2(H)-C_6H_5[99] (**Gu-1**) in Table 4.18.

In all complexes the N1-C1 and N2-C1 bond lengths of around 1.33 Å for the amidinato and 1.34 Å for the guanidinato complexes lie between the N-C single and N=C double bond lengths for the uncoordinated amidine and guanidine, respectively, indicating a delocalization of the negative charge over the N1-C1-N2 chelate rings in the complexes. The deviation of the N1-C1-N2 angles in the complexes of around 108° from the free amidine or guanidine angle of around 123° can be explained by the distortion due to chelate coordination to the metal center. A correlation between the basicity of the ligands (amidinato < guanidinato) and the N1-Ru/N2-Ru bond lengths is not observed. In comparison with the triazenido ruthenium complexes the angles of the N-E-N (E = N, CR, CNR_2) fragments in the ligands of the amidinate- and guanidinate-ruthenium complexes as well as of the free ligands are larger with $\Delta\sphericalangle \approx 10°$ for the free ligands and $\Delta\sphericalangle \approx 5°$ for the complexes, respectively. This observation is in agreement with the valence shell electron pair repulsion (VSEPR) rules,[100] which attribute

Table 4.18: *Bond lengths (Å) and angles (°) in the Ru-N1-C1-N2 chelate ring in comparison with the free ligand.*

bond (Å)	**30**OTf	**31**PF_6	**32**	**33**	**34**PF_6	H**37**	**Gu-1**
Ru1-N1	2.102(3)	2.122(2)	2.088(4)	2.073(2)	2.122(2)		
Ru1-N2	2.107(3)	2.089(2)	2.092(4)	2.131(2)	2.089(2)		
N1-C1	1.323(6)	1.344(2)	1.339(6)	1.337(2)	1.324(3)	1.295(3)	1.291(9)
N2-C1	1.334(6)	1.354(1)	1.324(6)	1.342(2)	1.334(2)	1.360(3)	1.40(1)
angle (°)							
N1-N2-N3	108.3(4)	109.6(2)	106.6(4)	108.2(2)	109.6(2)	122.0(2)	124.1(6)

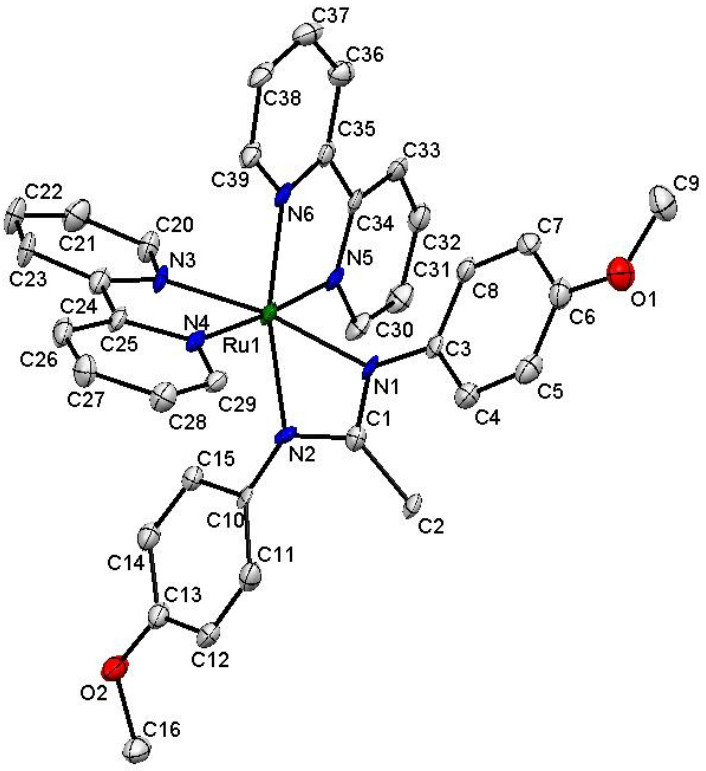

Figure 4.23: *Molecular structure of* ***30***$^+$ *in the crystal of* ***30***OTf.

a higher steric demand to the lone pair at the N2 atom of the triazenido ligand than to the C1-C2 bond in the amidinato or the C1-N3 bond in the guanidinato ligand.

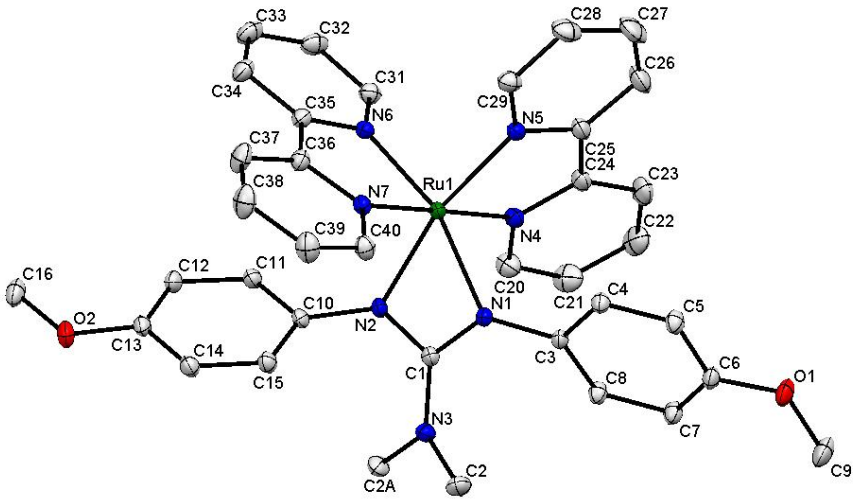

Figure 4.24: *Molecular structure of* ***31***$^{+}$ *in the crystal of* ***31***PF_6.

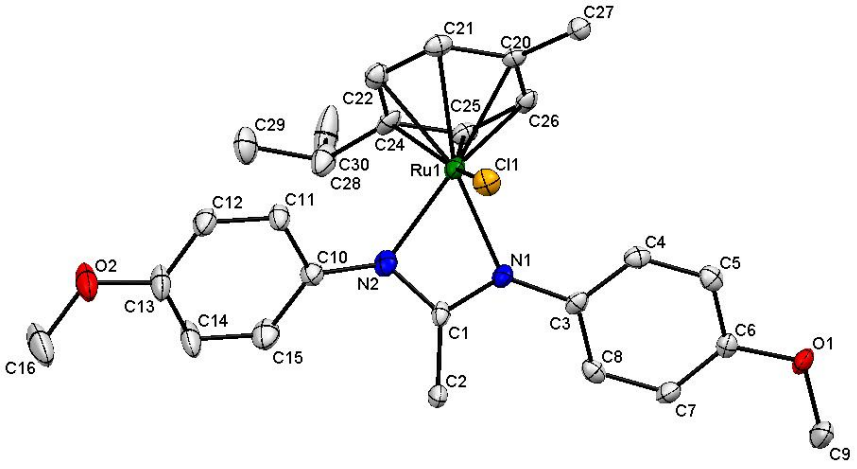

Figure 4.25: *Molecular structure of* ***32*** *in the crystal.*

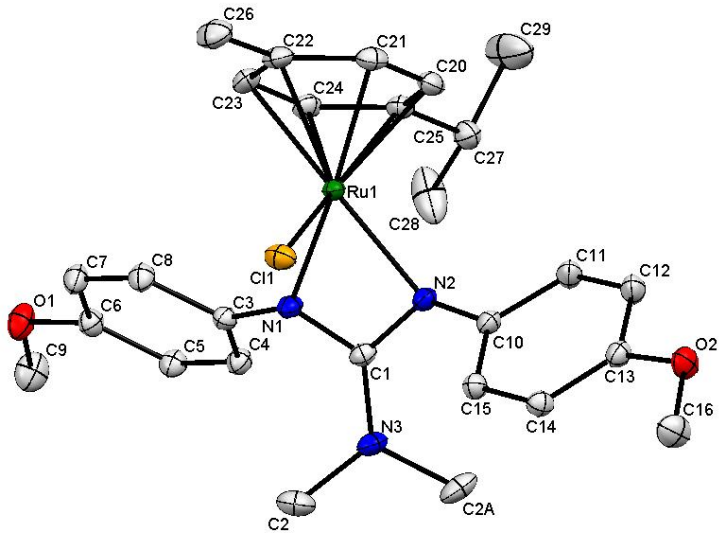

Figure 4.26: *Molecular structure of* ***33*** *in the crystal.*

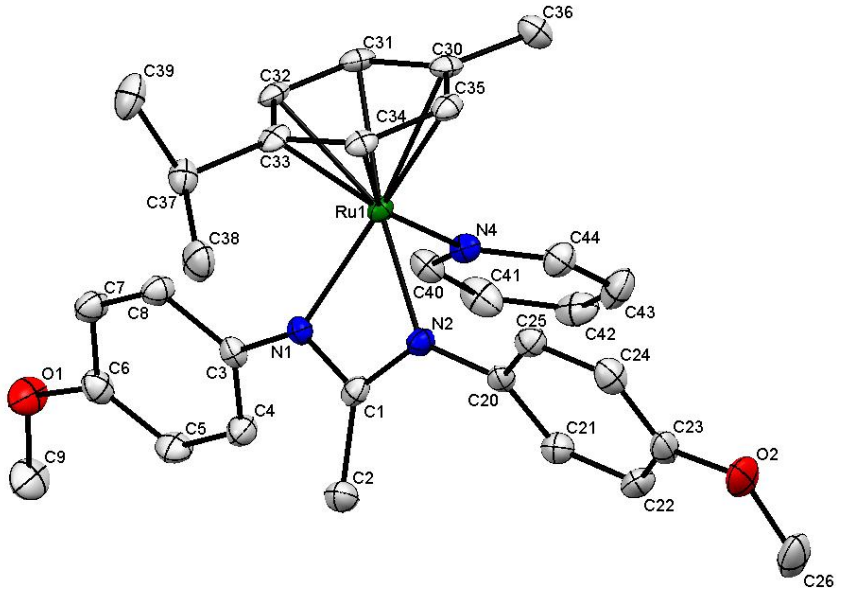

Figure 4.27: *Molecular structure of* $\boldsymbol{34}^{+}$ *in the crystal of* $\boldsymbol{34}PF_6$.

4.2.9 Cyclic voltammetry of the amidinato and guanidinato ruthenium complexes

All ruthenium amidinato and guanidinato complexes were investigated by cyclic voltammetry in 0.1 M CH_2Cl_2/NBu_4PF_6 at a scan rate of 100 mv/s. Exemplary plots of the cyclovoltammograms are illustrated in Figure 4.28. The redox potentials are summarized in Table 4.19.

The $Ru(bpy)_2$ amidinato and guanidinato complexes **30**PF_6 and **31**PF_6 exhibit two reversible oxidations each. It is striking that the oxidation potential for the amidinato complex is higher than the potential of the guanidinato complex (Δ E = 0.12 V), whereas for the Ru(p-cym)(py) complexes **34**PF_6 and **35**PF_6 an inverse behavior is observed (Δ E = 0.15 V). Since the first oxidation of **30**PF_6 and **31**PF_6 is expected to occur at the ruthenium, the potential shift indicates a better stabilization of Ru^{III} for the guanidinato complex. This observation is in agreement with the higher basicity of the guanidinato (**29**) versus the aminidinato (**28**) ligand. As the oxidation of **34**PF_6 and **35**PF_6 is expected to occur at the ligand, the inverse potential shift indicates that the guanidinato ligand is more difficult to oxidize than the corresponding amidinato ligand. The lower oxidation potential of $E_{1/2}$ = 0.13 V for **32** as compared to $E_{1/2}$ = 0.20 V for **33** also suggests a predominantly ligand centered oxidation for both compounds. As result of a substitution experiment a ligand participation was attributed to the second oxidation process of the triazenido complex **21**PF_6. Consequently, this character is also assigned to the second oxidation of the complexes **30**PF_6 and **31**PF_6.

A comparison with the oxidation potentials of the corresponding triazenido ruthenium complexes leads to the conclusion that the triazenido ligand stabilizes the Ru^{III} oxidation state as well as the amidinato ligand, since both $Ru(bpy)_2$ complexes **21**PF_6 and **30**PF_6 exhibit the same potential of $E_{1/2}$ = -0.10 V. Regarding the ligand-centered oxidation, the potential of the ruthenium triazenido complex **27**SbF_6 lies between the potentials of the amidinato (**34**PF_6) and the guanidinato ruthenium complex (**35**PF_6), suggesting a trend of the oxidation potentials of the ligands according to: amidinato $<$ triazenido $<$ guanidinato. The different ancillary ligands pyridine and acetonitrile, however, may bias this conclusion, because the stronger π-accepting acetonitrile ligand might lead to an increase of the oxidation potential of the triazenido complex **27**SbF_6. Therefore, the position of the triazenido and the amidinato ligand might rather be reversed in this series. To resolve this dispute, EPR spectroelectrochemistry was applied to the amidinato and guanidinato ruthenium complexes.

Table 4.19: *Redox otentials[a,b] of triazenido, amidinato and guanidinato ruthenium complexes in comparison.*

complex	E^0_{298} / V		complex	E^0_{298} / V
30PF_6	0.72	-0.10	**21**PF_6	-0.10
31PF_6	0.64	-0.22		
32	0.82[c]	0.13	**25**	0.24
33	0.87[c]	0.20		
34PF_6	1.00[c]	0.35	**25**SbF_6	0.39
35PF_6	1.19[c]	0.50		

[b] *Potentials vs* $Fc^{0/+}$. [b] *In* CH_2Cl_2*/0.1 M* Bu_4NPF_6*/scan rate 100 mV* $s^{-}1$. [c] *Anodic peak potential of irreversible process.*

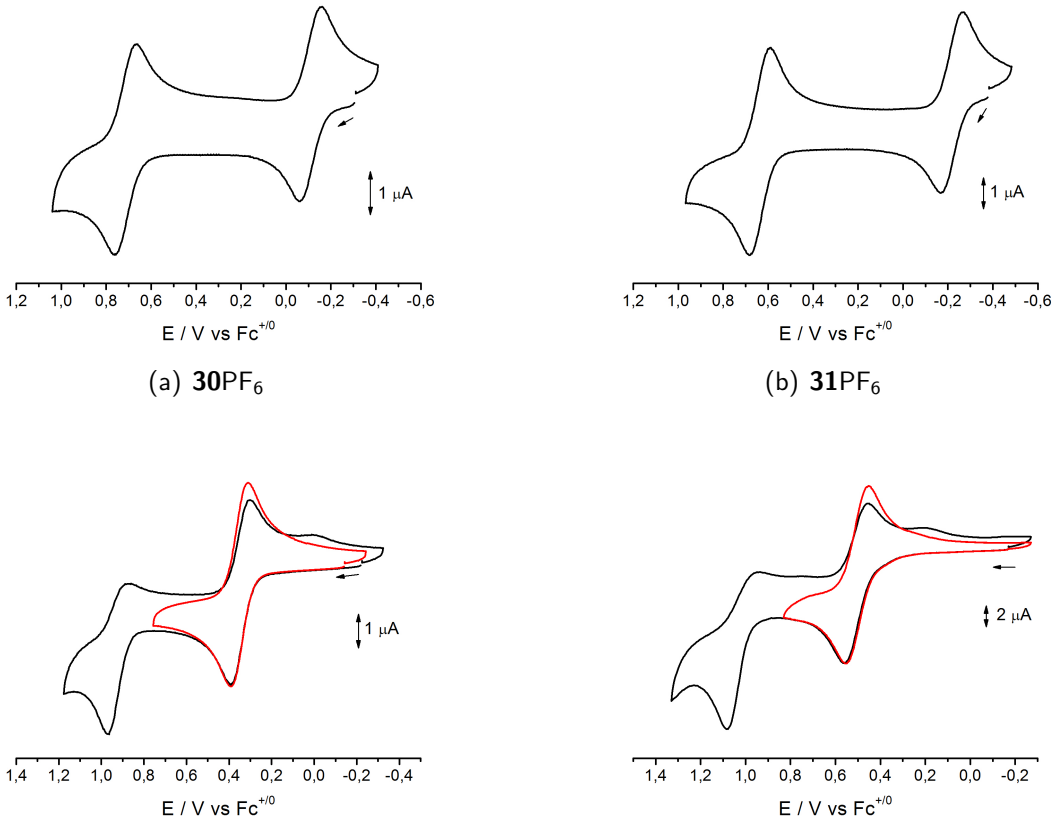

(a) **30**PF_6 (b) **31**PF_6

(c) **34**PF_6 (d) **35**PF_6

Figure 4.28: *Cyclic voltammetry of amidinato and guanidinato complexes in* CH_2Cl_2*/0.1 M* Bu_4NPF_6 *(scan rate 100 mV s).*

4.2.10 EPR spectroelectrochemistry of the amidinato and guanidinato ruthenium complexes

Cyclic voltammetry experiments resulted in a reversible oxidation for each of the amidinato and guanidinato complexes. To get an insight in the nature of the oxidation process (ruthenium vs amidinato/guanidinato), the oxidized forms of complexes **30**PF_6–**35**PF_6 were investigated by EPR spectroscopy. Exemplary plots of the EPR spectra of $\mathbf{30}^{2+}$–$\mathbf{35}^{2+}$ are depicted in Figure 4.29–4.30. The EPR data as well as the potentials of the first oxidation of all complexes are summarized in Table 4.20, indicating that the oxidation potentials and the g values are not in direct correlation.

The EPR spectra at 110 K of the $Ru(bpy)_2$ complexes show rhombic signals with a g anisotropy of $\Delta g = 0.312$ for $\mathbf{30}^{2+}$ and $\Delta g = 0.580$ for $\mathbf{31}^{2+}$, respectively, indicating a predominantly ruthenium centered spin situation $Ru^{III}(L^{-})$. For the p-cymene/chloride containing singly oxidized complexes with isotropic g values of $g = 2.028$ at 298 K and a g anisotropy of around $\Delta g = 0.04$ a mixed orbital radical situation $Ru^{III}(L^{-}) \leftrightarrow Ru^{II}(L^{\bullet})$ is observed. Whereas the isotropic spectra at 298 K do not exhibit a hyperfine structure, the low temperature spectra of $\mathbf{32}^{+}$ shows a coupling to the coordinating N atoms (quintet, 2 x $A(^{14}N) = 0.88$ mT) in the direction of g_1, indicating a considerable spin density at the amidinato ligand. Through the substitution of the chlorido with the neutral π-accepting pyridine ligand a poorly resolved but evident hyperfine structure emerges in the room temperature spectrum of $\mathbf{34}^{2+}$ (quintet, 2 x $A(^{14}N) = 0.53$ mT, 1 x $A(^{99,101}Ru) = 0.69$ mT, $\Delta B_{1/2} = 0.80$ mT) and $\mathbf{35}^{2+}$ (quintet, 2 x $A(^{14}N) = 0.59$ mT, 1 x $A(^{99,101}Ru) = 0.61$ mT, $\Delta B_{1/2} = 0.75$ mT). The occurrence of a hyperfine structure in conjunction with the relative low isotropic g values of $g = 2.015$ confirms the expected ligand centered radical situation $Ru^{II}(L^{\bullet})$. Additionally, the presence of a ligand centered radical is confirmed by the DFT calculated (ADF/PBE0) spin density (Figure 4.30c) for $\mathbf{34}^{2+}$ of 1.3 % at ruthenium and 16.4 % at each of the coordinating N atoms.The complexes $\mathbf{34}^{2+}$ and $\mathbf{34}^{2+}$ are the first examples of metal stabilized amidinyl and guanidinyl radicals, respectively.

In comparison to the triazenyl radical complex $\mathbf{27}^{2+}$, the EPR spectra of the amidinyl and guanidinyl radical complexes $\mathbf{34}^{2+}$ and $\mathbf{35}^{2+}$ exhibit a less resolved hyperfine splitting due to a larger linewidth and higher ruthenium coupling constant, indicating a somewhat higher spin density at the ruthenium center. Additionally, the g anisotropy of $\Delta g = 0.100$ for the $Ru(bpy)_2$ triazenido complex $\mathbf{21}^{2+}$ indicates a mixed-orbital situation, whereas the corresponding amidinato and guanidinato complexes $\mathbf{30}^{2+}$ and $\mathbf{31}^{2+}$ clearly exhibit ruthenium-centered spin. The EPR results thus attribute a lower oxidation potential to the triazenido ligand than to the corresponding amidinato and guanidinato ligands when coordinated to ruthenium and therefore alter the series for the oxidation potential, based on cyclic voltammetry results, to: triazenido $<$ amidinato $\approx$ guanidinato.

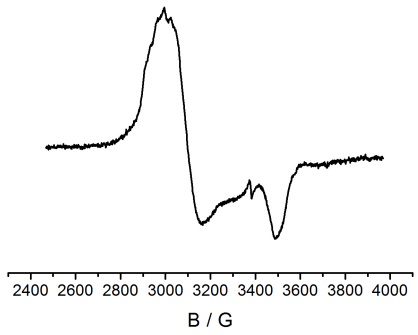

(a) $\mathbf{30}^{2+}$ at 110 K

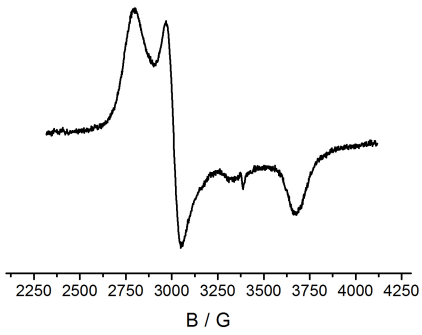

(b) $\mathbf{31}^{2+}$ at 110 K

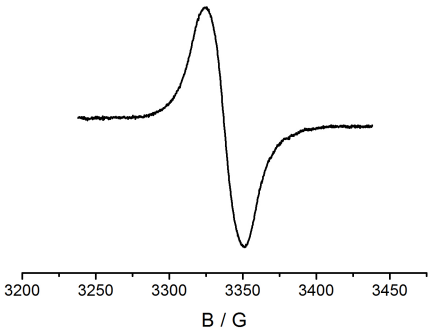

(c) $\mathbf{32}^{+}$ at 298 K

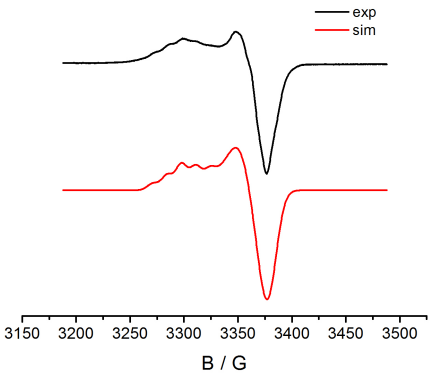

(d) $\mathbf{32}^{+}$ at 110 K

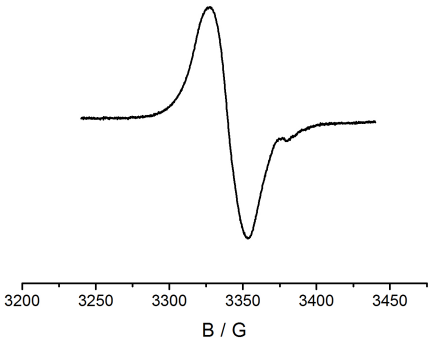

(e) $\mathbf{33}^{+}$ at 298 K

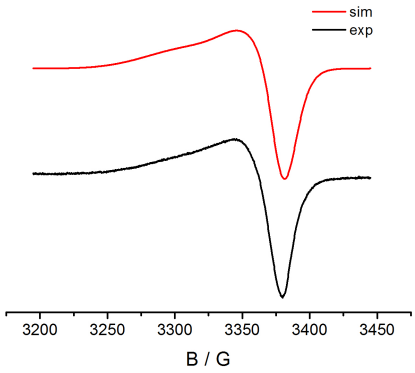

(f) $\mathbf{33}^{+}$ at 110 K

Figure 4.29: *EPR spectra of the amidinato ruthenium and guanidinato ruthenium complexes in CH_2Cl_2/0.1 M Bu_4NPF_6.*

Table 4.20: *EPR data for* ***30***$^{2+}$*–*$\mathbf{35}^{2+}$ *from electrochemical generation in* CH_2Cl_2*/0.1 M* Bu_4NPF_6.

complex	$E_{1/2}$	g_{iso} (298 K)	g_1, g_2, g_3 (110 K)	g_1-g_3
$\mathbf{30}^{2+}$	-0.10	2.136	2.250, 2.180, 1.938	0.312
$\mathbf{31}^{2+}$	-0.22	2.136	2.424, 2.250, 1.844	0.580
$\mathbf{32}^{+}$	0.13	2.028	2.032, 2.007, 2.000[c]	0.032
$\mathbf{33}^{+}$	0.20	2.028	2.051, 2.012, 2.004	0.047
$\mathbf{34}^{2+}$	0.35	2.015[c]	2.033, 2.010, 2.007	0.026
$\mathbf{35}^{2+}$	0.50	2.015[d]	2.026, 2.009, 2.008	0.018

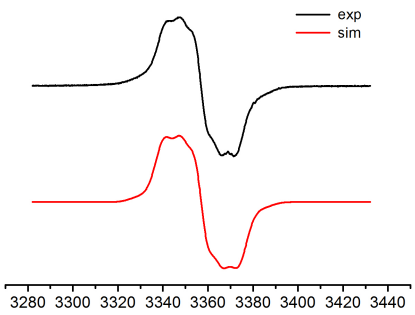

(a) EPR of $\mathbf{34}^{2+}$ at 298 K

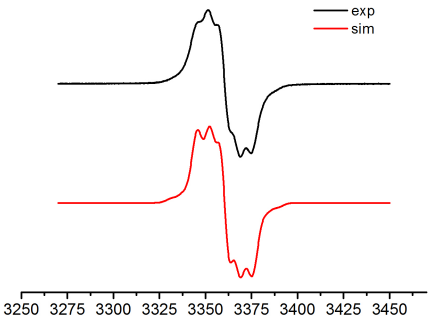

(b) EPR of $\mathbf{35}^{2+}$ at 298 K

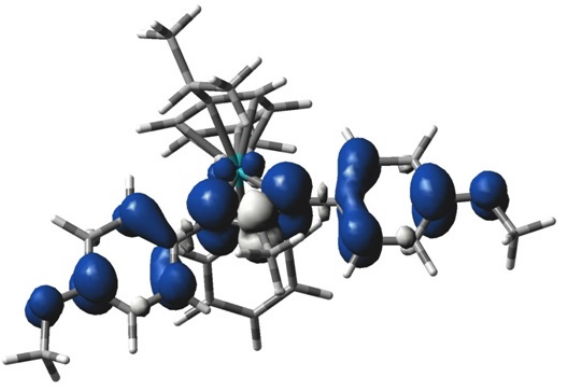

(c) Spin density of $\mathbf{34}^{2+}$

Figure 4.30: *a) and b): EPR spectra of* $\mathbf{34}^{2+}$ *and* $\mathbf{35}^{2+}$ *in* CH_2Cl_2*/0.1 M* Bu_4NPF_6 *at 298 K. c) DFT (ADF/PBE0) calculated spin density of* $\mathbf{34}^{2+}$.

4.2.11 UV-vis-NIR spectroelectrochemistry of amidinato and guanidinato ruthenium complexes

UV−vis−NIR spectroelectrochemical measurements of complex **30**PF_6–**35**PF_6 using an OTTLE cell are illustrated in Figures 4.31–4.33 and summarized in Table 4.21. The spectra of complex $\mathbf{30}^{n+}$–$\mathbf{33}^{n+}$ and $\mathbf{35}^{n+}$ are only briefly discussed based on EPR results and literature, since no TD-DFT calculations for an exact band assignment are available. The

transitions of complex $\mathbf{34}^{n+}$, however, were calculated by TD-DFT (CAM-B3LYP/PCM/6-311G(d)) methods. All calculations were performed by Dr. Stanislav Záliš. The TD-DFT assignment for the transitions of $\mathbf{34}^{n}$ (n = 0, +1) listed in Table A.2 in the appendix.

Although amidinato and guanidinato complexes containing the $Ru(bpy)_2$ are not represented in the literature, the absorption band of the bpy substituted complexes in the visible region at 550 nm are assigned to MLCT transitions. The bathochromic shift of $\Delta\lambda = 83$ nm compared to the corresponding triazenido complex ($\mathbf{21}^{+}$) can be explained through an increase in energy of the Ru(d) orbitals due to the stronger electron donating amidinato and guanidinato ligands. A similar effect is observed for complex $\mathbf{22}^{+}$ containing a *tert*-butyl substituted triazenido ligand (see Section 4.2.6). After the Ru^{II}/Ru^{III} oxidation both complexes exhibit an absorption band in the near infrared at 1060 nm for $\mathbf{30}^{2+}$ and at 950 nm for $\mathbf{31}^{2+}$, which are attributed to an LMCT ($L^{-} \rightarrow Ru^{III}$) character. Oxidation to the dication, associated with a $Ru^{III}(L^{\bullet})$ rather than a $Ru^{IV}(L^{-})$ configuration results in an additional near infrared band of higher intensity at 890 nm (ϵ = 12800 M^{-1} cm^{-1}) for $\mathbf{30}^{3+}$. The most intense band in the visible and near infrared region of complex $\mathbf{31}^{3+}$ appears at 645 nm (ϵ = 12800 $M^{-1}cm^{-1}$). Due to the absence of TD-DFT calculations and the complex electronic structure of $\mathbf{30}^{3+}$ and $\mathbf{31}^{3+}$ no reasonable band assignment can be made, explaining the disparity in the spectra.

All four p-cymene containing complexes display intense absorption bands around 300 nm accompanied by a shoulder at around 420 nm. Because the band at 300 nm is also present in the spectra of the bpy containing complexes, an ILCT character ($\pi \rightarrow \pi^*$) is assigned to this band. The shoulder at 420 nm probably represents a MLCT transition ($Ru^{II} \rightarrow \pi^*$-p-cymene/$\pi^*$-L). Upon oxidation of the chlorido containing amidinato complex **32** two bands in the near infrared region at 776 nm and 1010 nm emerge. The corresponding guanidinato complex displays a similar absorption pattern, however, the low energy band at 1500 nm (ϵ = 12 800 $M^{-1}cm^{-1}$) is less intense and extends across the accessible near infrared region. As EPR spectroscopy reveals a relatively high ligand contribution to the SOMO of $\mathbf{32}^{+}$ and $\mathbf{33}^{+}$, the long-wavelength bands are attributed a predominantly ILCT character.

A chlorido/pyridine ligand exchange results in the occurrence of a remarkably intense and narrow near infrared absorption band at 1010 nm (ϵ = 25 500 M^{-1} cm^{-1}; $\Delta_{1/2}$ = 1170 $cm^{-}1$) for complex $\mathbf{34}^{2+}$. TD-DFT calculations attribute this transition to a βHOMO–βLUMO ILCT excitation with slight LMCT admixture. The theoretical result also confirms the interpretation of the corresponding triazenido complex $\mathbf{27}^{2+}$. The frontier orbitals, mainly contributing to the low energy transition are depicted in Figure 4.32, and the data for all calculated transitions of complex $\mathbf{34}^{n+}$ (n = 1, 2) are summarized in Table A.1. Compared to the triazenyl and amidiyl radical complexes $\mathbf{27}^{2+}$ and $\mathbf{34}^{2+}$ the guanidinyl radical complex $\mathbf{35}^{2+}$ displays a significantly different spectrum in which the long-wavelength absorption is shifted to lower energy of 1570 nm. Additionally, a strong decrease in intensity (ϵ = 1 300 M^{-1} cm^{-1}) along with a significant line broadening is observed. The bathochromic shift may be explained by an extended spin

Table 4.21: *UV–vis–NIR data for amidinato ruthenium and guanidinato ruthenium complexes in various oxidation states from OTTLE spectroelectrochemistry in CH_2Cl_2/0.1 M Bu_4NPF_6.*

complex	λ_{max} [nm] (ϵ (M^{-1} cm^{-1}))
30^{+}	247(34 500), 295(57 200), 364(22 800), 490(6 500), 550(8 400), 710(5 000)sh
30^{2+}	247(34 500), 295(57 200), 400(11 900), 710(6 800), 1060(4 200)
30^{3+}	247(34 500), 282(42 700), 360(11 000), 430(7 400), 720(10 200), 890(12 800)
31^{+}	247(40 9000), 293(54 700), 351(18 000), 404(11 000), 505(7 600), 550(10 900), 700(1 600)sh, 950(4 500)
31^{2+}	247(44 300), 289(50 200), 390(10 600), 720(4 000), 950(4 400)
30^{3+}	247(44 300), 289(45 800), 377(8 100), 645(15 200), 950(5 000), 1170(2 100)
32	243(7 000), 318(7 400), 420(500)
32^{+}	285(12 200), 388 (23 400), 776(16 600), 1010(9 600)
33	238(33 200), 298(41 000), 427(3 300)
33^{+}	226(32 800), 289(29 300), 530(3 700), 835(4 700), 1400(1 500)sh
34^{+}	238(18 400), 297(21 800), 424(1 800)
34^{2+}	260(14 900), 400(21 300), 422(21 300), 730 (7 500), 1010(25 500)
35^{+}	235(15 900), 290(21 400), 404(1 900)
35^{2+}	235(14 900), 265(14 700), 350(850), 472(2 500), 800(3 600), 1570(1 300)

delocalization of the guanidinyl radical ligand radical over the CN_3 fragment, resulting in a decrease of the HOMO–LUMO gap. A low energy barrier of the rotation around the C1-N3 axis could cause the extreme line-broadening effect.

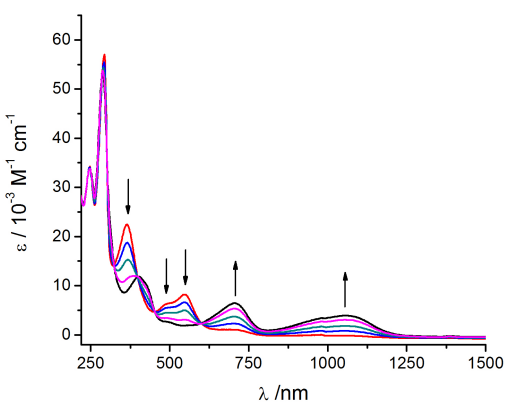

(a) $\mathbf{30}^{+} \rightarrow \mathbf{30}^{2+}$

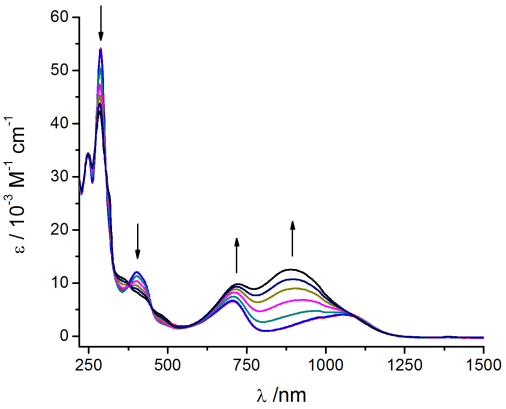

(b) $\mathbf{30}^{2+} \rightarrow \mathbf{30}^{3+}$

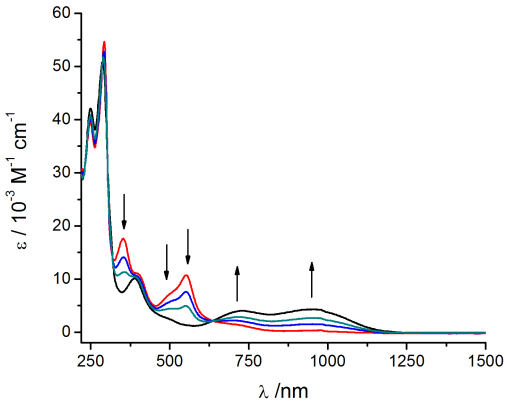

(c) $\mathbf{31}^{+} \rightarrow \mathbf{31}^{2+}$

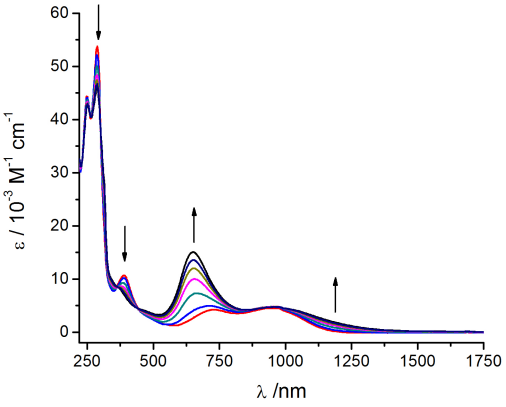

(d) $\mathbf{31}^{2+} \rightarrow \mathbf{31}^{3+}$

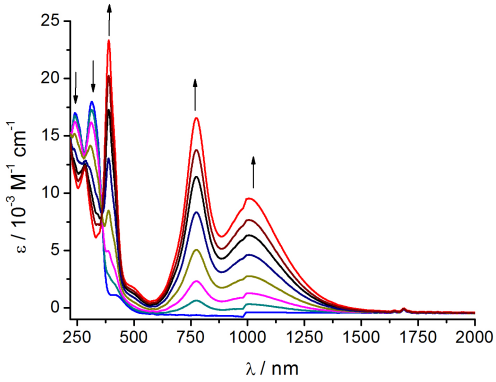

(e) $\mathbf{32} \rightarrow \mathbf{32}^{+}$

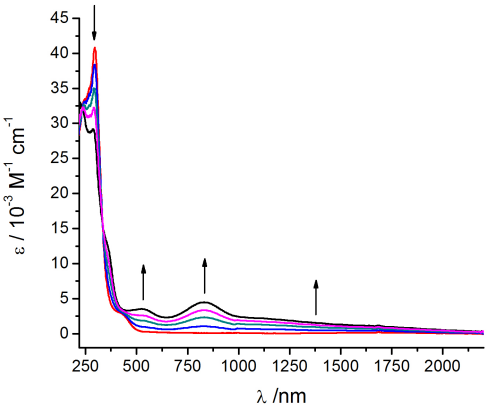

(f) $\mathbf{33} \rightarrow \mathbf{33}^{+}$

Figure 4.31: *UV–vis–NIR spectroelectrochemical response on oxidation of the amidinato ruthenium and guanidinato ruthenium complexes in CH_2Cl_2/0.1 M Bu_4NPF_6.*

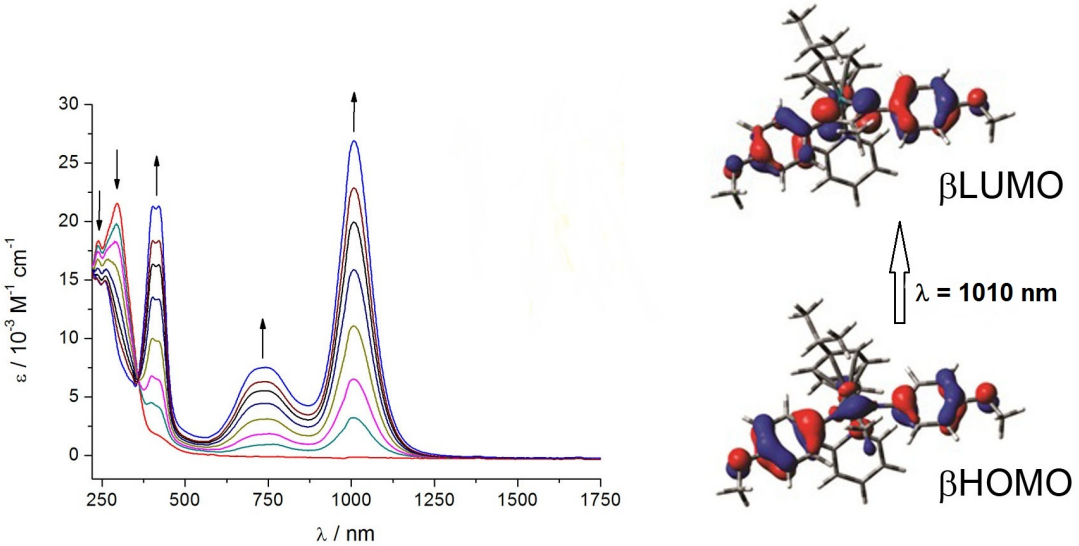

Figure 4.32: *UV–vis–NIR spectroelectrochemical response on oxidation of* ***34***$^{+}$ *in* CH_2Cl_2*/0.1 M* Bu_4NPF_6*, and frontier orbitals involved in the near infrared transition at 1010 nm.*

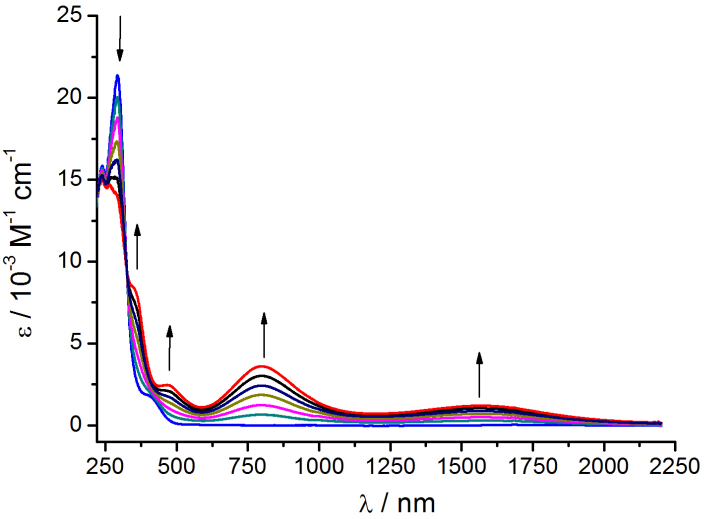

Figure 4.33: *UV–vis–NIR spectroelectrochemical response on oxidation of of* ***35***$^{+}$ *in* CH_2Cl_2*/0.1 M* Bu_4NPF_6*.*

4.3 Conclusion

The research goal of this Chapter was to reveal the potential non-innocent character of the class of heteroallylic ligands, hitherto thought to behave innocently. For reasons of simple synthetic modification and variation of the electronic structure, the triazenido ligand system was utilized as a model to work out the conditions under which this type of ligand system is prone to behave non-innocently. Accordingly, by systematic variation of the electronic structure of the ligand system itself as well as of the ancillary ligands a continuum was established for the oxidation of the triazenido ruthenium complexes, ranging from a) a ruthenium-centered spin situation $L_nRu^{III}(RNNNR^-)$ species via b) orbital-mixed systems $L_nRu^{III}(RNNNR^-) \leftrightarrow L_nRu^{II}(RNNNR^\bullet)$ to c) triazenyl radical complexes $L_nRu^{II}(RNNNR^\bullet)$.[101] The desired preference for the ligand-centered as opposed to the ruthenium-centered oxidation was eventually achieved by substitution of the triazenido ligand ($RNNNR^-$) with electron donating methoxy groups and using the π-accepting and non σ-donating p-cymene as ancillary ligand (L_n). This successful approach was then extended to amidinato and guanidinato ruthenium complexes, which could also be detected in the different valence isomeric forms a)–c) after oxidation by EPR spectroelectrochemical and DFT methods. Remarkably, no electronic tuning of the heteroallylic ligand was needed in case of the amidinato and guanidinato complexes. To analyse the tendency of the different ligand systems in their chelating coordination modes to be oxidized, EPR spectroelectrochemistry was found to provide the most precise information, since cyclic voltammetry experiments cannot discriminate between ligand- and metal-centered processes. Based on EPR data, which revealed a slightly more ligand-centered spin density in the triazenyl radical complex than in the amidinyl and guanidinyl radical complexes, a series for the magnitude of the oxidation potentials of the ruthenium coordinating ligands was established: triazenido $<$ amidinato $\approx$ guanidinato.

In addition to their novelty, the triazenyl and amidinyl radical complexes were found to exhibit a strong absorption in the near infrared region of the electromagnetic spectrum, which is attributed to a predominantly ILCT transition of the radical ligand. This remarkable feature makes such types of complexes attractive for applications in various NIR absorbing devices. For that purpose, these promising systems are further investigated in the following Chapter.

5 Amidinyl radical complexes: A new class of near infrared chromophores

5.1 Introduction

Among different other results was shown in Chapter 4 that triazenyl- and amidinyl ruthenium radical complexes exhibit electronic absorptions in the near infrared (NIR, 800 – 2500 nm, 12500 – 4000 cm^{-1}) region. These bands lie between 800 – 1000 nm and are of high intensitiy and narrow linewidth. Based on this striking observation it was thus planned to extend this promising approach to the development of new NIR chromophores of lower oxidation potentials, simplifying the isolation of the oxidized NIR active form and therefore allow a more detailed characterization as well as a possible application in NIR absorbing devices. Additionally, a shift to lower oxidation potentials of the NIR absorbing radical ligand precursor is expected to be accompanied by a low-energy shift of the electronic transition possibly extending as far as the telecommunication window (1310 nm or 1550 nm).[102]

NIR dyes have been intensively investigated due to their wide range of applications, for example in optoelectronic devices,[103] solar cells,[104] optical communication,[105] as well as chemosensors and probes.[106] Among these NIR absorbers there are purely organic molecules, the most

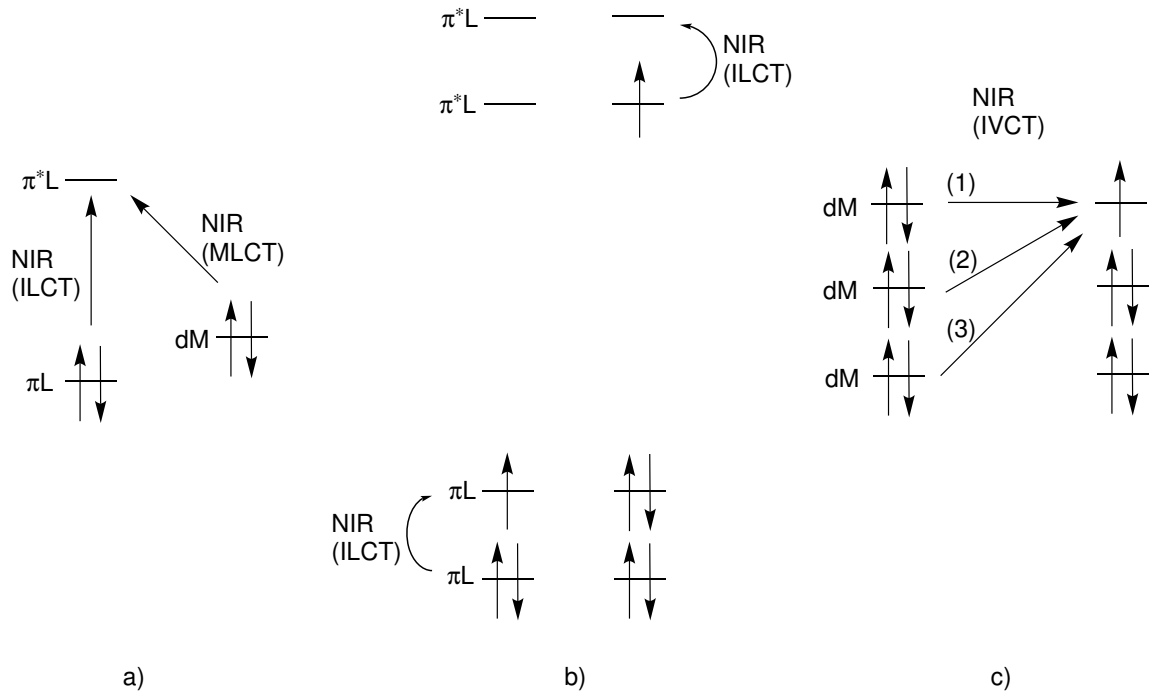

Figure 5.1: *Concepts for transition metal complexes absorbing in the NIR.*

representative being cyanines[107] and boron-dipyrromethene,[108] polymers,[109] and coordination compounds of different nuclearity.[110] For transition metal complexes absorbing in the NIR several concepts exist:[111] a) extended ligand π-systems which exhibit a low HOM–LUMO gap and therefore allow low-energetic LMCT or ILCT transitions, respectively; b) the presence of radical ion ligands with a low energy gap between SOMO and LUMO or SOMO and the highest doubly occupied orbital, respectively; c) mixed valency accompanied by IVCT transitions (Figure 5.6).

Chromophores containing π conjugated 4-dimethylaminophenyl (DMAP) groups of different charge (neutral donor, cationic acceptor) have been well employed in conventional dyestuff technology. The most prominent of the triphenylmethyl class of compounds are malachite green $[CPh(DMAP)_2]^+$ = **36a** and crystal violet $[C(DMAP)_3]^+$ = **36b** (Figure 5.2) with their large absorptivity in the visible region of the electromagnetic spectrum (λ_{max} = 621 nm (**36a**) and 590 nm (**36b**), ϵ = 105 00 M^{-1} cm^{-1} (**36a**) and 112 00 M^{-1} cm^{-1} (**36b**)).[112]

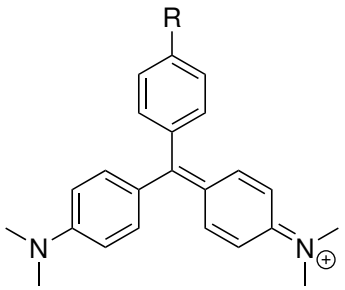

36a: R = H
36b: R = DMAP

Figure 5.2: *Molecular structure of malachite green **36a** and crystal violet **36b**.*

Inspired by this ubiquitous pigment class, it was intended to incorporate the DMAP group into the amidinyl radical system described previously to facilitate the oxidation of the amidinato ligand precursor and to decrease the energy gap between the frontier orbitals through extension of spin distribution. The effect of the ligands coordination mode as well as the influence of the coordinating metal on the NIR absorption behavior was to be investigated by synthesizing DMAP- amidinyl complexes with various metals, known to exhibit coordination environments different from from the piano stool structure of the Ru(p-cym)XL_2 system described in Chapter 4.

5.2 Results and discussion

5.2.1 Synthesis

The dimethylaminophenyl (DMAP) substituted amidine ligand H**37** was synthesized according to the previously described procedure for the methoxy substituted amidine ligand H**28** through the reaction of N,N-dimethyl-p-phenylenediamine with ethyl orthoacetate. To simplify the purification process of the desired product H**37**, the starting material N,N-dimethyl-p-phenylenediamine was sublimed under inert atmosphere before use. The raw product was purified using column chromatography and recrystallized from CH_2Cl_2/n-hexane to obtain white crystals.

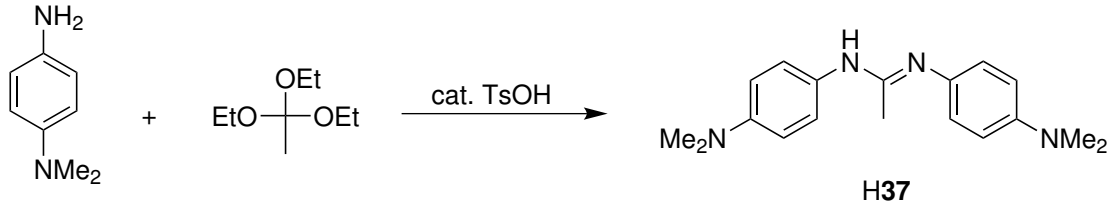

Figure 5.3: *Synthesis of the DMAP substituted amidinate H**37**.*

The complex Ru(p-cym)Cl(**37**) (**38**) was synthesized according to the procedure for the synthesis of **32** through the reaction of the precursor $[Ru(p\text{-cym})Cl_2]_2$ with H**37** under deprotonation. After the reaction was completed, the mixture was filtered through celite and the solvent was removed. To obtain a pure product the complex was recrystallized from CH_2Cl_2/n-hexane to afford red crystals.

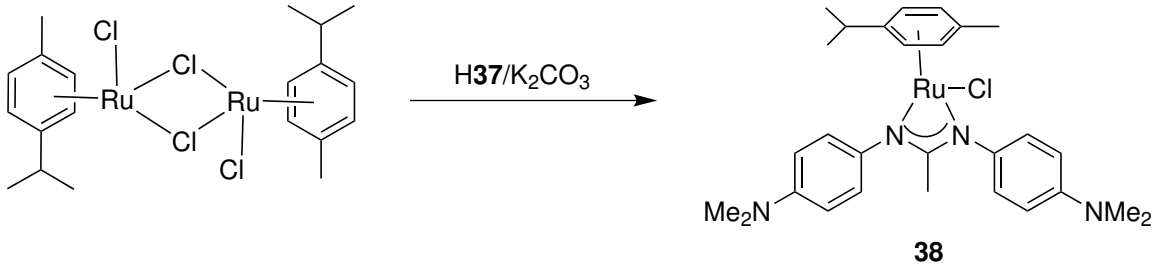

Figure 5.4: *Synthesis of the Ru(p-cym)Cl aminidinato complex (**38**).*

The oxidized form of **38** was obtained as **38**PF_6 through the reaction of **38** with ferrocenium hexafluorophosphate ($FcPF_6$) as oxidation agent for 1 h at room temperature in CH_2Cl_2. To obtain a pure product the complex was recrystallized from CH_2Cl_2/n-hexane to afford black crystals.

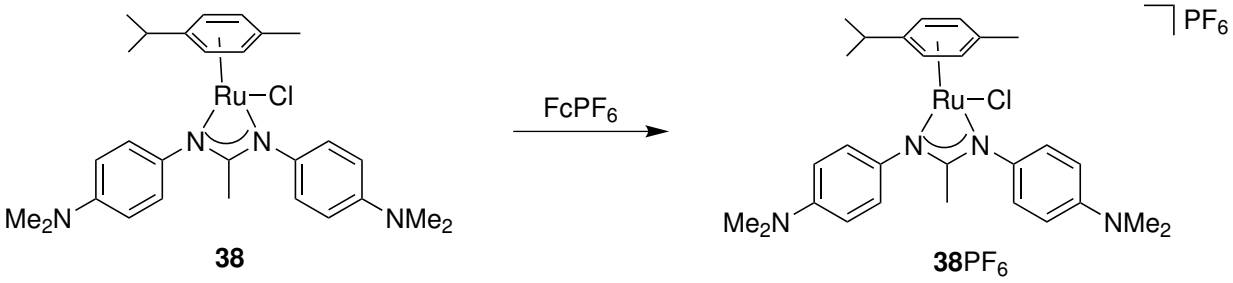

Figure 5.5: *Synthesis of the oxidized form* ***38****PF_6.*

For the synthesis of the palladium and the platinum complexes **39** and **40** the metal precursors $PdCl_2(MeCN)_2$ and $PtCl_2(dmso)_2$ were reacted under the same conditions (Cs_2CO_3, acetone, 60 °C, 15 h). Both complexes were purified using column chromatography. Despite equal reaction conditions, two different products were obtained. Whereas the palatinum complex exhibits a square planar coordination mode, the palladium complex shows a paddle wheel structure, where two palladium centers are bridged by four amidinato ligands.

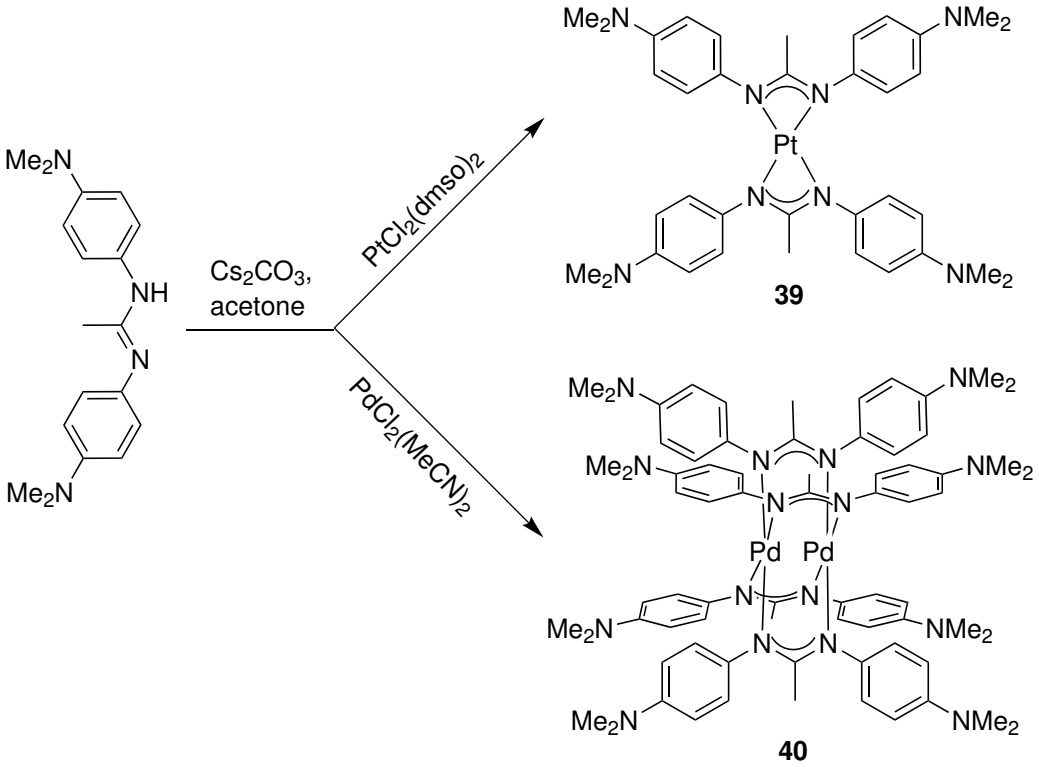

Figure 5.6: *Synthesis of the square planar platinum amidinato complex* ***39*** *and the paddle wheel structured palladium complex* ***40****.*

5.2.2 Molecular structure

The amidine ligand H**37** as well as the complexes **38**, **38**PF_6, **39** and **40** could be crystallized for X-ray structure analysis (Figures 5.8–5.12). The experimental as well as the DFT calculated (G09/PBE0/6-311G(d)) data of the important bond lengths and angles of **38** and **38**PF_6 are summarized in Table 5.22. Crystallization procedures were as follows. H**37**, **38**, **39** and **40**: slow evaporation of a solution of H**37**, **38**, **39** or **40**, respectively in CH_2Cl_2/n-hexane; **38**PF_6: slow diffusion of n-hexane into a solution of **38**PF_6 in CH_2Cl_2.

While the differences in bond lengths and angles between the uncoordinated amidine H**37** and the amidinato ligand were already discussed in Chapter 4, the focus of attention in this chapter lies in the structural differences of **38** and its oxidized form **38**PF_6. Whereas the N1-Ru1-N2 bite angle of 61.5° and the N1-C1-N2 chelate angle of 107.4° remain basically unchanged, significant variations are observed in the C-NMe_2 and C-$NC(CH_3)$N bond lengths of 1.41 Å in **38** vs 1.37 Å in **38**$^+$. These differences were confirmed by DFT calculations, illustrating a tendency towards formation of a p-quinonoid structure[113] in the oxidized form. With disregard of the octet rule[114] the spin distribution of the DMAP substituted amidinyl radical complex **38**$^+$ is thus represented by two major resonance structures (Figure 5.7), illustrating the expected high spin densities at the DMPA (A) as well as at the ruthenium coordinated nitrogen atoms (B).

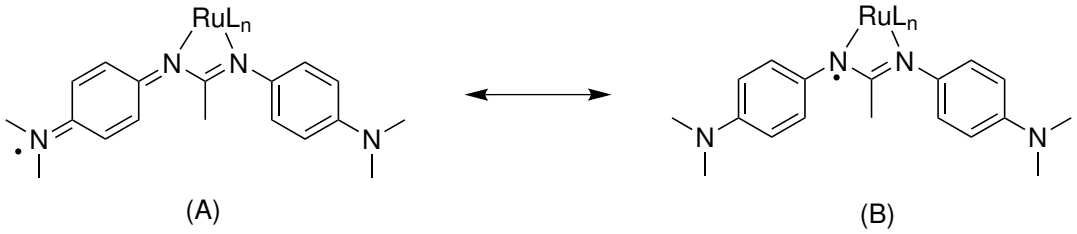

Figure 5.7: *Major resonance structures of the amidinyl radical ligand in* ***38***$^+$.

In the cases of the palladium and platinum complexes, crystal structure analysis reveals a square planar coordination mode with small bite angles of $\sphericalangle$(N1-Pt-N2) = 62.8(2)° and chelate angles of $\sphericalangle$(N1-C1-N2) = 108.2(6)° in **39** in contrast to the paddle wheel structure of **40** with much wider chelate angles of $\sphericalangle$(N1-C1-N2) = 120.7(3)°. Whereas the structural data of **39** with Pt-N bond lengths of 2.05 Å are in accordance with literature data,[115] the Pd(II)-Pd(II) bond length of 2.543 Å in **40** is significantly shorter than a proposed Pd(II)-Pd(III) bond (2.597 Å) with bond order of 1.5[116] but also longer than a Pd(III)-Pd(III) bond of 2.391 Å.[117] The structural difference between the palladium and platinum complexes nicely reflects the typical behavior of large metals binding to ligands with small bite angles.

Table 5.22: *Experimental and DFT calculated (G09/PBE0/6-311G(d)) bond lengths (Å) and angle (°) in **38** and **38**PF_6.*

	38		**38**PF_6	
bond	exp.	calc.	exp.	calc.
Ru1-N1	2.071(2)	2.092	2.084(2)	2.092
Ru1-N2	2.114(2)	2.094	2.093(2)	2.097
N1-C1	1.323(4)	1.326	1.345(3)	1.335
N1-C3	1.402(4)	1.394	1.383(3)	1.369
N2-C1	1.333(4)	1.327	1.339(3)	1.334
N2-C11	1.408(4)	1.386	1.382(3)	1.370
N3-C6	1.409(4)	1.387	1.370(4)	1.370
N4-C14	1.407(4)	1.387	1.364(3)	1.357
angle	exp.	calc.	exp.	calc.
N1-C1-N2	107.4(2)	107.8	105.8(2)	106.2
N1-Ru1-N2	61.50(9)	61.6	61.65(8)	61.2

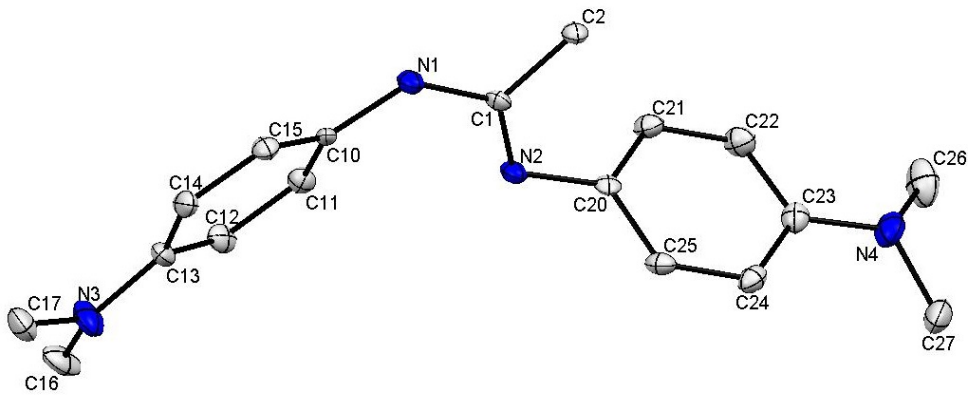

Figure 5.8: *Molecular structure of H**37** in the crystal.*

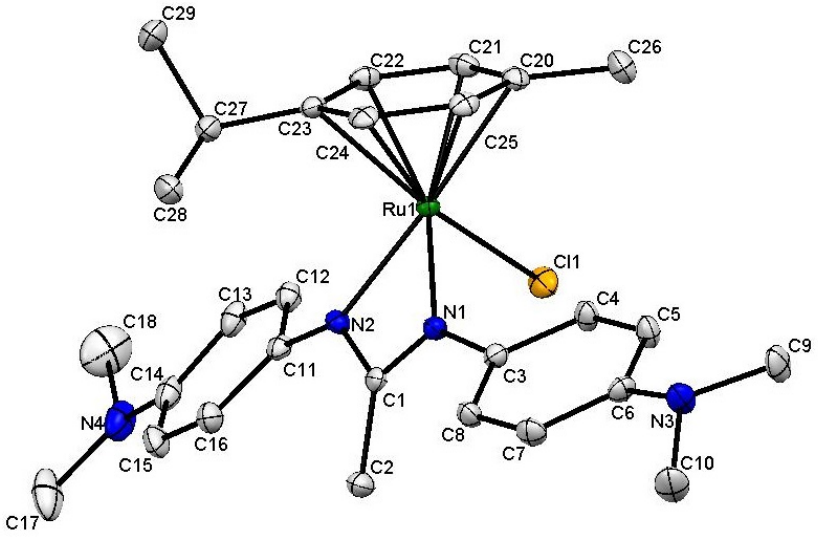

Figure 5.9: *Molecular structure of* ***38*** *in the crystal.*

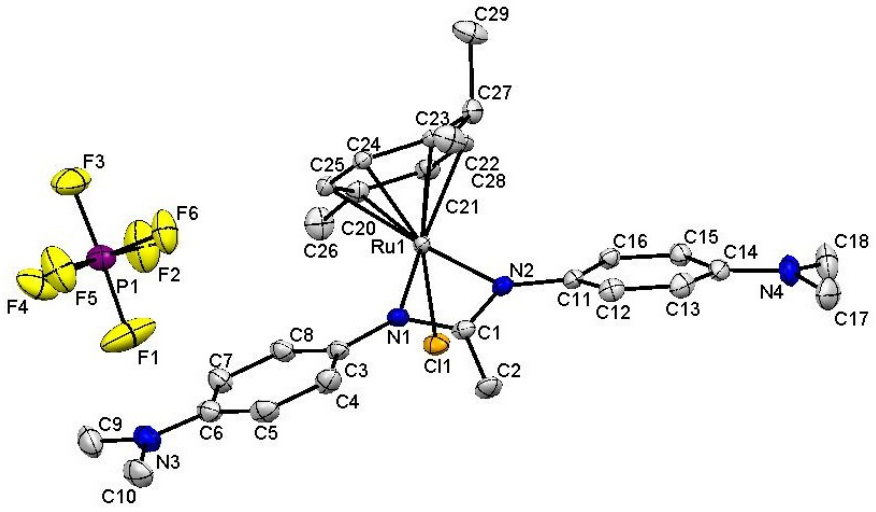

Figure 5.10: *Molecular structure of* ***38***PF_6 *in the crystal.*

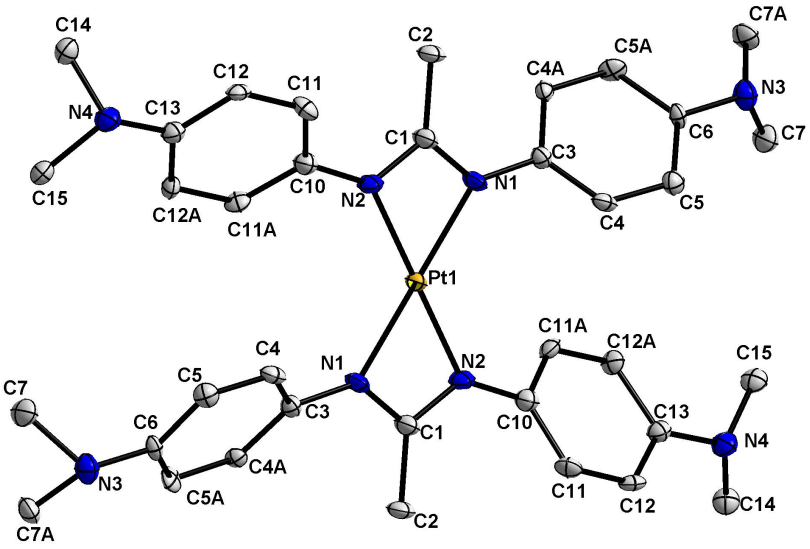

Figure 5.11: *Molecular structure of* ***39*** *in the crystal.*

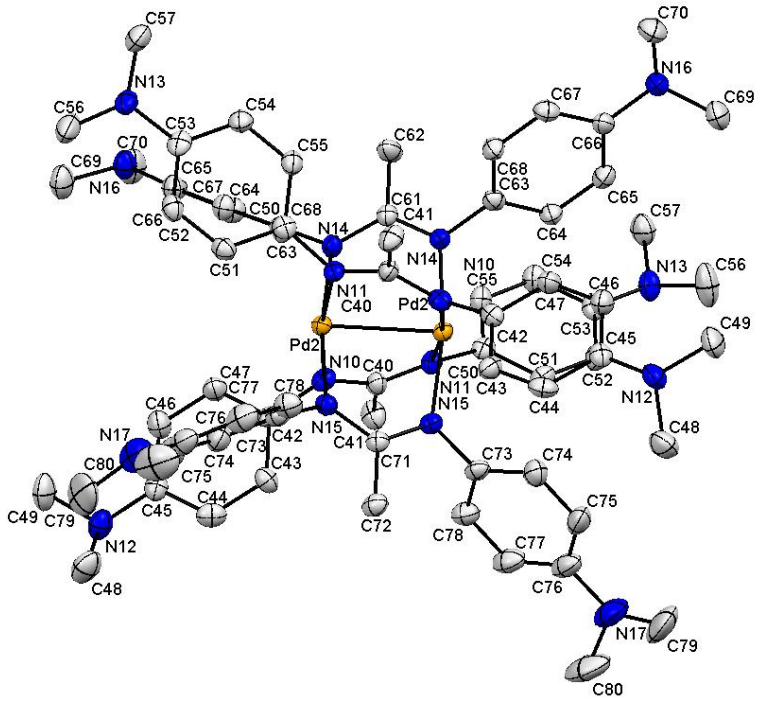

Figure 5.12: *Molecular structure of* ***40*** *in the crystal.*

5.2.3 Cyclic voltammetry

The complexes **38**, **39** and **40** were monitored with cyclic voltammetry in 0.1 M CH_2Cl_2/-NBu_4PF_6 at a scan rate of 100 mv/s. Plots of the cyclic voltammograms are illustrated in Figure 5.14, the oxidation potentials are summarized in Table 5.23.

Complex **38** undergoes two reversible oxidations at half-wave potentials of $E^1_{1/2}$ = -0.32 V and $E^2_{1/2}$ = 0.11 V, respectively, while the third oxidation is irreversible and exhibits the shape of an electrode adsorption process.[118] The cationic amidinyl radical complex **38**$^+$ is attributed a comproportionation constant of $K_c = 1.94x10^7$. Whereas complex **39** also shows two reversible oxidations at half-wave potentials of $E^1_{1/2}$ = -0.24 V and $E^2_{1/2}$ = 0.14 V, complex **40** exhibits only one reversible oxidation at $E^1_{1/2}$ = -0.42 V. The second process indicates two single electron oxidations which are very close in potential and shows a single two electron reduction after reversal of the potential. Further investigations which might have lead to a more precise description of this mechanism were not conducted. The low oxidation potentials of **40** might be caused by the high extent of delocalization of the formed radical intermediates.

Table 5.23: *Redox potentials[a,b] of the complexes **38**, **39** and **40**.*

complex	E^3	E^2	E^1
38	0.87[c]	0.11	-0.32
39		0.14	-0.24
40		0.02[c]	-0.42

[b] Potentials vs $Fc^{+/0}$. [b] In CH_2Cl_2/0.1 M Bu_4NPF_6/scan rate 100 mV s^{-1}. [c] Anodic peak potential of irreversible process.

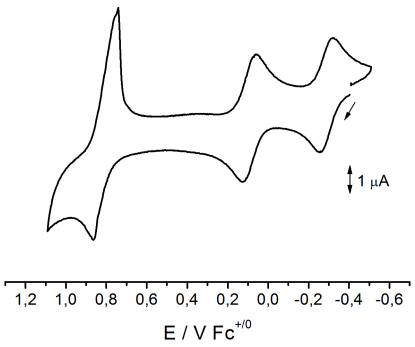

(a) **38**

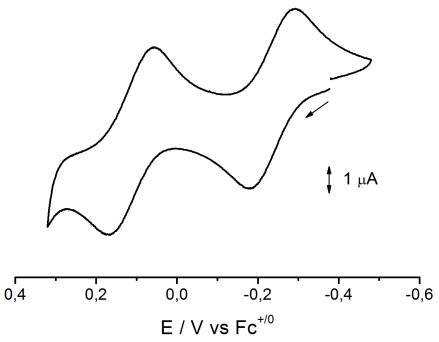

(b) **39**

Figure 5.13: *Cyclic voltammetry of the complexes **38** and **39** in CH_2Cl_2/0.1 M Bu_4NPF_6 (scan rate 100 mV s).*

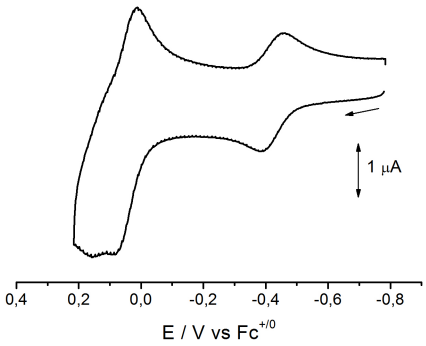

(a) **40**

Figure 5.14: *Cyclic voltammetry of the complex **40** in CH_2Cl_2/0.1 M Bu_4NPF_6 (scan rate 100 mV s; measured by Vasileios Filippou).*

5.2.4 EPR spectroelectrochemistry

The complexes **38**, **39** and **40** were investigated by EPR spectroelectrochemistry in their oxidized forms. The EPR spectra are illustrated in Figures 5.19–5.16 and the data are summarized in Table 5.24.

Complex $\mathbf{38}^+$ exhibits an unresolved isotropic EPR spectrum at room temperature and small g anisotropy of $\Delta g < 0.005$ at 110 K, indicating an amidinyl ligand-based spin. Additional evidence for a ligand-based spin is provided by the DFT calculated small metal spin density of 4.3 % (Figure 5.17). In contrast, the palladium and platinum complexes with considerable g anisotropies of $\Delta g = 0.106$ (**39**) and $\Delta g = 0.190$ (**40**) show a considerable amount of metal-based spin density. The hyperfine coupling constant $A(^{195}Pt) = 4.96$ mT in the isotropic room temperature spectrum of **39**, however, is in agreement with corresponding values of radical square planar platinum complex with 70 % ligand-based spin density.[119] A partially metal centered oxidation might be caused by the coordination of two strongly electron donating amidinato ligands per metal ion, which are well known to stabilize high metal oxidation states. The high spin orbit coupling constant of platinum is also expected to cause a larger g anisotropy than that observed in related ruthenium complexes. However, the g anisotropy of an almost identical methoxy substituted palladium paddle wheel structured complex ($\Delta g = 0.030$) discussed in the literature[116] is remarkably smaller than that observed for complex **40**.

Table 5.24: *EPR data for* ***38***$^+$*–****40***$^+$ *from electrochemical generation in* CH_2Cl_2*/0.1 M* Bu_4NPF_6.

complex	g_{iso} (298 K)	g_1, g_2, g_3 (110 K)	g_1-g_3
38$^+$	2.009	[a]	< 0.005
38$^+$	2.054[b]	2.083, 2.096, 2.189	0.106
38$^+$	2.058	1.984, 2.096, 2.174	0.190

[a] *g anisotropy not resolved.* [b] *Hyperfine splitting: 4.96 mT (1 x* ^{195}*Pt, I = ½, 33.8 % nat. abundance).*

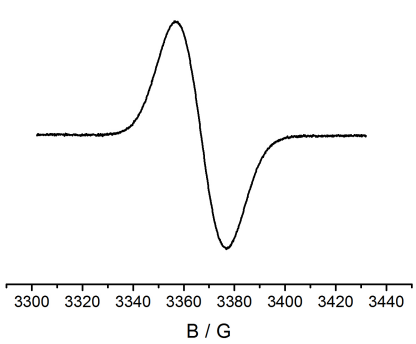

(a) **38**$^+$ at 298 K

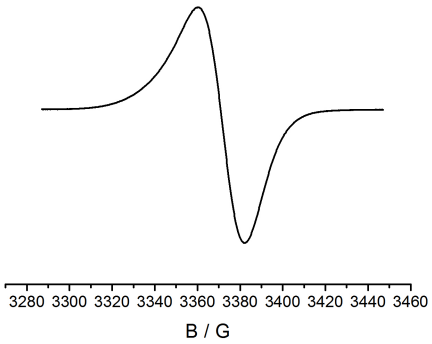

(b) **38**$^+$ at 110 K

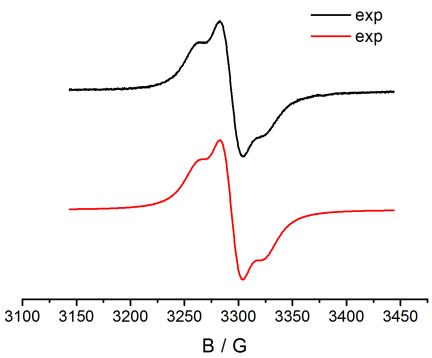

(c) **39**$^+$ at 298 K

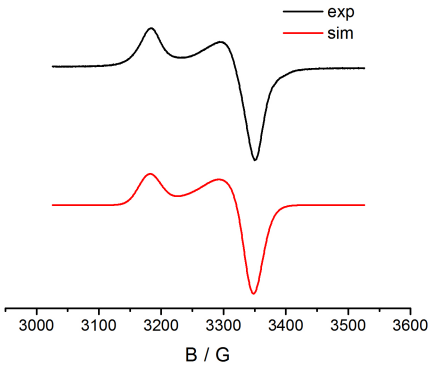

(d) **39**$^+$ at 110 K

Figure 5.15: *EPR spectra of the complexes* ***38***$^+$ *and* ***39***$^+$ *in* CH_2Cl_2*/0.1 M* Bu_4NPF_6 *(****39***$^+$ *measured by Vasileios Filippou).*

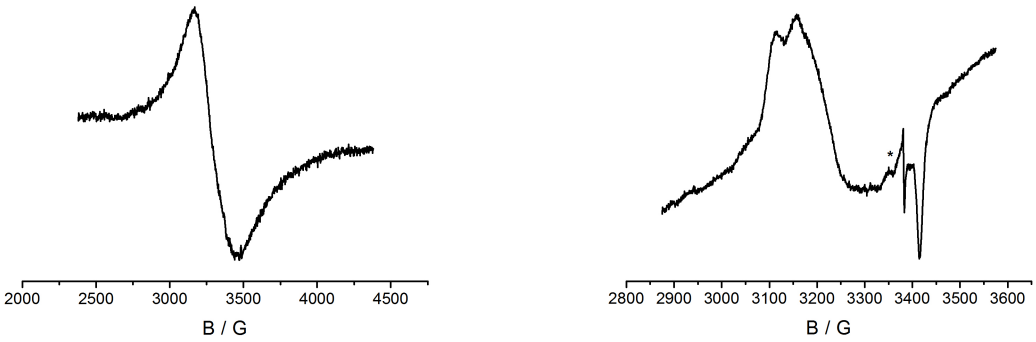

(a) $\mathbf{40}^+$ at 298 K (b) $\mathbf{40}^+$ at 110 K

Figure 5.16: *EPR spectra of the complex* $\boldsymbol{40}^+$ *in* CH_2Cl_2*/0.1 M* Bu_4NPF_6*. *Organic impurity due to electrolysis (measured by Vasileios Filippou).*

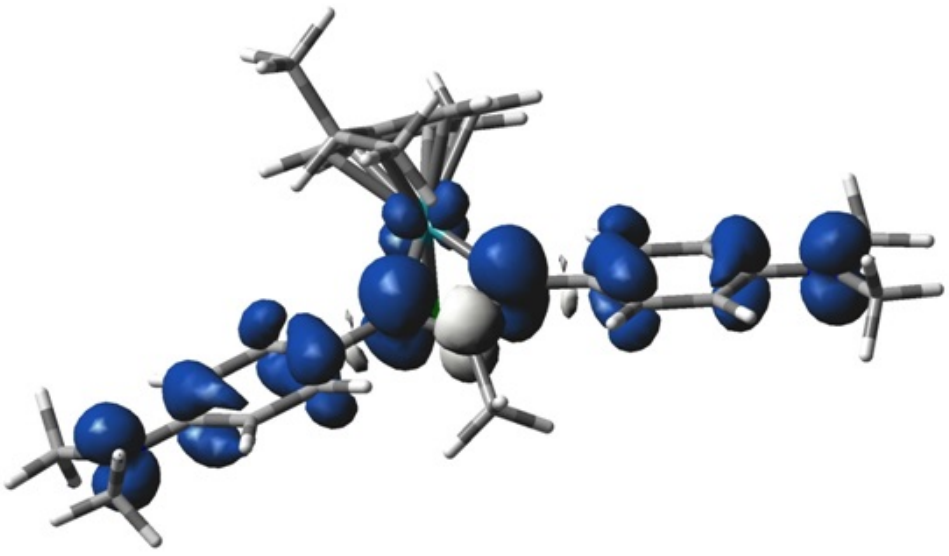

Figure 5.17: *DFT (G09/PBE0/PCM) calculated spin density of* $\boldsymbol{38}^+$*.*

5.2.5 UV–vis–NIR spectroelectrochemistry and DFT analysis

UV−vis−NIR spectroelectrochemical measurements of complex **38**PF_6–**40**PF_6 using an OTTLE cell are illustrated in Figures 4.31–4.33 and summarized in Table 5.25. The TD-DFT assignment for the transitions of **38**^{n} (n = 0, +1, +2) listed in Table A.2 in the appendix.

While complex **38** exhibits absorptions in the ultraviolet at 324 nm (ϵ = 18 900 M^{-1} cm^{-1}) and the visible at 440 nm (sh), oxidation to **38**$^+$ results in the occurrence of an intense (ϵ = 30 000 M^{-1} cm^{-1}) and narrow ($\Delta\nu_{1/2}$ = 1180 cm^{-1}) absorption band at λ_{max} = 1230 nm in the near infrared. Additionally, several less intense ($\epsilon \approx$ 4 000 M^{-1} cm^{-1}) absorption bands in the visible appear, causing the dark color of **38**PF_6. In comparison to the corresponding methoxy substituted complex **32**$^+$, the expected bathochromic shift of the NIR band ($\Delta\lambda_{max}$ = 220 nm, **32**$^+$ vs **38**$^+$) as well as a strong increase in intensity ($\Delta\epsilon$ = 26 000 M^{-1} cm^{-1}, **32**$^+$ vs **38**$^+$) is observed. The spectrum of **38**$^+$ could be reproduced by TD-DFT calculations which attribute the intense NIR band to a βHOMO → βLUMO ILCT transition with slight LMCT admixture (Figure 5.18). Calculation on the free radical ligand leads to an intense βHOMO→ βLUMO excitation at 943 nm. The shift to longer wavelengths in the complex is due to the metal contribution to the βLUMO.

Further oxidation to **38**$^{2+}$ results in a high-energy shift of the NIR transition to a partially structured absorption band at λ_{max} = 963 nm and 994 nm with an even higher intensity of ϵ = 40 000 M^{-1} cm^{-1}. The spectrum of **38**$^{2+}$ could as well be reproduced by TD-DFT calculation, assigning the transition in the near infrared to a HOMO → LUMO transition of predominantly ILCT character. Several higher energy MLCT/LLCT excitations contribute to the broad feature observed around 800 nm of **38**$^{2+}$. The orbitals involved in the transitions of **38**^{n} (n = 0, +1, +2)are depicted in Figure A.1 in the appendix.

Since no TD-DFT calculation were performed for **39** and **40**, the spectra can only be discussed in comparison to complex **38** and to literature data. Although the second oxidation of **39** seemed to be fully reversible in cyclic voltammetry, UV–vis-NIR spectroelectrochemistry revealed the irreversibility of this process, which is therefore not discussed. The square planar bis(amidinato) platinum complex **39** of light yellow color exhibits two absorption bands in the UV region at 296 nm and 391 nm. In the course of oxidation to **39**$^+$, a spectrum with an almost identical absorption pattern in the visible and NIR as for **38**$^+$ emerges, in which the NIR absorption band displays only a slight shift to higher energy of only to λ_{max} = 1225 nm accompanied by a slight increase in intensity to ϵ = 33 000 M^{-1} cm^{-1}. Due to the strong resemblance of the two spectra, mostly ligand orbitals of similar symmetry and energy to those of **38**$^+$ are expected to be involved in the electronic transitions of **39**$^+$, indicating the presence of a mainly ligand-centered radical complex. This observation clearly contradicts the EPR result which attributes a significant amount of spin density to the platinum center.

Table 5.25: *UV–vis–NIR data for **38–40** in various oxidation states from OTTLE spectroelectrochemistry in CH_2Cl_2/0.1 M Bu_4NPF_6.*

complex	λ_{max} [nm] (ϵ (M^{-1} cm^{-1}))
38	260(12 600), 324(18 900), 442(2 000)
38^{+}	270(10 500), 372(6 800), 450(18 500), 550(2 600), 743(3 100), 860(3 500), 1010(5 200), 1233(30 000)
38^{2+}	291(12 00), 352(5 200), 490(4 100),760(18 000)sh, 880(33 600)sh, 963(39 100), 994(40 200)
39	296(59 800), 391(17 800)
39^{+}	308(40 600), 454(17 100), 485(19 500), 665(3 400), 870(3 400), 1000(6 600), 1225(33 000), 1700(1 600)
40	245(23 500), 270(24 400), 306(27 100), 497(2 600)
40^{+}	245(26 200), 270(27 600), 306(29 400), 408(20 400), 708(4 000), 1120(7 100)

To resolve this conflict TD-DFT as well as spin density calculation for **39**$^{+}$ are of crucial importance and will therefore be performed in the future.

In contrast to the mononuclear platinum complex the dinuclear palladium complex showes a more intense red color due to an absorption band in the visible at 497 nm (ϵ = 2 600 M^{-1} cm^{-1}). The appearance of this band at lower energy might be due to the lower lying palladium d-orbitals and could therefore be a sign for an MLCT character of this transition. Oxidation to **40**$^{+}$ also results in the appearance of a qualitatively similar spectrum than for **38**$^{+}$ and **39**$^{+}$. The bridging function of the amidinato ligands, however, results in strongly decreased intensities of the absorptions. The most intense NIR transition at λ_{max} = 1220 nm therefore only exhibits a molar extinction of ϵ = 6 900 M^{-1} cm^{-1}. An analog mono cationic palladium paddle wheel complex in the literature[116] shows a similar absorption pattern, although its g anisotropy is much smaller than in **40**$^{+}$, indicating a variation of the electronic structure.

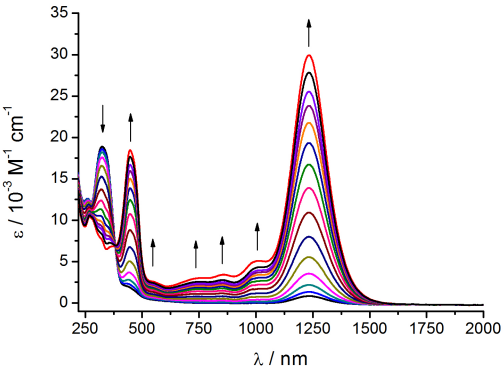

(a) **38** → **38**$^+$

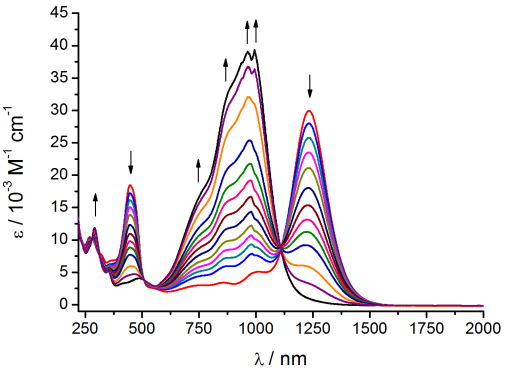

(b) **38**$^+$ → **38**$^{2+}$

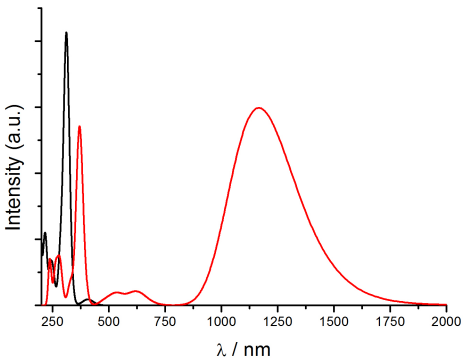

(c) **38** → **38**$^+$ (DFT)

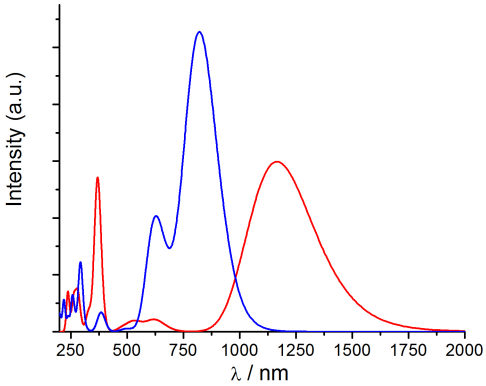

(d) **38**$^+$ → **38**$^{2+}$ (DFT)

Figure 5.18: *a) and B) UV–vis–NIR spectroelectrochemical response on stepwise oxidation of the complexe **38** in CH_2Cl_2/0.1 M Bu_4NPF_6. TD-DFT simulations of the UV–vis–NIR spectra of **38** in various oxidation states (calculated by Dr. Stanislav Záliš).*

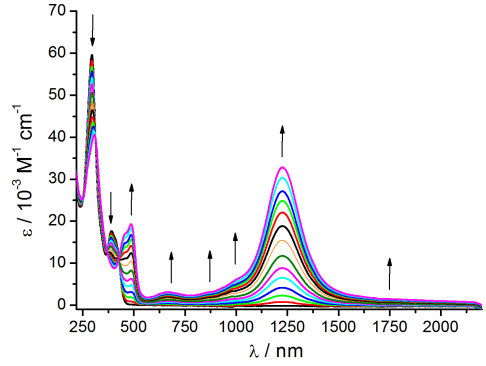

(a) **39** → **39**$^+$

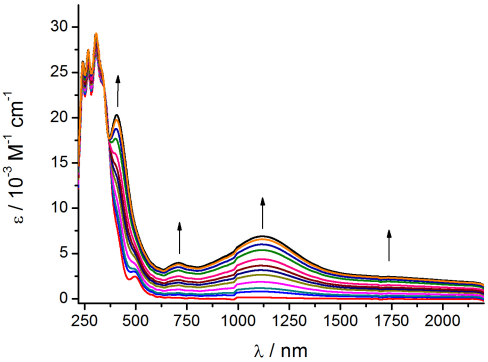

(b) **40** → **40**$^+$

Figure 5.19: *UV–vis–NIR spectroelectrochemical response on oxidation of the complexes **39** and **40** in CH_2Cl_2/0.1 M Bu_4NPF_6 (measured by Vasileios Filippou).*

5.3 Conclusion

The aim of this Chapter was development of novel amidinyl radical-based NIR chromophores structurally related to the conventional dyes malachite green and crystal violet. For this purpose a new bis(4-dimethylaminophenyl) substituted amidine ligand (L_{DMAP}) was synthesized and structurally characterized. The corresponding Ru(p-cym)Cl(L_{DMAP}) complex exhibits intense absorptions in the near infrared in its singly oxidized radical form Ru(p-cym)Cl(L_{DMAP})$^+$ as well as in its doubly oxidized form Ru(p-cym)Cl(L_{DMAP})$^{2+}$. DFT calculations assign the long wavelengths excitations to ILCT transition. The NIR absorption band of Ru(p-cym)Cl(L_{DMAP})$^+$ exhibits the desired shift to lower energy ($\lambda_{max} = 1230$ nm), whereas Ru(p-cym)Cl(L_{DMAP})$^{2+}$ absorbs at approximately similar wavelength than the corresponding methoxy substituted amidinato ruthenium complex **32**$^+$.

To investigate the effect of the metal as well as of different coordination geometries on the NIR absorption behavior, a square planar amidinato platinum complex Pt(L_{DMAP})$_2$ and a palladium complex of paddle wheel structure $Pd_2(L_{DMAP})_4$ were employed. Surprisingly, both complexes show an almost identical absorption pattern after oxidation to the mono cation, although EPR spectroscopy locates a significant amount of spin density at the metal. The spectrum of complex $Pd_2(L_{DMAP})_4^+$, however, exhibits much lower intensities than complex Pt(L_{DMAP})$_2^+$, which shows similar absorption intensities than Ru(p-cym)Cl(L_{DMAP})$^+$. In conclusion, the coordination mode (chelate vs bridging) seems to have a greater influence on the absorption behavior of DMAP-amidinyl radical complexes than the nature of the metal.

6 Summary

During the last decades the redox-active ("non-innocent") character of evermore ligand systems has been established. Among the class of redox-active ligands the hetero-1,3-diene chelate system involving for instance the α-diimines and the α-dicarbonyls (including the o-quinone/o-semiquinone/catecholate series) belongs to the most widely used in coordination chemistry. Despite the ubiquity of such particular ligands inside the class of hetero-1,3-diene ligands, not all of the actually possible combinations of heteroatoms have yet been described in the literature. Whereas for the α-azocarbonyl ligand function only one coordination compound containing the Cu(dppf) fragment is known to date, the α-azothiocarbonyl ligand function is presently not established in coordination chemistry.

To fill this gap in the series of non-innocent hetero-1,3-diene ligands, the electron rich α-azocarbonyl complexes $Ru(acac)_2L_O$ (**3**) and α-azothiocarbonyl $Ru(acac)_2L_S$ (**9**) as well as the more electron deficient α-azocarbonyl complexes $[Ru(bpy)_2L_O]PF_6$ (**9**PF_6) and α-azothiocarbonyl $[Ru(bpy)_2L_S]PF_6$ (**10**PF_6) were synthesized and structurally characterized (Chapter 2). Whereas both α-azocarbonyl complexes could be synthesized according to straightforward methods starting from the α-azocarbonyl ligand and the corresponding metal precursor, the α-azothiocarbonyl ligand had to be generated *in situ*, since it is not stable in free form.[37] As organic precursor bis[α-(phenylhydrazono)phenyl]disulfide was found to react with $Ru(acac)_2(MeCN)_2$ as well as $Ru(bpy)_2Cl_2$ under cleavage of the disulfide bond and formal hydrogen abstraction to the desired α-azocarbonyl ruthenium complexes (Figure 6.1).

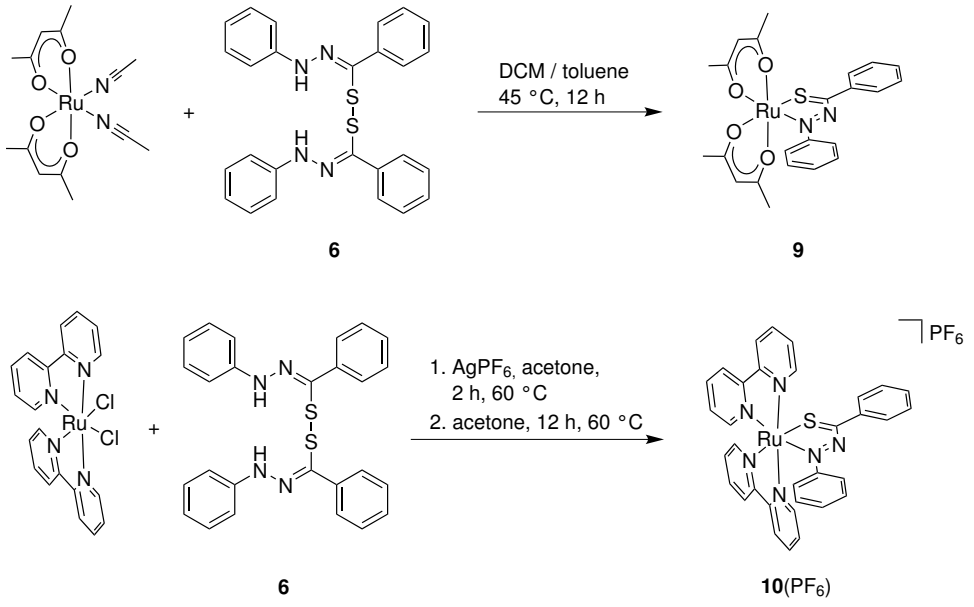

Figure 6.1: In situ *synthesis of α-azothiocarbonyl containing complexes*

.

Structure analysis regarding the N-N bond lengths in the coordinated ligands revealed their existence in a singly reduced form L_O^- and L_S^- and therefore attributes non-innocent character to the ligands. Investigation of the complexes in different oxidation states by using cyclic voltammetry as well as EPR, and UV-vis-NIR spectroelectrochemistry resulted in two related redox-series (Figure 6.2). The differences are caused by the different ancillary ligands, electron donating $acac^-$ and π-accepting bpy. In contrast, variation of the L_O and L_S ligands does not lead to qualitatively different redox-behavior of the complexes.

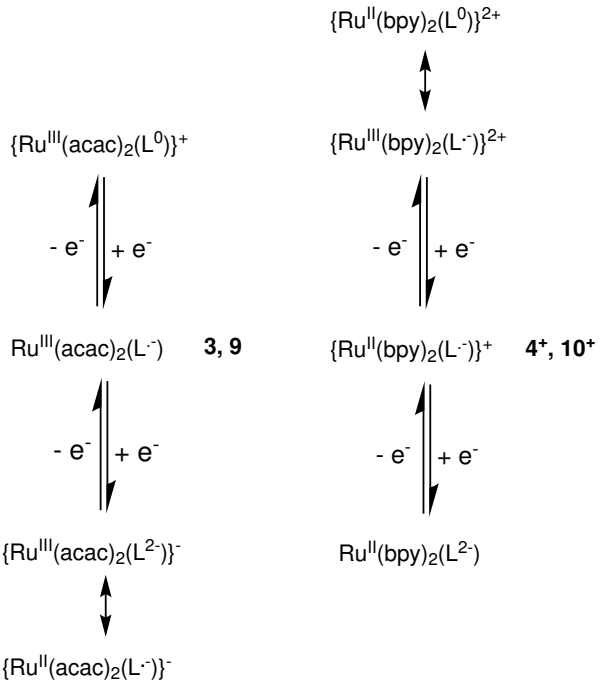

Figure 6.2: *Redox series of donor and acceptor substituted ruthenium α-azocarbonyl and α-azothiocarbonyl complexes.*

After demonstrating the accessibility of the elusive α-azothiocarbonyl ligand system by *in situ* formation, a demand for different organic molecules which yield an N-N-C-S coordination arrangement after reaction with a metal precursor emerged. Under this aspect, the neglected 2-azothiophenes where identified to undergo such type of reaction with $Ru(acac)_2(MeCN)_2$ (Chapter 3). In this instance, however, the reaction resulted in the formation of dinuclear 1,3,5-hexatrienediyl bridged bis(α-azothiocarbonyl) ruthenium complexes $(acac)_2Ru(\mu$-hte-NNCS-$NO_2)Ru(acac)_2$ (**13**) and $(acac)_2Ru(\mu$-hte-NNCS-$CO_2Et)Ru(acac)_2$ (**14**)(Figure 6.3). This reaction involves a new type of ring opening of thiophenes with subsequent C-C coupling and formation of two five-membered Ru-N-N-C-S chelate rings. Additionally, the novel conjunction of a hexatiene π-conjugated bridge with two non-innocent chelate arrangements may be of future interest, since the hexatriene entity serves as model system for larger π-systems e.g. carotene and the pigments of vision.

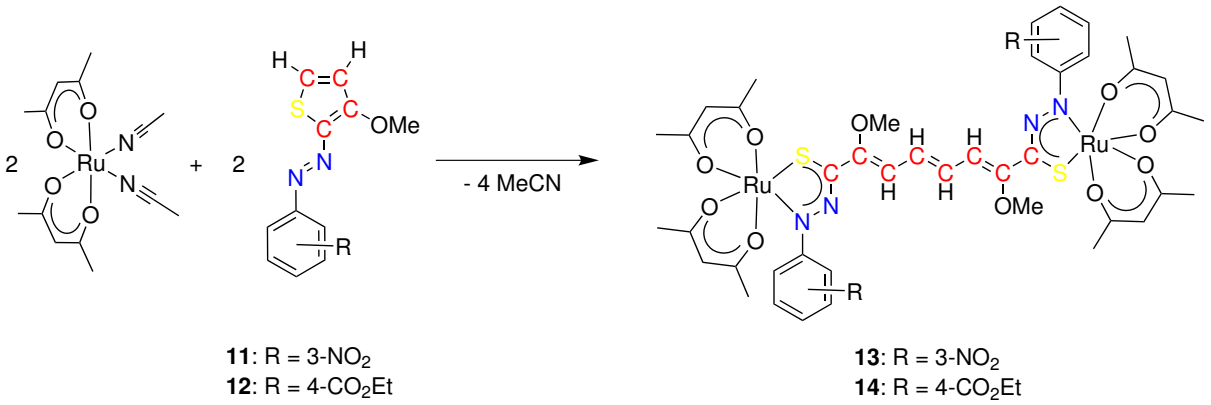

11: R = 3-NO_2
12: R = 4-CO_2Et

13: R = 3-NO_2
14: R = 4-CO_2Et

Figure 6.3: *Synthesis of dinuclear 1,3,5-hexatrienediyl bridged bis(α-azothiocarbonyl) complexes.*

Structure analysis supports the formulation of a difunctional bridging ligand and two Ru^{III} centers and therefore the existence of a unique and hitherto unknown four-spin system Ru$^{\bullet}$-$^{\bullet}$NIL-π-NIL$^{\bullet}$-$^{\bullet}$Ru. This type of spin system results in a strongly field and temperature dependent magnetic behavior which was investigated by SQUID suszeptometry and DFT methods. The complexity of the spin system is also demonstrated by the appearance of a well resolved and unshifted NMR spectrum at room temperature, whereas at low temperature (10 K) a paramagnetic ruthenium-based EPR signal is observed. The singly reduced forms of the dinuclear complexes **13** and **14** are weakly coupled mixed-valent species of Class II, evidenced by the low comproportionation constants of around $K_c = 1000$ (see cyclovoltammogram in Figure 6.4a) and broad absorption bands ranging across the accessible near infrared region of the electromagnetic spectra, assigned to intervalence charge transfer (IVCT) transitions (Figure 6.4b).

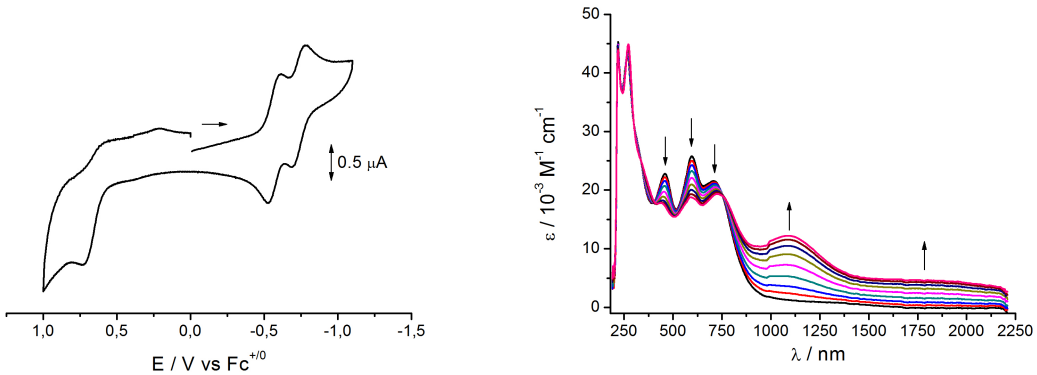

(a) Cyclic voltammogram of **13** at 298 K

(b) UV–vis–NIR spectra of **13** → **13**$^{-}$

Figure 6.4: *a) Cyclic voltammetry of **13** at 298 K in CH_2Cl_2/0.1 M Bu_4NPF_6. b) UV-vis-NIR spectroelectrochemistry of **13** in CH_2Cl_2/0.1 M Bu_4NPF_6*

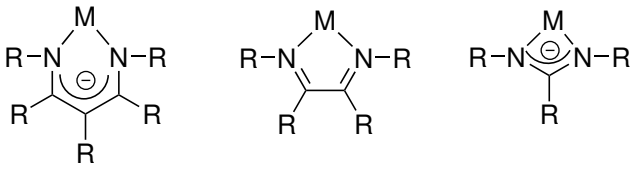

Figure 6.5: *The chelating coordination modes of the β-diketonate (**A**), 1,4-diazabutadiene (**B**) and amidinate (**C**) ligands.*

Besides the redox-active hetero-1,3-diene ligands, which form five-membered chelate rings when coordinated to a metal, the β-diiminates and β-diketonates, forming a six membered chelate rings as well as the heteroallylic ligands featuring four membered chelate rings are widely used ligand systems in coordination chemistry (Figure 6.5). Whereas the non-innocent character of the β-diiminates and β-diketonates has lately been revealed, the heteroallylic ligand systems are not known to exhibit non-innocent behavior in coordination compounds. The research described in Chapter 4 was thus aimed at demonstrating that the class of heteroallylic ligands is also prone to show non-innocent behavior under specific conditions.

For reasons of simple synthetic modification of the electronic structure, triazenido, amidinato and guanidinato ligands were utilized as model systems for heteroallylic ligands. Ruthenium was chosen as metal for complexation of these ligands, since the two extreme situations of ruthenium-centered spin L'$_n$Ru^{III}(L$^-$) and ligand-centered spin L'$_n$Ru^{II}(L$^\bullet$) (Figure 6.6) are easily distinguished via EPR spectroscopy.

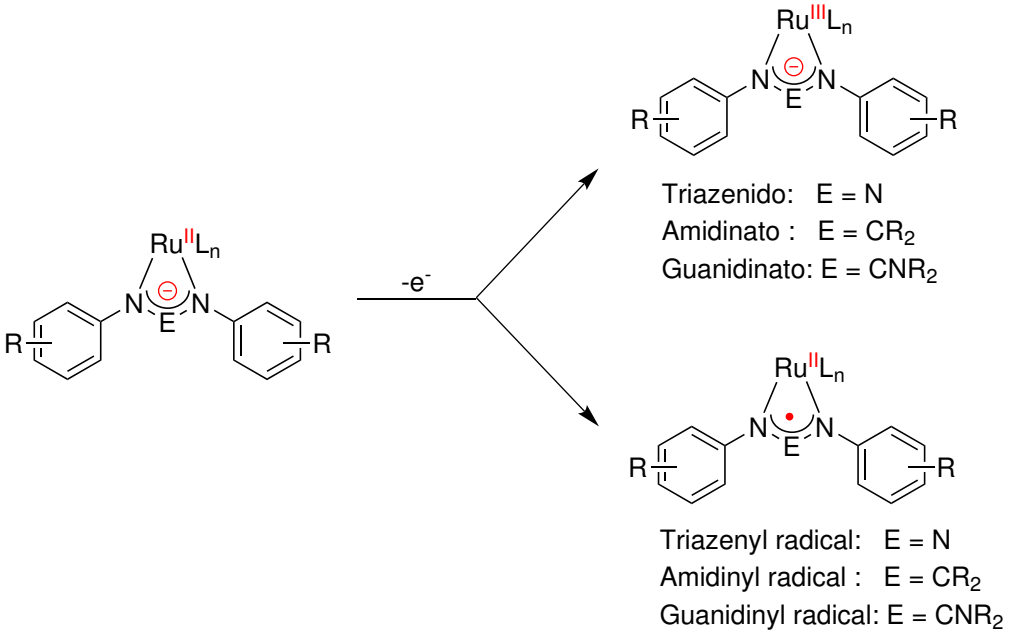

Figure 6.6: *The different pathways for the oxidation of a Ru^{II} complex with triazenido, amidinato or guanidinato ligands.*

To work out the conditions under which heteroallylic ligands behave non-innocently, differently substituted ruthenium(II) triazenido complexes of various electronic structure were synthesized. Remarkably, a continuum was established for the oxidation of the precursors [L_nRu^{III}(RNNNR)], ranging from a) ruthenium-centered spin situation Ru^{III}(RNNNR$^-$) species via b) orbital-mixed systems L_nRu^{III}(RNNNR$^-$) ↔ L_nRu^{II}(RNNNR$^\bullet$) to c) triazenyl radical complexes L_nRu^{II}(RNNNR$^\bullet$). The appearance of the different electronic situations was evidenced by EPR spectroscopy and confirmed by DFT calculated spin densities. Figure 6.7 illustrates the experimental and theoretical evidences for the first triazenyl radical complex ever observed.

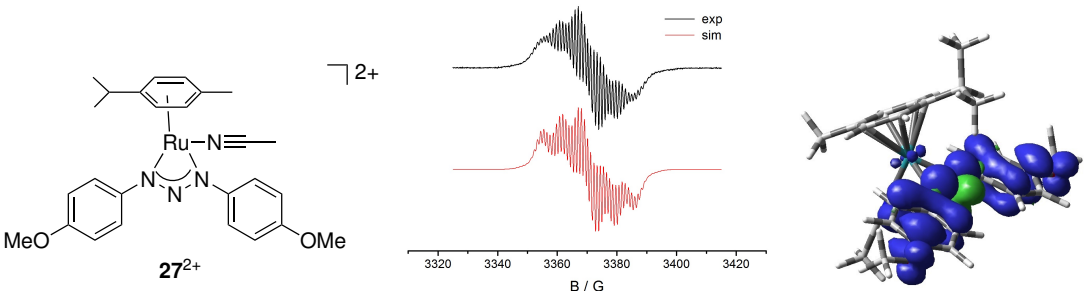

Figure 6.7: *a) Structure of* ***27***$^{2+}$*; b) EPR spectrum of* ***27***$^{2+}$ *in* CH_2Cl_2*/0.1 M* Bu_4NPF_6*; c) DFT calculated (G09/PBE0/6-311G(d)/PCM-*CH_2Cl_2*) spin density.*

The key step towards formation of the desired triazenyl radical complex was the utilization of the π-accepting and non σ-donating p-cymene ancillary ligand instead of π-accepting but also σ-donating N-heterocyclic ligands such as substituted 4,4'-bipyridines or 2-phenylazopyridine. This successful approach was then extended to amidinato and guanidinato ruthenium complexes, which could also be detected in the different electronic situations (a)–(c) after oxidation of the corresponding precursors. The complexes **27**$^{2+}$, **34**$^{2+}$ and **35**$^{2+}$ are the first triazenyl, amidinyl and guanidinyl radical complexes observed.

Additionally, EPR spectroelectrochemistry was found to be a helpful tool in establishing a series for the magnitude of the redox-potentials of the different ligand systems when coordinated to ruthenium: triazenido < amidinato < guanidinato, using the g anisotropy of the EPR active species. An additional feature of the novel triazenyl and aminidyl radical complexes is their intense and narrow absorption band in the near infrared.

Using this information and knowledge about the intense absorption of prominent dyes like malachite green and crystal violet, dimethylaminophenyl (DMAP) groups were incorporated into the amidinato ligand (Chapter 5). The aim was to achieve a more convenient isolation of the oxidized amidinyl radical form as well as a low-energy shift of the NIR absorption band towards the telecommunication window. It was possible to isolate and structurally charac-

terize both the complexes [RuCl(p-cym)(L_{DMAP})] (**38**) as well as its oxidized form [RuCl(p-cym)(L_{DMAP})]PF_6 (**38**PF_6) (Figure 6.8). The main structural differences concern the C-NMe_2 and N-C(CH_3)N bond lengths of 1.41 Å in **38** and 1.37 Å in $\mathbf{38}^+$ illustrating a tendency towards formation of a p-quinonoid structure in the oxidized form. UV–vis–NIR spectroelectrochemistry reveals an intense (ϵ = 30000 M^{-1} cm^{-1}) and narrow ($\Delta\nu_{1/2}$ = 1180 cm^{-1}) absorption band at λ_{max} = 1230 nm in the near infrared for the singly oxidized form $\mathbf{38}^+$. Further oxidation to $\mathbf{38}^{2+}$ results in a high-energy shift towards an even more intense (ϵ = 40000 M^{-1} cm^{-1}) absorption band at λ_{max} = 994 nm (Figure 6.9). The electronic spectra of $\mathbf{38}^n$ in various oxidation states (n = 0, +1, +2) could be reproduced by TD-DFT calculations, assigning the NIR absorptions of $\mathbf{38}^+$ and $\mathbf{38}^{2+}$ to ILCT transitions with slight metal to ligand LMCT admixture (Figure 6.10).

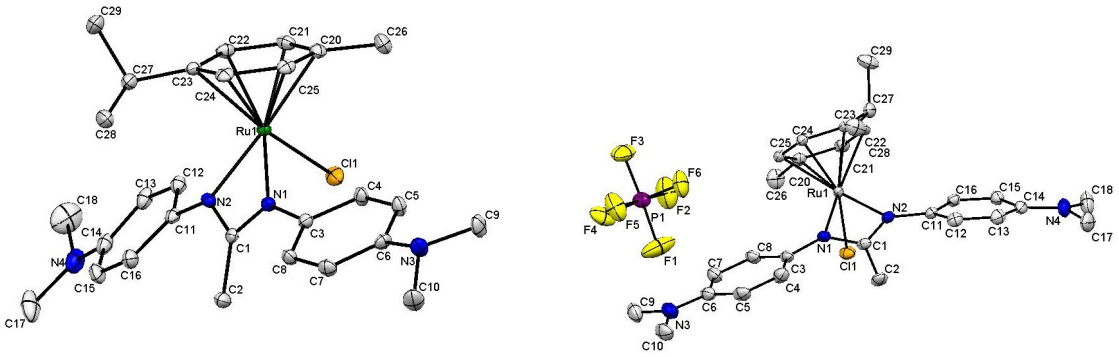

(a) (b)

Figure 6.8: *Molecular structure of a)* ***38*** *and b)* ***38***PF_6 *in the crystal.*

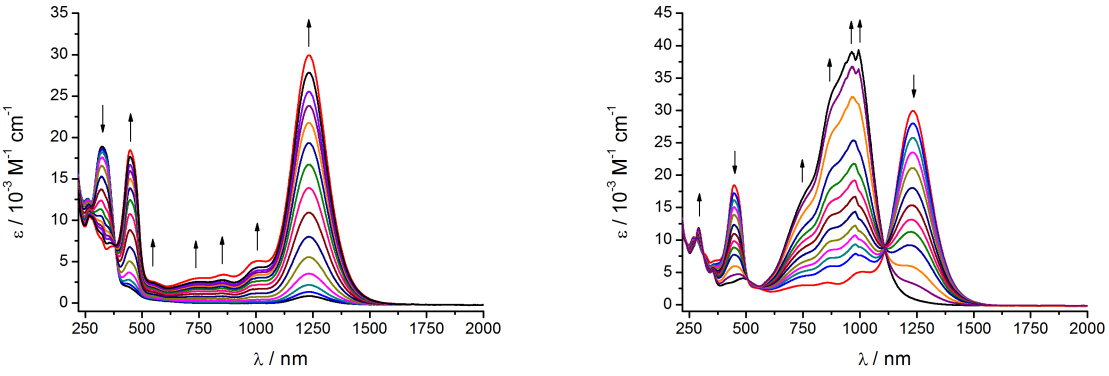

(a) **38** → $\mathbf{38}^+$ (b) **38** → $\mathbf{38}^{2+}$

Figure 6.9: *UV–vis–NIR spectroelectrochemical response on stepwise oxidation of* ***38****.*

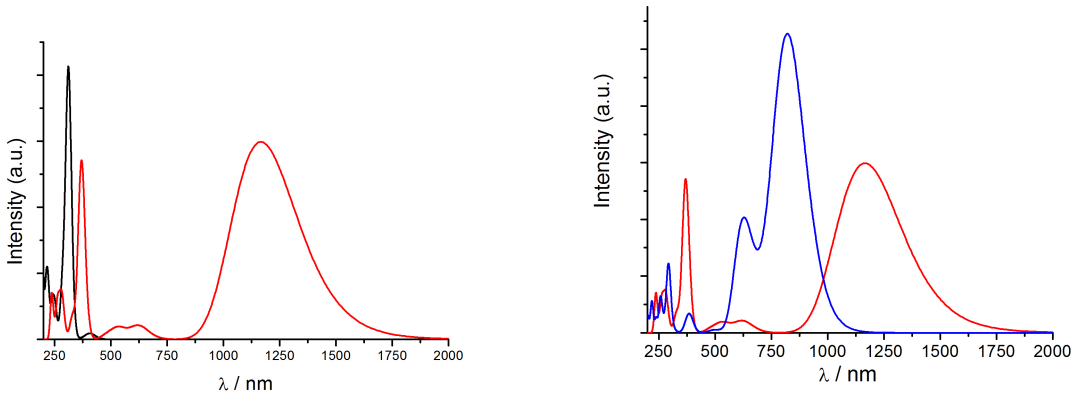

(a) **38** (black) → **38**$^{+}$ (red) (b) **38** (red) $^{+}$ → **38**$^{2+}$ (blue)

Figure 6.10: *TD-DFT calculated spectra of **38** in various oxidation states.*

To investigate how the metal and the coordination mode of the ligand effects the absorption behavior, a square planar platinum complex Pt(L_{DMAP})$_2$ (**39**) and a palladium complex of paddle wheel structure $Pd_2(L_{DMAP})_4$ (**40**) were synthesized (Figure 6.11) and investigated by UV-vis-NIR spectroelectrochemistry.

Surprisingly, the singly oxidized forms of both complexes exhibit an absorption pattern, qualitatively similar to that of the spectrum of **38**$^{+}$ (Figure 6.12), although EPR spectroscopy revealed a higher metal contribution to the SOMO. The main differences in the spectra are the much lower intensities of the absorptions of **40**$^{+}$ in comparison to those of **38**$^{+}$ and **39**$^{+}$.

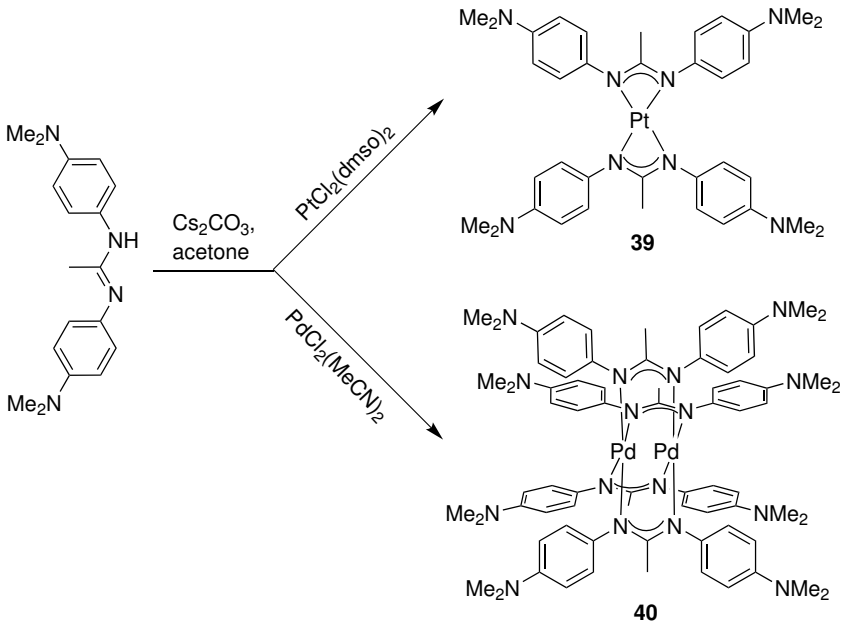

Figure 6.11: *Synthesis of the square planar platinum amidinato complex **39** and the paddle wheel structured palladium complex **40**.*

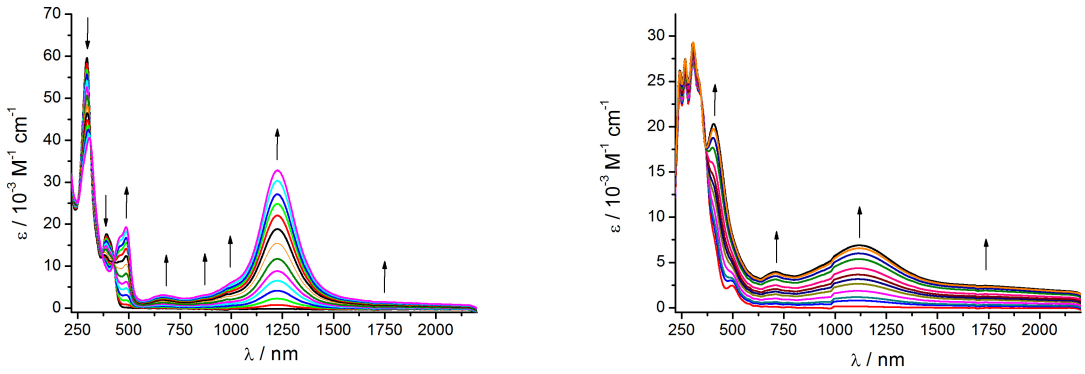

(a) **39** → **39**$^+$ (b) **40** → **40**$^+$

Figure 6.12: *UV–vis–NIR spectroelectrochemistry in CH_2Cl_2/0.1 M Bu_4NPF_6.*

This observation leads to the conclusion that the coordination mode (chelate vs bridging) has a greater influence of the absorption pattern than the metal.

In summary, this thesis presents the discovery of various new kinds of non-innocent ligands. The synthesis and full characterization of these ligand systems and their complexes not only resulted in new types of chemical reactions but also revealed the outstanding properties of the resulting coordination arrangements. In this respect it could be demonstrated that the terminal coupling of 1,3,5-hexatrienes with non-innocent chelate functions leads to materials with novel but also very complicated magnetic behavior, imposing a demand for more detailed experimental and theoretical investigations in the future. The importance for the development of small π-conjugated prototypical systems became obvious ever since the Nobel Prize in Chemistry 2013 was awarded to Karplus, Levitt and Warshel for employing the 1,6-diphenyl-1,3,5-hexatriene system as basis for the development of computational methods addressing more extended structures. The newly discovered feature of metal stabilized heteroallyl radical species exhibiting intense absorptions in the near infrared may also give rise to further development in this research area, since NIR dyes are utilized in a wide range of applications. Thus it might be possible that replacement of the methyl group at the amidinyl-carbon with a donor substituted phenyl group for example, possibly will shift the NIR absorption towards the interesting telecommunication window around 1300 nm.

The introduced strategy for creating coordination environments which facilitate non-innocent behavior of various ligand systems may also be adopted in the search for new redox-active molecules. Given its structural relationship to heteroallyl ligands, the nitrite anion could be a possible candidate for showing non-innocent behavior under specific conditions. Demonstrating its redox-activity would in fact help in understanding biological processes involving nitrite, e.g. in the reactions of nitrite reductase.[120]

7 Zusammenfassung

Während der letzten Jahrzehnte konnte der redox-aktive („nicht-unschuldige“) Charakter vieler Ligandensysteme aufgedeckt werden. Die Klasse der non-innocent Hetero-1,3-dien-Chelatliganden mit ihren bekannten Vertretern wie zum Beispiel die α-Diimine oder α-Dicarbonyle, mit ihrer Unterklasse der Chinone, o-Semichinone und Catecholate, gehört zu den am weitesten verbreiteten redox-aktiven Ligandensystemen in der Komplexchemie. Trotz des großen Bekanntheitsgrads dieser Verbindungsklassen im System der Hetero-1,3-dien-Liganden sind noch nicht alle möglichen Kombinationen in der Literatur beschrieben. Für Komplexe mit der α-Azocarbonyl-Ligandenfunktion gibt es bisher nur ein Beispiel, welches das Cu(dppf)-Fragment enthält, während die α-Azothiocarbonyl-Ligandenfunktion noch nicht literaturbekannt ist.

Um die Lücke in der Serie der non-innocent Hetero-1,3-dien-Liganden zu füllen, wurden die elektronenreichen α-Azocarbony- und α-Azothiocarbonyl-Komplexe $Ru(acac)_2L_0$ (**3**) und $Ru(acac)_2L_S$ (**9**) sowie die elektronenärmeren α-Azocarbonyl- und α-Azothiocarbonyl-Komplexe $[Ru(bpy)_2L_0]PF_6$ (**4**PF_6) und $[Ru(acac)_2L_S]PF_6$ (**10**PF_6) synthetisiert und strukturell charakterisiert (Kapitel 2). Während die beiden α-Azocarbonylkomplexe nach gewöhnlichem Vorgehen aus dem freien Liganden und der entsprechenden Metallvorstufe dargestellt werden konnten, musste der α-Azothiocarbonylligand *in situ* erzeugt werden, da er in freier Form nicht stabil ist.[42] Die organische Verbindung Bis[α-(phenylhydrazono)phenyl]disulfide erwies sich hierfür als geeignete. Es wurde gezeigt, dass dieses Molekül unter Spaltung der Disulfidbindung sowie unter formaler Wasserstoffabspaltung mit den Metallvorstufen $Ru(acac)_2(MeCN)_2$ und $Ru(bpy)_2Cl_2$ zu den gewünschten α-Azothiocarbonylkomplexen reagiert (Abbildung 7.1).

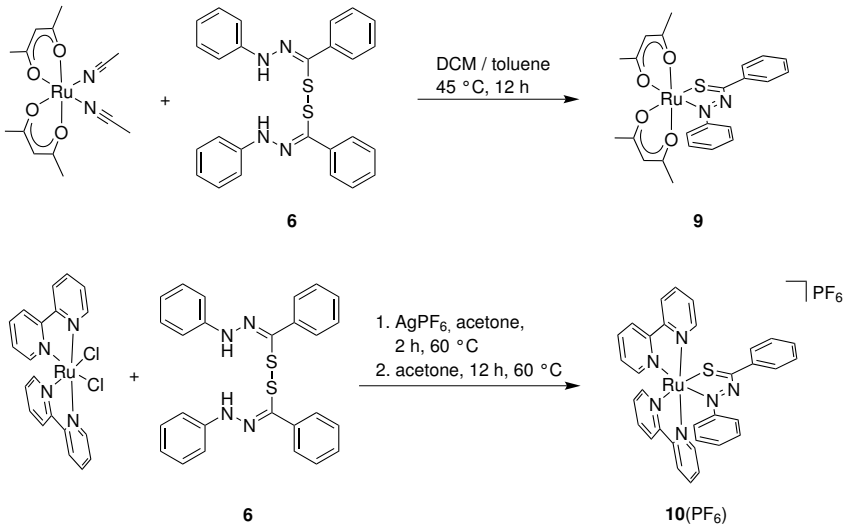

Abbildung 7.1: In situ *Synthese von α-Azothiocarbonylkomplexen.*

Mittels Röntgenstrukturanalyse konnte anhand der N-N-Bindungslängen der koordinierten Liganden gezeigt werden, dass sowohl der α-Azocarbonyl- als auch der α-Azothiocarbonylligand in ihrer reduzierten Form L_0^- bzw. L_S^- vorliegen und somit ein nicht-unschuldiges Verhalten aufweisen. Die Untersuchung der Komplexe in ihren verschiedenen Oxidationsstufen wurde mittels Cyclovoltammetrie sowie ESR- und UV-vis-NIR-spektoelektrochemischer Methoden durchgeführt und resultierte in zwei vergleichbaren Redoxserien (Abbildung 7.2). Die Unterschiede in den beiden Redoxserien werden durch die unterschiedlichen Coliganden $acac^-$ (π-Donor) und bpy (π-Akzeptor) hervorgerufen; der Austausch von L_O gegen L_S führt hingegen nicht zu einem deutlichen unterschiedlichen Redoxverhalten der Komplexe.

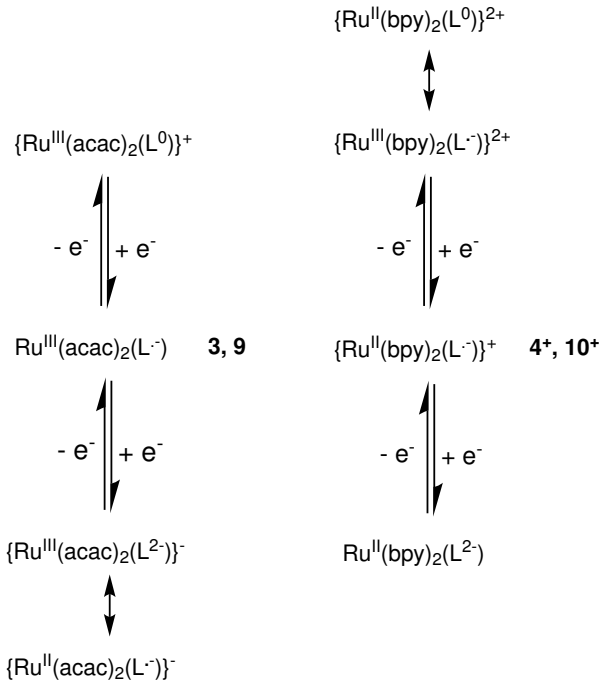

Abbildung 7.2: *Redoxserie von Donor- und Akzeptorsubstituierten α-Azocarbonyl- and α-Azothiocarbonylrutheniumkomplexen.*

Nachdem gezeigt wurde, dass die schwer zugängliche α-Azothiocarbonylfunktion *in situ* aus einer geeigneten Vorstufe erzeugt werden kann, erschien es interessant weitere organische Moleküle zu entdecken, welche nach Reaktion mit einer geeigneten Metallvorstufe einen N-N-C-S-Chelatkomplex ausbilden. In dieser Arbeit ist es gelungen, den bisher wenig beachteten 2-Azothiophenen diesen Charakter zuzuweisen, indem gezeigt wurde, dass diese Moleküle nach der Reaktion mit $Ru(acac)_2(MeCN)_2$ tatsächlich eine N-N-C-S-Chelatbildung aufweisen. Im Falle der 2-Azothiophene führte die Reaktion jedoch zu den 1,3,5-Hexatriendiyl-verbrückten Bis(αazothiocarbonyl)rutheniumkomplexen $(acac)_2Ru(\mu$-hte-NNCS-$NO_2)Ru(acac)_2$ (**13**) und $(acac)_2Ru(\mu$-hte-NNCS-$CO_2Et)Ru(acac)_2$ (**14**) (Abbildung 7.3). Die Reaktion selbst beinhaltet eine neue Art von Ringöffnungsreaktion der Thiophene mit anschließender C-C Bindungsknüpfung und Ausbildung eines fünfgliedrigen N-N-C-S-Chelatrings. Die neuartige Fusion zweier

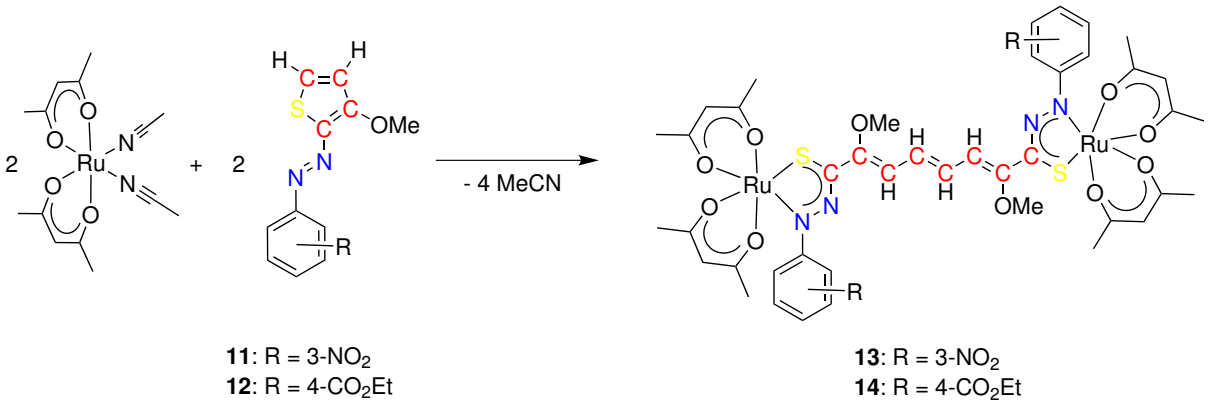

11: R = 3-NO_2
12: R = 4-CO_2Et

13: R = 3-NO_2
14: R = 4-CO_2Et

Abbildung 7.3: *Synthese von zweikernigen 1,3,5-Hexatrienediyl-verbrückten Bis(α-azothiocarbonyl)komplexen.*

non-innocent Chelatsysteme mit einer π-konjugierten Hexatrienbrücke könnte auch zukünftig von Interesse sein, da die Hexatrieneinheit oft als Modellsystem für größere π-Systeme wie zum Beispiel das β-Karotin Verwendung findet.

Die Röntgenstrukturanalyse von **13** zeigt das Vorhandensein eines difunktionellen Brückenliganden mit zwei Ru^{III} Zentren, was auf das Vorliegen eines bisher unbeobachteten Vierspinsystems der Art $Ru^{\bullet}$-$^{\bullet}$NIL-π-NIL$^{\bullet}$-$^{\bullet}$Ru hindeutet. Dieses neuartige Spinsystem wurde mittels SQUID-Suszeptometrie als extrem feld- und temperaturabhängig beschrieben. Die Komplexität des Spinsystems ist auch durch das bei Raumtemperatur beobachtete NMR-Spektrum von hoher Auflösung sowie durch das rutheniumzentrierten ESR-Signal bei 10 K wiedergegeben. Die einfach reduzierten Formn der Komplexe **13** und **14** sind schwach gekoppelte gemischtvalente Verbindungen der Klasse II. Dies geht aus den niedrigen Komproportionierungskonstanten von ca. $K_c = 1000$ (siehe Cyclovoltammogramm in Abbildung 7.4a) und den breiten Absorptionsbanden im nahen Infrarotbereich des elektromagnetischen Spektrums, welche als Intervalence-Charge-Transfer-(IVCT) Banden identifiziert wurden, hervor.

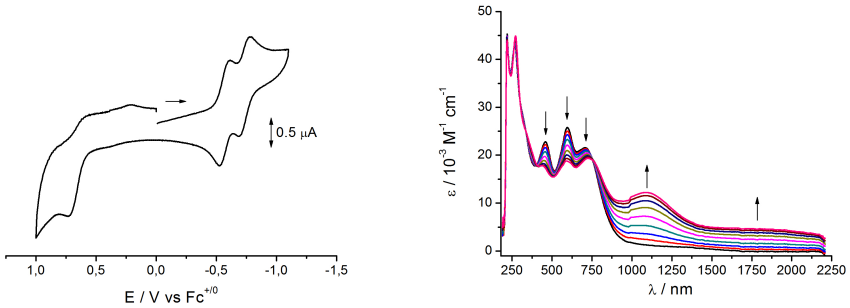

(a) Cyclic voltammogram of **13** at 298 K (b) UV–vis–NIR spectra of **13** → **13**$^{-}$

Abbildung 7.4: *a) Cyclovoltammetrie von **13** bei 298 K in CH_2Cl_2/0.1 M Bu_4NPF_6. b) UV-vis-NIR-Spektroelektrochemie von **13** in CH_2Cl_2/0.1 M Bu_4NPF_6*

Neben den redox-aktiven Hetero-1,3-dien-Liganden, welche durch Koordination an ein Metallzentrum einen fünfgliedrigen Chelatring ausbilden, sind auch die β-Diiminate und β-Diketonate, welche sechsgliedrige Chelatringe ausbilden, und die heteroallylischen Liganden, welche einen viergliedrigen Chelatring ausbilden, weitverbreitete Ligandensysteme in der Koordinationschemie (Abbildung 7.5). Während der non-innocent Charakter der β-Diiminate und β-Diketonate unlängst aufgezeigt wurde, konnte der Klasse der Heteroallylliganden bisher noch kein non-innocent Verhalten nachgewiesen werden. Die in Kapitel 4 beschriebene Arbeit zielte deshalb darauf hin zu zeigen, dass auch heteroallylische Liganden unter bestimmten Bedingungen ein non-innocent Verhalten aufweisen können.

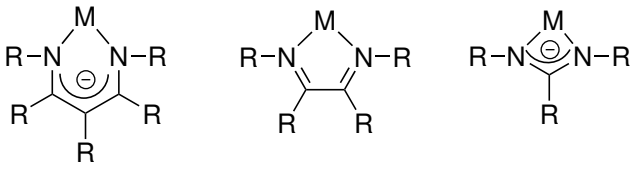

Abbildung 7.5: *Der chelatisierende Koordinationsmodus des β-Diketonat- (**A**), 1,4-Diazabutadien- (**B**) und Amidinatliganden (**C**).*

Aufgrund der einfachen synthetischen Modifizierbarkeit ihrer elektronischen Struktur wurden die Triazenido-, Amidinato- und Guanidinatoliganden als Modelle für die gesamte Klasse der heteroallylischen Liganden eingesetzt. Als Metall für die Komplexierung der Liganden wurde Ruthenium gewählt, da sich die beiden Extremfälle von rutheniumzentriertem L'$_n$Ru^{III}(L$^-$) und ligandenzentriertem Spin L'$_n$Ru^{II}(L$^\bullet$) (Abbildung 7.6) einfach mittels ESR Spektroskopie voneinander unterscheiden lassen.

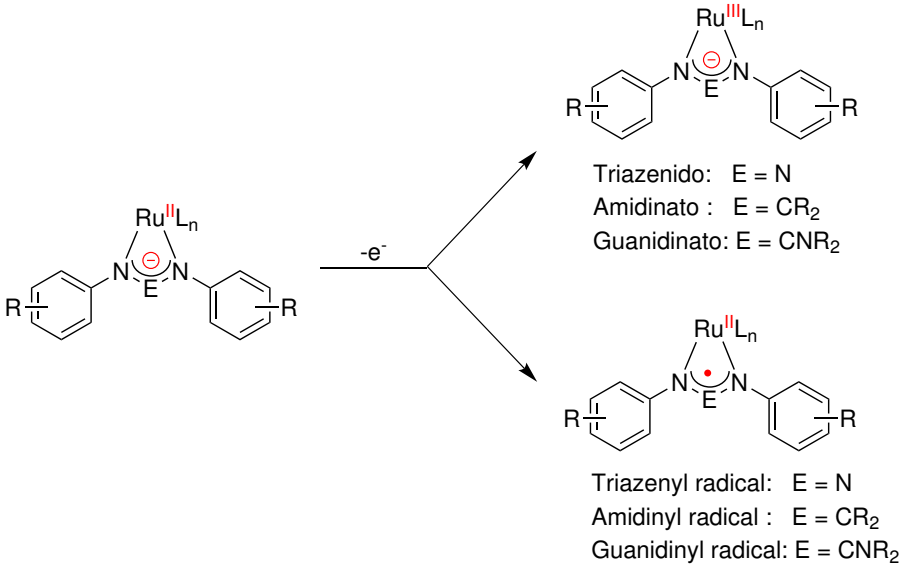

Abbildung 7.6: *Verschiedene Reaktionspfade für die Oxidation von Triazenido-, Amdinato- und Guanidinatokomplexen mit Ru^{II}.*

Um die Bedingungen, welche zu einem nicht-unschuldiges Verhalten der aufgeführten Liganden führen, ausfindig zu machen, wurde eine Reihe verschieden substituierter Ruthenium(II)triazenidokomplexe synthetisiert. Somit konnte ein beachtliches Kontinuum an Komplexen generiert werden, welches sich von a) einer rutheniumzentrierten Spinsituation [$L_nRu^{III}(RNNNR^-)$] via b) eines gemischten Orbitalsystems [$L_nRu^{III}(RNNNR^-)$] ↔ [$L_nRu^{II}(RNNNR^\bullet)$] zu c) einem Triazenylradikalkomplex $L_nRu^{II}(RNNNR^\bullet)$] erstreckt. Das Auftreten der einzelnen Spezies konnte mittels ESR-Spektroskopie nachgewiesen und mittels DFT berechneter Spindichten bestätigt werden. Abbildung 7.7 zeigt den experimentellen und theoretischen Nachweis für den ersten jemals beobachteten Triazenylradikalkomplex.

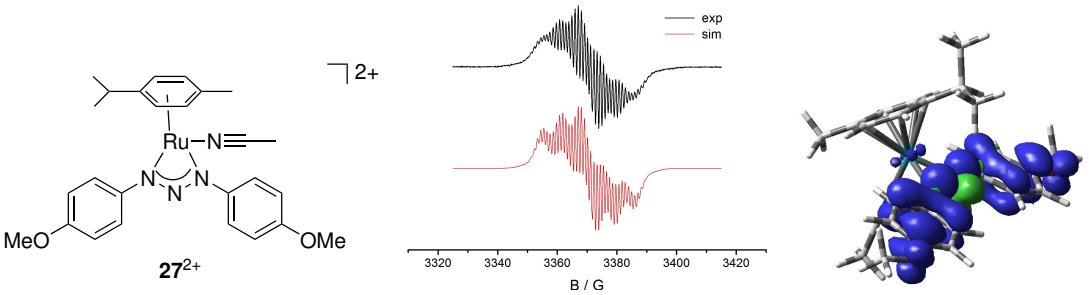

27^{2+}

(a) (b) (c)

Abbildung 7.7: *a) Struktur von* **27**$^{2+}$*; b) ESR Spektrum von* **27**$^{2+}$ *in* CH_2Cl_2*/0.1 M* Bu_4NPF_6*; c) DFT berechnete (G09/PBE0/6-311G(d)/PCM-*CH_2Cl_2*) Spindichte.*

Der entscheidende Schritt zur Ausbildung des gewünschten Triazenylradikalkomplexes lag in der Verwendung von p-Cymol als Coligand, welches nebst seiner π-Akzeptorfähigkeit keine σ-Donorfähigkeit besitzt. Hingegen führte die Verwendung von π-Akzeptor-/σ-Donor-Coliganden wie z.B. akzeptorsubstituiertes 4,4'-Bipyridin oder 2-Phenylazopyridin nicht zur Ausbildung eines eindeutig nachweisbaren Radikalkomplexes. Die erfolgreiche substitutionsstrategie konnte nun auf Amidinato- und Guanidinatokomplexe übertragen werden, welche dadurch ebenfalls nach Oxidation in den verschiedenen elektronischen Strukturen a)–c) nachgewiesen werden konnten. Die Komplexe **27**$^{2+}$, **34**$^{2+}$ und **35**$^{2+}$ sind die ersten bekannten Triazenyl-, Amidinyl- und Guanidinylradikalkomplexe.

Desweiteren konnte mittels ESR-Spektroelektrochemie eine Reihe aufgestell werden, welche die relative Größe des Redoxpotentials der koordinierten Liganden wiederspiegelt: Triazenido < Amidinato < Guanidinato. Als entscheidender Parameter diente hierfür die bei 110 K gemessene g-Anisotropie. Eine weitere bemerkenswerte Eigenschaft der neuartigen Triazenyl- und Amidinylradikalkomplexe ist ihre intensive und schmale Absorptionsbande im nahen Infrarotbereich.

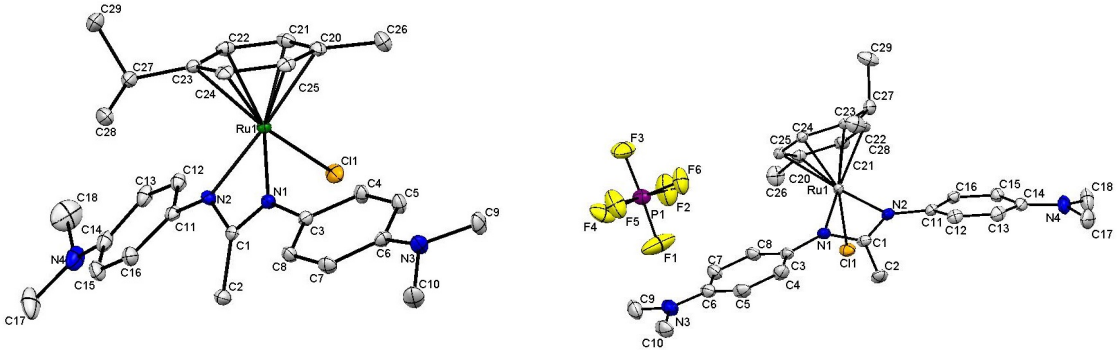

(a) (b)

Abbildung 7.8: *Molekülstruktur von a)* ***38*** *und b)* ***38***PF_6 *im Kristall.*

Diese neue Erkenntnis sowie das Wissen über die intensiven Absorptionsbanden der bekannten Farbstoffe Malachitgrün und Kristallviolett, führte zu einer Versuchsreihe in der die Amidinatoliganden mit der Dimethylaminophenylgruppe (DMAP) substituiert wurden. Es sollte dadurch eine einfachere Isolierung der Amidinylradikalform sowie eine Verschiebung der NIR-Bande zu noch niedrigeren Energien in Richtung des Telekommunikationsfensters erreicht werden. Auf diesem Wege war es nun möglich, den Komplex [RuCl(p-cym)(L_{DMAP}] (**38**) sowie dessen oxidierte Form [RuCl(p-cym)(L_{DMAP}]PF_6 (**38**PF_6) in kristalliner Form zu erhalten und mittels Röntgenstrukturanalyse zu charakterisieren (Abbildung 7.8). Der wesentliche Unterschied der beiden Strukturen betrifft die C-NME_2 und die N-C(CH_3)N Bindungslängen von 1.41 Å in **38** und 1.37 Å in $\mathbf{38}^+$, welche eine Tendenz zur Ausbildung einer p-chinoiden Struktur in der oxidierten Form aufzeigen. UV–vis–NIR-spektroelektrochemische Untersuchungen von $\mathbf{38}^+$ zeigen eine intensive (ϵ = 30000 M^{-1} cm^{-1}) und schmale ($\Delta\nu_{1/2}$ = 1180 cm^{-1}) Absorptionsbande im nahen Infrarotbereich bei λ_{max} = 1230 nm. Weitere Oxidation zu $\mathbf{38}^{2+}$ führt zu einer hypsochrom verschobenen NIR-Bande bei λ_{max} = 994 nm mit noch höherer Intensität (ϵ = 40000 M^{-1} cm^{-1}). Die Absorptionsspektren von $\mathbf{38}^{n+}$ in verschiedenen Oxidationsstufen (n = 0, +1, +2) konnten mit Hilfe von DFT-Rechnungen, welche der NIR-Absorptionsbande in $\mathbf{38}^+$ und $\mathbf{38}^{2+}$ einen überwiegenden Intraligand-Charge-Transfer-(ILCT)-Charakter zuordnen, reproduziert werden (Abbildung 7.9).

Um zu prüfen in wieweit sich die Art des Metalls und der Koordinationsmodus des Liganden auf das Absorptionsverhalten auswirken, wurden ein Platinkomplex von quadratisch-planarer Geometrie Pt(L_{DMAP})$_2$ **39** sowie ein Palladiumkomplex mit „paddle wheel"-Struktur Pd_2(L_{DMAP})$_4$ **40** synthetisiert (Abbildung 7.10) und mittels UV–vis–NIR-spektroelektrochemischer Methoden untersucht.

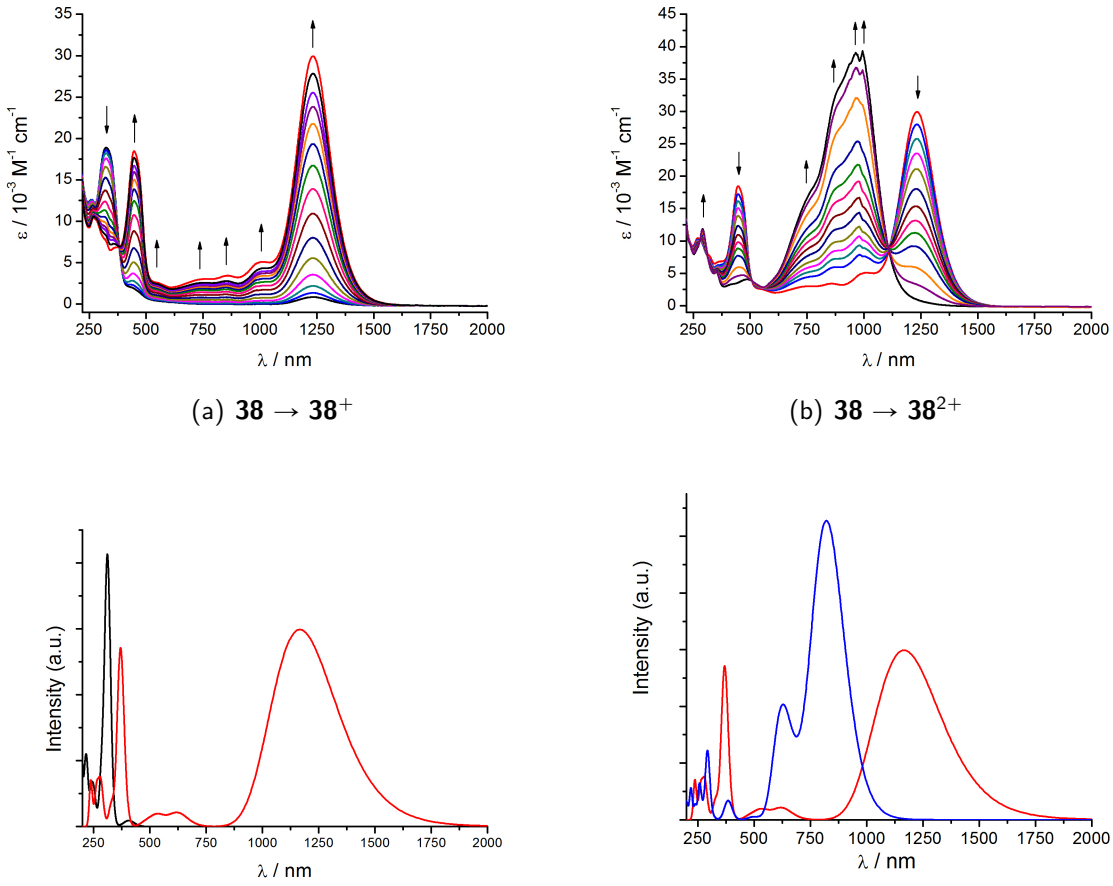

(a) **38** → **38**$^{+}$ (b) **38** → **38**$^{2+}$

(c) **38** (black) → **38**$^{+}$ (red) (d) **38** (red) $^{+}$ → **38**$^{2+}$ (blue)

Abbildung 7.9: *a) und b) UV–vis–NIR-Spektroelektrochemie des Komplexes **38**; c) und d) TD-DFT-berechnete Spektren.*

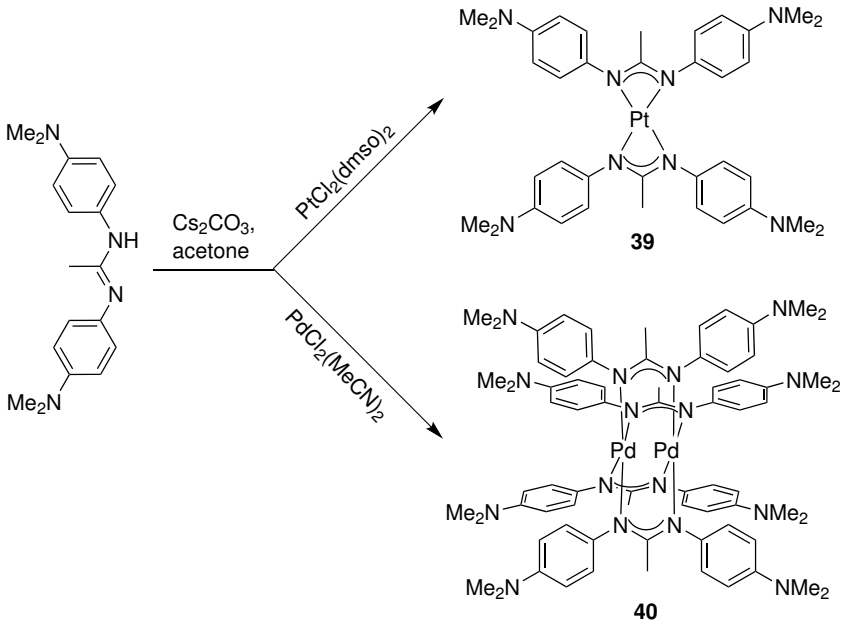

Abbildung 7.10: *Synthese des quadratisch-planaren Platinamidinatokomplexes **39** und des Palladiumamidinatokomplexes mit paddle wheel Struktur **40**.*

Überraschenderweise zeigt die jeweils einfach oxidierte Form der beiden Komplexe ein nahezu identisches Absorptionsmuster wie es im Spektrum von **38**$^+$ zu beobachten ist (Abbildung 7.11), obwohl ESR-spektroskopische Untersuchungen auf einen größeren Metallbeitrag zum SOMO hindeuten. Der auffallendste Unterschied in den Spektren ist die wesentlich geringere Intensität der Absorptionsbanden von **40**$^+$ im Vergleich zu denen von **38**$^+$ und **39**$^+$. Diese Beobachtung führt zu der Annahme, dass der Koordinationsmodus (Chelat vs verbrückend) einen größeren Einfluss auf das Absorptionsverhalten ausübt als das Metall.

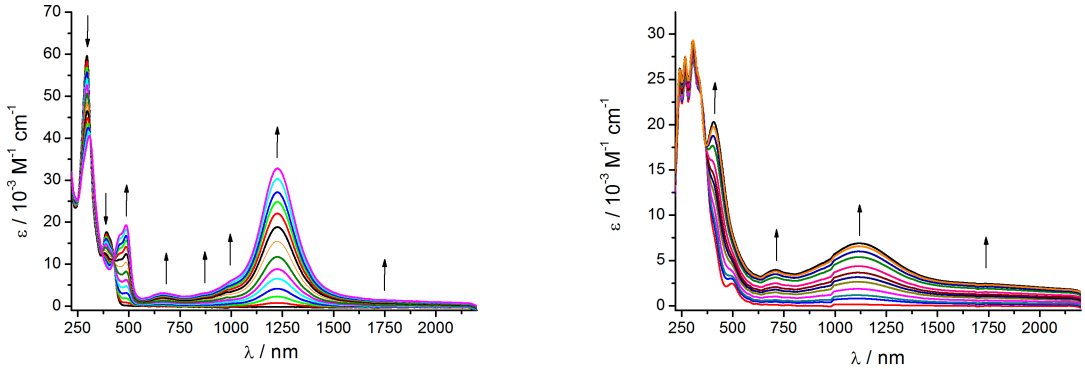

(a) **39** → **39**$^+$ (b) **40** → **40**$^+$

Abbildung 7.11: *UV–vis–NIR-Spektroelektrochemie der Komplexe **39** und **40** in CH_2Cl_2/0.1 M Bu_4NPF_6.*

Zusammenfassend wird in dieser Dissertation die Entdeckung von verschiedenartigen neuen nicht-unschuldigen Liganden beschrieben. Die Synthese sowie die vollständige Charakterisierung dieser neuartigen Ligandensysteme und deren Komplexe führten nicht nur zur Entwicklung neuer chemischer Reaktionen sondern auch zur Enthüllung der besonderen Eigenschaften dieser Verbindungen. So konnte gezeigt werden, dass die terminale Kopplung von 1,3,5-Hexatrienen mit nicht-unschuldigen Chelatfunktionen zu Materialien mit besonderem aber auch sehr kompliziertem magnetischen Verhalten führt, welches zum besseren Verständnis noch intensiverer zukünftiger Untersuchungen bedarf. Insbesondere die Verleihung des Nobelpreises für Chemie 2013 an Karplus, Levitt und Warshel, für die Entwicklung theoretischer Methoden zur Berechnung größerer Struktureinheiten auf Basis des 1,6-Diphenyl-1,3,5-hexatrien-Moleküls, verdeutlicht die Relevanz von π-konjugierterten Modellsystemen. Die neugewonnene Erkenntnis, dass metallstabilisierte Heteroallylradikale intensive Absorptionen im nahen Infrarotbereich aufweisen, sollte ebenfalls einen Anreiz für die Weiterentwicklung solcher Systeme schaffen, da NIR-Farbstoffe im allgemeinen einen weiten Anwendungsbereich besitzen. Eine Substitution der Methylgruppe am Amidinylkohlenstoffatom durch eine donorsubstituierte Phenylgruppe könnte gegebenenfalls mit einer weiteren Verschiebung der NIR-Absorptionsbande in Richtung des Telekommunikationsfensters bei 1300 nm einhergehen.

Auch die entwickelte Strategie zur Schaffung von Koordinationsumgebungen, welche das nicht-unschuldige Verhalten verschiedenster Ligandensysteme ermöglichen, wird vermutlich in der Suche neuer redoxaktiver Moleküle einen Beitrag leisten. In Anbetracht seiner strukturellen Ähnlichkeit mit den heteroallylischen Liganden ist zum Beispiel das Nitrit-Anion ein möglicher nächster Kandidat für das Aufzeigen von nicht-unschuldigem Verhalten unter bestimmten Bedingungen. Ein Nachweis über sein redoxaktives Verhalten würde mit Sicherheit für ein besseres Verständnis biologischer Prozesse, in welchen das Nitrit-Anion involviert ist, z.B. Reaktionen der Nitritreduktase,[120] sorgen.

8 Experimental section

8.1 Instrumentation

8.1.1 EPR spectroscopy

X-band EPR spectra at 9.5 GHz were obtained from Bruker system ESP 300 equipped with a Hewlett-Packard Frequency counter 5350B, a Bruker ER035M gaussmeter for g values determination as a Bruker system EMX and a continuous flow cryostat ESR 900 of Oxford instruments for measurements at liquid helium temperature (4 K). For measurements between 110-300K, same instrumental configuration was used with liquid nitrogen cryostat. A two-electrode capillary[121] served to electrogenerate intermediates for X-band EPR. Simulations of the spectra were done by using the easyspin software package.[122]

8.1.2 NMR spectroscopy

^{1}H-NMR spectroscopy at a frequency of 250 MHz was carried out by Mrs. Török and Mrs. Benzinger on a Bruker AC 250 spectrometer. Tetramethylsilane (TMS) was used as the external standard.

8.1.3 UV-vis-NIR spectroscopy

Absorption spectra were recorded on Shimadzu UV-160 spectrometer (200-3200 nm). For measurements Quartz cuvettes of 1 cm path length were used.

8.1.4 UV-vis-NIR spectroelectrochemistry

UV-vis-NIR and IR spectroelectrochemistry measurements were done by Mr. Jan Fiedler. The measurements were performed under argon atmosphere using an Optically Transparent Thin Layer Electrochemical (OTTLE) cell developed by Mr. Krejcik.[49] The windows of the cell consists of CaF_2 plates. Between the cell working (platinum mesh), auxiliary (platinum mesh) and reference electrodes (silver wire as pseudo reference) are melt-sealed.

8.1.5 Cyclic voltammetry

Cyclic and Differential Pulse voltammetry measurements were performed on an EG&G PAR 273 potentiostat. The measurements were carried out under argon atmosphere in 0.1 M tetra-butylammonium hexafluorophosphate solutions using a three electrode configuration (platinum as working electrode, platinum as counter electrode and silver as pseudoreference electrode). The ferrocene/ferrocenium couple served as the internal reference.

8.1.6 X-ray diffraction

X-ray diffraction experiments were performed by Dr. Wolfgang Frey [Bruker Apex II Duo] with monochromatic Mo-K_α radiation ($\lambda = 0.71073$ Å; Monochromator: Graphite) or Cu-K_α radiation ($\lambda = 1.5406$ Å) at 110(2) K. Structure refinment was performed by Dipl. Chem. Martina Bubrin with the SHELX-97[123] software package. The vibrational ellipsoides are depicted in ORTEP format with 50 % probability. Hydrogen atoms, solvent molecules and counter ions are omitted due to clarity.

8.1.7 DFT calculations

DFT calculations were performed by Dr. Stanislav Záliš (J. Heyrovsky Institute of Physical Chemistry, Academy of Sciences of the Czech Republic, Department of Electrochemistry, Prag). The software package Gaussian 09.C01[124] with the included package Amsterdam Density Functional (ADF2012.01).[125]

8.1.8 Elemental analysis

Elemental analysis was performed on Perkin Elmer Analyzer 240 by Mrs. B. Förtsch.

8.2 Working conditions

8.2.1 Solvents

All metal complexes were synthesized under argon atmosphere using conventional Schlenk techniques. The ligands were synthesized in air. Solvents were dried by refluxing under argon over calcium hydride (dichloromethane and acetonitrile), magnesium oxide (ethanol), sodium (toluene, diethyl ether and n-hexane). They were degassed by freeze-pump-thaw method.

8.2.2 Chemicals

Following compounds were commercially available:
Aldrich: S-(thiobenzoyl)thioglycolic acid, 3-methoxythiophene
ABCR: ruthenium(III) chloride dihydrate, silver(I) tetrafluoroborate, silver(I) hexafluoroantimonate, silver(I) hexafluorophosphate, thalium(I) hexafluorophosphate, p-anisidine, N,N-dimethyl-p-phenylenediamine, 3-(trifluoromethyl)aniline, 3-nitroaniline, di-μ-chlorobis[(p-cymene)chlororuthenium(II)], triethyl orthoacetate, *tert*-butyl chloride

8.3 Synthesis

The complexes with hexafluorophosphate anions used for crystallization were synthesized according to the procedure for the tetrafluoroborate containing complexes, only that $AgPF_6$ was used instead of $AgBF_4$.

$Ru(acac)_2(L_0)$ (**3**):
250 mg (0.66 mmol) of $Ru(acac)_2(MeCN)_2$[40] and 139 mg (0.66 mmol) of N-benzoyl-N'-phenyldiazene were dissolved in a mixture of CH_2Cl_2/toluene (5 : 1) and stirred at 45 °C for 12 h under argon. The solvent was removed and the red material purified by column chromatography (aluminium oxide, CH_2Cl_2/MeCN 200 : 1).

Yield: 213 mg (63 %). Anal. Calcd. for $C_{23}H_{24}N_2O_5Ru$: C 54.22, H 4.75, N 5.50. Found: C 54.15, H 4.65, N 5.14. ^{1}H-NMR (250 MHz, CD_2Cl_2): δ(ppm) = 1.98 (s, 3H), 2.10 (s, 3H), 2.18 (s, 3H), 2.43 (s, 3H), 5.21 (s, 1H), 5.66 (s, 1H), 7.30-7.38 (m, 2H), 7.47-7.60 (m, 3H), 7.75-7.83 (m, 1H), 8.30-8.38 (m, 2H), 8.43-8.64 (m, 2H). ESI-MS m/z calcd. (found) for **3**: 510.07 (510.08).

$[Ru(bpy)_2(L_O)]PF_6$ (**4**PF_6):
200 mg (0.38 mmol) of $Ru(bpy)_2Cl_2{*}2H_2O$[91] and 214 mg (0.85 mmol) of $AgPF_6$ were dissolved in acetone and refluxed for 2 h. The precipitate of AgCl was filtered of through Celite. To the red solution were added 81 mg (0.38 mmol) of N-benzoyl-N'-phenyldiazene and the mixture was stirred at 60 °C for 12 h under argon. After evaporation of the solvent the crude product was purified by column chromatography (aluminium oxide, CH_2Cl_2/MeCN 8 : 2) to give a green material.

Yield 239 mg (81 %). Anal. calcd. for $C_{33}H_{26}F_6N_6OPRu$: 0.1 CH_2Cl_2: C 51.57, H 3.41, N 10.93. Found: C 51.16, H 3.40, N 10.81. ESI-MS m/z calcd. (found) for **4**$^+$: 624.12 (624.12).

$Ru(acac)_2(L_S)$ (**9**):
250 mg (0.66 mmol) of $Ru(acac)_2(MeCN)_2$ and 300 mg (0.66 mmol) bis[α-(phenylhydrazono)phenyl]disulfide were dissolved in a mixture of CH_2Cl_2/toluene (5 : 1) and stirred at 45 °C for 12 h under argon. The solvent was removed and the red-violet material purified by column chromatography (silica, CH_2Cl_2/MeCN 10 : 1).

Yield 212 mg (61 %). Anal. calcd. for $C_{23}H_{24}N_2O_4RuS$: C 52.56, H 4.60, N 5.33. Found: C 52.48, H 4.59, N 5.32. ^{1}H-NMR (250 MHz, acetone-d_6): δ(ppm) = 1.79 (s, 3H), 1.84 (s, 3H), 1.97 (s, 3H), 2.33 (s, 3H), 5.19 (s, 1H), 5.70 (s, 1H), 7.36-7.43 (m, 2H), 7.56-7.67 (m, 4H),

7.95-7.99 (m, 2H), 8.48-8.49 (m, 2H). ESI-MS m/z calcd. (found) for **9**: 526.05(526.06).

$[Ru(bpy)_2(L_S)]BF_4$ (**10**BF_4):
200 mg (0.38 mmol) of $Ru(bpy)_2Cl_2{*}2H_2O$ and 165 mg (0.85 mmol) of $AgBF_4$ were dissolved in acetone and refluxed for 2 h. The precipitate of AgCl was filtered of through Celite. To the red solution were added 173 mg (0.38 mmol) of bis[α-(phenylhydrazono)phenyl]disulfide and the mixture was stirred at 60 °C for 12 h under argon. After evaporation of the solvent the crude product was purified by column chromatography (aluminium oxide, CH_2Cl_2/MeCN 8 : 2) to give a green material.

Yield 226 mg (78 %). Anal. calcd. for $C_{33}H_{26}BF_4N_6SRu$: C 54.55, H 3.61, N 11.57. Found: C 54.11, H 3.26, N 11.38. ESI-MS m/z calcd. (found) for **10**$^+$: 640.10 (640.10).

$(acac)_2Ru\mu$-hte(NNCS-NO_2)$_2$Ru$(acac)_2$ (**13**) and $(acac)_2Ru\mu$-hte(NNCS-$CO_2Et)_2Ru(acac)_2$ (**14**):
250 g (0.66 mmol) of $Ru(acac)_2(MeCN)_2$ and 1 eq. of the corresponding 2-azothiophene were dissolved in CH_2Cl_2/toluene (3:1) and stirred at 55 °C for 12 h under argon. The solvent was removed, and the green material purified by column chromatography (silica, CH_2Cl_2/MeCN 8:2).

13: Yield 236 mg (64 %). Anal. Calcd. for $C_{42}H_{46}N_6O_{14}Ru_2S_2$: C 44.84, H 4.12, N 7.47. Found: C 44.95, H 4.16, N 7.33. ESI-MS m/z calcd. (found) for **13**+Na: 1149.05 (1149.05). ^{1}H-NMR (400 MHz, CD_2Cl_2) δ(ppm): 1.86(s, 2H), 2.00(s, 6H), 2.39(s, 6H), 4.06(s, 6H), 5.20(s, 2H), 5.65(s, 2H), 7.23(s, 2H), 7.55-7.61 (m, 4H), 8.18-8.20(d, 2H), 8.37-8.39(d, 2H), 8.66(s, 2H).

14: Yield 193 mg (50 %). Anal. calcd. for $C_{48}H_{56}N_4O_{14}Ru_2S_2$: C 48.89, H 4.79, N 4.75. Found: C 48.43, H 4.79, N 4.60. ESI-MS m/z calcd (found) for **14**+Na: 1203.12 (1203.12). ^{1}H-NMR (400 MHz, CD_2Cl_2) δ(ppm): 8.00(d, 4H), 7.83(d, 4H), 7.60(d, 2H), 7.20(d, 2H), 5.63(s, 2H), 5.16(s, 2H), 4.37(q, 4H), 4.04(s, 6H), 2.38(s, 6H), 1.98(s, 6H), 1.87(s, 6H), 1.83(s, 6H), 0.92(t, 6H).

$[Ru(bpy)_2($**15**$)]BF_4$ (**19**BF_4), $[Ru(bpy)_2($**16**$)]BF_4$ (**20**BF_4), $[Ru(bpy)_2($**17**$)]BF_4$ (**21**BF_4) and $[Ru(bpy)_2($**18**$)]BF_4$ (**22**BF_4):
$Ru(bpy)_2Cl_2{*}2H_2O$ (200 mg, 0.38 mmol) and (165 mg, 0.85 mmol) of $AgBF_4$ (165 mg, 0.85 mmol) were dissolved in acetone and refluxed for 2 h. The precipitate of AgCl was filtered through Celite. To the red solution were added 2 equivalents (0.76 mmol) of the corresponding triazene and Et_3N (3 eq, 1.14 mmol), and the mixture was stirred at 60 °C for 12 h under argon.

After evaporation of the solvent, the crude products were purified by column chromatography (aluminum oxide, CH_2Cl_2/MeCN 8:2) to give reddish brown solids.

19BF_4: Yield 272 mg (86 %). Anal. calcd. for $C_{34}H_{24}BF_{10}N_7Ru*0.2CH_2Cl_2$: C 48.36, H 2.90, N 11.54. found: C 47.85, H 3.27, N, 11.27. ESI-MS m/z calcd. (found) for **19**$^+$: 746.10 (746.10). ^{1}H-NMR (250 MHz, acetone-d_6) δ(ppm): 7.02-7.05 (d, 2H), 7.15-7.21 (t, 2H), 7.30-7.37 (m, 4H), 7.50-7.54 (dd, 2H), 8.57-8.60 (d, 2H), 8.72-8.75 (d, 2H), 9.22-9.24 (d, 2H).

20BF_4: Yield 225 mg (85 %). Anal. calcd. for $C_{32}H_{26}BF_4N_7Ru$: C 55.18, H 3.76, 14.08. Found: 55.03, 4.01, 14.00. ESI-MS m/z calcd. (found) for **20**$^+$: 609.68 (609.68). ^{1}H-NMR (250 MHz, acetone-d_6) δ(ppm): 8.91 (d, 2H), 8.77 (d, 2H), 8.70 (d, 2H), 8.21 (td, 2H), 8.04 (td, 2H), 7.97 (d, 2H), 7.80 (td, 2H), 7.42 (td, 2H), 7.02 (t, 4H), 6.88 (t, 2H), 6.70 (d, 4H).

21BF_4: Yield 239 mg (83 %). Anal. calcd. $C_{34}H_{30}BF_4N_7O_2Ru$: C 53.98, H 4.00, N 12.96. Found: C 54.02; H 4.20; N, 12.74. ESI-MS m/z calcd. **21**$^+$: 670.15 (670.15). ^{1}H-NMR (250 MHz, acetone-d_6) δ(ppm): 3.66 (s, 6H), 6.57-6.66 (m, 8H), 7.40-7.45 (m, 2H), 7.78-7.84 (m, 2H), 7.93-7.96 (m, 2H), 8.01-8.08 (m, 2H), 8.18-8.25 (m, 2H), 8.70-8.73 (d, 2H), 8.77-8.80 (d, 2H), 8.92-8.95 (m, 2H).

22BF_4: Yield 239 mg (88 %). Anal. calcd. $C_{34}H_{30}BF_4N_7O_2Ru$: C 51.23, H 5.22, N 14.93. Found: C 51.24, H 5.63, N 14.38. ESI-MS m/z calcd. **22**$^+$: 570.19 (570.19). ^{1}H-NMR (250 MHz, acetone-d_6) δ(ppm): 0.75 (s, 9H), 7.25 (t, 2H), 7.73 (d, 2H), 7.90 (m, 4H), 8.22 (t, 2H), 8.60 (d, 2 H), 8.76 (d, 2H), 9.23 (d, 2H).

[Ru(4,4'-EtCO_2-bpy)$_2$(**17**)]BF_4 (**23**BF_4):
Ru(4,4'-EtCO_2-bpy)$_2Cl_2$[92] (150 mg, 0.19 mmol) and of $AgBF_4$ (83 mg, 0.42 mmol) were dissolved in acetone and refluxed for 2 h. The precipitate of AgCl was filtered through Celite. To the red solution were added 2 equivalents (0.38 mmol) of H**17** and Et_3N (3 eq, 0.57 mmol), and the mixture was stirred at 60 °C for 12 h under argon. After evaporation of the solvent, the crude products were purified by column chromatography (aluminum oxide, CH_2Cl_2/MeCN 8:2) to give a reddish brown material.

Yield 155 mg (78 %). ESI-MS m/z calcd. (found) for **23**$^+$: 957.98 (957.98). ^{1}H-NMR (250 MHz, CD_2Cl_2) δ(ppm): 1.44 (m, 12H), 3.66 (s, 6H), 4.48 (m, 8H), 6.53 (m, 8H), 7.81 (m, 4H), 8.14 (m, 2H), 8.91 (m, 2H), 9.01 (m, 4H)

[Ru(pap)$_2$(**17**)]BF_4 (**24**BF_4):
α-Ru(pap)$_2Cl_2$[93] (150 mg, 0.28 mmol) and of $AgBF_4$ (119 mg, 0.85 mmol) were dissolved in acetone and refluxed for 2 h. The precipitate of AgCl was filtered through Celite. To the red solution were added 2 equivalents (0.56 mmol) of H**17** and Et_3N (3 eq, 0.84 mmol), and

the mixture was stirred at 60 °C for 12 h under argon. After evaporation of the solvent, the crude product was purified by column chromatography (aluminum oxide, CH_2Cl_2/MeCN 8:2) to give a reddish brown material.

Yield 117 mg (63 %). ESI-MS m/z calcd. (found) for **24**$^+$: 724.17 (724.17). ^{1}H-NMR (250 MHz, acetone-d_6) δ(ppm): 3.71 (s, 6H), 6.78 (m, 8H), 7.14 (m, 4H), 7.35 (m, 4H), 7.52 (t, 2H), 8.03 (t, 2H), 8.43 (t, 2H), 8.81 (d, 2H), 8.91 (d, 2H).

Ru(p-cym)Cl(**17**) (**25**):
A mixture of $[(Ru(p\text{-}cym)_2Cl_2)]_2$ (150 mg, 0.25 mmol) and $AgBF_4$ (95 mg, 0.5 mmol) was dissolved in 20 ml acetonitrile and stirred for 15 minutes. The precipitate of AgCl was filtered through Celite. To the yellow solution were added 1,3-bis(4-methoxyphenyl)triazene (128 mg, 0.5 mmol) and Et_3N (0.16 ml, 1.14 mmol), and the mixture was stirred at 60 °C for 2 h under argon. After evaporation of the solvent, the crude product was purified by column chromatography (silica, CH_2Cl_2/MeCN 9:1) to give a red solid.

Yield 221 mg (84 %). Anal. calcd. for $C_{24}H_{28}ClN_3O_2Ru$: C 54.70, H 5.36, N 7.97. Found: C 54.25, H 5.58, N 7.88. ESI-MS m/z calcd. (found) for **25**+Na 550.08 (550.08). ^{1}H-NMR (250 MHz, acetone-d_6) δ(ppm): 1.23 (d, 6H), 2.27 (s, 3H), 2.80 (sept., 1H), 3.78 (s, 6H), 5.56 (d, 2H), 6.03 (d, 2H), 6.85 (d, 4H), 7.27 (d, 4H).

Ru(p-cym)CN(**17**) (**26**):
A mixture of **25** (150 mg, 0.28 mmol) and KCN (0.56 mmol) were dissolved in acetonitrile and stirred for 15 h under reflux. The mixture was filtered through Celite. After evaporation of the solvent, the crude product was purified by column chromatography (silica, CH_2Cl_2/MeCN 9:1) to give a yellow material.

Yield 183 mg (64 %). Anal. calcd. for $C_{25}H_{28}N_4O_2Ru$: C 57.90, H 5.64, N 10.80. Found: C 55.80, H 5.52, N 10.64. ESI-MS m/z calcd. (found) for **26**+Na: 541.12 (541.12). ^{1}H-NMR (250 MHz, acetone-d_6) δ(ppm): 1.23 (d, 6H), 3.34 (s, 3H), 2.84 (sept., 1H), 3.77 (s, 6H), 5.71 (d, 2H), 6.07 (d, 2H), 6.85 (d, 4H), 7.18 (d, 4H).

[Ru(p-cym)MeCN(**17**)]SbF_6 (**27**SbF_6):
A mixture of **25** (150 mg, 0.28 mmol) and $AgSbF_6$ (128 mg, 2.80 mmol) were dissolved in acetonitrile and stirred for 15 h under reflux. The precipitate of AgCl was filtered through Celite. After evaporation of the solvent, the crude product was purified by column chromatography (aluminium oxide, CH_2Cl_2/MeCN 8:2) to give a red material.

Yield 183 mg (85 %). Anal. calcd. for $C_{26}H_{31}F_6N_4O_2RuSb$: C 40.64, H 4.07, N 7.29. Found: C 40.48, H 4.23, N 7.47. ESI-MS m/z calcd (found) for **27**$^+$: 533.15 (533.15). ^{1}H-NMR (250 MHz, acetone-d_6) δ(ppm): 1.28 (d, 6H), 2.41 (s, 3H), 2.59 (s, 3H), 2.80-93 (sept., 1H), 3.83 (s, 6H), 6.14-6.16 (d, 2H), 6.52-6.55 (d, 2H), 6.95 (d, 4H), 7.35 (d, 4H).

[Ru(bpy)$_2$(**28**)]PF_6 (**30**PF_6) and [Ru(bpy)$_2$(**29**)]PF_6 (**31**PF_6):
Ru(bpy)$_2Cl_2$*2H_2O (200 mg, 0.38 mmol) and of $AgPF_6$ (165 mg, 0.85 mmol) were dissolved in acetone and refluxed for 2 h. The precipitate of AgCl was filtered through Celite. To the red solution were added HL (2 eq, 0.76 mmol) and Et3N (3 eq, 1.14 mmol), and the mixture was stirred at 60 °C for 12 h under argon. After evaporation of the solvent, the crude product was purified by column chromatography (aluminum oxide, CH_2Cl_2/MeCN 8: 2) to give a reddish brown material.

30PF_6: Yield 270 mg (86 %). Anal. Calcd. for $C_{36}H_{33}PF_6N_6O_2Ru$: C 52.24, H 4.02, N 10.15. Found: C 53.64; H 4.60; N, 9.25. ESI-MS m/z calcd (found) for **30**$^+$: 683.17 (683.17). ^{1}H-NMR(250 MHz, acetone-d_6) δ(ppm): 3.61 (s, 3H), 6.32 (s, 4H), 6.50 (d, 4H), 7.23 (t, 2H), 7.81-7.90 (m, 6H), 8.17 (t, 2H), 8.53 (d, 2H), 8.67 (d, 2H), 9.30 (d, 2H).

31PF_6: Yield 273 mg (84 %). Anal. Calcd. for $C_{37}H_{36}PF_6N_7O_2Ru$: C 51.87, H 4.24, N 11.44. Found: C 51.84; H 4.26; N, 11.33. ESI-MS m/z calcd (found) for **31**$^+$: 712.20 (712.20). ^{1}H-NMR(250 MHz, $CDCl_3$) δ(ppm): 2.54 (s, 6H), 3.74 (s, 6H), 5.26 (d, 4H), 7.08 (d, 2H), 7.43 (t, 4H), 7.70 (d, 2H), 7.81-7.94 (m, 4H), 8.02 (d, 2H), 9.25 (s, 2H).

Ru(p-cym)Cl(**28**) (**32**) and Ru(p-cym)Cl(**29**) (**33**):
A mixture of [(Ru(p-cym)$_2Cl_2$)]$_2$ (100 mg , 0.16 mmol), HL (2 eq, 0.33 mmol) and potassium carbonate (225 mg, 1.63 mmol) was stirred in acetone for 3 h at room temperature under argon. After the solution was filtered through Celite and the solvent was removed the remaining material was recrystallized from CH_2Cl_2/n-hexane to afford red needles.

32: Yield 155 mg (87 %). Anal. Calcd. for $C_{26}H_{31}ClN_2O_2Ru$ (540.07 g/mol): C 57.82, H 5.79, N 5.19. Found: C 57.58; H 5.97; N, 5.23; ESI-MS m/z calcd (found) for **32**-Cl: 505.14 (505.14). ^{1}H-NMR(250 MHz, $CDCl_3$) δ(ppm): 1.19 (d, 6H), 1.70 (s, 3H), 2.16 (s, 3H), 2.60 (sep, 1H), 3.76 (s, 6H), 5.18 (d, 2H), 5.39 (d, 2H), 6.85-6.78 (m, 4H), 7.12-7.18 (m, 4H).

33: Yield 160 mg (85 %). Anal. Calcd. for $C_{26}H_{31}ClN_2O_2Ru$: C 56.98, H 6.02, N 7.38. Found: C 56.28; H 5.94; N, 7.08. ESI-MS m/z calcd. (found) for **33**-Cl: 534.17 (534.17). ^{1}H-NMR(250 MHz, $CDCl_3$) δ(ppm): 1.25 (d, 6H), 1.70 (s, 3H), 2.33 (s, 6H), 2.74 (sep, 1H), 3.82 (s, 6H), 4.91 (d, 2H), 5.12 (d, 2H), 6.80-6.86 (m, 4H), 7.00-7.06 (m, 4H).

[Ru(p-cym)(py)(**28**)]PF_6 (**34**PF_6) and [Ru(p-cym)Cl(**29**)]PF_6 (**35**PF_6):
A mixture of **32** or **33** (1 eq., 0.28 mmol) and $AgPF_6$ (70 mg, 0.28 mmol) was dissolved in 5 ml of pyridine and stirred for 2 h at room temperature. The precipitate of AgCl was filtered through Celite. After evaporation of the solvent, the crude product was purified by column chromatography (silica, CH_2Cl_2/MeCN 6: 4) to give a yellow material.

34PF_6: Yield 169 mg (83 %). Anal. Calcd. for $C_{31}H_{36}F_6N_3O_2PRu$: C 51.10, H 4.98, N 5.77. Found: C 51.02; H 5.13; N, 5.27; ESI-MS m/z calcd (found) for **34**$^+$-pyridine: 505.14 (505.14). ^{1}H-NMR(250 MHz, benzene-$d_6$4) δ(ppm): 1.25 (d, 6H), 1.97 (s, 3H), 2.39 (s, 6H), 2.63 (sep, 1H), 3.80 (s, 6H), 5.37 (d, 2H), 5.54 (d, 2H), 6.82-6.93 (m, 8H), 7.47 (t, 2H), 8.05 (t, 1H), 8.60 (d, 2H).

35PF_6: Yield 161 mg (76 %). Anal. Calcd. for $C_{32}H_{39}F_6N_4O_2PRu$: C 50.72, H 5.19, N 7.39. Found: C 50.14; H 5.19; N, 7.38. ESI-MS m/z calcd (found) for **35**$^+$-pyridine: 634.17 (634.17). ^{1}H-NMR(250 MHz, CD_2Cl_2) δ(ppm): 1.12 (d, 6H), 1.82 (s, 3H), 2.24 (s, 6H), 2.43 (sep, 1H), 3.73 (s, 6), 4.93 (d, 2H), 5.11 (d, 2H), 6.61 (d, 4H), 6.73 (d, 4H), 7.23 (t, 2H), 7.79 (t, 1H), 8.25 (d, 2H).

N,N'-Bis(4-dimethylaminophenyl)-ethanimidamide (H**37**/L_{DMAP}):
A mixture of triethyl orthoacetate (1.08 g, 6.67 mmol), freshly sublimed N,N-dimethyl-p-phenylendiamin (2.00 g, 14.68 mmol) and p-toluenesulfonic monohydrate (127 mg, 0.67 mmol) acid monohydrate was stirred at 140 °C for 5 h. After the ethanol was removed under reduced pressure, the reaction mixture was taken up in a small volume of ethyl acetate and put on a silica column. The column was flushed with 100 % ethyl acetate to remove the impurities. Afterwards the product was eluated with a mixture of 95 % ethyl acetate and 5 % triethylamine. The solvent was removed and the product was recrystallized from CH_2Cl_2/n-hexane to give white crystals.

Yield: 1.34 g (68 %). Anal. calcd. for $C_{18}H_{24}N_4$: C 72.94, H 8.16, N 18.90. Found: C 72.55, H 8.06, 18.73. ^{1}H-NMR (250 MHz, DMSO-d_6) δ(ppm): 1.84 (s, 3H), 2.81 (s, 12H), 6.60 (m, 6H), 7.56 (s, 2H), 8.42 (s, 1H).

Ru(p-cym)Cl(**37**) (**38**):
28: A mixture of $[(Ru(p\text{-}cym)_2Cl_2)]_2$ (100 mg , 0.16 mmol), H**37** (97 mg, 0.33 mmol) and potassium carbonate (225 mg, 1.63 mmol) was stirred in acetone for 3 h at room temperature under argon. After the solution was filtered through Celite and the solvent was removed the remaining material was recrystallized from CH_2Cl_2/n-hexane to afford red needles.

Yield: 159 mg (86 %). Anal. calcd. for $C_{24}H_{28}ClN_5O_2Ru$: C 59.40, H 6.59, N 9.90. Found: C 59.08, H 6.48, N 9.68. ESI-MS m/z calcd. (found) for **28**: 566.17 (566.17).^{1}H-NMR (250

MHz, DMSO-d_6) δ(ppm): 1.05 (d,3H), 1.67 (s, 3H), 2.04 (s,3H), 2.6 (s,13H), 4.70 (d,2H), 4.93 (d,2H), 6.72 (d,4H), 7.43 (d,4H).

[Ru(p-cym)Cl(**37**)]PF_6 (**38**PF_6):
28PF_6: A mixture of **28** (50 mg, 0.09 mmol), and ferrocenium hexafluorophosphate (29 mg ,0.09 mmol) was stirred for 1 h at room temperature. The resulting mixture was layered with n-hexane and the resulting black material recrystallized from CH_2Cl_2/n-hexane. Yield: 49 mg (78 %). Anal. calcd. $C_{24}H_{28}ClF_6N_5O_2PRu$: C 47.29, H 5.24, N 7.88. Found: C 47.12, H 5.30, N 7.75.

$Pt(L_{DMAP})_2$ (**39**) and $Pd_2(L_{DMAP})_4$ (**40**):
39 and **40**: A mixture of $Pt(dmso)_2Cl_2$ or $Pd(MeCN)_2Cl_2$ (1 eq., 0.24 mmol), H**27** (140 mg, 2 eq., 0.48 mmol) and Cs_2CO_3 (782 mg, 10 eq., 2.40 mmol) was stirred in acetone at 60 °C for 15 h. After the solution was filtered through Celite and the solvent was removed the remaining material was purified by column chromatography (CH_2Cl_2/MeOH 9:1) to afford a material product.

39: Yield 150 mg (80 %). Anal. calcd. for $C_{36}H_{48}N_8Pt$: C 54.88, H 6.14, N 14.22. Found: C 54.47, H 5.83, N 13.92. ESI-MS m/z calcd. (found) for **39**: 786.36 (786.36). ^{1}H-NMR(250 MHz, CD_2Cl_2) δ(ppm): 1.79 (s, 6H), 2.82 (s, 24H), 6.42 (m, 8H), 6.62 (m, 8H).

40: Yield 140 mg (84 %). Anal. calcd. for $C_{144}H_{192}N_{16}Pd_2$: C 61.84, H 6.92, N 15.44. Found: C 62.07, H 6.77, N 15.44. ESI-MS m/z calcd. (found) for **39**: 1394.58 (1394.58). ^{1}H-NMR(250 MHz, CD_2Cl_2) δ(ppm): 1.57 (s, 12H), 2.91 (s, 48H), 6.19 (m, 16H), 6.52 (m, 16H).

9 Appendix

9.1 DFT calculated UV–vis–NIR data

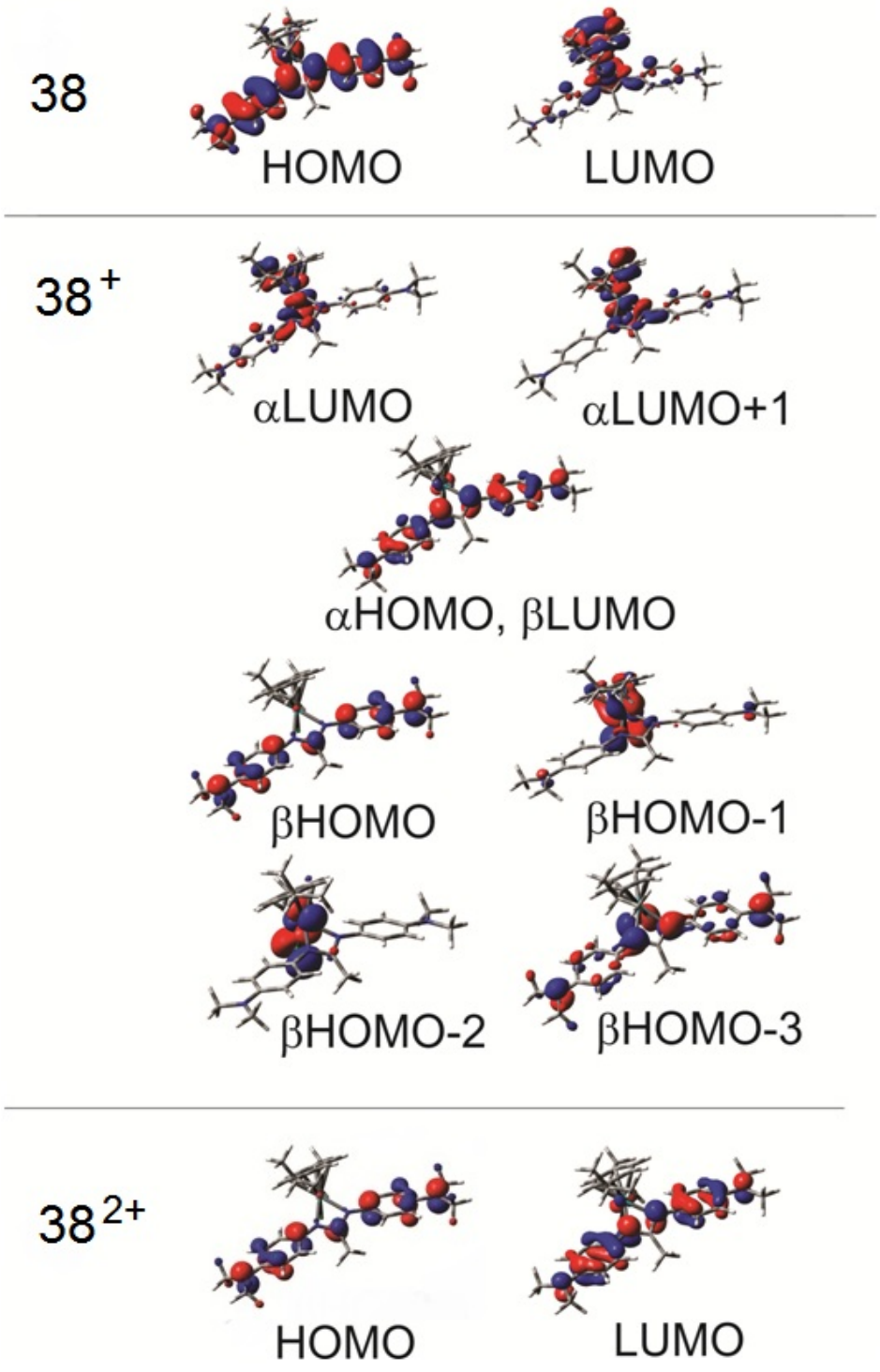

Figure A.1: *Frontier orbitals of* ***38*** *in various oxidation states.*

Table A.1: *TD-DFT (CAM-B3LYP/PCM-CH_2Cl_2) calculated lowest singlet excitation energies (eV) for **34**^{n} with oscillator strengths larger than 0.005. MOs involved in excitations are depicted in Figure* **??**.

n	State	Main contributing excitations (%)	Transition energy eV (nm)	Osc. str.
	^1A	mixed	3.35 (369)	0.010
	^1A	mixed	3.43 (361)	0.007
1	^1A	mixed	3.92 (316)	0.023
	^1A	63 (HOMO → LUMO+3)	4.15 (298)	0.009
	^1A	mixed	4.38 (283)	0.387
	^1A	mixed	4.42 (280)	0.240
	^2A	93 (βHOMO → βLUMO)	1.19 (1039)	0.380
	^2A	91 (βHOMO-1 → βLUMO)	2.00 (619)	0.035
	^2A	87 (βHOMO-2 → βLUMO)	2.16 (575)	0.085
2	^2A	64 (βHOMO-3 → βLUMO)	2.51 (495)	0.016
	^2A	mixed	4.84 (437)	0.013
	^2A	mixed	3.45 (359)	0.036
	^2A	mixed	3.49 (355)	0.100
	^2A	mixed	3.55 (349)	0.097
	^2A	mixed	3.63 (342)	0.114

Table A.2: *TD-DFT (CAM-B3LYP/PCM-CH_2Cl_2) calculated lowest singlet excitation energies (eV) for **38**^{n} with oscillator strengths larger than 0.005. MOs involved in excitations are depicted in Figure* **??**.

n	State	Main contributing excitations (%)	Transition energy eV (nm)	Osc. str.
	^1A	53 (HOMO → LUMO)	3.02 (410 nm)	0.022
		47 (HOMO-2 → LUMO)		
0	^1A	mixed	3.21 (386 nm)	0.007
		mixed	3.96 (331 nm)	0.136
	^1A	63 (HOMO → LUMO+3)	3.98 (311 nm)	0.955
		14 (HOMO → LUMO+2)		
	^2A	96 (βHOMO → βLUMO)	1.06 (1166)	0.688
	^2A	93 (βHOMO-1 → βLUMO)	1.99 (623)	0.047
	^2A	93 (βHOMO-2 → βLUMO)	2.31 (536)	0.038
1	^2A	86 (βHOMO-3 → βLUMO)	2.53 (491)	0.015
	^2A	34 (αHOMO → αLUMO)	4.68 (369)	0.559
		23 (αHOMO → αLUMO+1)		
	^2A	mixed	4.72 (262)	0.013
	^1A	88 (HOMO → LUMO)	1.51 (883 nm)	1.202
	^1A	96 (HOMO-1 → LUMO)	1.77 (702 nm)	0.069
2	^1A	84 (HOMO-2 → LUMO)	1.98 (625 nm)	0.447
	^1A	90 (HOMO-3 → LUMO)	2.49 (498 nm)	0.012
	^1A	37 (HOMO-2 → LUMO+1)	3.17 (391 nm)	0.011
	^1A	55 (HOMO-4 → LUMO)	3.20 (387 nm)	0.049

9.2 Selected crystallographic data

Table A.3: *Selected crystallographic data for **3**, **4**PF_6 and **6**.*

	3	**4**PF_6	**6**
mol formula	$C_{23}H_{24}N_2Ru$, CH_3OH	$C_{33}H_{26}N_6ORu$, PF_6	$C_{26}H_{22}N_4S_2$
Fw	541.55	768.64	454.60
temp (K)	100(2)	100(2)	298(2)
cryst sym	triclinic	monoclinic	-
space group	p-1	P 2_1/c	-
a (Å)	8.7692(4)	12.9570(6)	17.5049(7)
c (Å)	12.2019(8)	16.4648(7)	7.9089(3)
c (Å)	12.5343(9)	16.8146(7)	17.6023(7)
α (°)	70.921(3)	90.00	90.00
β (°)	70.309(3)	101.689(2)	106.705(2)
γ (°)	74.557(3)	90.00	90.00
V (Å^3)	1174.87(13)	3512.7(3)	2334.10(16)
Z	2	4	4
$D_{calc.}$ (g cm^{-3})	1.531	1.453	1294
μ (mm^{-1})	0.709	0.559	0.249
F(000)	556	1548	952
2 Θ range (°)	2.84 to 27.12	1.60 to 30.57	2.37 to 25.15
data / restraints / parameters	5140/0/303	10714/0/478	4128/0/290
GOF	1.096	1.056	1.041
R_1 / wR2 [$I > 2\sigma(I)$]	0.0710/0.1165	0.0301/0.0760	0.0510/0.1416
R_1 / wR2 (all data)	0.1247/0.1356	0.0400/0.0797	0.069/0.1488
largest diff. peak/hole (e Å^{-3})	0.070 and -0.788	0.602 and -0.560	0.198 and -0.237

Table A.4: *Selected crystallographic data for* ***9***, ***10***PF_6 *and* ***11***.

	9	**10**PF_6	**11**
mol formula	$C_{23}H_{24}N_2O_4RuS$	$C_{33}H_{26}N_6RuS$, PF_6	$C_{11}H_9N_3O_3S$
Fw	525.57	784.70	263.27
temp (K)	100(2)	100(2)	110(2)
cryst sym	monoclinic	monoclinic	monoclinic
space group	P $2_1/c$	P $2_1/c$	P 2_1
a (Å)	16.4704(5)	10.5702(19)	10.5350(7)
c (Å)	14.3426(5)	8.8205(15)	4.7067(3)
c (Å)	9.4783(3)	33.470(6)	10.5350(7)
α (°)	90.00	90.00	90.00
β (°)	97.3060(10)	98.853(4)	109.115(4)
γ (°)	90.00	90.00	90.0
V (Å^3)	2220.86(12)	3083.4(9)	573.58(6)
Z	4	4	2
$D_{calc.}$ (g cm^{-3})	1.572	1.690	1.524
μ (mm^{-1})	0.832	0.701	0.286
F(000)	1072	1580	272
2 Θ range (°)	1.89 to 30.56	1.95 to 25.22	1.76 to 28.33
data / restraints / parameters	6771/0/285	4455/0/460	2838/1/164
GOF	1.045	1.134	1.010
R_1/wR2 [I $> 2\sigma$(I)]	0.0230/0.0586	0.0626/0.1106	0.0297/0.0678
R_1/wR2 (all data)	0.0262/0.0586	0.1160/0.1378	0.0362/0.0710
largest diff. peak/hole (e Å^{-3})	0,625 and -0.625	0.865 and -1.303	0.247 and -0.166

Table A.5: *Selected crystallographic data for **13**, H**17** and **21**ClO_4.*

	13	H**17**	**21**ClO_4
mol formula	$C_{55}H_{56}Cl_6N_6O_{14}Ru_2S_2$	$C_{14}H_{15}N_3O_2$	$C_{34}H_{30}N_7O_2Ru$, ClO_4
Fw	1504.02	257.29	769.17
temp (K)	100(2)	100(2)	100(2)
cryst sym	triclinic	triclinic	monoclinic
space group	P-1	P-1	P $2_1/c$
a (Å)	8.0073(16)	8.0372(8)	13.6529(10)
c (Å)	10.204(2)	13.2094(8)	24.171(2)
c (Å)	21.155(4)	13.3212(10)	21.9477(16)
α (°)	92.71(3)	74.058(3)	90.00
β (°)	99.11(3)	76.296(3)	114.993(5)
γ (°)	101.16(3)	86.325(2)	90.00
V (Å^3)	1.496	1321.16(18)	6564.6(9)
Z	1	4	8
$D_{calc.}$ (g cm^{-3})	1.496	1.294	1.557
μ (mm^{-1})	0.818	0.089	0.617
F(000)	762	544	3136
2 Θ range (°)	1.96 to 24.99	1.60 to 26.61	1.33 to 30.57
data / restraints / parameters	5607/0/397	5361/2/355	20079/1/913
GOF	1.059	1.020	1.054
R_1/wR2 [I $> 2\sigma$(I)]	0.0658/0.1766	0.0493/0.1178	0.0485/0.1241
R_1/wR2 (all data)	0.0777/0.1864	0.0763/0.1339	0.0664/0.1412
largest diff. peak/hole (e Å^{-3})	3.502 and -0.914	0.582 to -0.315	2.714 to -1.526

Table A.6: *Selected crystallographic data for **27**SbF_6, **30**OTf and **31**PF_6.*

	27SbF_6	**30**OTf	**31**PF_6
mol formula	$C_{26}H_{31}N_4O_2Ru$, SbF_6	$C_{36}H_{33}N_6O_2Ru$, CF_3O_3S	$C_{37}H_{36}N_7O_2Ru$, PF_6
Fw	768.37	831.82	856.77
temp (K)	100(2)	100(2)	100(2)
cryst sym	triclinic	triclinic	monoclinic
space group	P-1	P-1	P $2_1/c$
a (Å)	11.8226(7)	11.8341(11)	10.4457(9)
c (Å)	15.5126(9)	12.6582(12)	25.550(2)
c (Å)	16.8764(10)	13.7257(12)	14.3640(12)
α (°)	101.939(3)	108.658(5)	90.00
β (°)	106.896(3)	90.236(5)	105.719(4)
γ (°)	90.795(3)	112.067(5)	90.00
V (Å^3)	2888.4(3)	1787.1(3)	3690.2(5)
Z	4	2	4
$D_{calc.}$ (g cm^{-3})	1.767	1.546	1.542
μ (mm^{-1})	1.528	0.565	0.543
F(000)	1520	848	1744
2 Θ range (°)	1.35 to 27.50	1.58 to 27.50	1.76 to 30.55
data / restraints / parameters	13272/1/733	8205/0/481	11285/0/491
GOF	1.038	1.063	1.189
R_1/wR2 [I $> 2\sigma$(I)]	0.0362/0.0825	0.0759/0.2005	0.0286/0.0772
R_1/wR2 (all data)	0.0404/0.0863	0.0759/0.2282	0.0286/0.0760
argest diff. peak/hole (e Å^{-3})	3.318 and - 3.887	3.659 and -3.485	0.527 and -0.888

Table A.7: *Selected crystallographic data for* ***32***, ***33*** *and* ***34***BPh_4.

	32	**33**	**34**BPh_4
mol formula	$C_{26}H_{31}ClN_2O_2Ru$	$C_{27}H_{34}ClN_3O_2Ru$	$C_{31}H_{36}N_3O_2Ru$, $C_{24}H_{20}B$
Fw	540.05	569.09	902.91
temp (K)	100(2)	100(2)	100(2)
cryst sym	monoclinic	monoclinic	orthorhombic
space group	P $2_1/c$	P $2_1/n$	P 2_1
a (Å)	18.0517(9)	10.1139(7)	10.8622(6)
c (Å)	8.4356(5)	21.8548(16)	14.2128(8)
c (Å)	32.3705(18)	12.5129(9)	29.6107(17)
α (°)	90.00	90.00	90.00
β (°)	94.858(2)	111.302(3)	90.00
γ (°)	90.00	90.00	90.00
V (Å^3)	4911.6(5)	2576.9(3)	4571.4(4)
Z	8	4	4
$D_{calc.}$ (g cm^{-3})	1.461	1.467	1.312
μ (mm^{-1})	0.772	0.741	3.119
F(000)	2224	1176	1888
2 Θ range (°)	1.62 to 25.08	1.86 to 30.75	2.98 to 66.43
data / restraints / parameters	8668/6/585	7919/0/314	7780/0/565
GOF	1.030	1.084	1.026
R_1/wR2 [I $> 2\sigma$(I)]	0.0490/0.0965	0.0207/0.0518	0.0198/0.0482
R_1/wR2 (all data)	0.0934/0.1070	0.0241/0.0551	0.0210/0.0479

Table A.8: *Selected crystallographic data for H**37**, **38**PF_6 and **39**.*

	H**37**	**38**PF_6	**39**
mol formula	$C_{18}H_{24}N_4$	$C_{28}H_{37}ClN_4Ru$, PF_6	C_{36} H_{46} N_8 Pt, $2(CH_2Cl_2)$
Fw	296.41	711.11	884.85
temp (K)	100(2)	100(2)	100(2)
cryst sym	orthorhombic	monoclinic	monoclinic
space group	$Pca2_1$	P $2_1/n$	C $2/m$
a (Å)	8.7719(6)	15.0164(9)	24.345(5)
c (Å)	12.0135(7)	9.1681(6)	7.5156(17)
c (Å)	31.1285(19)	22.7126(14)	11.526(2)
α (°)	90.00	90.00	90.00
β (°)	90.00	107.685(3)	113.104(9)
γ (°)	90.00	90.00	90.00
V (Å^3)	3280.4(4)	2979.1(3)	1939.7(7)
Z	8	4	2
$D_{calc.}$ (g cm^{-3})	1.200	1.585	1.515
μ (mm^{-1})	0.073	0.733	3.792
F(000)	1280	1452	892
2 Θ range (°)	0.073	1.88 to 30.55	1.82 to 28.43
data / restraints / parameters	6660/1/416	9037/0/378	2580/6/191
GOF	1.083	1.066	1.099
R_1/wR2 [I $> 2\sigma$(I)]	0.0569/0.01389	0.0385/0.0837	0.0435/0.1084
R_1/wR2 (all data)	0.0618/0.1389	0.0589/0.0938	0.0456/0.1101
largest diff. peak/hole (e Å^{-3})	0.321 and -0.265	1.260 and -1.112	3.213 and -1.674

Table A.9: *Selected crystallographic data* ***38*** *and* ***40****.*

	38	**40**
mol formula	$C_{28}H_{37}ClN_4Ru$	$C_{72}H_{89}N_{16}Pd_2$
Fw	566.14	1391.39
temp (K)	100(2)	100(2)
cryst sym	monoclinic	monoclinic
space group	P $2_1/c$	P $2/n$
a (Å)	13.6648(9)	17.6921(15)
c (Å)	8.0090(5)	19.5211(17)
c (Å)	24.0310(15)	20.7805(17)
α (°)	90.00	90.00
β (°)	97.112(3)	91.570(5)
γ (°)	90.00	90.00
V (Å^3)	2609.8(3)	7174.3(11)
Z	4	4
$D_{calc.}$ (g cm^{-3})	1.441	1.288
μ (mm^{-1})	0.727	4.444
F(000)	1176	2900
2 Θ range (°)	1.63 to 29.00	2.26 to 66.37
data / restraints / parameters	6759/0/315	12261/0/833
GOF	1.188	1.057
R_1, wR2 [I $> 2\sigma$(I)]	0.0402/0.1002	0.0357/0.0886
R_1, wR2 (all data)	0.0468/0.1036	0.0472/0.0937
largest diff. peak/hole (e Å^{-3})	1.501 and -2.900	0.662 and - 0.668

9.3 Abbreviations

IVCT	Inter Valence Charge Transfer
MLCT	Metal to Ligand Charge Transfer
LMCT	Ligand to Metal Charge Transfer
ILCT	Intra Ligand Charge Transfer
LLCT	Ligand to Ligand Charge Transfer
HOMO	highest occupied molecular orbital
LUMO	lowest unoccupied molecular orbital
SOMO	singly occupied molecular orbital
exp.	experimental
calc.	calculated
nat.	natural
dppf	1,1'-bis(diphenylphosphino)ferrocene
eq.	equivalent
L	ligand
M	metal
eq	equivalent
dmso	dimethylsulfoxide
pap	2-phenylazopyridine
bpy	2,2'-bipyridine
acac	acetylacetonato
p-cym	p-cymene
DMAP	dimethylaminophenyl
py	pyridine
EPR	electron paramagnetic resonance
NMR	nuclear magnetic resonance
SQUID	superconducting quantum interference device
DDQ	2,3-dichloro-5,6-dicyano-p-benzoquinone
vs	versus
V	volt
eV	electron volt
h	hour
UV	ultra violet
vis	visible
NIR	near infrared
ppm	part per milion
Z	atomic number
mT	militesla
mV	milivolt
°	degree
°C	degree centigrade

References

[1] Kaim, W.; Schwederski, B. *Coord. Chem. Rev.* **2010**, *254*, 1580–1588.

[2] Guo, Y.; Langlois,; M., J.; Goddard, W. A. *Science* **1998**, *239*, 896.

[3] Zhao, H.; Bazile, J.; Mervin, J.; Galan-Mascaros, J. R.; Dunbar, K. R. *Angew. Chem. Int. Ed.* **2003**, *42*, 1015–1018.

[4] Geoffroy, G. L.; Wrighton, M. S. *Organometallic Photochemistry*; Academic Press, New York, 1979.

[5] (a) Praneeth, V. K. K.; Ringenberg, M. R.; Ward, T. R. *Angew. Chem. Int. Ed.* **2012**, *51*, 10228–10234; (b) Chirik, P.; Wieghardt, K. *Science* **2010**, *327*, 749–745; (c) Lyaskovskyy, V.; de Bruin, B. *ACS Catalysis* **2012**, *2*, 270–279.

[6] Munha, R. F.; Zarkesh, R. A.; Heyduk, A. F. *Dalton Trans.* **2013**, *42*, 3751–3766.

[7] Jørgensen, C. K. *Coord. Chem. Rev.* **1966**, *1*, 164–178.

[8] (a) Kaim, W.; Matheis, W. *J. Chem. Soc., Chem. Commun.* **1991**, 597–598; (b) Cloke, F. G. N.; Hanson, G. R.; Henderson, M. J.; Hitchcock, P. B.; Raston, C. L. *J. Chem. Soc., Chem. Commun.* **1989**, 1002–1003.

[9] Chaudhuri, P.; Verani, C. N.; Bill, E.; Bothe, E.; Weyhermüller, T.; Wieghardt, K. *J. Am. Chem. Soc.* **2001**, *123*, 2213–2223.

[10] Sixt, T.; Sieger, M.; Krafft, M. J.; Bubrin, D.; Fiedler, J.; Kaim, W. *Organometallics* **2010**, *29*, 5511–5516.

[11] Ward, M. D.; McCleverty, J. A. *J. Chem. Soc., Chem. Commun.* **2002**, 275.

[12] Kaim, W. *Inorg. Chem.* **2011**, *50*, 9752–9765.

[13] (a) Das, A.; Scherer, T. M.; Mobin, S. M.; Kaim, W.; Lahiri, G. K. *Chem. Eur. J.* **2012**, *18*, 11007–11018; (b) Bhattacharya, S.; Gupta, P.; Basuli, F.; Pierpont, C. G. *Inorg. Chem.* **2002**, *41*, 5810–5816.

[14] Kaim, W.; Kasack, V. *Angew. Chem. Int. Ed.* **1982**, *21*, 700–705.

[15] (a) Lorkovic, I. M.; Wrighton, M. S.; Davis, W. M. *J. Am. Chem. Soc.* **1994**, *116*, 6220–6228; (b) Boyer, J. L.; Cundari, T. R.; DeYonker, N. J.; Rauchfuss, T. B.; Wilson, S. R. *Inorg. Chem.* **2009**, *48*, 638–645.

[16] (a) Ray, K.; Bill, E.; Weyhermüller, T.; Wieghardt, K. *J. Am. Chem. Soc.* **2005**, *127*, 5641–5654; (b) Kapre, R. R.; Bothe, E.; Weyhermüller, T.; DeBeer George, S.; Muresan, N.; Wieghardt, K. *Inorg. Chem.* **2007**, *46*, 7827–7839; (c) Sproules, S.; Benedito, F. L.; Bill, E.; Weyhermüller, T.; DeBeer George, S.; Wieghardt, K. *Inorg. Chem.* **2009**, *48*, 10926–10941.

[17] Kaim, W.; Fiedler, J. *Chem. Soc. Rev.* **2009**, *38*, 3373–3382.

[18] Remenyi, C.; Kaupp, M. *J. Am. Chem. Soc.* **2005**, *127*, 11399–11413.

[19] (a) Hinchliffe, A. *Theoret. chim. Acta* **1967**, *7*, 25–31; (b) Boguslawski, K.; Jacob, C. R.; Reiher, M. *J. Chem. Theo. Comp.* **2011**, *7*, 2740–2752; (c) Kossmann, S.; Neese, F. *J. Phys. Chem. A* **2010**, *114*, 11768–11781.

[20] (a) Gerson, F. *High Resolution E.S.R. Spectroscopy*; Wiley / Verlag Chemie, Weinheim, 1970; p 137; (b) Symons, M. *Chemical and Biochemical Aspects of Electron-Spin Resonance Spectroscopy*; Van Nostrand-Reinhold, New York, 1987.

[21] Jochen, A. *J. Phys. Chem.* **2012**, *126*, 150902.

[22] Stone, A. J. *Mol. Phys.* **1964**, *7*, 311.

[23] Kaim, W. *Eur. J. Inorg. Chem.* **2012**, *2012*, 343–348.

[24] (a) Darmon, J. M.; Stieber, S. C. E.; Sylvester, K. T.; Fernandez, I.; Lobkovsky, E.; Semproni, S. P.; Bill, E.; Wieghardt, K.; DeBeer, S.; Chirik, P. J. *J. Am. Chem. Soc.* **2012**, *134*, 17125–17137; (b) Shaffer, D. W.; Szigethy, G.; Ziller, J. W.; Heyduk, A. F. *Inorg. Chem.* **2013**, *52*, 2110–2118.

[25] Mondal, P.; Ehret, F.; Bubrin, M.; Das, A.; Mobin, S. M.; Kaim, W.; Lahiri, G. K. *Inorg. Chem.* **2013**, *52*, 8467–8475.

[26] (a) Kaim, W.; Sieger, M.; Greulich, S.; Sarkar, B.; Fiedler, J.; Záliš, S. *J. Organomet. Chem.* **2010**, *695*, 1052–1058; (b) Bock, H.; Dieck, H. *Angew. Chem. Int. Ed.* **1966**, *5*, 520–522; (c) Koten, G. V.; Vrieze, K. 1,4-Diaza-1,3-butadiene (Î±-Diimine) Ligands: Their Coordination Modes and the Reactivity of Their Metal Complexes. In *1,4-Diaza-1,3-butadiene (Î±-Diimine) Ligands: Their Coordination Modes and the Reactivity of Their Metal Complexes*; Stone, F., West, R., Eds.; Academic Press, 1982; Vol. 21, pp 151 – 239.

[27] Scarborough, C. C.; Wieghardt, K. *Inorg. Chem.* **2011**, *50*, 9773–9793.

[28] (a) Ernst, S.; Kaim, W. *J. Am. Chem. Soc.* **1986**, *108*, 3578–3586; (b) Kaim, W. *Coord. Chem. Rev.* **2002**, *230*, 127–139.

[29] Spikes, G. H.; Bill, E.; Weyhermüller, T.; Wieghardt, K. *Angew. Chem. Int. Ed.* **2008**, *47*, 2973–2977.

[30] (a) Balch, A. L. *J. Am. Chem. Soc.* **1973**, *95*, 2723–2724; (b) Pierpont, C. G.; Lange, C. W. *Prog. Inorg. Chem* **1994**, *41*, 331.

[31] (a) Eisenberg, R.; Gray, H. B. *Inorg. Chem.* **2011**, *50*, 9741–9751; (b) Vlcek, A. *Coord. Chem. Rev.* **2010**, *254*, 1357.

[32] (a) Maroney, M. J.; Trogler, W. C. *J. Am. Chem. Soc.* **1984**, *106*, 4144–4151; (b) Gross, M. E.; Trogler, W. C.; Ibers, J. A. *J. A* **1981**, *103*, 192–193; (c) Gross, M. E.; Trogler, W. C.; Ibers, J. A. *Organometallics* **1982**, *1*, 732–739; (d) Overbosch, P.; Van Koten, G.; Spek, A. L.; Roelofsen, G.; Duisenberg, A. J. M. *Inorg. Chem.* **1982**, *21*, 3908–3913.

[33] (a) Poddel'sky, A. I.; Cherkasov, V. K.; Abakumov, G. A. *Coord. Chem. Rev.* **2009**, *253*, 291–324; (b) Lu, C. C.; Bill, E.; Weyhermüller, T.; Bothe, E.; Wieghardt, K. *Inorganic Chemistry* **2007**, *46*, 7880–7889.

[34] Kaim, W. *Coord. Chem. Rev.* **2001**, *219-221*, 463–488.

[35] (a) Düerr, S.; Hählein, U.; Schobert, R. *J. Organomet. Chem.* **1993**, *458*, 89–96; (b) Pilia, L.; Artizzu, F.; Espa, D.; Marchio, L.; Mercuri, M. L.; Serpe, A.; Deplano, P. *Dalton Trans.* **2010**, *39*, 8139–8142.

[36] Roy, S.; Sieger, M.; Sarkar, B.; Schwederski, B.; Lissner, F.; Schleid, T.; Fiedler, J.; Kaim, W. *Angew. Chem. Int. Ed.* **2008**, *47*, 6192–6194.

[37] Barton, D. H. R.; Ducker, J. W.; Lord, W. A.; Magnus, P. D. *J. Chem. Soc., Perkin Trans. 1* **1976**, 38–42.

[38] Modelli, A.; Jones, D.; Rossini, S.; Distefano, G. *Tetrahedron* **1984**, *40*, 3257–3262.

[39] (a) Bowman, W. R.; Forshaw, J. A.; Hall, K. P.; Kitchin, J. P.; Mott, A. W. *Tetrahedron* **1996**, *52*, 3961–3972; (b) Molina, C. L.; Chow, C. P.; Shea, K. J. *Syn. Comm.* **1997**, *27*, 3197.

[40] Kasahara, Y.; Hoshino, Y.; Shimizu, K.; S., G. P. *Chem.Lett.* **1990**, *19*, 381–384.

[41] Sullivan, B. P.; Salmon, D. J.; Meyer, T. J. *Inorg. Chem.* **1978**, *17*, 3334–3341.

[42] Askari, S. H.; Moss, S. F.; Taylor, D. R. *J. Chem. Soc., Perkin Trans. 1* **1981**, 360–365.

[43] Wolkoff, P.; Hammerum, S.; Callaghan, P. D.; Gibson, M. S. *Can. J. Chem.* **1974**, *52*, 879–883.

[44] Jocelyn, P. C. *Eur. J. Biochem.* **1967**, *2*, 327–331.

[45] Sarkar, B.; Patra, S.; Fiedler, J.; Sunoj, R. B.; Janardanan, D.; Lahiri, G. K.; Kaim, W. *J. Am. Chem. Soc.* **2008**, *130*, 3532–3542.

[46] Li, W. K.; Zhou, G. D.; Mak, T. C. W. *Advanced Structural Inorganic Chemistry*; Oxford University Press: Oxford, U.K., 2008; p 522.

[47] Patra, S.; Sarkar, B.; Mobin, S. M.; Kaim, W.; Lahiri, G. K. *Inorg. Chem.* **2003**, *42*, 6469.

[48] (a) Patra, S.; Sarkar, B.; Maji, S.; Fiedler, J.; Urbanos, F. A.; Jimenez-Aparicio, R.; Kaim, G. K., W.; Lahiri *Che. Eur. J.* **2006**, *12*, 489; (b) Kar, S.; Sarkar, B.; Ghumaan, S.; Janardanan, D.; van Slageren, J.; Fiedler, J.; Puranik, V. G.; Sunoj, R. B.; Kaim, W.; Lahiri, G. K. *Chem. Eur. J.* **2005**, *11*, 4901.

[49] Krejcik, M.; Danek, M.; Hartl, F. *Electroanal. Chem.* **1991**, *317*, 179.

[50] (a) Haga, M.; Dodsworth, E. S.; Lever, A. B. P. *Inorg. Chem.* **1986**, *25*, 447–453; (b) Masui, H.; Lever, A. B. P.; Auburn, P. R. *Inorg. Chem.* **1991**, *30*, 2402–2410.

[51] Ehret, F.; Bubrin, M.; Hübner, R.; Schweinfurth, D.; Hartenbach, I.; Záliš, S.; Kaim, W. *Inorg. Chem.* **2012**, *51*, 6237–6244.

[52] (a) Dong, L.; Duckett, S. B.; Ohman, K. F.; Jones, W. D. *J. Am. Chem. Soc.* **1992**, *114*, 151–160; (b) Bianchini, C.; Herrera, V.; Jimenez, M. V.; Meli, A.; Sanchez-Delgado, R.; Vizza, F. *J. Am. Chem. Soc.* **1995**, *117*, 8567–8575; (c) Choi, M. G.; Angelici, R. J. *Organometallics* **1992**, *11*, 3328–3334.

[53] (a) Gates, B. C.; Katzer, G.; A., S. C. *Chemistry of Catalytic Processes*; McGraw-Hill, New York, 1979; (b) Prins, R.; J De Beer, V. H. J.; Somojai, G. A. *Catal. Rev. Sci. Eng.* **1989**, *31*, 1; (c) Benson, J.; Schrader, G. L.; Angelici, R. J. *J. Mol. Catal.* **1995**, *96*, 283.

[54] (a) Dullaghan, C. A.; Sun, S.; Carpenter, G. B.; Weldon, B.; Sweigart, D. A. *Angew. Chem. Int. Ed.* **1996**, *35*, 212–214; (b) Rauchfuss, T. B. *Prog. Inorg. Chem* **2007**, *39*, 259; (c) Hachgenei, J. W.; Angelici, R. J. *Angew. Chem. Int. Ed.* **1987**, *26*, 909.

[55] (a) Warshel, A.; Karplus, M. *J. Am. Chem. Soc.* **1972**, *94*, 5612–5625; (b) Hudson, B. S.; Kohler, B. E.; Schulten, K. *Excited States* **1982**, *6*, 1.

[56] Kirchner, K.; Calhorda, M. J.; Schmid, R.; Veiros, L. F. *J. Am. Chem. Soc.* **2003**, *125*, 11721–11729.

[57] (a) Reppe, W.; Schlichting, O.; Klager, K.; Toepel, T. *Justus Liebigs Annalen der Chemie* **1948**, *560*, 1–92; (b) Reppe, W.; Schlichting, O. *Justus Liebigs Annalen der Chemie* **1948**, *560*, 104–116; (c) Reppe, W.; Schlichting, O.; Meister, H. *Justus Liebigs Annalen der Chemie* **1948**, *560*, 93–104.

[58] Liu, S. H.; Xia, H.; Wen, T. B.; Zhou, Z.; Jia, G. *Organometallics* **2003**, *22*, 737–743.

[59] Abe, M. *Chem. Rev.* **2013**, *113*, 7011–7088.

[60] Kaim, W.; Lahiri, G. K. *Angew. Chem. Int. Ed.* **2007**, *46*, 1778–1796.

[61] (a) Kaim, W.; Bruns, W.; Poppe, J.; Kasack, J. *Mol. Struct.* **1993**, *292*, 221; (b) *Mixed Valency Systems–Applications in Chemistry, Physics and Biology (Ed.: K. Prassides)*; Kluwer Academic Publisher, 1991.

[62] (a) Creutz, C.; Taube, H. *J. Am. Chem. Soc.* **1969**, *91*, 3988; (b) Creutz, C.; Taube, H. *J. Am. Chem. Soc.* **1973**, *95*, 1086.

[63] Taube, H. *Angew. Chem. Int. Ed.* **1984**, *23*, 329.

[64] Robin, M. B.; Day, P. *Adv. Inorg. Chem. Radiochem.* **1967**, *10*, 247.

[65] Salaymeh, F.; Berhane, S.; Yusof, R.; de la Rosa, R.; Fung, E. Y.; Matamoros, R.; Lau, K. W.; Zheng, Q.; Kober, E. M.; Curtis, J. C. *Inorg. Chem.* **1993**, *32*, 3895–3908.

[66] (a) Lay, P. A.; Magnuson, R. H.; Taube, H. *Inorg. Chem.* **1988**, *27*, 2364–2371; (b) Ye, S.; Sarkar, B.; Duboc, C.; Fiedler, J.; Kaim, W. *Inorg. Chem.* **2005**, *44*, 2843–2847.

[67] Mosher, P. J.; Yap, G. P. A.; Crutchley, R. J. *Inorg. Chem.* **2001**, *40*, 1189–1195.

[68] Fraysse, S.; Coudret, C.; Launay, J.-P. *J. Am. Chem. Soc.* **2003**, *125*, 5880–5888.

[69] (a) Launay, J.-P. *Chem. Soc. Rev.* **2001**, *30*, 386–397; (b) Fagalde, F.; Katz, N. E. *Polyhedron* **1995**, *14*, 1213–1220.

[70] (a) Scheiring, T.; Kaim, W.; Olabe, J. A.; Parise, A. R.; Fiedler, J. *Inorg. Chim. Acta* **2000**, *300–302*, 125–130; (b) Callahan, R. W.; Keene, F. R.; Meyer, T. J.; Salmon, D. J. *J. Am. Chem. Soc.* **1977**, *99*, 1064–1073.

[71] Sarkar, B.; Kaim, W.; Klein, A.; Schwederski, B.; Fiedler, J.; Duboc-Toia, C.; Lahiri, G. K. *Inorg. Chem.* **2003**, *42*, 6172–6174.

[72] Demadis, K. D.; Hartshorn, C. M.; Meyer, T. J. *Chem. Rev.* **2001**, *101*, 2655–2686.

[73] (a) D'Alessandr, D. M.; Keene, F. R. *Chem. Rev.* **2006**, *106*, 2270–2298; (b) D'Alessandro, D. M.; Keene, F. R. *Chem. Soc. Rev.* **2006**, *35*, 424–440.

[74] Hush, N. S. *Prog. Inorg. Chem* **1967**, *8*, 391.

[75] (a) Richard Keene, F. *Chem. Soc. Rev.* **1998**, *27*, 185–194; (b) Kelso, L. S.; Reitsma, D. A.; Keene, F. R. *Inorg. Chem.* **1996**, *35*, 5144–5153.

[76] Zelewsky, A. *Stereochemistry of Coordination Compounds*; Wiley, Chichester, 1996.

[77] (a) Ernst, S.; Kasack, V.; Kaim, W. *Inorg. Chem.* **1988**, *27*, 1146–1148.

[78] Maji, S.; Sarkar, B.; Mobin, S. M.; Fiedler, J.; Urbanos, F. A.; Jimenez-Aparicio, R.; Kaim, W.; Lahiri, G. K. *Inorg. Chem.* **2008**, *47*, 5204–5211.

[79] Maji, S.; Sarkar, B.; Patra, S.; Fiedler, J.; Mobin, S. M.; Puranik, V. G.; Kaim, W.; Lahiri, G. K. *Inorg. Chem.* **2006**, *45*, 1316–1325.

[80] Matharu, A.; Huddleston, P.; Jeeva, S.; Wood, M.; Chambers-Asman, D. *Dyes and Pigments* **2008**, *78*, 89–92.

[81] Weil, J. A.; Bolton, J. R. *Paramagnetic Resonance*; John Wiley & Sons, Inc., Hoboken, New Jersey, 2007; p 190.

[82] (a) Levin, E. *Mag. Mater.* **2013**, *340*, 113–119; (b) Yoon, J. H.; Lee, W. R.; Ryu, D. W.; Lee, J. W.; Yoon, S. W.; Suh, B. J.; Kim, H. C.; Hong, C. S. *Inorg. Chem.* **2011**, *50*, 10777–10785; (c) Jia, H.-P.; Li, W.; Ju, Z.-F.; Zhang, J. *Chem. Commun.* **2008**, 371–373; (d) Huang, Y.-G.; Yuan, D.-Q.; Pan, L.; Jiang, F.-L.; Wu, M.-Y.; Zhang, X.-D.; Wei,; Gao, Q.; Lee, J. Y.; Li, J.; Hong, M.-C. *Inorg. Chem.* **2007**, *46*, 9609–9615.

[83] (a) Khusniyarov, M. M.; Bill, E.; Weyhermüller, T.; Bothe, E.; Wieghardt, K. *Angew. Chem. Int. Ed.* **2011**, *50*, 1652–1655; (b) Das, A.; Scherer, T. M.; Mondal, P.; Mobin, S. M.; Kaim, W.; Lahiri, G. K. *Chem. Eur. J.* **2012**, *18*, 14434–14443.

[84] Roberts, P. B.; Winter, N. J. *J. Chem. Soc., Perkin. Trans. 2* **1979**, 1353–1362.

[85] Edelmann, F. T. *Adv. Orgmet. Chem.* **2008**, *57*, 183–352.

[86] (a) Carrasco, M.; Curado, N.; Maya, C.; Peloso, R.; Rodriguez, A.; Ruiz, E.; Alvarez, S.; Carmona, E. *Angew. Chem. Int. Ed.* **2013**, *52*, 3227–3231.

[87] (a) Kotera, A.; Morita, T.; Aoyagi, S.; Kakiuchi, Y.; Nagakura, S.; Kume, K. *Chem. Abstr.* **1961**, *55*, 15128; (b) Kiro, Z. B.; Teterin, Y. A.; Nikolenko, L. N.; Stepanov, B. I. *Chem. Abstr.* **1972**, *78*, 135210z; (c) Perrin, D. D. *Dissociation Constants of Organic Bases in Aqueous Solution*; Butterworths, London, 1965.

[88] Hauber, S.-O.; Lissner, F.; Deacon, G. B.; Niemeyer, M. *Angew. Chem. Int. Ed.* **2005**, *44*, 5871–5875.

[89] Kumar, R. K.; Ali, M. A.; Punniyamurthy, T. *Org. Lett.* **2011**, *13*, 2102–2105.

[90] Brand, J. C.; Roberts, B. P. *J. Chem. Soc., Perkin. Trans. 2* **1982**, 1549–1558.

[91] Starr, J. T.; Rai, G. S.; Dang, H.; McNelis, B. *J. Syn. Comm.* **1999**, *27*, 3197.

[92] Wolfbauer, G.; Bond, A. M.; MacFarlane, D. R. *Inorg. Chem.* **1999**, *38*, 3836–3846.

[93] Bao, T.; Krause, K.; Krause, R. A. *Inorg. Chem.* **1988**, *27*, 759–61.

[94] (a) Goswami, S.; Mukherjee, R.; Chakravorty, A. *Inorg. Chem.* **1983**, *22*, 2825–2832; (b) Ohsawa, Y.; DeArmond, M. K.; Hanck, K. W.; Morris, D. E.; Whitten, D. G.; Neveux, P. E. *J. Am. Chem. Soc.* **1983**, *105*, 6522–6524.

[95] Wu, S.-H.; Burkhardt, S. E.; Yao, J.; Zhong, Y.-W.; Abru na, H. D. *Inorg. Chem.* **2011**, *50*, 3959–3969.

[96] Banerjee, P.; Das, S.; Fanwick, P. E.; Goswami, S. *J. Orgmet. Chem.* **2006**, *691*, 2915–2923.

[97] Kobayashi, M.; Uneyama, K. *J. Org. Chem.* **1996**, *61*, 3902–3905.

[98] Kelley, M. R.; Rohde, J.-U. *Inorg. Chem.* **2013**, *52*, 2564–2580.

[99] Sudha, L.; Senthil Selvan, J.; Subramanian, K.; Steiner, T.; Koellner, G.; Srinivasan, N.; Ramdas, K. *Acta Crystallographica Section C* **1995**, *51*, 2323–2325.

[100] Jolly, W. L. *Modern Inorganic Chemistry*; McGrawhill, 1984.

[101] Ehret, F.; Bubrin, M.; Záliš, S.; Kaim, W. *Angew. Chem. Int. Ed.* **2013**, *52*, 4673–4675.

[102] Borek, C.; Hanson, K.; Djurovich, P. I.; Thompson, M. E.; Aznavour, K.; Bau, R.; Sun, Y.; Forrest, S. R.; Brooks, J.; Michalski, L.; Brown, J. *Angew. Chem. Int. Ed.* **2007**, *46*, 1109–1112.

[103] (a) Qian, G.; Zhong, Z.; Luo, M.; Yu, D.; Zhang, Z.; Wang, Z. Y.; Ma, D. *Advanced Materials* **2009**, *21*, 111–116; (b) Godbert, N.; Dattilo, D.; Termine, R.; Aiello, I.; Bellusci, A.; Crispini, A.; Golemme, A.; Ghedini, M. *Chem. Asian J.* **2009**, *4*, 1141–1146.

[104] (a) Mayerhöffer, U.; Deing, K.; Gruß, K.; Braunschweig, H.; Meerholz, K.; WÃ¼rthner, F. *Angew. Chem. Int. Ed.* **2009**, *48*, 8776–8779; (b) Mor, G. K.; Kim, S.; Paulose, M.; Varghese, O. K.; Shankar, K.; Basham, J.; Grimes, C. A. *Nano Lett.* **2009**, *9*, 4250–4257; (c) Hyun, B.-R.; Zhong, Y.-W.; Bartnik, A. C.; Sun, L.; AbruÃ±a, H. D.; Wise, F. W.; Goodreau, J. D.; Matthews, J. R.; Leslie, T. M.; Borrelli, N. F. *ACS Nano* **2008**, *2*, 2206–2212.

[105] Tessler, N.; Medvedev, V.; Kazes, M.; Kan, S.; Banin, U. *Science* **2002**, *295*, 1506.

[106] (a) Ran, C.; Xu, X.; Raymond, S. B.; Ferrara, B. J.; Neal, K.; Bacskai, B. J.; Medarova, Z.; Moore, A. *J. Am. Chem. Soc.* **2009**, *131*, 15257–15261; (b) McDonnell, S. O.; O'Shea, D. F. *Org. Lett.* **2006**, *8*, 3493–3496; (c) Kiyose, K.; Kojima, H.; Urano, Y.; Nagano, T. *J. Am. Chem. Soc.* **2006**, *128*, 6548–6549.

[107] Samanta, A.; Vendrell, M.; Das, R.; Chang, Y.-T. *Chem. Commun.* **2010**, *46*, 7406–7408.

[108] Umezawa, K.; Nakamura, Y.; Makino, H.; Citterio, D.; Suzuki, K. *J. Am. Chem. Soc.* **2008**, *130*, 1550–1551.

[109] Yue, W.; Zhao, Y.; Shao, S.; Tian, H.; Xie, Z.; Geng, Y.; Wang, F. *J. Mater. Chem.* **2009**, *19*, 2199–2206.

[110] (a) Marshall, K. L.; Painter, G.; Lotito, K.; Noto, A. G.; Chang, P. *Mol. Cryst. Liq. Cryst.* **2006**, *454*, 47; (b) Kaim, W.; Kasack, V.; Binder, H.; Roth, E.; Jordanov, J. *Angew. Chem. Int. Ed.* **1988**, *27*, 1174–1176; (c) Kasack, V.; Kaim, W.; Binder, H.; Jordanov, J.; Roth, E. *Inorg. Chem.* **1995**, *34*, 1924–1933; (d) Moscherosch, M.; Waldhoer, E.; Binder, H.; Kaim, W.; Fiedler, J. *Inorg. Chem.* **1995**, *34*, 4326–4335.

[111] Kaim, W. *Coord. Chem. Rev.* **2011**, *255*, 2503–2513, Controlling photophysical properties of metal complexes: Towards molecular photonics.

[112] Zollinger, H. *Color Chemistry: Synthesis, Properties and AApplication of Organic Dyes and Pigments*, 3rd ed.; Helvetica Chimica Acta, Zürich, 2003.

[113] Das, H. S.; Weisser, F.; Schweinfurth, D.; Su, C.-Y.; Bogani, L.; Fiedler, J.; Sarkar, B. *Chem. Eur. J.* **2010**, *16*, 2977–2981.

[114] Langmuir, I. *J. Am. Chem. Soc.* **1919**, *41*, 868–934.

[115] Barker, J.; Kilner, M.; Gould, R. O. *J. Chem. Soc., Dalton Trans.* **1987**, 2687–2694.

[116] Berry, J. F.; Bill, E.; Bothe, E.; Cotton, F. A.; Dalal, N. S.; Ibragimov, S. A.; Kaur, N.; Liu, C. Y.; Murillo, C. A.; Nellutla, S.; North, J. M.; Villagran, D. *J. Am. Chem. Soc.* **2007**, *129*, 1393–1401.

[117] Cotton, F. A.; Gu, J.; Murillo, C. A.; Timmons, D. J. *J. Am. Chem. Soc.* **1998**, *120*, 13280–13281.

[118] Grischer, H.; Scherson, D. A. *J. Electroanal. Chem.* **1985**, *188*, 33–38.

[119] Deibel, N.; Hohloch, S.; Sommer, M. G.; Schweinfurth, D.; Ehret, F.; Braunstein, P.; Sarkar, B. *Organometallics* **2013**, *32*, 7366–7375.

[120] Basu, S. et al. *Nat. Biol. Chem.* **2007**, *3*, 785–794.

[121] Kaim, W.; Ernst, S.; Kasack, V. *J. Am. Chem. Soc.* **1990**, *112*, 173–178.

[122] Stoll, S.; Schweiger, A. *J. Magn. Reson* **2006**, *178*, 42–55.

[123] M., S. G.; SHELXL97, *Program for the Refinement of Crystal Structure: University Göttingen, Germany 1997*, year.

[124] Frisch, M. J. et al. Gaussian, Inc., Wallingford, CT, 2009.

[125] te Velde, G.; Bickelhaupt, E. J., F. M.and Baerends; Fonseca, G.; Gisbergen, S. J. A.; Snijders, J. G.; T., Z. *J. Comput. Chem.* **2001**, *22*, 931.